Development of a Methodology for Performance Optimisation and Manufacturing Sensitivity Studies for Radial Flow Turbocharger Compressors for 21st Century Legislation

Thesis submitted in accordance with the requirements of the University of Lincoln for the degree of Doctor in Philosophy

by

OSAROBO FAMOUS OKHUAHESOGIE
December 2018

Academic Supervisors: Prof. Ronald Bickerton
Prof. Chris Bingham
Dr Mike Riley

Industrial Supervisor: Mr Frank Heyes

School of Engineering, University of Lincoln, LN6 7TS, Lincoln, England

UNIVERSITY OF LINCOLN

LIST OF PUBLICATIONS

Conference Papers

1. O. F. Okhuahesogie, J. Stewart, F.J.G. Heyes, P.E. Roach. "Design Optimisation of two-stage turbocharger compressor impeller", *KTP Associates Conference*, Brighton, UK, 14th June 2012.*

2. O. F. Okhuahesogie, J. Stewart, M.J.W. Riley, F. Heyes, P. Roach. "A 1-D Analytical Code for the Design and Multi-objective Optimisation of high-pressure Compressors within Two-Stage Turbochargers for Marine Applications". *Institution of Mechanical Engineers 11th International Conference on Turbochargers and Turbo charging*, London, UK, May 12 – 14, 2014.

3. O. F. Okhuahesogie, M.J.W. Riley, F.J.G. Heyes, P. Roach. "Implementation of a High Throughput Computing System for Engineering Design Optimisation: A Case Study of a Turbocharger Centrifugal Compressor Aerodynamic Multi-Objective Optimisation". *KTP Associates Conference*, Brighton, UK, 19th June 2014.

**Received award for best paper presentation*

DECLARATION

I hereby declare that all of the work contained within this thesis has not been submitted for any other qualification.

Signed: _____

Date: _____

ABSTRACT

The use of algorithmic optimisation techniques whereby several designs are evaluated automatically in batches using Computational Structural Mechanics (CSM) and or Computational Fluid Dynamics (CFD) modelling to improve performance, has become an integral part of turbomachinery design process. Designing radial compressors for better performance as well as manufacturing the impeller such that there are no discrepancies between the designed surface and machined surface represents a significant challenge for the industry. Accounting for geometric variability (to model manufacturing errors) during the design/optimisation phase where hundreds of candidate geometries are evaluated is costly due to the large number of calculations required to analyse the possible combinations of manufacture errors for each new geometry design. This thesis addressed the problem by separating the design phase from the manufacture uncertainty calculations phase, focusing on a common 5-axis milling type error – *undercut*; and using a low cost high throughput computing cluster to meet the computational requirements of both phases.

A bespoke parametric CAD algorithm was developed to automate the geometry creation during the optimisation phase. The Differential Evolution for Multi-Objective Optimisation (DEMO) algorithm was used to drive the optimisation calculations. In-house meshing software from Napier Turbochargers Ltd, subsequently referred to as Napier, was used to mesh the computational domain, which was then solved using a commercial CFD solver. The compressor in the high-pressure (HP) stage of a two-stage turbocharger was optimised, and shows significant improvements in measured parameters - up to 1.6 points of efficiency gain and 20% increase in map width, respectively. The calculations were carried out on a HTCondor cluster of 8 Linux workstations.

Moreover, a study on the sensitivity of radial compressor aerodynamic performance to the presence of an undercut on the impeller surface was also carried out. In-house software from Napier was used to create an undercut on the impeller surface by modifying the CAD geometry file. The impact of the undercut on performance was quantified using detail 3D CFD analysis. Various undercut height and width levels at 13 different locations on the blade surface were analysed for three compressor designs. A unique sensitivity distribution for each compressor impeller is calculated and used to create a variable tolerance map on the impeller surface. This approach was shown to facilitate savings in cost by reducing scrap rate.

In addition, a bespoke 1-D algorithm for estimating the size of a radial compressor impeller required to meet a design mass flow and pressure ratio at a given rotor speed was developed. The model can be used

as a preliminary tool when designing a new compressor (where there is no previous experimental or numerical data). The algorithm is based on a combination of fundamental turbomachinery physics equations, correlations extracted from literature and statistical modelling.

Finally, an algorithm for calculating the flow area and air mass flow of the low pressure (LP) and high pressure (HP) compressors and turbines in a two-stage turbocharger required to meet a diesel engine specification was developed. The algorithm was used to validate the flow specification of a two-stage turbocharger for a test diesel engine.

Keywords: *Two-stage turbocharger, radial compressor, vane-less diffuser, optimisation, differential evolution, manufacturing, impeller undercut, sensitivity analysis, geometry parameterisation*

CONTENT

NOMENCLATURE

Abbreviations

AC	Aftercooler
AMI	Arbitrary Meshing Interface
ASTM	American Society of Testing and Materials
BDC	Bottom Dead Centre
BMEP	Brake Mean Effective Pressure
BSAC	Brake Specific Air Consumption
BSFC	Brake Specific Fuel Consumption
CAD	Computer Aided Design
CAE	Computer Aided Engineering
CAM	Computer Aided Manufacturing
CFD	Computational Fluid Dynamics
CFL	Courant–Friedrichs–Lewy
CNC	Computer Numerical Controlled
CSM	Computational Structural Mechanics
DE	Differential Evolution
DEF	Diesel Exhaust Fluid
DEMO	Differential Evolution for Multi-Objective Optimisation
DPF	Diesel Particulate Filter
EGR	Exhaust Gas Recirculation
FEA	Finite Element Analysis
GA	Genetic Algorithm
GUI	Graphical User Interface
HP	High Pressure
HPC	High Pressure Compressor or High Performance Computing
HPT	High Pressure Turbine
HTC	High Throughput Computing
IC	Intercooler
ICE	Internal Combustion Engine
IGV	Inlet Guide Vane

IMO	International Maritime Organisation
KTP	Knowledge Transfer Partnership
LE	Leading Edge
LP	Low Pressure
LPC	Low Pressure Compressor
LPT	Low Pressure Turbine
MPM	Mixing Plane Model
MRF	Multiple Reference Frame
OOP	Object Oriented Programming
RANS	Reynolds Averaged Navier-Stokes
SCR	Selective Catalytic Reduction
SMM	Sliding Mesh Model
SRF	Single Rotating Frame
TDC	Top Dead Centre
TDMA	Tri-Diagonal Matrix Algorithm
TE	Trailing Edge

Subscripts

0	Stagnation
1	Inlet
2	Outlet
s	Isentropic or shroud
h	Hub
ts	Total-to-Static
tt	Total-to-Total
b	Blade
m	Meridional
rms	Root mean square
acr	Actual compression ratio
ocr	Overall compression ratio
a	Air
f	Fuel

th	Thickness
me	Meridional
mech	Mechanical
corr	Corrected

List of Symbols

H	Total energy
T	Temperature
P	Pressure
V	Volume
U	Blade speed
C	Absolute velocity
W	Relative velocity
$\dot{W}$	Work output
$\dot{m}$	Mass flow rate
C_p	Specific heat capacity at constant pressure
R	Gas constant or radius
s.t.p	Standard temperature and pressure
b	Blade height
N	Angular speed
L	Axial length
x, y, z	Cartesian coordinates
rpm	revolution per minute
$\vec{\boldsymbol{r}}$	Reference measurement coordinate
$\vec{\boldsymbol{r}}_{\boldsymbol{o}}$	Position vector
M	Mach number
$\vec{w}$	Relative angular velocity
$\vec{v}_r$	Relative velocity
$\vec{v}$	Absolute velocity
$\vec{u}_r$	Velocity due to moving frame
p	Pressure
S_h	Energy source term
$\bar{\bar{\tau}}_r$	Viscous stress

$\vec{F}$	External body force
E_r	Relative internal energy
H_r	Relative total energy
n_b	Number of blades
V_s	Swept volume of engine cylinder
η_v	Engine volumetric efficiency
S_r	Scavenging ratio
A_F	Flow area

Greek Symbols

α	Gas absolute flow angle
β	Gas relative flow angle
β_b	Blade angle
η	Efficiency
θ	Blade wrap angle or tangential component of velocity
λ	Work input coefficient
μ	Slip factor
ρ	Density
γ	Gas constant
σ	Standard deviation
ω	Angular velocity
π	PI or compression ratio
∇	Del operator
Ψ	Rake angle
Φ	Blade thickness rotation angle
ε	Intercooler effectiveness

ACKNOWLEDGEMENT

It has been very challenging studying as a part-time and having a full-time job. I would first of all like to thank Dr Jill Stewart who was my initial PhD supervisor between 2012 and 2013 for making me aware of the Knowledge Transfer Partnership (KTP) project which also offered me the opportunity to study for a PhD.

I would also like to thank Dr Mike Riley for his guidance and support during the critical times of this research work between 2013 and 2015 for introducing me to various concepts such as multi-objective optimisation and high throughput computing, which formed the back-bone of this research.

I have to also mention the KTP scheme for providing the resources to attend relevant training and conferences during this research study between 2012 and 2014.

I would also like to thank my supervisor Professor Ronald Bickerton for guiding me through this research. Special thanks for all his valuable ideas in our late evening meetings and helping to highlight key contributions from the research. I would also like to thank him for helping me to polish my thesis into a finished product and encouraging me to press on in the most difficult times.

I would also like to thank Prof. Chris Bingham for helping to re-arrange this thesis flow and highlighting the contributions from this research.

Special thanks also go to my industrial supervisor at Napier Turbochargers Ltd Mr Frank Heyes for his constant technical and moral support throughout the entire period of the PhD research. Also, thanks to Dr P.E. Roach for all his advice and helpful discussions.

I would like to thank all my friends and family for their support throughout my PhD. A special thanks to my wife Omoye Okhuahesogie for her patience and support, and my daughter Olivia Iyobosa Okhuahesogie who was born on 6th December 2016. You both made my PhD journey worthwhile.

Finally, I would like to thank God almighty for the grace and patience to complete this PhD.

CHAPTER 1
INTRODUCTION

This thesis specifically addresses the following:

- The need to design optimised two-stage turbochargers
- The need to reduce impeller manufacture scrap rate
- The need to design a new compressor using no prior empirical knowledge
- The need to size two-stage turbochargers for a given diesel engine power specification

1. The Need to Design Optimised Two-Stage Turbochargers

Problem Background

Napier Turbochargers Ltd (subsequently referred to as Napier) design, manufacture and provide support for the operation of industrial turbochargers. Napier is a major supplier of industrial turbochargers for diesel engines in the marine shipping industry. New product development at Napier is driven by customer requirements and legislations within customer industries. New International Maritime Organisation (IMO) legislation III, which will be effective from 2021 (previously 2016), requires the reduction of NOx emissions from marine vessels to around 20% of current levels, as shown in Figure 1.1.

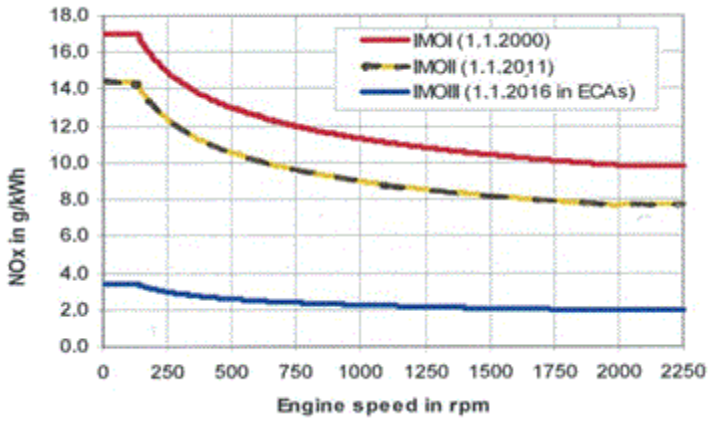

Figure 1.1 – IMO III NOx legislation for marine diesel engines [1]

The latest legislation has led researchers to investigate new optimisation design techniques which can be classified as follows – in-cylinder technologies, air systems and after-treatment technologies [2]. In-cylinder technologies include those for advanced fuel injection systems, advanced combustion, Miller cycle combined with variable valve timing and electronic control. Air systems technologies include high boost pressure using two-stage turbo charging providing pressure ratios of up to 8:1, high efficiency single stage turbochargers, use of variable air systems such as waste gate, variable geometry turbocharger with bypass valves and exhaust gas recirculation (EGR). After treatment technologies include the use of selective catalytic reduction (SCR) or diesel particulate filters (DPF).

Two-stage turbo charging represents a very promising method of meeting the IMO III requirements when combined with an in-cylinder technique, such as Miller timing and other after treatment techniques. In a two-stage turbocharger, the air is compressed in the low pressure (LP) compressor, cooled, and then compressed again in the high pressure (HP) compressor to a higher pressure ratio. Since the density of air is increased in the LP stage, the HP compressor is usually smaller than the LP compressor for a given volumetric flow. In the Miller cycle, during the engine intake stroke, the inlet valve is closed before the piston head reaches the bottom dead centre (BDC) of the cylinder. The air expands during the intake stroke, cooling the charged air in the process. This results in a lower combustion air temperature and lower compression ratio. The reduced combustion air temperature lowers NOx formation during combustion.

Using a two-stage turbocharger on a diesel engine with Miller timing compensates for the mass flow and compression ratio loss as a result of the Miller timing, and also allows for a larger expansion ratio in the power stroke, resulting in a high thermal efficiency [3]. Studies carried out by Codan E. *et al.* [1] and Yi Cui *et al.* [4] reveals the benefits of combining Miller timing with a two-stage turbocharger to reduce NOx production in marine diesel engines. Codan E. *et al.* [1] also show the benefits afforded by using an after treatment technique such as SCR along with a two-stage turbocharger to reduce NOx formation in marine diesel engines. The authors [1, 4] show that the adverse effect of placing an SCR unit before the turbine in a single stage turbocharger is reduced if the SCR unit is placed between the LP and HP turbines of a two-stage turbocharger. It is shown that the SCR unit adversely affects the transient operation of a diesel engine if placed before the HP turbine of a two-stage turbo charger. This is a result of the SCR unit removing the pulse energy from the engine and slowing the response of the HP turbine to engine exit conditions, which leads to a lag in the HP compressor responding to engine air demand, for example,

during rapid acceleration. Moreover, it was also shown that an SCR unit performs best if installed between the HP and LP turbine, as a result of more favourable temperatures.

In addition to the legislation requirements for NOx emissions and the need for two-stage turbochargers, the increasing demand by engine manufacturers for turbomachinery with higher efficiency, pressure-ratio, design mass flow and wider operating map, has driven the need to improve existing design methodologies. High performance turbomachinery must be delivered at a low cost so that engine manufacturers can remain competitive in the market place. For Napier, it is important for the design process of turbochargers to be as short and cheap as possible so that new and high performance products can be introduced into the market in a competitive timescale.

Problem Definition

The new IMO legislation encourages diesel engine manufacturers for the marine industry to use two-stage turbo chargers as a method of reducing NOx emissions. Presently, Napier does not have experience of designing two-stage turbochargers. In particular, the design of the high pressure (HP) stage is a new challenge since the inlet conditions are not at standard atmospheric conditions. Moreover, a wide operating map is desired for the HP stage, particularly during transient operations or rapid acceleration when the diesel engine will rapidly require increased air input. The HP compressor is more responsive to transient operations due to its smaller size and lower inertia. A vane-less diffuser is required for the HP compressor as it allows for a wider operating map [5]. A vane-less diffuser does not limit the maximum mass flow through the compressor which is controlled by the impeller, however, minimum mass flow can be limited by stall in the vane-less diffuser [5].

In addition to the incoming IMO legislation, it is also important for Napier to remain competitive in the market by designing high efficiency products quickly ahead of its competitors. This need is driven by competitor manufacturers who constantly seek higher efficiencies, a wider operating map and high flow capacity compressor designs. There is therefore a need to improve the design methodology of existing and new products at Napier without increasing the design cost. A major source of expense in the design of industrial machines is the high license cost of commercial design software. Moreover, computing hardware required to carry out analysis quickly adds to design costs. A primary contribution of the work in this thesis is the development of algorithms and techniques to reduce analysis overhead and overall design cost. The two objectives of this research are:

- Research and realize a system for the design and multi-objective optimisation of industrial machines, such as radial compressors. The system should meet the following requirements:
    - Low cost
    - Shorten the time to carry out batch CFD/FEA analysis
    - Be reliable with high availability
- To be able to use the developed techniques to design a highly efficient compressor for the HP stage of a new two-stage turbocharger for a marine diesel engine.

A bespoke parametric CAD program "RC_CAD" written in C++ has been developed as part of this research. The program replaces ANSYS BladeGen in the design cycle and removes BladeGen licence cost. "RC_CAD" is a command line program used to create the impeller and vane-less diffuser profile of a radial compressor. Napier's in-house meshing program, written in FORTRAN, is used to mesh the geometry created by the bespoke CAD program. A commercial CFD solver TBLOCK [6] is used to resolve the flow field. Although TBLOCK is commercial, it is cheaper than mainstream commercial CFD solvers. In addition, no additional licence costs are incurred by running multiple instances of TBLOCK. The open source post-processing software ParaView [7] is used to visualise the flow field. A modified version [8] of an open source optimisation algorithm – Differential Evolution for Multi-Objective Optimisation (DEMO) [9] is used to drive the optimisation process. A computer program called "Mapper" is also developed during this research. This algorithm runs the CAD and meshing programs and then executes the flow solver for different operating conditions to produce the performance data of each compressor CAD model over a range of mass flows at constant rotor speed. The algorithm then calculates 8 objective functions based on the 23 CAD input parameters for DEMO to evolve new CAD models to meet the target objectives. Another script "condorManager.py" is developed to manage the communication between DEMO and HTCondor [28] cluster jobs. All of the tools used in the optimisation system are command line driven with each executable less than 1.3MB, making it readily deployable on an HTCondor cluster.

The compressor in the high-pressure (HP) stage of a two-stage turbocharger has already been optimised using algorithms implemented during this thesis. Significant improvements in measured parameters were achieved viz. - up to 1.6 points of efficiency gain and 20% increase in compressor map width, respectively.

2. The Need to Reduce Impeller Manufacture Scrap Rate

Problem Background

Flank milling is used to machine impellers at Napier, and scrapping impellers due to machining errors during 5-axis flank milling represents a significant cost. The aim of this research is to reduce the current scrap rate by at least 50%. Errors during 5-axis milling can be due to many factors such as tool deflection, tool wear, feed drives vibration, tool trajectory path programming error and so on [10]. Examples of errors common during 5-axis milling include undercut, overcut and surface roughness [10].

Current practice at Napier is to scrap impellers where the designed surface deviates from the machined surface above a set tolerance limit of 0.1mm. Five axis flank milling computer numerical controlled (CNC) machines are commonly used during the manufacture of aerospace parts and turbomachinery parts such as turbine impellers and compressor impellers. Compared to 3-axis CNC machines where collisions between the cutting tool and impeller are common, 5-axis milling provides better control of the cutting tool there by reducing collisions [11]. Flank milling type errors can be categorised into two groups – error due to tool trajectory (e.g. overcut, undercut, surface roughness) and error due to tool geometry (e.g. tool deflections, tool energy, flank forces) [10]. 5-axis flank milling of centrifugal compressor impeller blade can introduce geometric variability to the blade. This variability can lead to reduction in performance or sometimes rejection of the manufactured impeller if the variability is outside of the tolerance limit for the design [12]. It is therefore necessary to make "robust" compressor designs where there is no significant change in compressor performance due to deviation between the designed surface and machined surface. Designing compressors to be insensitive to variations introduced by the machining process require modelling the variations during the CFD design process. This will significantly increase the design time up to 10 times. The major research objective of this work is to model the sensitivities of designs to such errors, thus reducing both computational design and development time whilst also reducing scrap rate and increasing understanding of the effect of these errors on performance.

Problem Definition

The computational time required to design a new impeller blade and then model various possible milling defects to gain confidence of the robustness of the design is not a feasible engineering solution. Instead, this thesis is focused on quantifying the impact of a particular type of machining error – *undercut*, on the

performance of a centrifugal compressor. An undercut happens when excess metal is left on a machined surface compared to the designed surface. In this case, the study is focused on undercut on compressor impeller blade surface. An undercut study was chosen because it is the most common type of milling error during flank milling. An undercut is very common during 5-axis flank milling of centrifugal compressor impellers when the cutting tool is worn and removes less material from the blade surface [10].

The decision was made to separate the design phase for which numerous commercial systems exist from a test for robustness phase to save computational time. It is this robustness phase that relies on the novelty of this research. The objectives in this problem are:

1. To numerically analyse the impact of typical impeller undercut on the aerodynamic performance of a radial compressor.
2. Develop a novel tolerance template for each new compressor design to screen undercuts as they occur based on the result of CFD analysis.

Compared to current practice in the industry where a fixed undercut tolerance limit is set for a range of designs and irrespective of location on the blade surface – leading edge, suction side, pressure side, etc; this thesis presents a method for calculating variable tolerance limits at different locations on impeller surface and unique to every compressor design. After a new design is analysed using a CFD solver, performance values of interest such as total-to-static efficiency, choke mass flow, surge mass flow, etc are used as a reference result. An in-house FORTRAN computer program (the undercut program) was then used to modify the point data file that defines the impeller blade surface to include an undercut. The modified design was then analysed using CFD and compared with the reference original design. The sensitivity (calculated as % change in measured performance parameters) of the compressor is used to judge if a particular undercut results in significant change in performance. For example, sensitivity less than 0.5% is classed as insignificant for efficiency parameters. Various combinations of undercut settings were analysed e.g. location on blade surface, width, and height level.

The engineering design optimisation system [13] used for the multi-objective optimisation phase was also used but with a slight modification. In this phase, the design was fixed, hence the use of the optimiser – DEMO was not needed, so it was removed from the work flow. TBLOCK CFD solver [6] and ParaView [7] were also used as CFD solver and post-processor respectively. The linking program was modified to run the undercut creation program, and to not run the CAD program in instances where an external geometry file is being investigated. The approach used to achieve the objectives of fast, cheap and reliable computing system in the optimisation phase also applied to the undercut study phase. All of the tools used

in the undercut study were command line driven, hence easy to deploy on the HTCondor cluster. The HTCondor cluster was expanded from 8 machines (32 cores) to 17 machines (44 cores) for the sensitivity studies to increase the computational resources for the 1,248 analysis cases required

The undercut program was used to place undercuts of varying height and width levels at different locations on the impeller blade surface. Three radial compressors with vane-less diffusers were investigated during this research. Undercut height levels of 0.075, 0.1, 0.25 and 0.6 mm; and width levels of 0.01, 0.02, 0.05 and 0.1 were created. These undercuts were placed at 13 different meridional locations on the main and splitter blade surface. The undercut height levels were chosen based on Napier‟s current tolerance limit of 0.1mm. All possible combinations of undercut height levels, width levels and locations were analysed using CFD. The percentage change in 8 performance parameters of the undercut impeller was calculated relative to the same impeller without an undercut.

3. The Need to Design a New Compressor Using No Prior Empirical Knowledge

It is often required to design a new radial compressor from just performance requirements where there is no reference experimental or numerical design. In such circumstances, it is important to have a quick way of estimating the geometric dimensions of the impeller based on the target operating point mass flow, pressure ratio and rotor speed. The geometric parameters of interest include - the number of blades, hub radius, shroud radius, impeller radius and axial length. Other parameters of interest are the blade angles at the impeller inlet and exit as well as the impeller exit blade height. An algorithm based on a combination of fundamental turbomachinery physics 1-D equations, correlations extracted from literature and statistical modelling was developed. The algorithm is being used during the preliminary design phase of radial compressors at Napier. The contribution to knowledge is the development of 3 novel mathematical equations.

4. The Need to Size Two-Stage Turbochargers for a Given Diesel Engine Specification

Selecting a two-stage turbocharger to meet the power requirements of a diesel engine is a challenging process. The work split between the low pressure and high pressure stage must be carefully chosen based on the application of the turbocharger. Matching a two-stage turbocharger to an engine requires

calculating the flow areas of the LP and HP compressors and turbines, as well as the mass flow needed to meet the engine power demands in all operating conditions. An algorithm for estimating the mass flow and flow area is proposed in this thesis. The objective is to develop an algorithm to estimate the size (flow area) of the LP and HP compressor and turbines in a two-stage turbocharger required for a given diesel engine specification such as number of cylinders, bore size, brake mean effective pressure (BMEP), engine speed, fuel consumption, etc. The algorithm also works out the mass flow of air through the compressor, as well as the effectiveness of the inter cooler and after cooler. The algorithm has been used at Napier in the early stages of this research to validate LP and HP compressor and turbine size estimates for a customer‟s diesel engine.

5. Contributions of the Research

Specific contributions to knowledge are:

- Bespoke parametric CAD algorithms have been developed and integrated into a multi-objective, multi-physics (CFD and FEA) optimisation design process at Napier. The advanced parametric features of the CAD algorithms, for example using 5 Bezier control points to define the hub and shroud meridional profile, provides additional flexibility to designers for developing optimised designs.

- A new approach for reducing the number of variables that define a radial compressor hub and shroud meridional profile without reducing the order of the Bezier curve.

- A method of constraining control points that define the hub and shroud meridional profile of a radial compressor impeller to always move in the same direction. This ensures the bounding box of the Bezier curve does not have a high aspect ratio and always guarantees a valid hub and shroud meridional profile distribution.

- Use of a mid control point between the first two and last two control points at the shroud to improve local control of shroud profile curvature

- A mapping algorithm for calculating operating points on a radial compressor map that ensures the surge point is a valid solution. This was used to predict accurate compressor map width in Chapter 6.

- A demonstration of multi-objective optimisation of a radial compressor with up to 8 conflicting objectives, including map width enhancement

- The discovery of new impeller blade design topology with large blade angles (or back sweep angle) at the exit. The large blade angle impeller designs showed higher efficiency, but lower pressure ratio. However, since the HP stage compressor pressure ratio is merely around 2:1, the low pressure ratio of large back sweep impeller is not a disadvantage

- A novel variable tolerance limit plot on the impeller surface ("heat map") is developed for the impeller designs evaluated. This template could serve as a guideline to manufacturing engineers to decide if a machined surface defect such as an undercut could result in significant deviation from design performance. This could reduce scrap rate and result in cost savings. To the author"s knowledge, this is the first 3D CFD analysis of the effects of undercut on a radial compressor impeller surface on its performance.

- Performance parameters such as peak total-to-static efficiency, design point mass flow, etc are more sensitive to undercut height, than to undercut width.

- The study shows that as undercut height increases, design point efficiency and target mass flow (or design point mass flow) will reduce for any impeller design. Also, the average mass flow along the speed line will reduce.

- Analysis of sensitivity data show that placing an undercut on the splitter blade may increase peak efficiency and average speed line efficiency.

- For all three cases of designs investigated, surge mass flow was determined to be the most sensitive to undercut, irrespective of the location, width and height level of the undercut. This is not so surprising because surge is an unsteady phenomenon in turbo-machinery where the flow separates rapidly.

- The study shows that a highly optimised design is more sensitive to undercut, as in the case of the optimised design investigated in this research.

- Every compressor impeller design has its own unique sensitivity distribution depending on its shape and operating conditions, hence it is important to have unique screening template for each new compressor design.

6. Thesis Structure

This thesis is structured into Chapters as follows:

Chapter 1 describes the problems addressed and research contributions of this thesis

Chapter 2 presents a background to what a turbocharger is and its main components – compressor and turbine. Various types of compressors and components of a radial compressor are also discussed in this Chapter, as well as techniques used in the manufacture of radial compressor impellers. The Chapter also provides a background to internal combustion engines (ICE) and techniques for reducing emissions in ICE"s.

Chapter 3 describes the development of preliminary design algorithms for two-stage turbochargers and radial compressors, as well as contributions to knowledge.

Chapter 4 presents a brief overview of state-of-the art techniques in radial compressor design and optimisation. Various CAD modelling techniques and optimisation algorithms commonly used in the turbomachinery community are discussed in this Chapter. The Chapter also presents the governing fluid dynamics equations of turbomachinery flow physics.

Chapter 5 presents the development of a bespoke command-line driven parametric CAD algorithm for designing radial compressor impellers and vane-less diffuser. The Chapter also outlines the process of realising a high throughput computing (HTC) system used to facilitate automatic batch CFD calculations during this research.

Chapter 6 presents the utilisation of the HTC system to carry out multi-objective optimisation of a new radial compressor in the HP stage of a two-stage turbocharger. The Chapter presents a significant gain in total-to-static efficiency up by 1.6% points compared to a reference design.

Chapter 7 presents a novel study on the impact of manufacturing undercut on the aerodynamic performance of three sample radial compressors. The Chapter begins with a detailed literature survey on existing and or similar studies carried out. The Chapter contributes a variable tolerance limit template creation process, so that unique tolerance limits can be used for every new compressor impeller design, instead of using a fixed value at every location on the impeller surface.

Chapter 8 presents the conclusion and future work on the research presented in this thesis.

CHAPTER 2

BACKGROUND ON TURBOCHARGER

This Chapter describes what a turbocharger is, and its main constituent components. Emphasis is placed on the compressor side of a turbocharger. Various types of compressors and components of a radial compressor are discussed. Techniques used in the manufacture of radial compressor impellers are also considered. Finally, the Chapter provides a background to internal combustion engines (ICEs) and techniques for reducing emissions.

2.1 TURBOCHARGER DEVELOPMENT

The first turbocharger was developed by Dr. Alfred J. Büchi of Switzerland between 1909 and 1912 while he was working in the research department at Sulzer Brothers. In 1915, Büchi proposed the first prototype of a turbocharged diesel engine and ten years later, the first successful turbocharger application appeared on two German ships fitted with 2,000hp turbocharged diesel engines [14]. Since the first successful application of a turbocharger, they have been applied widely in various industries, such as in automotive, marine, power generation and rail applications. A turbocharger is essentially a radial compressor powered by a turbine that is driven by an engine's exhaust gases.

A turbocharger increases the mass of air entering the engine cylinder (forced induction) by compressing it so that more fuel can be burnt in the engine cylinder to produce more power. This results in improved performance in terms of power and efficiency because energy is recovered from the waste gas. Figure 2.1 provides an example of an assembled turbocharger unit, and Figure 2.2 is a schematic of a turbocharger fitted to an engine.

Figure 2.1 - An assembly of a turbocharger [Napier 7 Series Turbo]

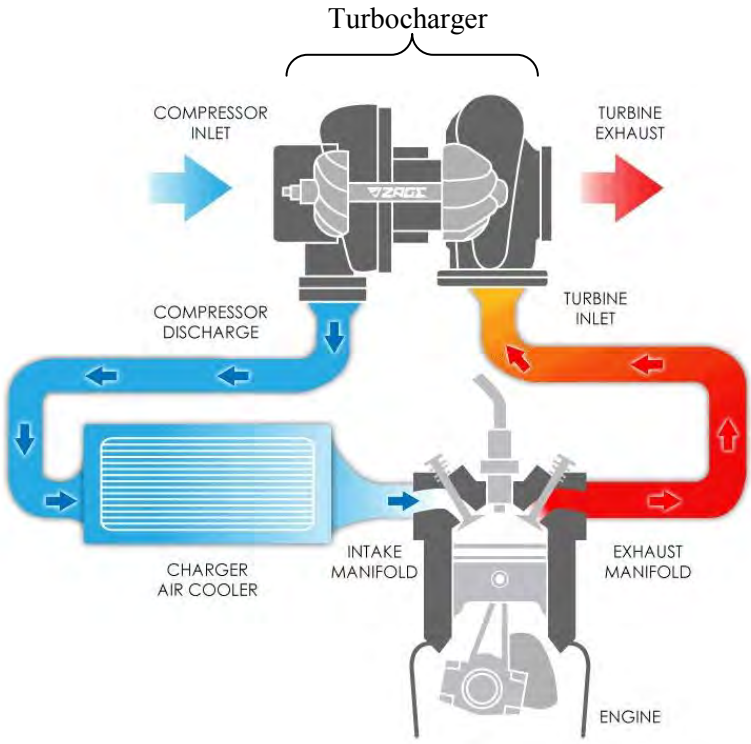

Figure 2.2 - Schematic of a turbocharger fitted to an engine [Source: www.autorounders.com]

2.1.1 Components of a Turbocharger

A turbocharger primarily consists of a turbine and a compressor which are connected together with a shaft resting on bearings. The primary purpose of the turbine is to extract energy from the high-temperature high-pressure exhaust gas from an internal combustion engine (ICE) by expanding it down to a lower pressure, producing shaft work in the process. The turbine shaft work is used to drive the compressor. The rotating compressor impeller increases the dynamic pressure and density of the inlet air into the ICE. The high density and pressure air entering the ICE means more fuel can be burnt to produce more power in the ICE, resulting in better engine performance.

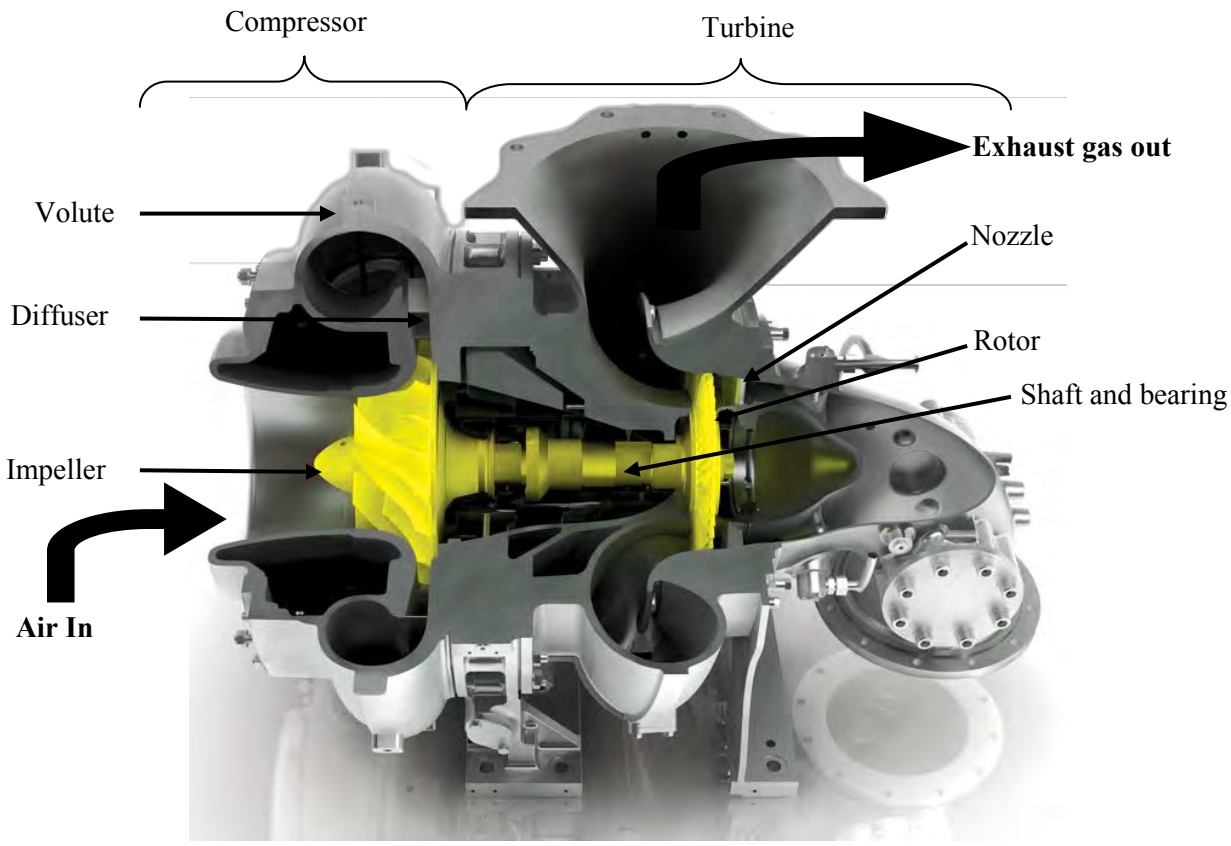

Figure 2.3 - Cross-section of a turbocharger showing the compressor and turbine sections and main components [Napier 7 Series Turbo]

There are different types of turbines and compressors widely used in the turbomachinery industry, but not all are suitable for use in a turbocharger. Most turbochargers can be fitted with a radial or an axial turbine. In Figure 2.3, the turbine is an axial turbine – where the inlet flow direction is parallel to the shaft axis through the nozzle and rotor. In a radial turbine, the flow enters the nozzle perpendicular to the shaft and is turned towards the axial direction as it flows through the rotor. Radial compressors are commonly

chosen for turbo charging applications because they deliver significant pressure boost over a wide range of flow rate, as depicted in Figure 2.4. The compressor of the turbocharger in Figure 2.3 is a radial compressor.

In a radial/centrifugal compressor, air enters the compressor in the axial direction and exits in the radial direction. Radial compressors increase the dynamic pressure of the gas by adding kinetic energy/velocity to the gas via the rotational motion of the impeller/rotor. Additional static pressure rise is achieved in the diffuser by slowing down the gas velocity in the diffuser. The ratio of pressure rise in the impeller to pressure rise in the diffuser depends on the design and operating point of the compressor. Centrifugal compressors are most efficient when operating at medium flow rates and high pressure ratios [15].

In an axial compressor, the gas flows parallel to the axis of rotation. Dynamic pressure rise in an axial compressor is due to the rotation torque exerted on the fluid by the rotor blades. The stator blades slow down the gas and convert the circumferential component of the gas velocity into static pressure. The main advantage of axial compressors is high efficiency and mass flow. However, several stages of rotor and stator blades are often required to achieve required pressure rise. Axial compressors are usually found in gas turbines such as jet engines.

Positive displacement compressors operate by reducing the volume of the closed chamber where the gas is stored. This results in an increase in pressure of the gas. An example of a positive displacement compressor is a piston-type, found in domestic refrigerators. Figure 2.5 and 2.6 are examples of an axial compressor and a positive displacement compressor respectively. Other examples of positive displacement compressors include sliding vane, squash plate; screw type etc will not be discussed here since this thesis considers a radial compressor in a two-stage turbocharger. In the next Section, a detail insight into the various components of a radial compressor is presented.

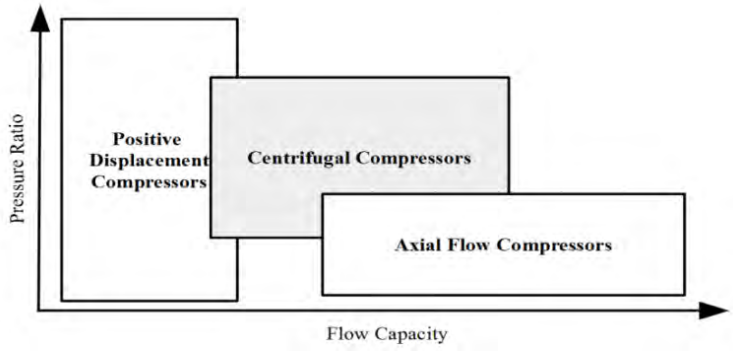

Figure 2.4 - Performance characteristics of different types of compressors. Adapted from [15]

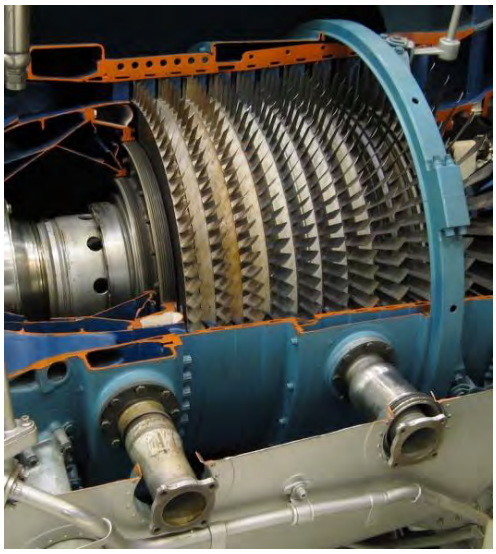

Figure 2.5 - A cross-section of Pratt & Whitney TF30 turbofan engine

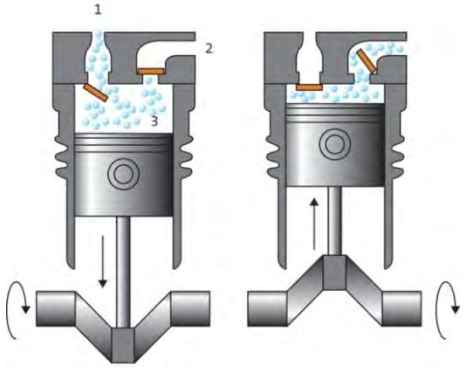

Figure 2.6 – Illustration of gas flow in a reciprocating compressor
[Source: https://www.reciprocatingcompressor.org]

2.1.2 Components of a Radial Compressor

The three main components of a radial compressor are the impeller, diffuser and volute. Air filter and or Inlet Guide Vanes (IGV"s) may be fitted at inlet to the compressor in some cases. The air filter helps to filter the air before entering the compressor to remove debris that my cause damage to the compressor. Figure 2.7 is a cross-section of a radial compressor showing the various components.

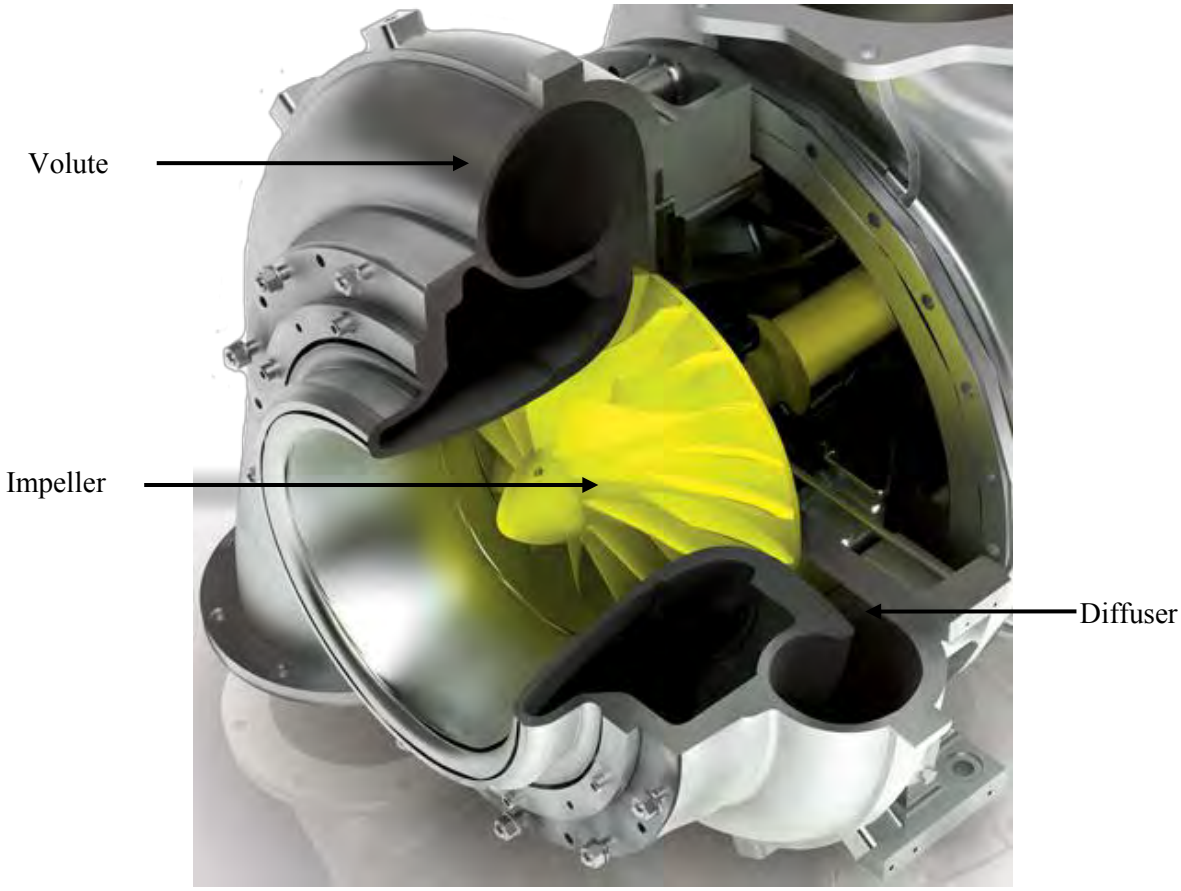

Figure 2.7 - Cross-section of a radial compressor [Napier 7 Series Turbo]

Impeller

The impeller is the rotating part of the radial compressor that transfers energy unto the fluid in the impeller blades as it turns it through 90 degrees. It is also called the rotor. Energy is transferred from the rotor to the fluid particles as it moves through the rotor. Some of this energy is converted into pressure while, the other part is converted into kinetic energy [16]. Figure 2.8 shows a 3-D view of a compressor impeller indicating direction of rotation. The so-called meridional view of the impeller is shown in Figure 2.9. The inducer region - the flow area between the main blade leading edge and the splitter blade leading edge, is also illustrated in Figure 2.8.

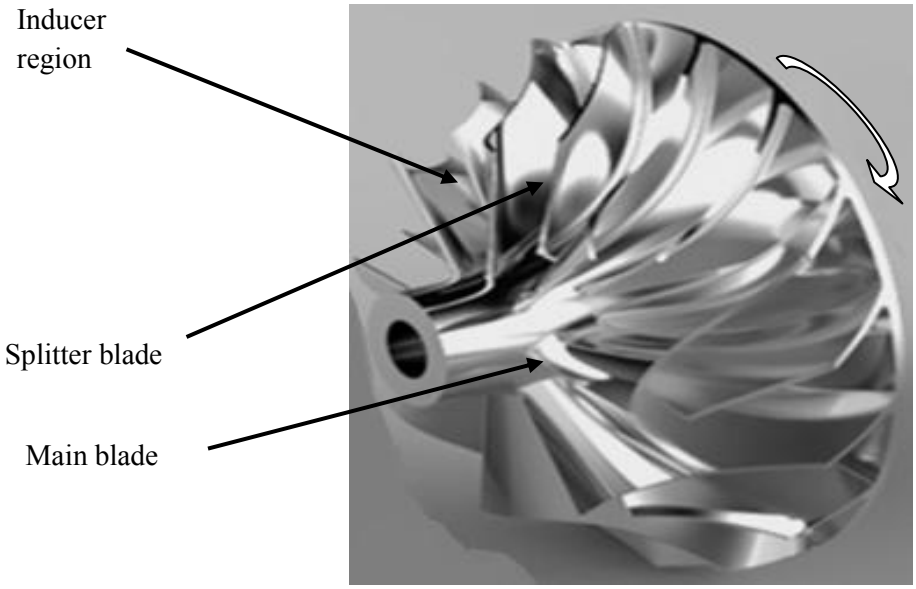

Figure 2.8 - 3D View of an impeller

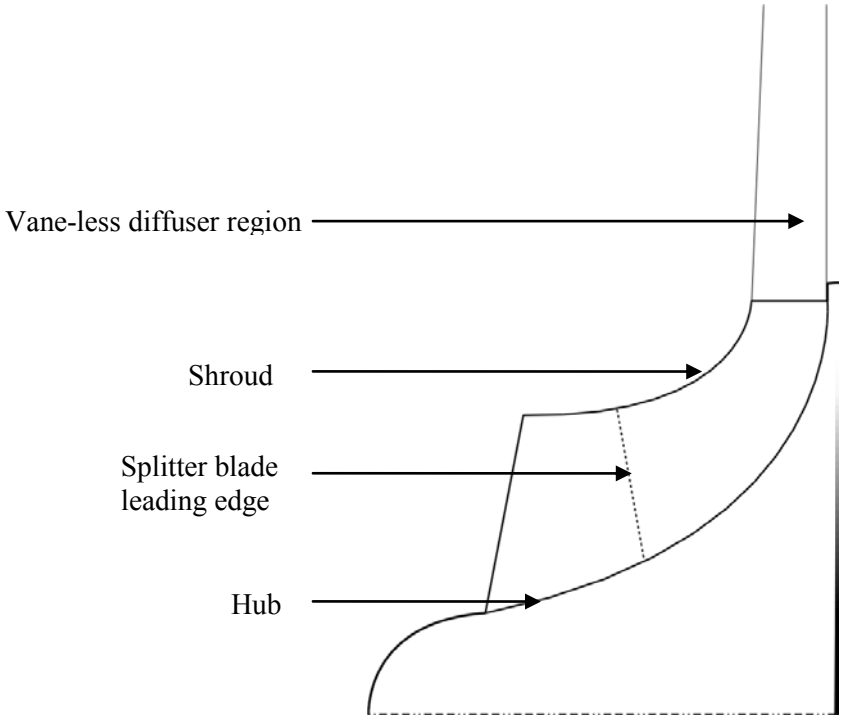

Figure 2.9 - Meridional view of an impeller

Diffuser

The diffuser helps to recover static pressure from the kinetic energy (high velocity) of the gas by expanding the gas from inlet to outlet. This can be explained using the Benoulli equation for compressible flow:

$$\frac{v^2}{2} + \left(\frac{\gamma}{\gamma - 1}\right)\frac{p}{\rho} = \left(\frac{\gamma}{\gamma - 1}\right)\frac{p_0}{\rho_0} \tag{2.1}$$

where p_o is the stagnation pressure, ρ_o is the stagnation density, p is the static pressure, ρ is the static density, v is the gas velocity and γ is the gas constant. The stagnation pressure and density does not change during the expansion process. The reduction in gas velocity in the diffuser therefore results in an increase in static pressure. The diffuser should be designed to control the expansion rate. Too much expansion in the diffuser could lead to flow separation, while in-sufficient expansion reduces the pressure recovery of the diffuser.

Two classes of diffusers exist – vane-less and vaned. Vane-less diffuser allow for wider operating map compared to vaned diffuser since there are no vanes in the diffuser to limit the choke mass flow; instead choke mass flow is determined by the impeller. Choke mass flow is the maximum mass flow capacity of a compressor at rotor speed. Also, a vane-less diffuser has the desired characteristic of a relatively flat efficiency curve over a wider range compared to vaned diffuser. The major disadvantages of a vane-less diffuser compared to a vaned diffuser are its larger size and lower peak efficiency. Examples of vaned diffuser include channel diffuser, pipe diffuser and wedge diffuser. A vane-less diffuser region is shown in Figure 2.9. A vaned-diffuser is shown in Figure 2.10.

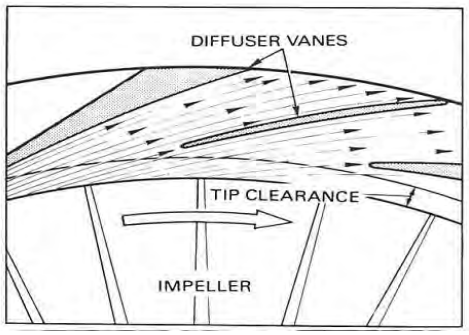

Figure 2.10 – Illustration of a vaned diffuser [http://aeromodelbasic.blogspot.co.uk]

Volute

The volute essentially serves as a collector and is carefully designed to ensure its interaction with the diffuser does not have an adverse effect on the performance of the compressor. In some cases, the volute may help recover pressure, but this is usually small compared to the diffuser pressure recovery. Figure 2.7 shows the volute in a radial compressor.

Inlet Guide Vanes (IGV's)

The IGVs are used to turn the flow before it enters the impeller. Not all compressors are fitted with an IGV. An inlet guide vane was not considered in the analysis carried out in this thesis. An IGV has the capacity to stabilise the compressor operation close to the surge region leading to a wider operating map compressor. Figure 2.11 is an illustration of a compressor fitted with an inlet guide vane at the entrance of the impeller.

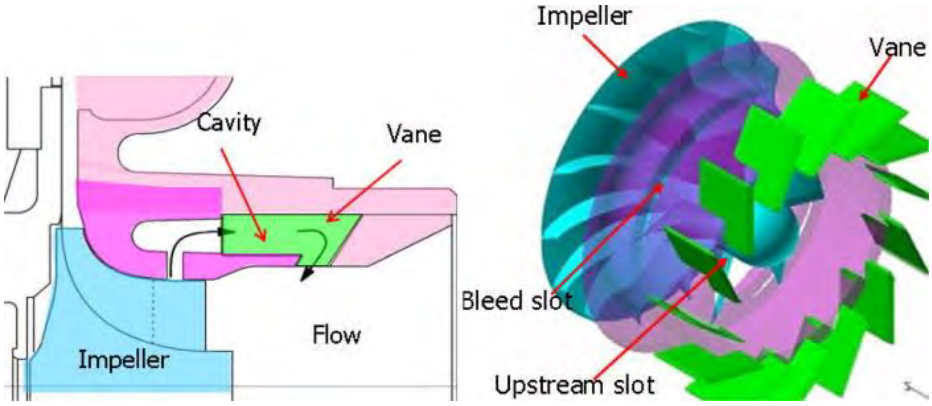

Figure 2.11 – Illustration of a compressor fitted with an IGV [17]

2.1.3 Radial Compressor Performance Calculation using CFD

Efficiency of a turbo machine relates the actual work transfer to that which would occur if the working fluid followed a constant entropy or ideal flow process [27]. For a compressor, the efficiency is written as:

$$\eta = \frac{Work\ input\ in\ an\ ideal\ process\ between\ two\ defined\ end\ states}{Actual\ work\ input} \tag{2.2}$$

Figure 2.12a shows the temperature – entropy state diagram for a typical compression process. Figure 2.12b is a meridional schematic of a radial compressor impeller, diffuser and volute showing the corresponding state locations depicted in Figure 2.12a. As the gas is compressed in the compressor, it changes from state 1 to state 2 as depicted in Figure 2.12a. In Figure 2.12a, stagnation states have subscript „0", while isentropic states have a subscript „s". For example, P_{01} and T_{01} are inlet stagnation pressure and temperature respectively. The corresponding static pressure and temperature are P_1 and T_1. T_{02s} refers to the stagnation temperature at state 2 if the compression process was isentropic. Stagnation state can also be referred to as total state.

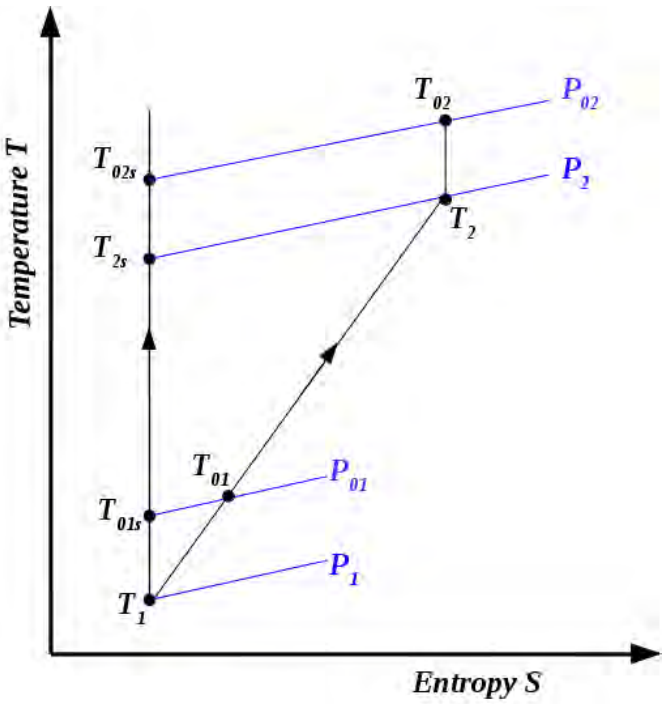

Figure 2.12a – Temperature – entropy diagram of a gas compression process

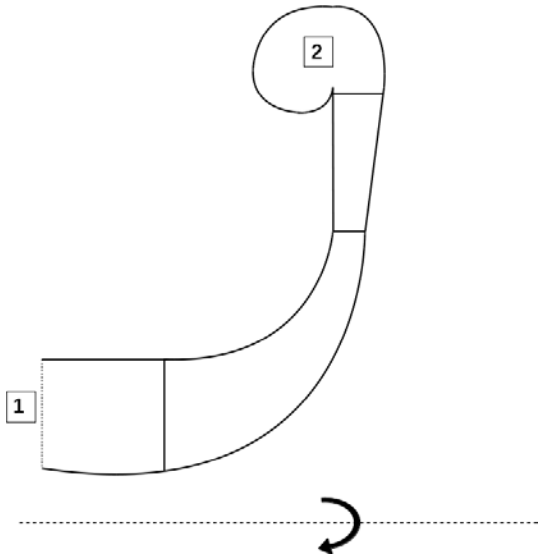

Figure 2.12b – Meridional view of a compressor impeller, diffuser and volute

When calculating the efficiency of a compressor, the stagnation conditions (i.e. P_{01} and T_{01}) are used to define the inlet conditions so that all the kinetic energy is available to the machine. The total work per unit mass flow of air can be expressed as:

$$\frac{\dot{W}}{\dot{m}} = C_p(T_{02} - T_{01}) \tag{2.3}$$

Using Figure 2.12a as reference, a compressor total-to-static efficiency can be expressed as

$$\eta_{ts} = \frac{T_{2s} - T_{01}}{T_{02} - T_{01}} = \frac{\left({}^{P_2}/_{P_{01}}\right)^{\frac{\gamma-1}{\gamma}} - 1}{\left({}^{T_{02}}/_{T_{01}}\right) - 1} \tag{2.4}$$

It is possible to estimate the flow capacity and pressure ratio of a centrifugal compressor using fundamental 1-D turbomachinery equations [27]. However, more accurate predictions can be obtained using advanced computational fluid dynamics (CFD) analysis. Computational Fluid Dynamics is the analysis of systems involving heat transfer, mass flow, phase change or chemical reaction with the aid of computer-based simulation [106]. The use of CFD has become an integral part of several industries such as aerospace, automotive, nuclear, etc. CFD codes are based on numerical algorithms that can represent the flow problem to be solved. For example, the Navier-Stokes equation [106] is solved to model viscous flow phenomena.

CFD analysis process starts with a pre-processing stage where the geometry of interest is sub-divided into a smaller, non-overlapping sub-domains or cells. In this stage, the boundary conditions and fluid properties are defined. The physical phenomena that need to be modelled are defined also. The next stage is to solve the physics in the computational domain using an appropriate solution technique. A common solution technique in commercial CFD solvers is the finite volute method, where the solution variables are computed and stored at the centre of each cell in the computational domain [106]. Another common and more fundamental solution technique is the finite difference method where the solution variables are computed and stored at the nodes of the cells. The CFD solver used during this research is based on a finite difference solution technique. The last phase is post-processing, where the fluid features can be visualised and useful properties extracted from the CFD result data.

Most flows encountered in engineering consist of high turbulence (high velocity flow, with unsteadiness). Flows at lower velocity with no unsteadiness are referred to as laminar flows. Most flows in engineering consist of laminar and turbulent regimes. Numerical schemes can be used to capture the unsteadiness in turbulence flow by approximating the flow into steady and unsteady components as depicted in Figure 2.12c. The steady component of velocity is modelled as part of Navier-Stokes equations, while turbulence models are developed to represent the fluctuating component of velocity. The CFD solver TBLOCK [6] used during this research uses a linear scale mixing length turbulence model to represent the fluctuating component of velocity as a fraction of distance from the nearest wall within the computational domain. Details of other turbulence models, for example k-epsilon, can be found in [106].

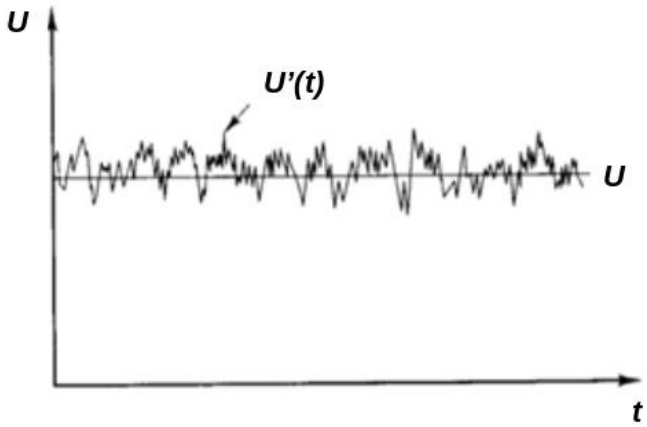

Figure 2.12c – Illustration of steady and unsteady component of velocity

TBLOCK allows the user to set up inlet and outlet boundary conditions to run a simulation. Inlet stagnation temperature and pressure must be specified as well as an outlet static pressure and operating speed. The solver then iterates to find a stable and converged solution while calculating mass flow rate and efficiency. The converged solution contains information about the operating point such as mass flow, pressure ratio and efficiency. To obtain another operating point, the user must change the outlet static pressure and run the solver again to obtain a new mass flow and efficiency. A collection of operating points at same speed makes up a speedline. A collection of speedlines make up a map. An example compressor map is shown in Figure 2.12d.

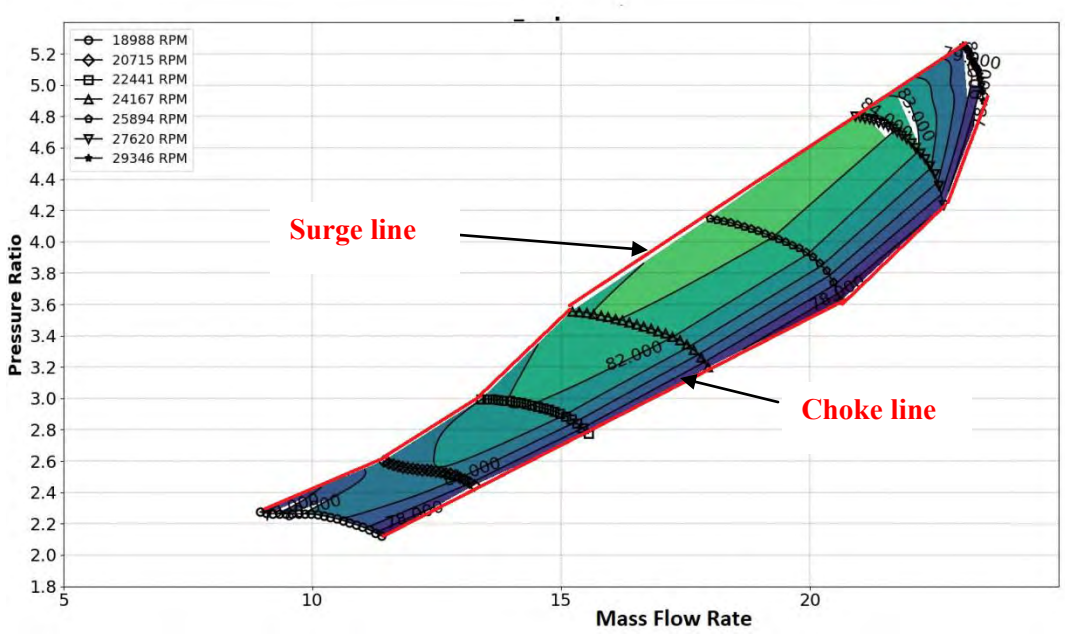

Figure 2.12d – An example compressor map with efficiency contours.

A compressor map specifies the operating range of a compressor design and its efficiency at different speeds. The maximum mass flow on any speedline of a compressor map is called the choke mass flow. The choke line is depicted in Figure 2.12d. Similarly, the minimum mass flow is known as surge mass flow as depicted in Figure 2.12d. At this point, it is important to explain these terms as well as other useful terms.

Surge is characterised by total breakdown of continuous and steady flow in the blade passages. In paractice, surge must be avoided as the large fluctuations in the flow can lead to a mechanical breakdown of the equipment. Briefely, surge is a full blown stall. In this study, the surge mass flow and efficiency are calculated at an averaged stall condition.

Stall occurs before surge; and is indicated by the breakaway of the flow from the suction side of the blade. Stall is an unsteady phenomenon generally characterised by reverse flow near the tip of the blade, which distupts the velocity distribution causing an adverse effect on the performance of the compressor. The reverse flow around the tip of the blade causes a pressure gradient that forces the velocity vectors in the radial direction around the inducer region.

Choke occours when the velocity of the flow reaches the speed of sound at the impeller throat cross-section where the impeller is no longer able to pass more mass flow through. The mass flow at this condition is the choke mass flow. Choke may also occour in the diffuser if there are vanes in the diffuser.

2.2 INTERNAL COMBUSTION ENGINE

The internal combustion engine (ICE), reciprocating or rotary (i.e. Diesel, Otto, Brayton cycle), is a heat engine used to transfer chemical energy into useful mechanical energy. Fuel is burned in the presence of an oxidiser (usually air) in the confined combustion chamber of an ICE to produce high-temperature and high-pressure gases. The expansion of the gas applies force to engine components such as piston or rotor, turbine blades, which converts the gas energy to rotary motion of a connected shaft. The term internal combustion engine is commonly associated with reciprocating engines found in automobiles. In reality, combustion engines such as jet engines, industry gas turbine engines and rocket engines also fall into the category of internal combustion engine. Since this thesis considers turbo charger design and manufacture for marine reciprocating diesel engines, the remainder of this Chapter will focus on reciprocating diesel engines.

2.2.1 Standard Diesel Engine

Figure 2.13a is a schematic of the internal combustion engine for a diesel engine. The internal combustion engine of a marine diesel engine undergoes a four stroke cycle - intake, compression, power and exhaust as shown in Figure 2.13b. During the intake stroke, the intake valve opens up allowing air to flow in while the piston moves downwards, then closes. The piston moves back up during the compression stroke, compressing the trapped air in the process. As the piston reaches the top dead centre (TDC), fuel is injected and ignited. Compared to gasoline engines where a spark plug is used to ignite a compressed mixture of fuel and air, the fuel ignites by itself in a diesel engine because of higher compression and temperatures up to 800^{o}C. The hot gas expansion (at constant pressure for a diesel engine) forces the piston to the bottom dead centre (BDC). In the exhaust stroke, the exhaust valve opens and the upward movement of the piston pushes the exhaust gases out of the combustion chamber and the cycle repeats continuously. The pressure volume diagram of a typical diesel engine is shown in Figure 2.14.

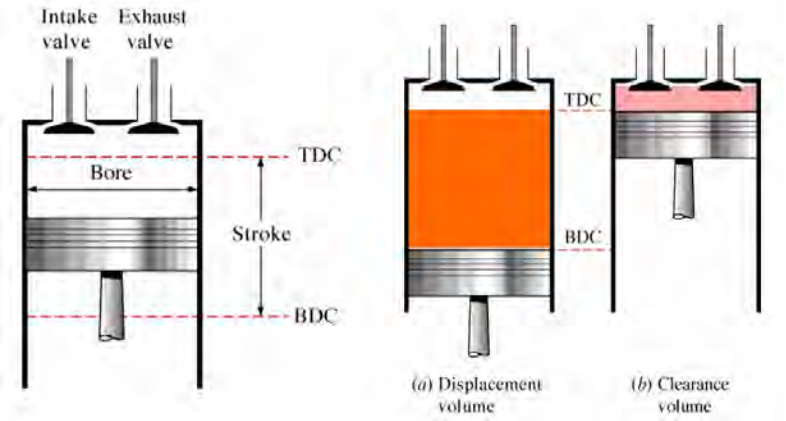

Figure 2.13a- Schematic of the combustion chamber of a diesel engine [M. Surahman, 2011]

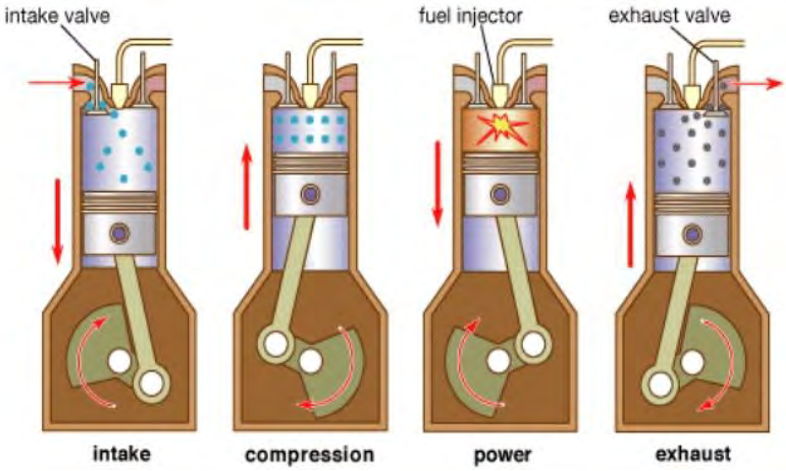

Figure 2.13b - Four strokes in a diesel engine
[Source https://www.britannica.com/technology/automobile]

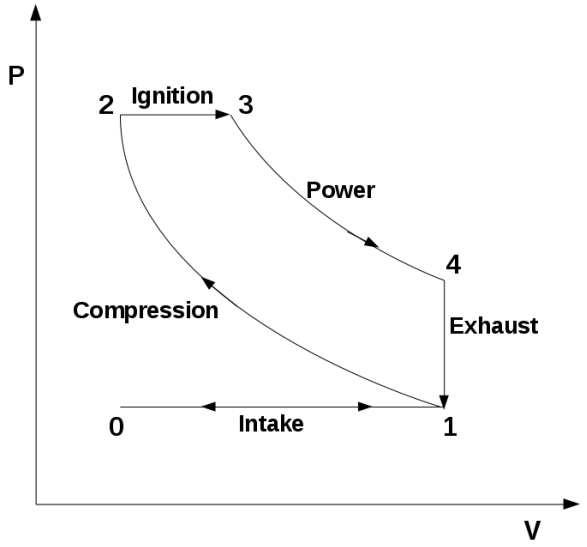

Figure 2.14 – P-V Diagram for the ideal Diesel cycle

2.2.2 Diesel Engine with Miller Timing

In marine diesel engines, a technique called "Miller timing" is widely used. Using this technique, the engine cylinder inlet valve closes just before the piston reaches the bottom dead centre. This reduces the work of compression and the combustion temperature, which results in lower emissions and higher engine efficiency. Since the rate of NOx formation is increased at higher temperatures, Miller timing reduces the rate of NOx formation, resulting in a high thermal efficiency [18]. However, the application of Miller timing decreases the mean effective pressure in the engine cylinder due to expansion in the intake stroke. This also reduces the power density of the engine. Figure 2.15 is a cycle diagram of a diesel engine with Miller timing. The formation of NOx at high temperature is explained by the Zeldovich mechanism [107] as shown in Equations 2.5 and 2.6

$$N_2 + O \leftrightarrow NO + N \quad (2.5)$$

$$N + O_2 \leftrightarrow NO + O \quad (2.6a)$$

$$N_2 + O_2 \leftrightarrow 2(NO) \quad (2.6b)$$

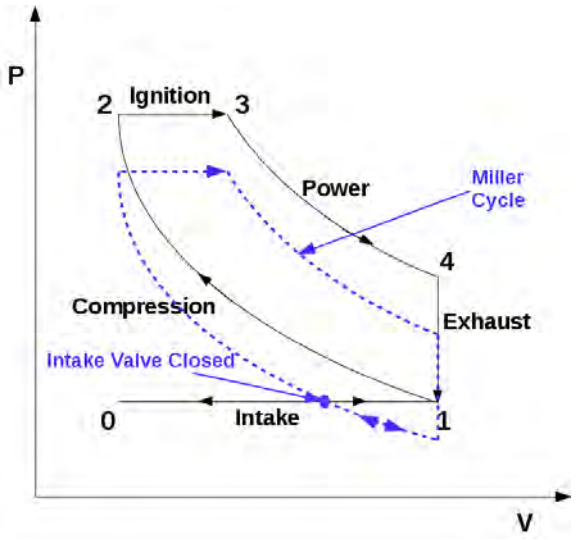

Figure 2.15 – P-V Diagram for a Diesel cycle with Miller timing

2.3 THE NEED FOR TWO-STAGE TURBOCHARGER

In a two-stage turbocharger, two compressors are connected in series to deliver higher pressure ratio as shown in Figure 2.16. The compressors in series are powered by two turbines in series. The exhaust gas leaving the engine first drives the HP turbine which drives the HP compressor. The exhaust gas then flows through the LP turbine stage which powers the LP compressor stage. Ambient air is admitted into the LP compressor where the density is raised. A further gain in density can be achieved through inter-stage cooling. The higher density air is further compressed in a smaller HP compressor stage to even higher pressure. The air is then cooled again by a charge air cooler or after-cooler to increase density. The HP compressor in a two-stage turbo charger is smaller because of mass conservation between the LP and HP stage. The HP stage then requires a smaller volume flow rate because the density of air is already increased from the LP stage. On the turbine side, complete expansion of the exhaust gases does not occur in the HP stage, making it smaller than it would be for a single stage turbocharger. Further expansion occurring in the LP stage, means a larger LP turbine.

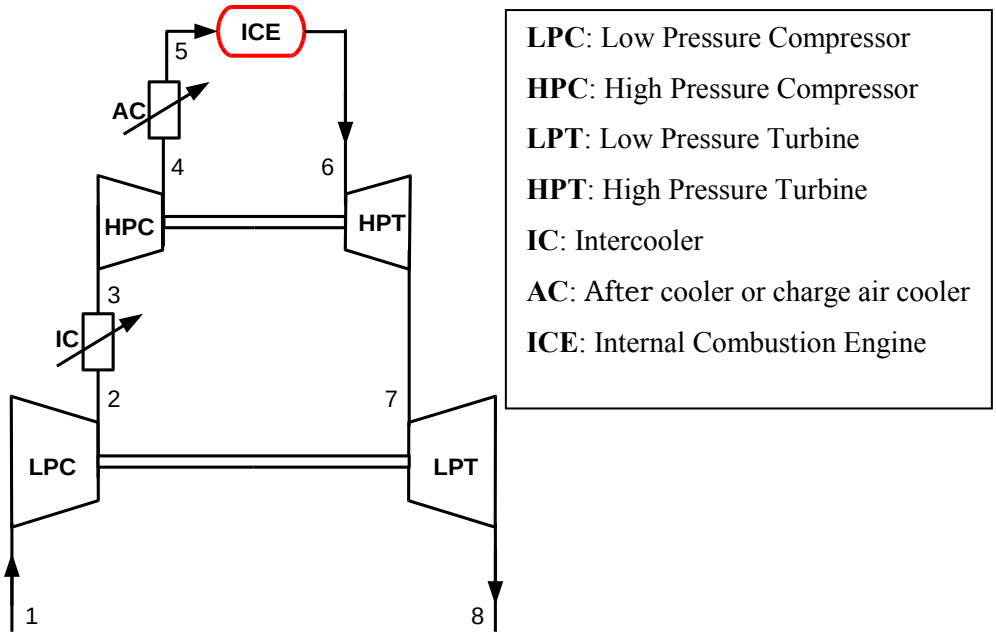

Figure 2.16 - A schematic of a two-stage turbo charger

2.3.1 High Pressure Ratio Compression

The drawback of reduced cylinder air mass when Miller timing is used in a diesel engine can be compensated for by increasing the engine intake manifold pressure so that when induction occurs in the intake stroke, the increased manifold density is sufficient to produce the needed air mass for combustion. In the marine industry, a higher boost pressure (usually >= 8:1) is needed to take advantage of the benefits of Miller timing and this requires the use of two stage turbo charging. This is also due to material limits of Aluminium at high temperatures if a single stage turbocharger is used. Research developed over the past 40 years have shown that no further gain in pressure is possible beyond 6:1 for Aluminium when in a single stage compression as shown in Figure 2.17. This is due to high temperatures greater than 200^{o}C at pressure ratios > 5, resulting in high thermal expansion and softening of aluminium. In Figure 2.17, the impeller tip temperatures are shown at the various pressure ratios assuming an impeller inlet stagnation temperature and pressure of 298K and 1bar respectively, calculated using the Equation:

$$T_2 = T_1 \left(\frac{P_2}{P_1}\right)^{\frac{\gamma-1}{\gamma}} \tag{2.7}$$

Using a more expensive material such as titanium instead of aluminium can overcome the stress issues at high temperatures. However, since titanium is very expensive compared to aluminium; and very difficult

to machine, it is not economically feasible for use in the marine industry. Moreover, attempting to achieve a very high compression ratio in a single stage compressor requires a considerably larger compressor thereby increasing the system inertia, which is particularly disadvantageous during transient ship operations or rapid acceleration when the compressor is required to respond quickly to engine demand for more air.

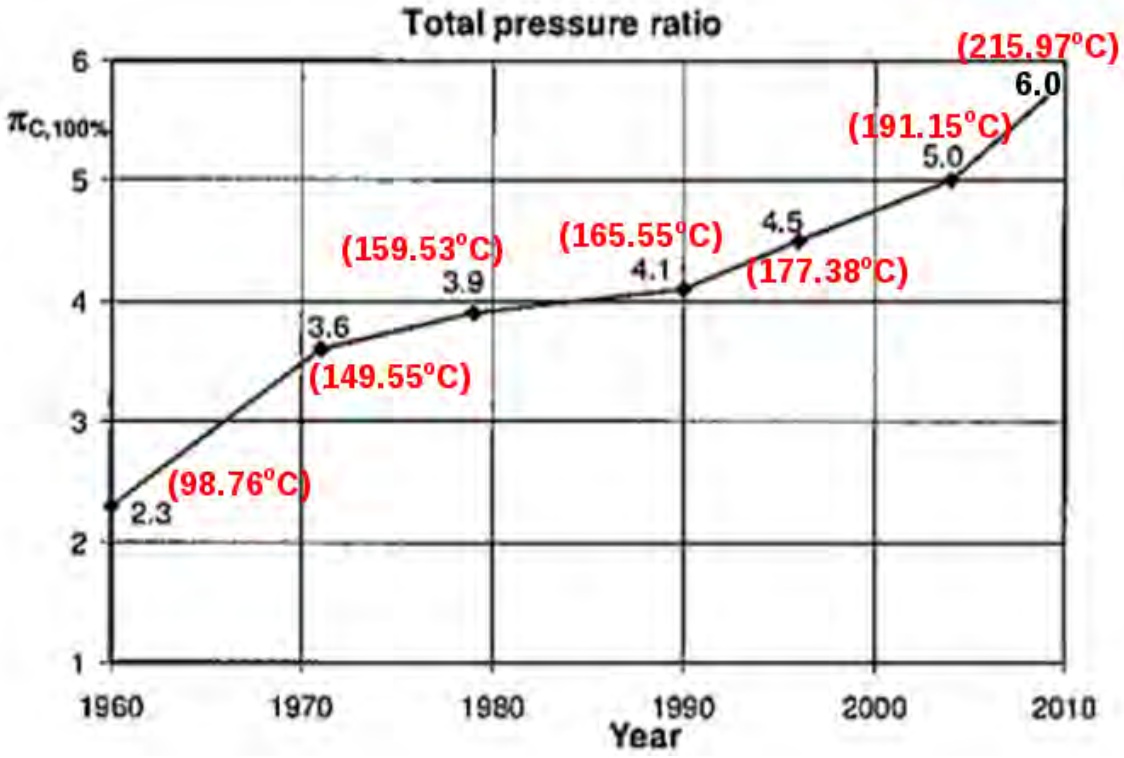

Figure 2.17 - Pressure Ratio with single stage Aluminium compressor [Modified from [19]]

2.3.2 Combining Two-Stage Turbo charging with Miller Timing

Using a two stage turbocharger with inter cooler overcomes the draw backs of achieving high compression ratios in a single stage system using aluminium and provides the additional benefits of using Miller timing. In a two-stage system, the HP compressor is smaller than the LP and has a lower inertia so it responds quicker during transient operations/rapid acceleration. The use of two stage turbo charging also provides the additional benefits of better overall turbo charging system efficiency, afforded by inter cooling between the compressor stages [18]. However, the effect of lower charge air temperature has the unwanted side effect of making the ignition of the fuel more difficult, especially under low load conditions. This can be solved by using an air intake heating system from the engine cooling water

system. Two-stage turbo chargers also favour smaller mass flows at higher pressures due to the smaller size of the HP compressor resulting in wider compressor map in the surge region. Two-stage turbo chargers also allow for easy integration of emission reduction devices such as EGR and SCR [1]. Figure 2.18 shows the higher engine intake pressure when a diesel engine with Miller timing is used with a two-stage turbocharger.

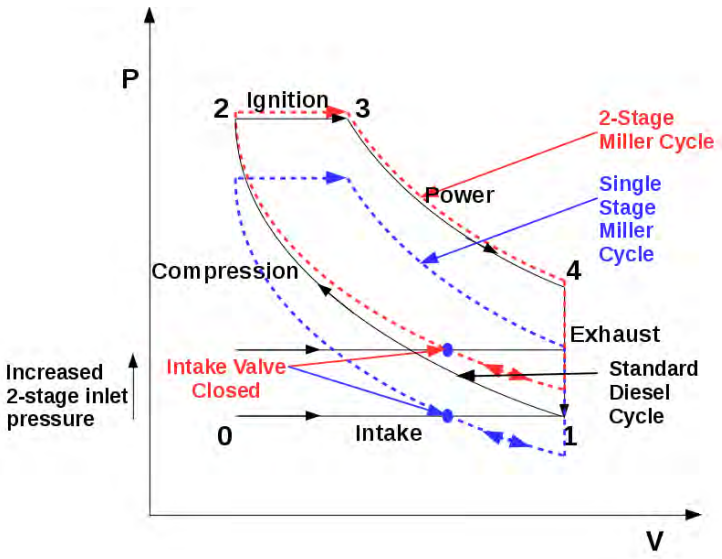

Figure 2.18 - P-V diagram of a Miller cycle diesel engine with two-stage turbo charging intake

2.4 OTHER EMISSION REDUCTION TECHNIQUES

In this Section two methods of reducing NOx emission in diesel engines will be discussed.

2.4.1 Exhaust Gas Recirculation (EGR)

Exhaust gas recirculation is a technique for reducing oxides of nitrogen (NOx) emissions in internal combustion engines. EGR works by diluting the oxygen and nitrogen in the air stream entering the internal combustion engine by re-circulating a portion of the engines exhaust gas back into the engine cylinders. The re-introduction of inert gases/exhaust gases into the engine cylinder helps to absorb the combustion heat and reduce the peak temperatures in the cylinder. Since NOx production is favoured by high engine temperatures up to 1500^{o}C, EGR helps to reduce its formation. NOx formation as described in the Equations below:

$$N_2 + O_2 \rightarrow NO \text{ (Nitric oxide).} \quad (2.8)$$

The nitric oxide reacts with more oxygen to form nitrogen dioxide.

$$2NO + O_2 \rightarrow 2NO_2 \tag{2.9}$$

However, there are some drawbacks to using EGR. The reduced oxygen in the engine cylinder due to EGR reduces the air-fuel-ratio and favours the production of particulates (fuel that is partially combusted). This results in a lower peak power produced by the engine. In some application, EGR is turned off when peak power is required or to limit smoke and particulate matter formation in the engine. Figure 2.19 is a schematic of an EGR integration in an internal combustion engine.

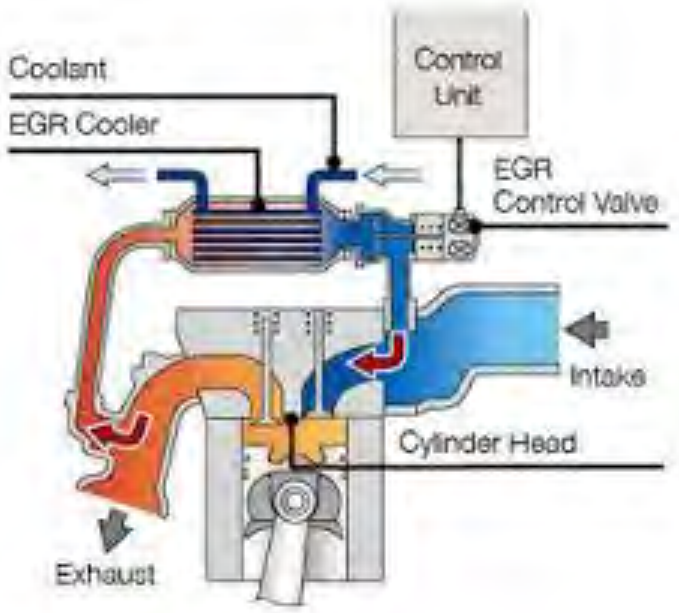

Figure 2.19 - Schematic of EGR unit integration in an internal combustion engine [source: www.physicsforums.com]

2.4.2 Selective Catalytic Reduction (SCR)

Selective Catalytic Reduction (SCR) is a NOx reduction technique that makes use of a catalyst to break down NOx into di-atomic nitrogen N_2 and water H_2O. Excess NOx from a diesel engine can be reduced by 90% using selective catalytic reduction. SCR introduces a urea solution $(NH_2)_2CO$ known as diesel exhaust fluid (DEF) to neutralize nitrogen oxides (NOx) in the exhaust stream. Urea is a solution that can be used to produce ammonia (NH_4). The DEF and the exhaust gases are mixed in a catalytic converter which reduces the NOx to Nitrogen and Oxygen elements with the aid of a catalyst. The catalyst is usually made of oxides of base metals such as tungsten, vanadium, molybdenum, zeolites or a

combination of various precious metals. DEF is a solution of 32.5% urea and purified water. The reaction of urea with nitric oxide in an SCR unit is shown in the Equation below:

$$4NO + 2(NH_2)_2CO + O_2 \rightarrow 4N_2 + 4H_2O + 2CO_2 \quad (2.10)$$

Figure 2.20 is a schematic of a SCR system.

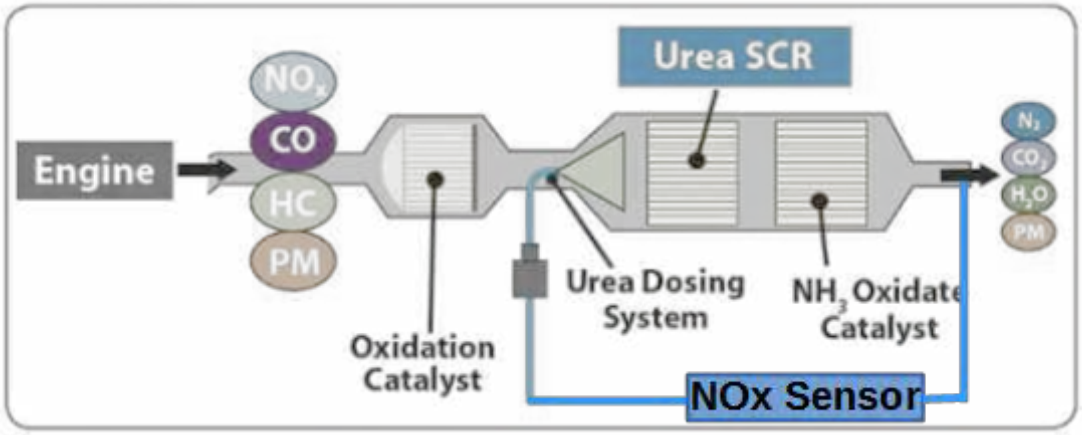

Figure 2.20 - Schematic of an SCR unit [source: www.dieselforum.org]

2.5 MANUFACTURE OF RADIAL IMPELLERS

The goal of every impeller manufacturing process is to ensure the manufacturing method does not have any negative impact on the impeller performance, irrespective of the manufacturing method used e.g. casting or machining, where the manufacturing process results in an inherent surface roughness [20]. In this Section, three manufacturing methods are discussed.

2.5.1 Milling

Milling is a machining process that involves using rotary cutter(s) to remove material from a solid forged material. The advent of computer numerical control (CNC) milling means the manufacturing process can be automated. CNC milling allows the automation of machine tools that are operated by programmed commands loaded onto the CNC machine, as opposed to manually controlling the cutting tool by hand.

3-axis CNC router milling machines can cut along the X, Y and Z axis at the same time. Moving the router bit from front to back cuts along the X-axis, moving the router bit from left to right cuts along the Y-axis; and cutting along the Z-axis moves it from up to down. 3-axis CNC machines are particularly

suited for cutting 2-dimensional parts or flat surfaces. 4-axis CNC router milling machines add rotation to each axis of a 3-axis CNC milling machine. 5-axis CNC machining can rotate in two additional rotary axes (A and B). This helps the cutting tool approach the part from many directions. 5-axis CNC machines can cut five edges of a part simultaneously.

During the milling of a radial compressor impeller from a block of material, the solid material is fed to the cutter at an angle relative to the axis of the cutter. As opposed to casting which is a mass production method in the automotive industry, 5- axis machining is becoming a promising mass production method of turbocharger radial compressor impellers [20]. Compared to 3-axis or 4-axis milling, 5-axis milling allows compressor designers to design more complex impeller shapes that were almost impossible to manufacture using 3-axis or 4-axis milling.

Two common milling methods used in turbomachinery are discussed – flank milling and point milling. Machining a turbocharger impeller from a solid of metal has many advantages such as maintaning the integrity of the material proprerties, geometric accuracy and shorter design-to-production time compared to cast impellers. However, the machining cost is high compared to casting [21]. Five axis flank milling has a much higher material removal rate compared to point milling and takes about half as long as point milling to machine an impeller. During flank milling, the long side of the cutter is used to remove material as shown in Figure 2.21. Compared to flank milling, point milling makes use of the cutter tool tip instead of the long side as shown in Figure 2.22, and as a result takes a longer time. Flank milled blades are less accurate compared to point milled blade in terms of deviation from the designed surface. However, flank milled blades are smoother than 1.6 μm *Ra* (arithmetic average over the evaluation length), but point milled blades slightly exceed 1.6 μm *Ra* [20].

During flank milling of radial compressor impellers, it is important to avoid errors due to tool trajectory or tool geometry that can reduce the quality of surface finishing. Tool trajectory errors, for example, due to power cut can result in an undercut or overcut. Tool geometry errors, for example a blunt cutter can result in and undercut. Also, a newly fitted cutter may initially remove excess material and should be blunted slightly before use to minimise overcuts. More so, overheating of the CNC machine cabinet can lead to a sudden stop resulting in localised deep cuts on the impeller.

Surface roughness on a flank milled impeller is streamlined along the flow direction. Significant deviation in surface roughness will distort the flow in the impeller, resulting in a reduced compressor and turbocharger efficiency.

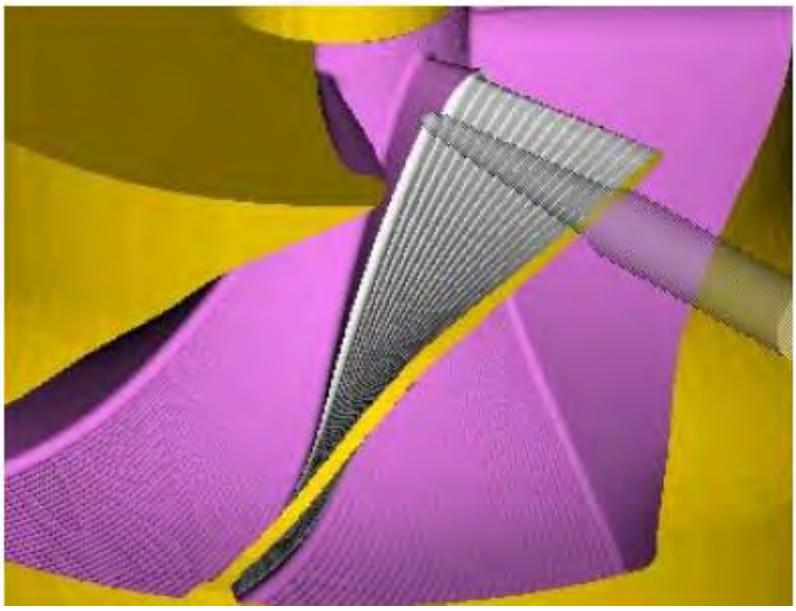

Figure 2.21 - Flank milling [21]

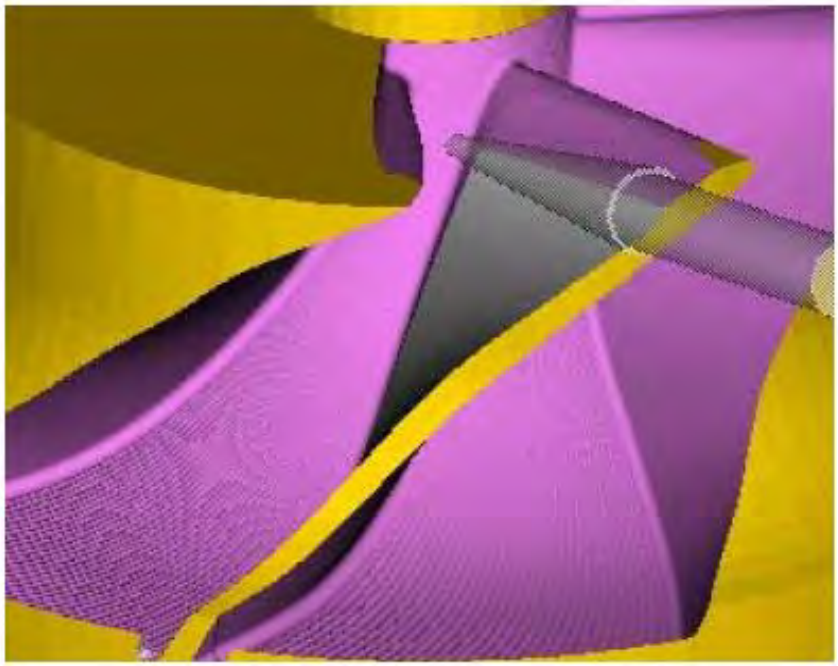

Figure 2.22 - Point milling [21]

2.5.2 Casting

Casting method where the metal is heated to melting state and cast into the impeller shape is commonly used in the automotive industry where the cost of the impeller is the main driver and must be kept as low

as possible. However cast impellers do not offer the level of surface finishing required for larger compressor impellers used for large diesel engine turbo chargers. This poor surface finishing can result in significant deviation from the design performance of the compressor [21]. For this reason, larger radial compressor impellers are usually manufactured by machining. Another reason why milling is preferred to cast impellers is that the surface finish of milled impellers is streamlined along blade surface and flow direction. This is not the case with sand cast impellers. Although the lost wax cast process used in the automotive industry produces better surface finish compared to sand casting, it is not feasible for large compressor impellers because of the high aspect ratio of impeller blade profiles.

2.5.3 3D Printing

3D printing, also termed additive manufacturing is a process of creating three dimensional objects through material addition. An additive process requires "adding" layers of material required to create the final product. In a microscopic scale, each of these layers can be seen as horizontal slices of the material. The digital file could be from a CAD program or a scan of an existing 3D object. In recent times, top companies like Google and Microsoft have enabled their hardware to do 3D scanning. A good example is Microsoft‟s Kinect [22]. These points to the possibility that 3D scanning will become common place and 3D printing will be more widely used. To print a 3D object of a digital file, the 3D modelling software creates thousands of horizontal sections of the 3D model from the digital file. The 3D printer then prints each of these layers blended together resulting in a three dimensional object. However, the layers are not blended together seamlessly, resulting in interlaminate weakness and poor surface finish. The American Society for Testing and Materials (ASTM) group classify the additive manufacturing processes into 7 categories according to Standard Terminology for Additive Manufacturing Technologies. These seven processes are - Vat Photo polymerisation, Material Jetting, Binder Jetting, Material Extrusion, Powder Bed Fusion, Sheet Lamination and Directed Energy Deposition [22]. Figure 2.23 is a schematic of material jetting. 3D printing has seen applications in tissue engineering such as bio-printing where organs or body parts are built using inkjet techniques. 3D printing has also seen application in printing sections of General Electrics‟ jet engine and combustion liners at NASA [22]. 3-D printing is not being investigated for impeller designs during this thesis, because at present, Napier has not invested in 3-D printing technology.

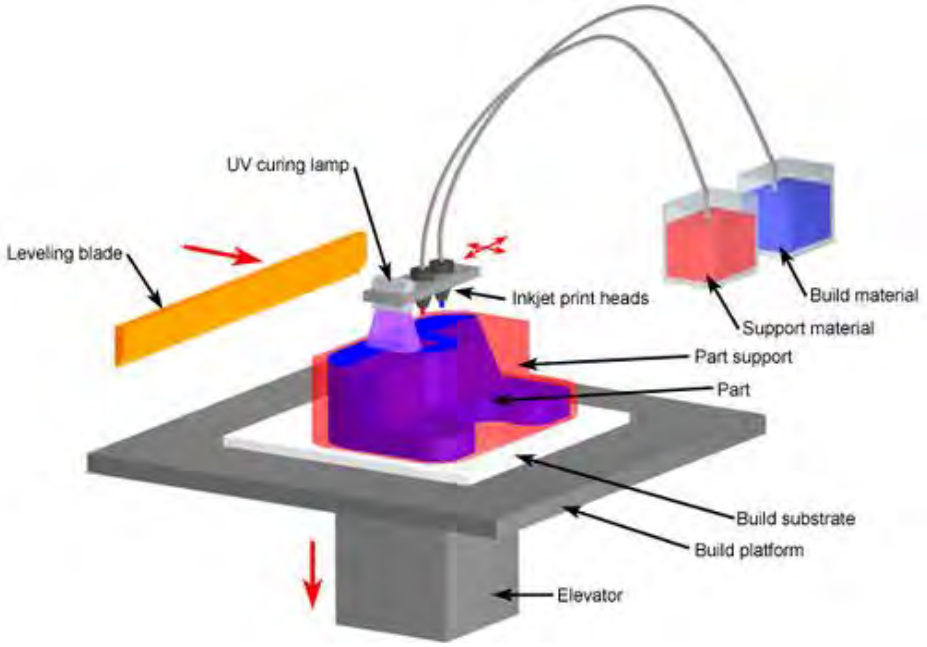

Figure 2.23 - Schematic of material jetting [source: www.custompartnet.com]

CONCLUSION

This Chapter provided an introduction to what a turbocharger is and its main components – compressor and turbine. The various types of compressors and components of a radial compressor are discussed. The various techniques used in the manufacture of radial compressor impellers are also briefly discussed as well as emission reduction techniques and some introduction to diesel engines. The next Chapter presents the development of numerical tools for preliminary design of two-stage turbochargers and radial compressors.

CHAPTER 3

DEVELOPMENT OF NUMERICAL TOOLS FOR PRELIMINARY DESIGN OF RADIAL COMPRESSORS AND TWO-STAGE TURBOCHARGER SIZING

This Chapter presents the development of numerical design tools for preliminary design of two-stage turbochargers and radial compressors. Two algorithms are presented:

- A matching algorithm for estimating mass flow rate and flow area of the LP and HP compressor and turbine of a two-stage turbocharger for a given diesel engine power specification. The matching algorithm is applied to a test diesel engine, and calculated parameters were within the required limit.
- An algorithm for estimating the geometric dimension of a radial compressor impeller given a target design point mass flow, pressure ratio, operating speed and inlet stagnation temperature and pressure. The algorithm is used to design 4 test case compressor impellers and compared with CFD analysis. The results show mass flow calculated using 3D CFD analysis was within 19% of target mass flow.

The contribution of this Chapter is the development of novel mathematical Equations for estimating impeller hub radius and number of main blades - 3.7, 3.8 and 3.9.

3.1 BACKGROUND

The development of a two-stage turbocharger for a diesel engine can be split into two main phases:

- Preliminary design to estimate the mass flow and flow area of the LP and HP compressor and turbine
- Design of the LP and HP compressor and turbine
    - Preliminary design to estimate the geometric dimensions of the compressor (impeller and diffuser) and turbine (nozzle and rotor)
    - Detail 3D CFD and FEA design and analysis

Preliminary design is an important step in the design of a two-stage turbocharger. It provides reasonable estimates of mass flow and flow area of a compressor and turbine in a short time. The one-dimensional equations solved during preliminary design are less computationally expensive compared to 3D equations solved during CFD analysis. Mass flow is estimated by matching the temperature and pressure states of the compressor and turbine stages, and ensuring that work extracted from the turbines is sufficient to drive the compressors. More so, preliminary design of a compressor or turbine helps to estimate the geometric dimensions of the compressor (impeller and diffuser) and turbine (nozzle and rotor). For example, an estimate of impeller inlet hub and shroud radius, and diameter can be calculated in a few seconds given the design mass flow, operating speed and pressure ratio.

3.2 ALGORITHM FOR ESTIMATING FLOW AREAS OF LP AND HP COMPRESSOR AND TURBINE

3.2.1 Introduction

During the preliminary design of a two-stage turbocharger to enhance the performance of a diesel engine, an initial estimate of air mass flow and inlet flow areas of the compressor and turbine stages is required. For a given diesel engine power specification such as, fuel consumption, engine speed, brake mean effective pressure (BMEP), number of cylinders, bore size, etc, it is possible to estimate the flow areas of the LP and HP compressors and turbines using a 1-D matching algorithm. This Section describes the matching algorithm developed (subsequently referred to as „TwoMatch“) during this research.

3.2.2 Matching Process

As a refresher, a schematic of a two-stage turbocharger is shown in Figure 3.1.

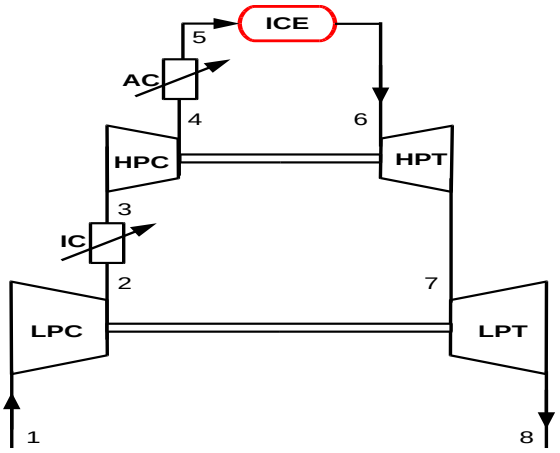

LPC: Low Pressure Compressor
HPC: High Pressure Compressor
LPT: Low Pressure Turbine
HPT: High Pressure Turbine
IC: Inter-cooler
AC: After cooler or charge air cooler
ICE: Internal Combustion Engine

Figure 3.1 - Schematic of a two-stage turbocharger in a diesel engine

At the start of the matching process, the following parameters are known:

- P_{01} LP compressor inlet stagnation pressure
- T_{01} LP compressor inlet stagnation temperature
- ΔP_i Pressure drop in the Inter-cooler
- T_3 Intercooler outlet static temperature
- ΔP_a Pressure drop in the after cooler or charge air cooler
- T_5 Engine receiver temperature/after-cooler exit static temperature
- π_{ACR} Actual compression ratio of the charge air system
- T_6 HP turbine inlet static temperature
- P_8 LP turbine outlet static pressure

The actual compression ratio is the product of the compression ratios of each compressor stage without accounting for pressure loss as defined by Equation 3.1. The overall compression ratio π_{OCR} between the engine intake and LP compressor inlet (including inter-stage losses) is given by Equation 3.2. The pressure ratio split between the LPC and HPC are determined at the start of the matching process. The pressure split is expressed as LPC: HPC, for example a split of x:y means that the compression ratio of the LPC is x/y of the HPC. The pressure ratios of the LP and HP compressor are derived from Equations 3.3 to 3.6. The matching algorithm is summarized in the flow chart shown in Figure 3.2. See *Appendix A* for details of the matching algorithm.

$$\pi_{ACR} = {}^{P_2}/_{P_{01}} \times {}^{P_4}/_{P_3} \tag{3.1}$$

$$\pi_{OCR} = {}^{P_3}/_{P_{01}} \times {}^{P_5}/_{P_3} = {}^{P_5}/_{P_{01}} \tag{3.2}$$

$$\pi_{LPC} = {}^{P_2}/_{P_{01}} \quad and \quad \pi_{HPC} = {}^{P_4}/_{P_3} \tag{3.3}$$

$$\pi_{HPC} = \frac{y}{x} \times \pi_{LPC} \quad and \quad \pi_{LPC} = \frac{x}{y} \times \pi_{HPC} \tag{3.4}$$

$$\pi_{ACR} = \pi_{LPC} \times \pi_{HPC} \tag{3.5}$$

$$\pi_{LPC} = \sqrt{\pi_{ACR} \times \frac{x}{y}} \qquad and \qquad \pi_{HPC} = \sqrt{\pi_{ACR} \times \frac{y}{x}} \tag{3.6}$$

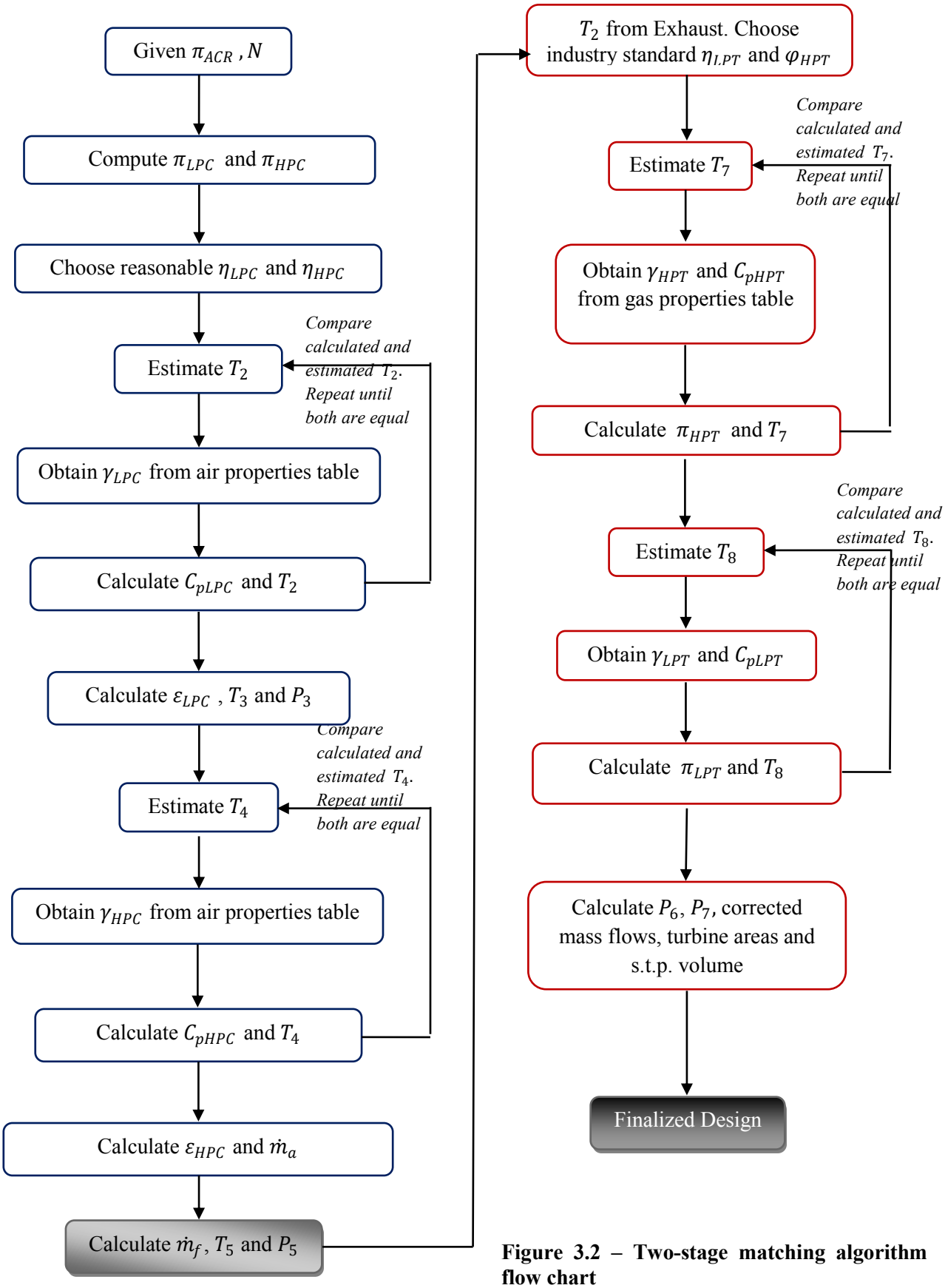

Figure 3.2 – Two-stage matching algorithm flow chart

The graphical user interface (GUI) of the matching program is shown in Figure 3.3

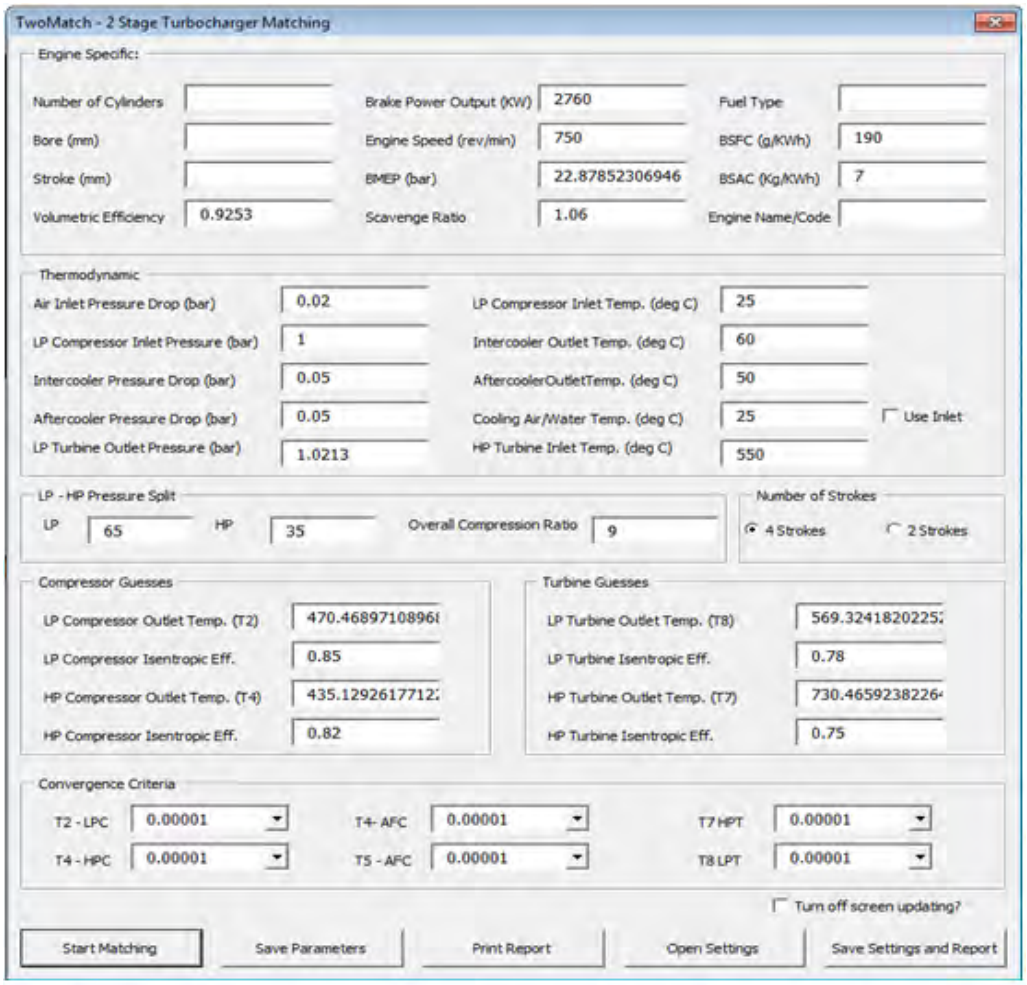

Figure 3.3 – GUI of the Matching Program

3.2.3. Case Study

The matching algorithm was used to specify the air-requirements of a two-stage turbocharger for a test diesel engine used in the marine industry by one of Napiers' customers. The engine has six cylinders with an in-line arrangement. The specification for the engine is shown in Table 3.1. The shaded rows are variable parameters calculated using the matching algorithm, showing all fall within the required limits. See Appendix A for details of equations solved.

A description of the bore and stroke of an engine can be found in Chapter 2. Volumetric efficiency is the ratio of volume of air induced into an engine cylinder to the volume of the engine cylinder. In an engine with Miller timing, the intake valve is closed before the piston reaches the bottom dead centre, so less air volume is injected compared to the full engine cylinder volume. The volumetric efficiency for the engine

case described in Table 3.1 is set to 0.502 as provided by the engine manufacturer. Brake Specific Fuel Consumption (BSFC) is the mass of fuel burnt per kW hour of brake power produced by an engine. Brake power is the measured power output of an engine. Brake Specific Air Consumption (BSAC) is the mass of air used in combustion per kW hour of brake power produced by an engine. The overall mechanical efficiency of a two-stage turbo charger system is the product of the total-to-static efficiencies of the compressor and turbine stages. Typical total-to-static efficiency for a compressor or turbine is 0.82, which works out to be a mechanical efficiency of about 0.45 (i.e. 0.82^4) for a two-stage turbocharger. See Appendix A for a description of compressor and turbine total-to-static efficiencies. Details of how temperatures in Table 3.1 were calculated can be found in Appendix A.

During the matching process, pressure ratio split between the LP and HP compressor is set to 65:35 based on the engine specification in Table 3.1. The cooling fluid temperature is assumed to be standard temperature at 25 degrees. The overall mechanical efficiency of the two-stage turbocharger was computed to be 41 %. The calculated compressor, turbine and cooler specifications are summarised in Tables 3.2, 3.3 and 3.4. Figure 3.4 is a sample detail report from the matching algorithm.

Test Engine Specification	**Requirement**	**Calculated**
Number of Cylinders	6	6
Bore (mm)	460	460
Stroke (mm)	600	600
Engine Power Output/Cyl. (kWb) – kW/cyl	1250 – 1320	**1320**
LP Comp. Power Consumed/Engine Cyl. (kW/cyl)	200 – 1000*	**431.71**
HP Comp. Power Consumed/Engine Cyl. (kW/cyl)	200 – 1000*	**255.48**
LP Compressor Volume Flow (V298) m3/s	11.5 – 13*	**12.96**
Air Mass Flow Rate Per Cylinder (kg/s)	2.35 – 2.5*	**2.48**
Engine Speed (rpm)	600	600
Fuel Type	HFO	HFO
BSFC (g/kWh)	190	190
BSAC (kg/kWh)	7	7
Number of Stokes/Cycle	4	4
Air Inlet Pressure Drop (bar)	0.02	0.02
LP Compressor Inlet Pressure (bar)	1.00	1.00
Inter Cooler Pressure Drop (bar)	0.03 – 0.07	0.05

Test Engine Specification	Requirement	Calculated
After Cooler Pressure Drop (bar)	0.05	0.05
Overall Compression ratio	8.4 – 9.84	9
LP Compressor Pressure Ratio	4 – 4.1*	**4.09**
HP Compressor Pressure Ratio	2.1 – 2.4*	**2.2**
LP Turbine Outlet Pressure (bar)	1.02	1.02
LP Compressor Inlet Temp (°C)	25	25
Intercooler outlet Temp (°C)	60	60
Aftercooler outlet Tempe (°C)	50	50
HP Turbine Inlet Temp (°C)	550	550

Table 3.1 – Comparison between engine specification and computed values

Parameter	Value
HP Compressor V298	3.39
LP Compressor V298	12.96
Compressor Mass Flow (kg/s)	14.86
LP Compressor $m\sqrt{T}$/P	39.79
HP Compressor $m\sqrt{T}$/P	10.42
Compression Ratio (P5/P1)	8.84
Actual Compression Ratio (P2/P01) * (P4/P3)	9.00

Table 3.2 – Compressor specification

Parameter	Value
HP Turbine V298	3.43
LP Turbine V298	5.96
Turbine Mass Flow (kg/s)	15.28
LP Turbine $m\sqrt{T}$/P	18.30

Parameter	Value
HP Turbine $m\sqrt{T}$/P	10.52
Overall Expansion Ratio	6.20
HP Turbine Area (cm^2)	3.43
LP Turbine Area (cm^2)	5.96

Table 3.3 – Turbine specification

Parameter	Value
Cooling Fluid Temp. (^oC)	25.00
Temperature Drop T2 – T3 (^oC)	137.32
Effectiveness	80%
Outlet Air Density (kg/m^3)	4.14

Table 3.4a – Intercooler specification

Parameter	Value
Cooling Fluid Temp. (^oC)	25.00
Temperature Drop T4 – T5 (^oC)	111.98
Effectiveness	82%
Outlet Air Density (kg/m^3)	9.33

Table 3.4b – Charge air cooler specification

Two-Stage Turbomatching Report Date 11/01/2011

My File Name

INPUT PARAMETERS

Engine Specific:	
Engine Name/Code	6146F
Number of Cylinders	6
Bore (mm)	320
Stroke (mm)	400
Power Output (KWb)	2760
Engine Speed (rpm)	750
Air Fuel Ratio	*75.82*
Fuel Mass Flow Rate (kg/s)	*0.15*
Fuel Type	HFO
BSFC (g/KWh)	190
BSAC (kg/KWh)	7
BMEP (bar)	*22.88*
Number of Stokes/Cycle	4
Volumetric Efficiency	0.9253
Scavenge Ratio	1.06

LP - HP Pressure Split:	
LP Compressor Pressure Fraction	65
HP Compressor Pressure Fraction	35

Pressure/Pressure Drops:	
Air Inlet Pressure Drop (bar)	0.02
LP Compressor Inlet Pressure (bar)	1.00
Inter Cooler Pressure Drop (bar)	0.05
After Cooler Pressure Drop (bar)	0.05
Overall Compression ratio	9.00
LP Turbine Outlet Pressure (bar)	1.02

Temperature/Temp. Drops:	
LP Compressor Inlet Temp (°C)	25.00
Intercooler outlet temperature (°C)	60.00
Aftercooler outlet temperature (°C)	50.00
Cooling Air/Water Temperature (°C)	25.00
HP Turbine Inlet Temperature (°C)	550.00
Gas Temperature at Valves (°C)	427.00

DESIGN PARAMETERS

LP Compressor:	
Outlet Temp. - T2 (°C)	197.32
(T2-T1)'	146.47
(T2-T1)	172.32
Avg T (°C)	111.16
Inlet Pres. - P1 (bar)	0.98
Compression Ratio (P3/P1)	4.04
Compression Ratio (P2/P1)	4.09
Outlet Pressure - P2 (bar)	4.01
Power Consumed (MegaW)	1.93
Isentropic Efficiency	0.85

HP Compressor:	
Inlet Temp. - T3 (°C)	60.00
Outlet Temp. - T4 (°C)	161.98
(T4-T3)'	83.62
(T4-T3)	101.98
Avg T (°C)	110.99
Inlet Presure - P3 (bar)	3.96
Compression Ratio (P5/P3)	2.19
Compression Ratio (P4/P3)	2.20
Outlet Pressure - P4 (bar)	8.71
Power Consumed (MegaW)	1.14
Isentropic Efficiency	0.82

Intercooler:	
Cooling Fluid Temp - Tcool (°C)	25.00
Temperature Drop T2-T3 (°C)	137.32
Effectiveness	0.80
Outlet Air Density (kg/m3)	4.14

Aftercooler:	
Cooling Fluid Temp - Tcool (°C)	25.00
Temperature Drop T4 - T5 (°C)	111.98
Effectiveness	0.82
Outlet Air Density (kg/m3)	9.33

LP Turbine:	
Inlet Temperature - T7 (°C)	457.32
(T7-T8)'	206.59
(T7-T8)	161.14
AvgT (°C)	376.75
Outlet Temperature - T8 (°C)	296.17
Inlet Pressure - P7 (bar)	3.52
Outlet Pressure - P8 (bar)	1.02
Expansion Ratio	3.44
Outlet Gas Density (kg/m3)	0.62
Turbine Power Output (MegaW)	1.93
Isentropic Efficiency	0.78

HP Turbine:	
Inlet Temperature - T6 (°C)	550.00
(T6-T7)'	123.58
(T6-T7)	92.68
AvgT (°C)	503.66
Outlet Temperature - T7 (°C)	457.32
Inlet Pressure - P6 (bar)	6.55
Outlet Pressure - P7 (bar)	3.52
Expansion Ratio	1.86
Outlet Gas Density (kg/m3)	1.68
Turbine Power Output (MegaW)	1.14
Isentropic Efficiency	0.75

SIZING PARAMETERS

HP Compressor VZ98	2.52
LP Compressor VZ98	9.63
Compressor Mass Flow (kg/s)	11.04
LP Compressor mRt(T)/P	29.58
HP Compressor mRt(T)/P	7.74
Compression Ratio (P5/P1)	8.84
Actual Compression (P2/P1)*(P4/P3)	9.00

HP Turbine Area (cm^2)	109.64
LP Turbine Area (cm^2)	182.22
Turbine Mass Flow (kg/s)	11.19
LP Turbine mRt(T)/P	13.08
HP Turbine mRt(T)/P	7.45
Overall Expansion Ratio	6.41
HP Turbine VZ98	2.43
LP Turbine VZ98	4.26

Overall Mechanical Efficiency 0.41

Figure 3.4 – A sample detailed report from „TwoMatch"

3.3 ALGORITHM FOR ESTIMATING GEOMETRIC DIMENSION OF A RADIAL COMPRESSOR IMPELLER

3.3.1 Introduction

This Section presents an algorithm for estimating the geometric dimensions of a radial compressor impeller given a target mass flow, pressure ratio, impeller rotating speed, and inlet stagnation temperature and pressure. The geometric parameters of interest include - the number of blades, hub radius, shroud radius, impeller radius and axial length. Other parameters of interest are the blade angles at the impeller inlet and exit as well as the impeller exit blade height. The algorithm presented here is a combination of fundamental turbomachinery physics equations, correlations extracted from literature and statistical modelling. The algorithm is used to calculate an initial estimate of compressor impeller geometric dimensions when designing a new compressor.

3.3.2 Background

The development of radial compressors is challenging in a highly competitive market place, particularly when the design process relies heavily on the use of computationally, and time-expensive CFD models. However, the preliminary design phase of radial compressors often applies a one-dimensional approach to solve the thermodynamics and fluid equations that describe the internal flow physics. This computationally inexpensive method gives results that guide the engineer towards the optimum design space for further exploration with 3-D CFD [23]. Yuri Biba and Peter Menegay [24] identified two main methods used in the preliminary design process for radial compressors - direct method and inverse design approach. In the direct method, performance is calculated from a given compressor geometry. In the inverse design approach, the geometry is calculated to meet a required performance. The inverse design algorithm implemented by Yuri Baba *et al.* [24] calculates the required one-dimensional geometry and relies on a trusted database of loss models. M. S. Kamaleshaiah *et al.* [25] implemented a radial compressor performance algorithm based on a direct prediction method with empiricism for the loss models and boundary layer growth within the blade channel. This method computes performance parameters such as stage pressure ratio and efficiency for a given geometry and inlet conditions. The one-dimensional method is a station-to-station calculation of performance or geometric parameters for direct and inverse method respectively as shown in Figure 3.5

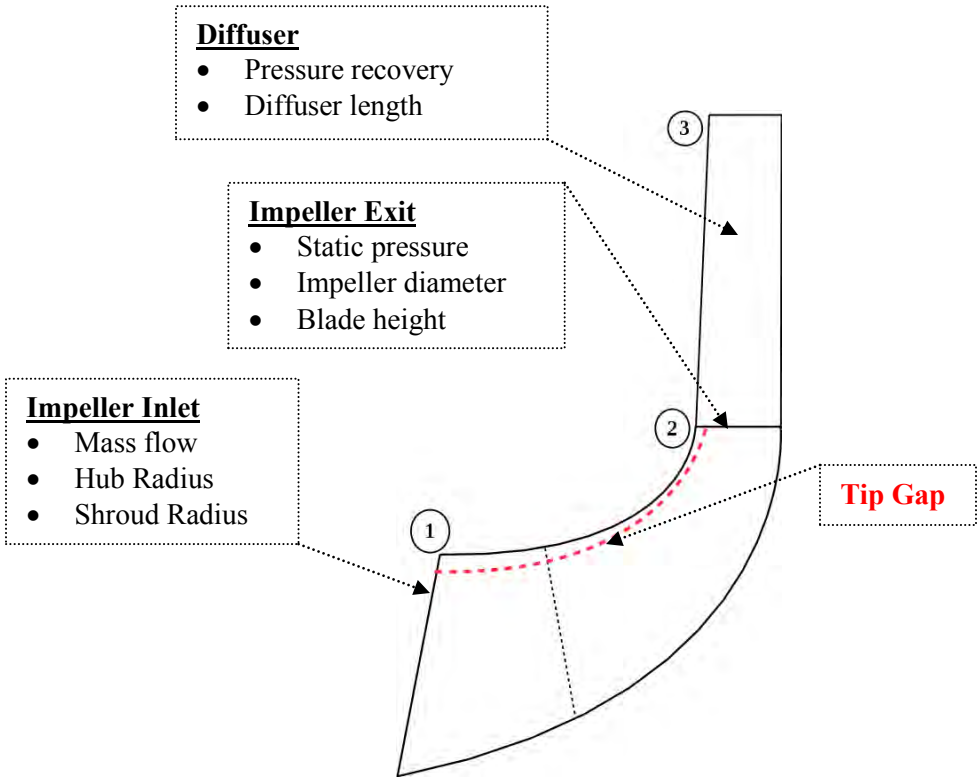

Figure 3.5 - One-dimensional modelling stations

3.3.3 Inverse Design Algorithm Description

The algorithm presented in this thesis is based on the inverse design approach. This approach requires the designer to specify the operating conditions and performance requirements of the impeller. A mathematical model is used to work out the approximate geometric dimensions of the impeller. The approximate geometry is used as a starting geometry for further 3D CFD analysis and optimisation. Novel mathematical equations were formulated while developing the algorithm. Table 3.5 shows the operating conditions and performance requirements required as input to the algorithm.

Operating conditions	Performance requirements
Shaft speed (rev/mins)	Target mass flow rate (kg/s)
Inlet stagnation temperature (K)	Pressure ratio
Inlet stagnation pressure (Pa)	

Table 3.5 - Operating conditions and performance requirements

R.A. van den Braembussche [26] states that the ratio of shroud to hub radius $^{R_{1s}}/_{R_{1h}}$ depends on the volume flow through the impeller. A very small value can result in blockage while a very large value can result in high stresses at the tip of the impeller blade. This blockage is due to shorter blade height at impeller inlet, resulting in a reduction in flow area. The minimum hub radius is determined by the radius required to transmit torque and number of impeller blades required. A value between 1.43 and 3.33 was suggested by [26]. R.A. van den Braembussche [26] also suggested that the blade angle at the shroud of the impeller inlet should not exceed 70 degrees to keep the Mach number below 1. Whitfield A., Baines N.C [27] suggested an optimum blade angle at the shroud to be between 61 and 65 degrees. Industrial experience suggests typical blade angles at the hub of between 10 and 30 degrees. The impeller exit blade angle (back sweep angle) is set to between 0 and 60 degrees. R.A. van den Braembussche [26] also suggested the ratio of impeller exit blade height to impeller radius $^{b_2}/_{R_2}$ should be between 0.05 and 0.15. The lower limit is set to avoid large clearance losses and friction losses in narrow channels. The upper limit is set to limit diffusion in the impeller, avoid separations downstream of the diffuser and limit centrifugal stresses at the impeller exit. However, industry experience suggests the upper limit can be increased to 0.18 as long as the peak stress at the impeller exit does not exceed the maximum permissible for the design conditions.

To overcome the non-availability of existing reference design, design guidelines based on literature [26, 27] and practical constraints as described in *Appendix B* are formulated into assumptions at the start of the design process. Geometric parameters are estimated based on design guidelines from the literature [26, 27]. The parameters are listed in Table 3.6. The inverse design algorithm is illustrated in Figure 3.6

Parameter	**Minimum Estimate**	**Maximum Estimate**
Ratio of shroud to hub radius $\left(^{R_s}/_{R_h}\right)$	1.43 (2.7)	3.5
Root mean square blade angle at impeller inlet (β_{1rms})	40	50
Root mean square blade angle at impeller exit (β_{2rms})	20	60
Ratio of impeller exit blade height to impeller radius $\left(^{b_2}/_{R_2}\right)$	0.05	0.18
Ratio of hub radius to hub blade thickness $\left(^{R_h}/_{Hub_{th}}\right)$	5	7

Table 3.6 - Range of assumptions values

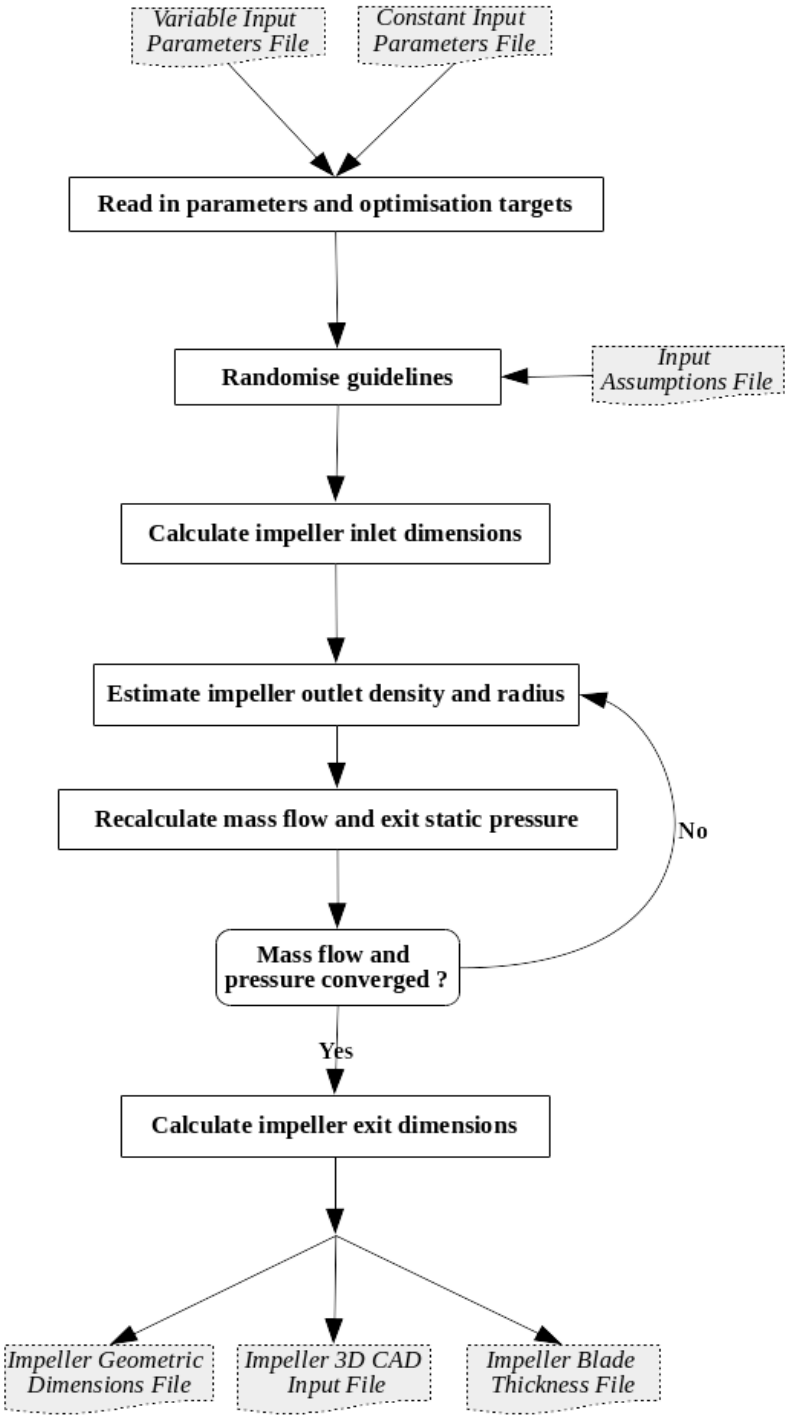

Figure 3.6 - Algorithm flow chart

Figure 3.7 illustrates the velocity triangle at the root-mean-squared (rms) span level at the inlet to the impeller as depicted by the red circle in Figure 3.7. The direction of rotation of impeller is indicated with an arrow. U_1 is the blade speed, W_1 is gas relative velocity along the blade profile (with components in the

meridional and tangential directions), C_1 is gas absolute velocity and β_{1rms} is the blade angle. Centrifugal force acting on the impeller is also depicted in Figure 3.7.

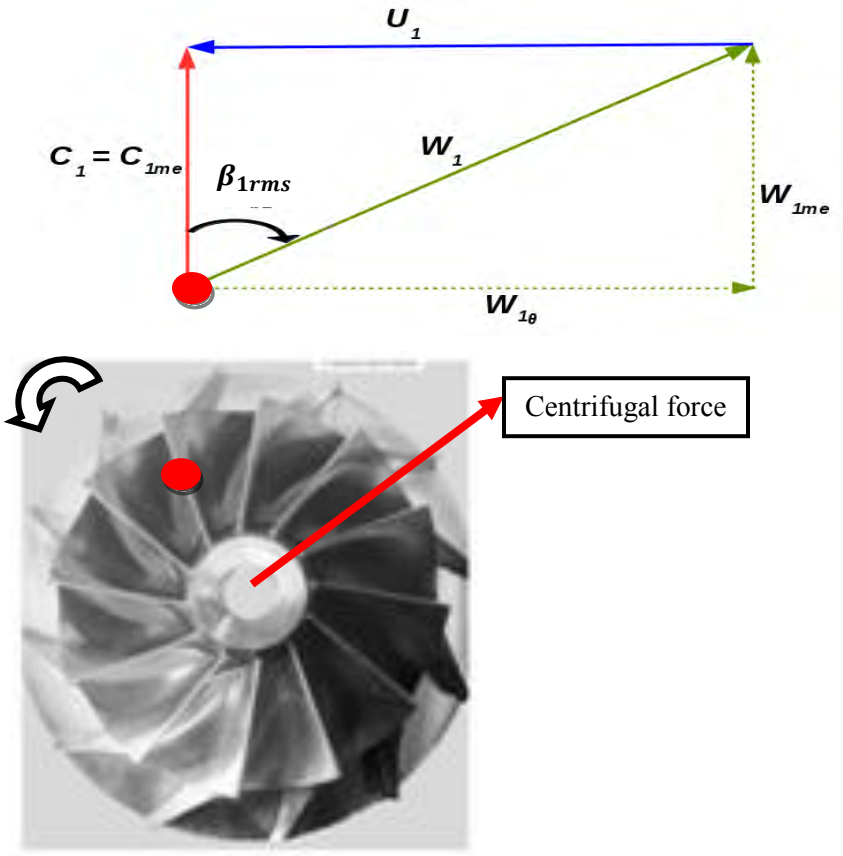

Figure 3.7 – Velocity Triangle at Impeller Inlet

Blade velocity U is blue, meridional velocity is red

For brevity, only the novel equations formulated are presented in this Section as listed in Equations 3.7 to 3.9. The Equations are derived by relating the geometric area of impeller inlet with mass flow rate equation as described in Appendix B.

$$C_{1me\_rms} = \frac{U_{rms}}{tan\beta_{1rms}} = \frac{\pi N R_h}{30 tan\beta_{1rms}} \left(\frac{n^2+1}{2}\right)^{1/2} \tag{3.7}$$

$$R_h = \left(\frac{C_{1me_{rms}} \times A_F \times 30 tan\beta_{1rms}}{\pi^2 N (n^2-1) \left(\frac{n^2+1}{2}\right)^{1/2}} \right)^{1/3} \tag{3.8}$$

$$N_{blades} = \frac{\pi R_h}{Hub_{th} \times K_b} \qquad 5 \leq K_b \leq 7 \tag{3.9}$$

where N is the impeller rotating speed in rev/min, n is the ratio of impeller shroud radius to hub radius $\left({R_s}/{R_h}\right)$, A_F is the impeller inlet flow/geometric area, $N_{blade\ s}$ is the number of main blades, Hub_{th} is the hub blade thickness and K_b is a constant based on geometric constraints at impeller leading edge hub due to blade blockage. A fully blocked impeller at leading edge hub happens when the blade occupies the entire hub circumference as described in Equation 4.0.

$$2\pi R_h = Hub_{th} \times N_{blades} \tag{4.0}$$

Introducing the constant K_b into Equation 4.0 and re-arranging, number of impeller blades N_{blades} can be expressed as in Equation 3.9, where $K_b = 0.5$ represents 100% blade blockage at the hub. Consequently, $K_b = 1$, $K_b = 2$ and $K_b = 4$ represents 50%, 25% and 12.5% blockage respectively. Additional information on fundamental flow physics in a radial compressor and diffuser is presented in *Appendix C*. The inverse design algorithm presented in this Chapter outputs the geometric dimensions of the impeller and the corresponding input file to „RC_CAD" – the parametric CAD program described in Chapter 5. The geometric parameters calculated are:

- Number of blades
- Hub radius
- Shroud radius
- Blade angle at hub
- Blade angle at shroud
- Back sweep angle at impeller exit
- Hub blade thickness
- Shroud blade thickness
- Impeller radius
- Impeller exit blade height

Other parameters required to create the 3-D impeller geometry such as blade angle distribution is assumed based on an existing geometry. The axial length is assumed to be 80% of the impeller radius. When the geometry created by the inverse algorithm is analysed using CFD code, the impeller geometry may not deliver the required mass flow rate, and will require manual modification to improve mass flow accuracy. The inverse algorithm does not always generate an aerodynamically efficient impeller. The impeller

design has to be optimised using CFD to improve the efficiency. In the next Section, four case studies where a new compressor impeller was designed using the algorithm is presented.

3.3.4 Validation of Inverse Design Algorithm with CFD

It is important to analyse estimated geometry created using the inverse design algorithm by carrying out CFD analysis on it to see how it compares with the target design requirements e.g. mass flow. The CFD solver TBLOCK [6] is used to analyse the geometries. Mesh convergence study and validation of TBLOCK is detailed in Sections 6.1 and 6.2 of this thesis respectively. A medium mesh distribution as described in Section 6.1 is used for the analysis presented in this Section. Table 3.7 shows the performance requirements for validation cases presented here. The cases are chosen to cover a wide range of applications. For example, case 4 is for a small turbocharger application in automotive. The range of mass flow from 0.5 to 20 kg/s and operating speeds as low as 10,000 RPM, and up to 100,000 RPM represents a wide range. The algorithm is used to calculate the geometric dimensions of the four validation cases listed in Table 3.7. The result of the calculated geometric parameters is show in Table 3.8.

No.	Mass Flow (kg/s)	Inlet Total Pressure (Pa)	Outlet Static Pressure (Pa)	Operating Speed (RPM)
1	2.1	100000	165000	40,000
2	11.4	350000	600000	25,000
3	20	100000	130000	10,000
4	0.5	100000	250000	100,000

Table 3.7 - Performance requirements for validation cases

Parameters	Case 1	Case 2	Case 3	Case 4
Number of Main Blades	6	5	8	8
R_{1h}	0.0180	0.0247	0.0622	0.0087
R_{1s}/R_{1h}	3.4111	3.5	3.3222	3.2333
R_{1s}/R_2	0.5828	0.5920	0.6030	0.62
b_2/R_2	0.1483	0.0956	0.1694	0.1694
Shroud LE blade angle	61.823	66.4791	61.6912	61.5488
Shroud Backsweep Angle	60	24.44	55.5556	20

Parameters	Case 1	Case 2	Case 3	Case 4
Hub LE blade thickness (mm)	2.841	4.722	9.180	1.282
Hub Maximum Blade Thickness (mm)	4.262	7.084	13.700	1.923
Hub TE blade Thickness (mm)	4.262	7.084	13.700	1.923
Shroud LE blade thickness (mm)	0.946	1.573	3.057	0.4268
Shroud Max. Blade Thickness (mm)	0.946	1.573	3.057	0.4268
Shroud TE blade Thickness (mm)	0.946	1.573	3.057	0.4268

Table 3.8 - Calculated geometric parameters

In order to carry out CFD analysis of the geometries created by the inverse design algorithm, established blade angle distribution and meridional profile distribution is used to generate the 3D geometry. The diffuser length is specified to be short (10% of impeller radius), as the focus is on the impeller. Table 3.9 shows the assumed geometric parameters. Case 1 geometry was obtained from [96] with a shroud tip gap of 4%, while case 2 geometry is an optimised design presented in Chapter 6 with a tip gap of 0.5%. Case 3 is a large scale version of case 2 and its tip gap is reduced accordingly. A shroud tip is illustrated in Figure 3.5. The purpose of the tip gap is to prevent the impeller blade from rubbing into the shroud casing while in operation. This can happen due to thermal expansion of the impeller.

CFD analysis of the four case studies is carried out, and the computed mass flow rate is compared with the target mass flow input to the inverse algorithm. Please refer to Chapter 6 for validation study of TBLOCK [6] CFD solver used during this research. A medium mesh size distribution as described in Chapter 6 is used for the analysis. Table 3.10 shows that the mass flow calculated deviate from the target mass flow rate by no more than 19%. A simple approach to increase or reduce the calculated mass flow is to modify the hub radius, shroud radius or blade thickness. Increasing the hub and or shroud radius will increase the mass flow rate due to increase in the inlet flow area. Also reducing the blade thickness will increase the mass flow. Table 3.11 shows a comparison between the total-to-static efficiencies calculated by the inverse algorithm and 3D CFD analysis. The CFD cases are set up with a diffuser length of 10% the impeller tip radius. The impeller total-to-static efficiency estimated using the inverse algorithm is based on a diffuser recovery of 10%. Although the algorithm presented here is for estimating impeller size, the total-to-static efficiency is also calculated and presented in Table 3.11. The dimensions of geometries for the various cases investigated are show in Figure 3.8. The geometry sizes are proportional to the target mass flows for each case.

Parameters	Cases 1 to 4
L/R_2	0.8
R_3/R_2	1.01
b_3/b_2	1
Inducer leading edge lean angle	5
Hub lean angle	5
Hub Wrap Angle Correction at Leading Edge	0
Hub Wrap Angle Correction at mid-span	4
Hub Wrap Angle Correction at trailing edge or Rake angle	25
Hub Meridional Control Point 2	0.5
Hub Meridional Control Point 3	0.5
Shroud Meridional Control Point 2	0.5
Shroud Meridional Control Point 3	0.5
Shroud Beta Angle 2	35
Shroud Beta Angle 3	35
Splitter Position Hub	0.35
Splitter Position Shroud	0.35

Table 3.9 - Assumed geometric parameters

No.	Target Mass Flow (kg/s)	CFD Mass Flow (kg/s)	% Deviation	Impeller Radius (cm)
1	2.2	1.85	-15.91	11
2	11.4	9.26	-18.77	5
3	20	21.23	+6.15	34
4	0.5	0.413	-17.4	5

Table 3.10 - Mass flow comparison

No.	1-D T-S Efficiency (%)	3-D CFD T-S Efficiency (%)	Difference
1	50.34	49.34	-1.00
2	49.71	50.39	-0.68
3	49.47	38.23	-11.24
4	50.13	44.49	-5.64

Table 3.11 - Efficiency comparison

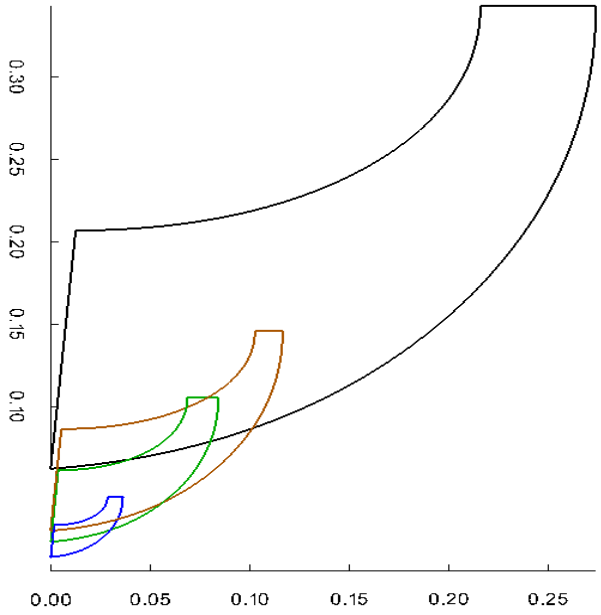

Figure 3.8 - Meridional view of four validation cases

CONCLUSION

This Chapter presented a matching algorithm used for estimating the flow areas of the LP and HP compressor and turbine in a two-stage turbocharger to meet a specified diesel engine power requirement. The matching algorithm was discussed in detail and it was used to match the compressors and turbines in a two-stage turbocharger to a test diesel engine. The results show the variable parameters calculated using the matching algorithm all fall within the required limits. A second algorithm for estimating the geometric dimensions of a radial compressor impeller given the operating speed, target mass flow and pressure ratio; and inlet stagnation conditions was also presented. The algorithm was discussed in detail, along with assumptions and correlations used. The algorithm was used to design 4 significantly different test case compressor impellers and compared with CFD analysis. The results show mass flow calculated using 3D CFD analysis was within 19% of target mass flow. In the next Chapter, a detail overview of state-of-the-art in radial compressor design is presented.

CHAPTER 4

STATE-OF-THE-ART IN RADIAL COMPRESSOR DESIGN

This Chapter discusses the state-of-the-art in the design of radial compressors, including:

- Geometry definition approaches
- Techniques for parameterising radial compressor impeller and vane-less diffuser
- Mesh generation and mesh types in turbomachinery
- Numerical modelling techniques and their governing equations
- Optimisation methods and algorithms used in the design optimisation of turbomachinery

There are no research contributions from this Chapter

4.1 GEOMETRY DEFINITION APPROACHES

Most commercial turbomachinery CAD packages such as ANSYS BladeModeler [29], ANSYS BladeGen[30], TURBOdesign CAD[31], AutoBlade^{TM} [32] and AxCent [33] provide a user friendly Graphical User Interface (GUI) for rapid design of geometries. In addition to using the GUI for turbomachinery design, CAD systems also offer methods of defining geometry, for example, text input file or via scripting, such that they can be modified automatically during an optimisation process. There are two major optimisation approaches used in CAD viz. parameter-based and parameter-free shape optimisation [34]. In a parameter-based optimisation, the geometry is built on parametric models, while parameter-free optimisation comprises topology optimisation and adjoint optimisation methods [34].

4.1.1 Parameter-Based Optimisation

In parametric modelling, the geometry is defined by means of important descriptions or parameters that may be independent or inter-dependent [35]. Parametric based modelling allows a product designer to access the impact of design parameters on the problem solution e.g. CFD solution, hence the reason for its popularity. Given sufficient computational resources, it is possible to carry out multi-objective, multi-

disciplinary parametric optimisation of 3D models with up to 200 varying parameters [34]. A geometric model can be fully parametric or partially parametric depending on whether the entire geometry is parameterised. Figures 4.1 and 4.2 give example parameterisations of the meridional profile of a radial turbine for aerodynamic and structural optimisation, by L Mueller *et al.* [36].

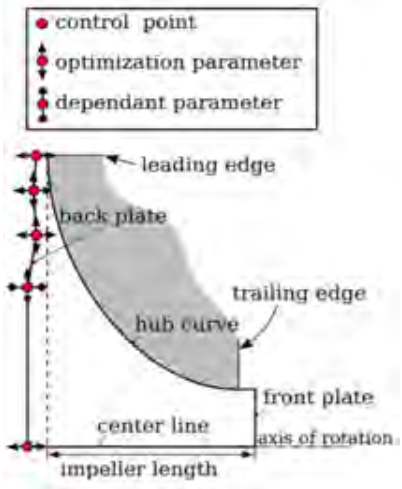

Figure 4.1 - Solid meridional profile [36]

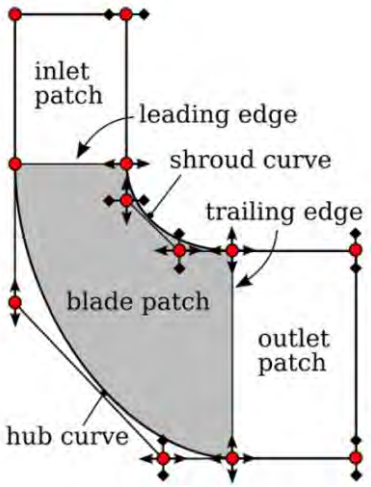

Figure 4.2 - Fluid meridional profile [36]

4.1.2 Parameter-Free Optimisation

The two main parameter-free optimisation approaches are topology optimisation and adjoint based simulation. Topology optimisation is mostly applied to internal flows or structural optimisation. In this approach, the computational domain is prescribed (usually larger than required) along with the inlet and outlet boundaries in the case of CFD. The most favourable internal flow path is then obtained

automatically for objectives such as pressure drop, flow uniformity, flow separation, etc. The available space is modified during the flow simulation until a best shape is established [35]. The best shape is then approximated in a CAD program taking into account manufacturing constraints. In the end, the final CAD model is analysed using CFD to validate it. Figure 4.3 is an example of FEA topology optimisation using Siemens NX software of a crane hook to reduce weight without compromising structural requirements. The optimised geometry is cleaned up in a CAD program in the final stage.

In adjoint simulation, in addition to solving the RANS equations; the so-called adjoint equations are also solved for the objectives of interest. These adjoint equations are as computationally expensive as the RANS equations. The primary (e.g. RANS) and adjoint equations are run on the same computational grid. The adjoint equations calculate sensitivities on the computational domain boundaries thereby providing insights to sections where the geometry can be pushed inwards or pulled outwards to improve the design [35]. In some instances, the designer may choose to combine a parametric-based approach with the adjoint simulation forming a hybrid solution. A summary of geometric definition optimisation approaches is shown in Figure 4.4.

Figure 4.3 - Topology optimisation of a crane hook using NX8 [source: 35]

Approach		Strong Points	Weak Points	Design Stage	State
Parameter-free optimisation	Topology optimisation	• Innovative and unconventional designs. • Fast (one extended solver run).	• Extra work in re-modelling results in CAD tool. • Sometimes difficult to correlate with constraints, e.g. for production. • Limited to re-defined objectives (e.g. pressure drop, homogeneity). • Used only for internal flows. • Difficult to apply in multi-objective and multi-disciplinary scenarios.	Concept design	• Successful projects in selected industries. • Ongoing R&D.
	Adjoint simulation	Fast (one additional solver run comparable to original simulation effort)	• Confined to small changes (unless utilized repetitively). • Limited to implemented objectives (e.g. drag, homogeneity). • Difficult to apply in multi-disciplinary scenarios.	Fine-tuning	• Scientific applications. • Ongoing R&D e.g. hybrid approach (parametric-adjoint).
Parameter-based optimisation	Fully-parametric modelling	• CAD geometry of high quality. • Direct incorporation of many constraints. • Applicable to multi-objective and multi-disciplinary optimisation. • Creates overview and insight.	• Many solver runs. • Investment into parametric model needed. • By definition confined to design space of parametric model.	Initial design to fine-tuning.	• Mature • Successful projects in many industries. • Ongoing R&D, e.g. robust design optimisation, HPC/Cloud
	Partially-parametric modelling	• Quick and easy to set up and conduct. • Focus on local changes. • Applicable to multi-objective and multi-disciplinary optimisation.	• Many solver runs. • By definition limited by design space of parametric model and baseline.	Initial design to fine-tuning	Mature. Widely used in many industries. Ongoing R&D, e.g. usability.

Figure 4.4 - Overview of shape optimisation approaches [adapted from [35]]

4.2 PARAMETER-BASED GEOMETRY DEFINITION FOR RADIAL COMPRESSOR IMPELLERS

The complex 3D shape of radial compressor impellers, highly turbulent flow and complex flow physics within the impeller limits radial compressor designers to use parameter-based approaches only for optimisation. Sensitive geometric features such as leading edge curvature, fillet radius, and shroud gap, hub and shroud curvature distribution, blade thickness distribution require direct control by the designer during the design process. In the next sub-sections, various parameter based curves/polynomial techniques for defining radial compressor impeller geometry are discussed in detail.

4.2.1 Bezier Curves

Bezier curves were invented in the late 50s and early 60s by Paul de Castelajau and Pierre E. Bezier working independently and almost simultaneously. Although Paul de Castelejau was the first to develop an algorithm by combination of polygon meshes to obtain smooth surfaces suitable for modelling car chassis now know as the Castelejau algorithm, he did not publish his work. However, Pierre E. Bezier work on intersection of partial cylinders to achieve the same goal was the first to be published and the method is today known as Bezier curves [37, 38]. A Bezier curve of degree *n* is defined by Equation 4.1

$$C(u) = \sum_{\mathrm{i}=0}^{\mathrm{n}} \mathrm{P_i}\, B_{i,n}(u) \qquad 0 \le u \le 1 \tag{4.1}$$

where the Bezier basis function or Bernstain polynomial is represented as

$$B_{i,n}(u) = \binom{n}{i} u^i (1-u)^{n-i} = \frac{n!}{i!\,(n-i)!} u^i (1-u)^{n-i} \tag{4.2}$$

Where $\mathrm{P_i}$ are the control points to be weighted and n is the degree of the curve.

To evaluate the curve $U \in (0,1)$, $n+1$ control points are iterated and the corresponding influence is computed. Figure 4.5 is a cubic curve segment with its Bezier polygon [a, b] where $u = a(1-t) + bt$.

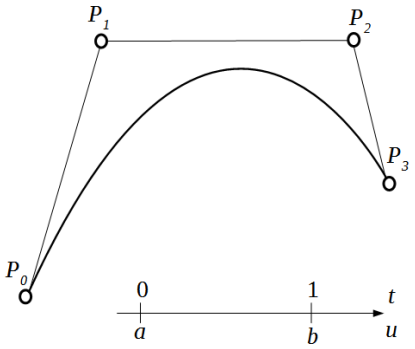

Figure 4.5 – A cubic curve segment with its Bezier polygon [a, b]

4.2.2 Lagrange Polynomial Interpolation

The Lagrange interpolation allows the designer to compute points $\boldsymbol{P}^n(t)$ on the interpolation polynomial through $n+1$ data points [39]. The explicit form of the interpolation polynomial $\boldsymbol{P}$ is given by Equation 4.3

$$\boldsymbol{P}(t) = \sum_{i=0}^{n} \boldsymbol{P}_i L_i^n(t) \tag{4.3}$$

where the Lagrange polynomials L_i^n is given by

$$L_i^n(t) = \frac{\prod_{j=0, j\neq i}^{n}(t - t_j)}{\prod_{j=0, j\neq 1}^{n} t_i - t_j} \tag{4.4}$$

However, Lagrange polynomial interpolation is not shape preserving because the polynomial interpolant may oscillate if the precision of the interpolation points is changed [39]. Also, the interpolant may oscillate especially near the ends of the interval depending on the distribution of the control points [40]. For this reason, Lagrange interpolation is used only for linear interpolation in the CAD algorithm presented in Chapter 5.

4.2.3 Cubic Spline Polynomial Interpolation

Interpolation with cubic splines is essentially equivalent to passing a flexible plastic ruler through data points, where the spline interpolants and its first two derivatives are continuous at the data points [40]. Splines are polynomials on subintervals that are connected in a smooth way. If $n+1$ points are taken,

which can be referred to as knots: $t_0 < t_1 \ldots\ldots < t_n$. A spline of degree k having knots $t_0, \ldots\ldots, t_n$ is a function $s(x)$ that satisfied the following properties:

1. On $[t_{i-1}, t_i\ ]$, $s(x)$ is a polynomial of degree $\leq k$ i.e., $s(x)$ is a polynomial on every subinterval that is defined by the knots
2. Smoothness: $s(x)$ has a continuous $(k-1)^{th}$ derivative on the interval $[t_0,\ t_n]$

A cubic spline is a spline for which the function is a polynomial of degree $\leq\ 3$ on every subinterval, and a function with two continuous derivates [41]. The polynomial equation of the spline is represented using Equation 4.5.

$$s(x) = \begin{cases} s_0(x), & x \in [t_0, t_1] \\ s_1(x), & x \in [t_1, t_2] \\ s_{n-1}(x), & x \in [t_{n-1}, t_n] \end{cases} \tag{4.5}$$

while the continuity condition Equations are;

$$s_i^{'}(t_{i+1}) = s_{i+1}^{'}(t_{i+1}), \quad s_i^{''}(t_{i+1}) = s_{i+1}^{''}(t_{i+1}) \qquad 0 \leq i \leq n-2 \tag{4.6}$$

Putting together the polynomial equations and continuity condition equations, there are $4n-2$ equations with $4n$ unknowns which allows for 2 degrees of freedom. This results in a system of equations of the matrix form $\boldsymbol{A}.\boldsymbol{m} = \boldsymbol{b}$, where $\boldsymbol{A}$ is a tri-diagonal matrix with elements expressed as a function of known knot points, $\boldsymbol{m}$ is a vector of unknown coefficients of the second derivative of the polynomial function on each interval and $\boldsymbol{b}$ is a known vector which is a function of the knot points. The matrix system can be solved using the Tri-diagonal Matrix Algorithm (TDMA) for the unknown vector $\boldsymbol{m}$ which is then used to calculate the polynomial between each interval to form the cubic spline. A cubic spline interpolation is much more accurate than Lagrange interpolation due to its stability. Although the computer program for spline interpolation is longer and more complicated than that for Lagrange interpolation, the object-oriented programming paradigm allows such algorithms to be written once for subsequent re-use, reducing the time taken to develop the program [40]. In the CAD algorithm developed in this thesis, all non-linear interpolation is carried out using a cubic spline interpolation algorithm.

4.2.4 B-Splines

A B-spline is a composed of a collection of piecewise polynomials. One of the main advantages of using B-splines over Beziers or cubic splines is that it offers local control of the shape. A B-spline can be viewed as a collection of Bezier curves as shown in Figures 4.6 and 4.7 [42].

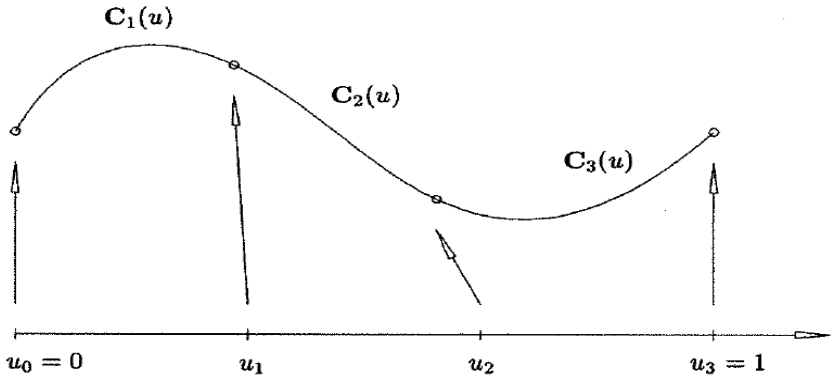

Figure 4.6 – A piecewise cubic polynomial curve with three segments [42]

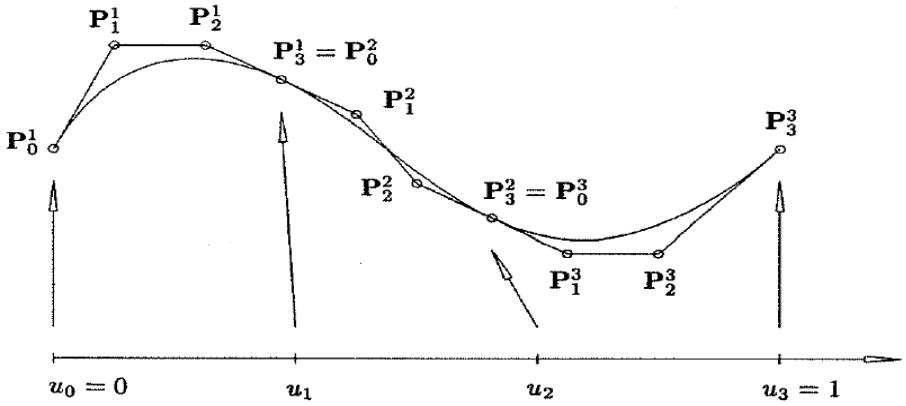

Figure 4.7 – Polynomial segments of a B-spline represented in Bezier form [42]

A *pth* degree B-spline curve is defined by

$$C(u) = \sum_{i=0}^{n} \mathrm{N}_{i,p}(u)\boldsymbol{P_i} \qquad a \le u \le b \tag{4.7}$$

where $\boldsymbol{P_i}$ are the control points, $\mathrm{N}_{i,p}(u)$ are the *pth* degree B-spline basis functions defined on a non-periodic knot vector $U = \{u_0, \ldots . u_m\}$, and m is the number of polynomial segments. The Basis function is defined as

$$N_{i,p}(u) = \begin{cases} 1 & if\ u_i \le u < u_{i+1} \\ 0 & otherwise \end{cases} \tag{4.8}$$

$$N_{i,p}(u) = \frac{u - u_i}{u_{i+p} - u_i} N_{i,p-1}(u) + \frac{u_{i+p+1} - u}{u_{i+p+1} - u_{i-1}} N_{i+1,p-1}(u) \tag{4.9}$$

4.3 GEOMETRY DISCRETISATION

The most common CFD mesh type used for turbomachinery applications is structured multi-block hexahedral mesh cells. One of the main advantages of a structured grid over unstructured grid is that it requires less memory for CFD simulations and allows a finer boundary layer resolution. Compared to unstructured meshes, high aspect ratio structured cells can be used around the leading and trailing edges to provide better geometry representation and solution resolution [43]. The hexahedral mesh used for CFD calculations during this research is qualitatively accessed in Chapter 6. Effort was made to minimise high aspect ratio cells in the computational domain by adjusting cells growth rate from wall boundaries. Figure 4.9 shows high aspect ratio structure grid around the leading edge of an aerofoil. Hexahedral mesh cells can be put together in different topologies – O-Grid, C-Grid and H-Grid as show in Figure 4.8. O-grid mesh topology has an additional advantage in turbo-machinery blade meshing because it helps to increase mesh orthogonality around the leading edge which improves the resolution of flow features in that region. Figures 4.9 and 4.10 are examples of O-grid and H-grid topology meshes respectively. Figure 4.11 is an example of a H-grid on a radial compressor impeller blade surface.

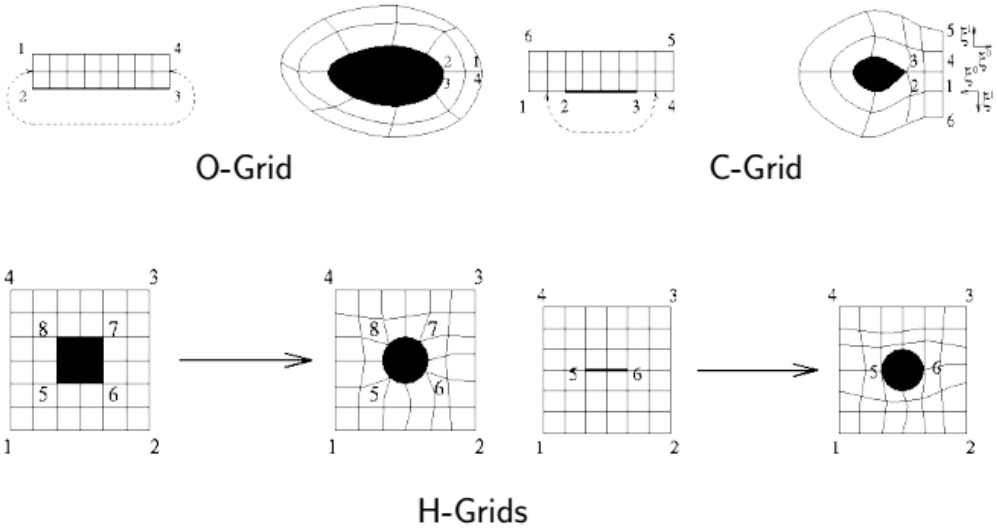

Figure 4.8 – Illustration of grid topologies [51]

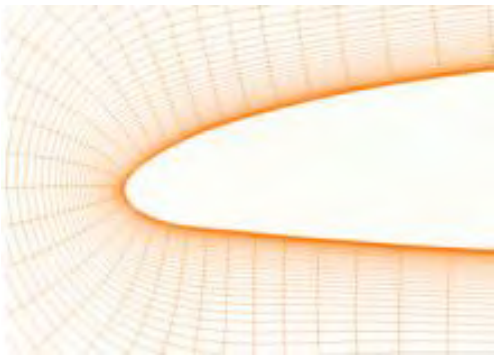

Figure 4.9 - O-grid topology around the leading edge of an aerofoil [source: 44]

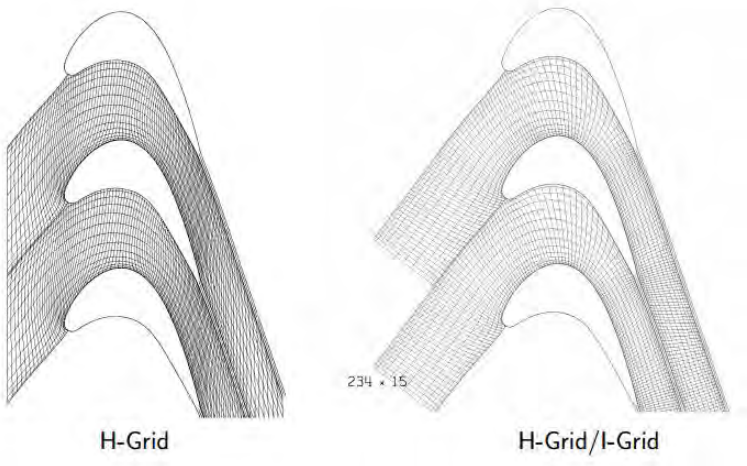

Figure 4.10 - Example H-Grid around an axial compressor blade [source: 44]

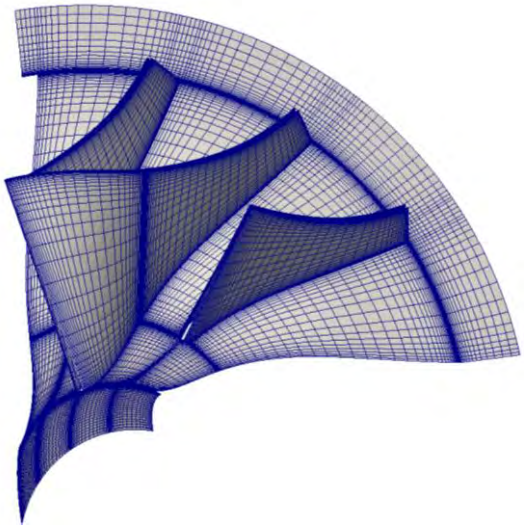

Figure 4.11 – H-Grid on a centrifugal compressor impeller

4.4 NUMERIAL MODELLING OF ROTATING MACHINERY

In most CFD problems, the equations of fluid flow and heat transfer are solved in a stationary (or inertia) reference frame. However, in problems involving moving parts such as rotating blades, it is more advantageous to solve the problem in a moving (non-inertia) reference frame. With a moving reference frame, the flow around the moving part can be modelled as a steady-state problem with respect to the moving reference frame. When a moving reference frame is used, the equations of motion are modified to take into account the acceleration terms which occur due to transformation from stationary to the moving reference frame [45]. Depending on the complexity of the problem, moving reference frame problems can be modelled as a single reference frame or a multiple reference frame problem. In a single reference frame problem, the entire computational domain is modelled in the relative reference frame. In a multiple reference frame problem, the domain is split into zones, with well-defined interfaces between zones. The governing equations for the various frame of reference methods are now presented.

4.4.1 Flow in a Rotating Reference Frame

The main reason for using a rotating reference frame model is to render a problem which is unsteady in a stationary frame of reference steady in a relative reference frame. For a blade rotating at a constant speed, it is possible to transform the governing equations of fluid motion to the rotating reference frame such that a steady-state solution is possible [45]. Using the co-ordinate system of a rotating frame illustrated in Figure 4.12, the stationary coordinate system of equations is modified to represent the rotating reference frame.

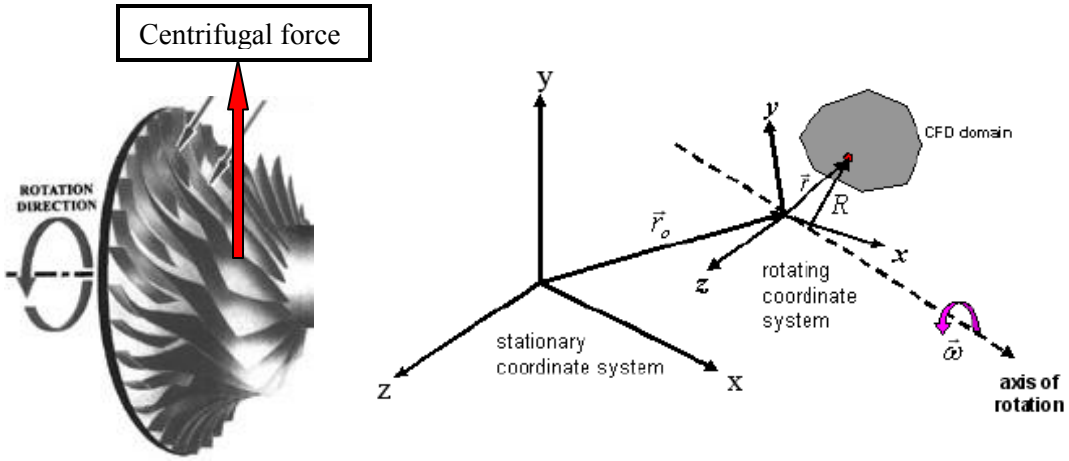

Figure 4.12 – Stationary and Rotating Reference Frames. Source [45]

The rotating coordinate system is rotating with an angular velocity $\vec{w}$ relative to the stationary coordinate system. The origin of the rotating frame is located by a position vector $\vec{r}_0$. The CFD domain for the problem is defined with respect to the rotating reference frame such that every point in the CFD domain is located by a position vector $\vec{r}$ from the origin of the rotating frame. The velocities in the stationary frame can be transformed to the rotating frame using Equation 4.10.

$$\vec{v}_r = \vec{v} - \vec{u}_r \tag{4.10}$$

where

$$\vec{u}_r = \vec{w} \times \vec{r} \tag{4.11}$$

In Equations 4.10 and 4.11, $\vec{v}_r$ is the relative velocity (the velocity viewed from the rotating frame), $\vec{v}$ is the absolute velocity (the velocity viewed from the stationary frame), and $\vec{u}_r$ is the velocity due to the moving frame. The equations of fluid motion for a steadily rotating frame can be formulated in two ways:

- The momentum equation can be expressed using the relative velocities as dependent variables (i.e. the relative velocity formulation).
- The momentum equation can be expressed using the absolute velocities as dependent variables (i.e. the absolute velocity formulation).

Relative Velocity Formulation

Conservation of mass:

$$\frac{\partial \rho}{\partial t} + \nabla \cdot \rho \vec{v}_r = 0 \tag{4.12}$$

Conservation of momentum:

$$\frac{\partial}{\partial t}(\rho \vec{v}_r) + \nabla \cdot (\rho \vec{v}_r \vec{v}_r) + \rho(2\vec{w} \times \vec{v}_r + \vec{w} \times \vec{w} \times \vec{r}) = -\nabla p + \nabla \bar{\bar{\tau}}_r + \vec{F} \tag{4.13}$$

Conservation of energy:

$$\frac{\partial}{\partial t}(\rho E_r) + \nabla \cdot (\rho \vec{v}_r H_r) = \nabla . \left(k \nabla T + \bar{\bar{\tau}}_r \cdot \vec{v}_r \right) + S_h \tag{4.14}$$

Here, ρ is density, p is pressure and S_h is an additional energy source term. Two additional acceleration terms are added to the momentum equations: the Coriolis acceleration ($2\vec{w} \times \vec{v}_r$), and the centripetal acceleration ($\vec{w} \times \vec{w} \times \vec{r}$). The viscous stress $\bar{\bar{\tau}}_r$ is defined using the relative velocity derivatives. $\vec{F}$ is an external body force. The energy equation is written in terms of the relative internal energy (E_r) and the relative total enthalpy (H_r) defined in the following Equations:

$$E_r = h - \frac{p}{\rho} + \frac{1}{2}\left(\vec{v}_r{}^2 - \vec{u}_r{}^2 \right) \tag{4.15}$$

$$H_r = E_r + \frac{p}{\rho} \tag{4.16}$$

Absolute Velocity Formulation

Conservation of mass:

$$\frac{\partial \rho}{\partial t} + \nabla \cdot \rho \vec{v}_r = 0 \tag{4.17}$$

Conservation of momentum:

$$\frac{\partial}{\partial t}(\rho \vec{v}_r) + \nabla \cdot (\rho \vec{v}_r \vec{v}) + \rho(\vec{w} \times \vec{v}) = -\nabla p + \nabla \bar{\bar{\tau}}_r + \vec{F} \tag{4.18}$$

Conservation of energy:

$$\frac{\partial}{\partial t}(\rho E) + \nabla \cdot (\rho \vec{v}_r H) = \nabla . \left(k \nabla T + \bar{\bar{\tau}}_r \cdot \vec{v}_r \right) + S_h \tag{4.19}$$

4.4.2 Flow in Single Rotating Reference Frames

A single rotating reference frame (SRF) modelling technique is used to model a problem that can be solved in a single reference frame. In an SRF model, the equations for rotating reference frame (relative velocity or absolute velocity formulation) are solved in all fluid cell zones in the computational domain. Steady-state solutions are achieved in SRF models provided the boundary conditions meet the following requirements:

- The no slip condition must be defined on moving walls in the relative frame such that the relative velocity is zero on the moving walls.
- Walls which are non-moving with respect to the stationary coordinate system can be defined, but these walls must be surfaces of revolution about the axis of rotation. The no slip condition is defined such that the absolute velocity at the wall is zero.

Rotational periodic boundary conditions can be used in instances where the surface is periodic about the axis of rotation. This is very common in turbo machine design where flow in a single blade row is modelled by assuming the flow is rotationally periodic and using a periodic domain about a single blade [45]. In a SRF method, only the rotating domain is solved without a stationary domain. The SRF model computes fluid flow in the rotating frame of reference, with the velocity and fluxes relative to the rotating reference frame. The corriolis and centrifugal source terms are included in the momentum equations. CFD solvers such as ANSYS Fluent [45] and OpenFOAM [46] provide techniques for modelling flow in a single rotating reference frame. Figure 4.13 provides a view of the frame of reference where the velocities and fluxes are calculated.

Figure 4.13 – Single reference frame view of flow quantities. Source [47]

4.4.3 Flow in Multiple Rotating Reference Frames

Modelling problems that involve multiple moving parts or contain stationary surfaces which are not a surface of revolution is beyond a SRF model. Such problems require the computational domain to be split into multiple zones, with interface boundaries between the zones. Zones containing moving parts are solved using the equations for a rotating reference frame, whereas stationary zones are solved using the stationary frame equations. The way the interface between the zones is modelled leads to two approaches for flows in multiple rotating reference frames.

- Multiple Rotating Reference Frames
  - Multiple Reference Frame (MRF) model
  - Mixing Plane Model (MPM)
- Sliding Mesh Model (SMM)

The MRF and MPM models are steady-state approximations while the SMM model is unsteady because of the motion of the mesh with time.

Multiple Reference Frame (MRF) Model

The MRF model is a steady-state approximation in which individual cell zones move at different rotational or translational speeds. If the zone is stationary($\vec{w} = 0$), the stationary equations are used; otherwise, the flow is solved using the moving reference frame equations. A local reference frame transformation is performed at the interfaces between cell zones to enable flow variables in one zone to be used to calculate fluxes at the boundary of the adjacent zone [45]. The MRF approach does not account for the relative motion of the moving zone with respect to the stationary zone (i.e. the grid remains fixed for the computation). This is analogous to freezing the motion of the rotating or translating part in a specific position and observing the instantaneous flow field with the rotor in that position. Hence, the MRF model is also referred to as the "frozen rotor approach". The MRF model or frozen rotor approach is very dependent on the positioning of the rotating/translating mesh and stationary mesh; that is why key flow features such as flow separation, high pressure gradients will always stay in exactly the same position for each new run if the positions of the rotating and stationary computational domains are kept constant. In practice, a frozen rotor simulation is mostly used to obtain a good starting flow-field before doing a transient sliding-mesh simulation. Although the MRF approach is a steady-state approximation of the flow field, it provides good results for turbomachinery applications in which rotor-stator interaction is relatively weak, and the flow is relatively uncomplicated at the interface between the stationary and moving zones [45]. Figure 4.14 illustrates the view of flow quantities in a MRF model.

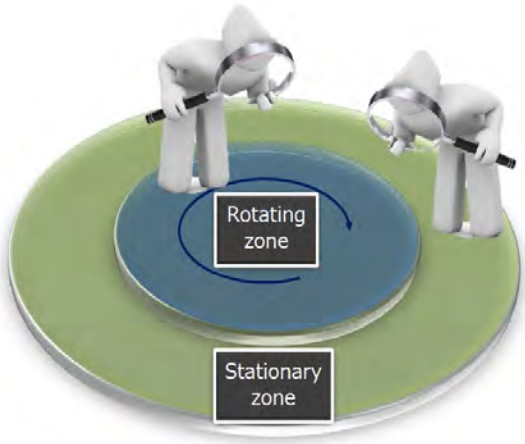

Figure 4.14 - Multiple reference frame view of flow quantities. Source [47]

Interface formulation in the MRF model

At the interface of MRF models, vector quantities such as velocity and velocity gradients require special treatment since these quantities change with a change in reference frame. Scalar quantities such as temperature, pressure, density etc. do not require any special treatment and thus are passed locally from one zone to the other without any change. Also, absolute velocity quantities do not change across the stationary and rotating frames. However, the relative velocity quantities require particularly careful attention. At the boundary between the zones, continuity of absolute velocity $\vec{v}$ is enforced. The velocities in each zone are computed relative to the motion of the zone. Velocities and velocity gradients are converted from the moving reference frame to the absolute reference frame using Equations 4.20 and 4.21. Figure 4.15 illustrates interface treatment for the MRF model.

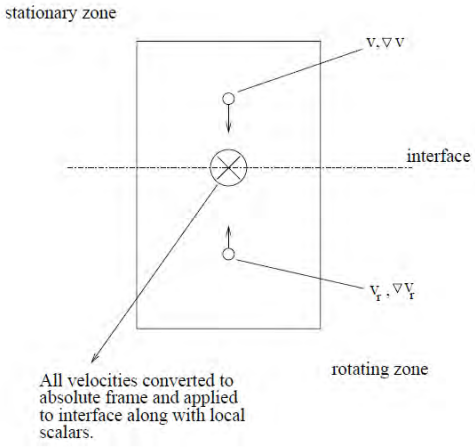

Figure 4.15 – Interface treatment of the MRF model. Source [45]

$$\vec{v} = \vec{v}_r + (\vec{w} \times \vec{r}) + \vec{v}_t \tag{4.20}$$

$$\nabla\vec{v} = \nabla\vec{v}_r + \nabla(\vec{w} \times \vec{r}) \tag{4.21}$$

where $\vec{v}_t$ is a translational velocity.

Mixing Plane Model (MPM)

The main difference between the mixing plane model (MPM) and the multiple reference frame (MRF) model is the treatment at the interface between the stationary and moving zones. In the MRF model, the adjacent cells in the rotating frame are used to update the cells on the stationary zone on the interface. In the MPM model, flow-field data from adjacent zones are passed as boundary conditions that are spatially averaged or "mixed" at the mixing plane interface [45]. The mixing process removes any circumferential variations in the passage-to-passage flow field (e.g. flow separations, wakes, jets), yielding a steady-state result. This approach removes the unsteadiness of the rotor-stator interaction making it more suitable for steady state simulations. The CFD solver, TBLOCK[6], used for CFD analysis in this thesis, implements the mixing plane model. Figure 4.16 is a schematic illustration of the mixing plane model concept. In the MPM model, the mesh in the stator and rotor do not have to be conformal and can be of different cell types. In Figure 4.16, the flow quantities computed at the rotor exit are used to update the boundary conditions at the stator inlet. Also, the flow quantities computed at the stator inlet are used as a boundary condition on the rotor exit [45]. This creates a mixing plane pair. Mass flow, swirl and total enthalpy are conserved across the mixing plane.

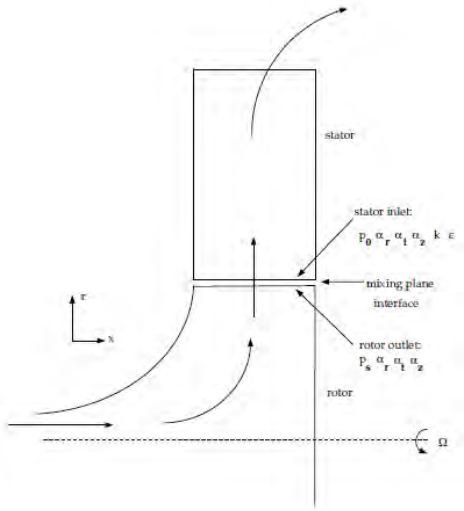

Figure 4.16 – Radial rotor-stator interaction illustration of the mixing plane concept. Source [45]

4.4.4 Sliding Mesh Model

In the sliding mesh model (SMM), the relative motion of the rotating domain and stationary domain gives rise to unsteady interactions between the domains. This unsteadiness can be due to pressure fluctuations, wake convection and shock waves propagation. The sliding mesh model takes into account the relative motion of the stationary and rotating components, hence it is the most accurate for solving unsteady flows in turbo machines, however, it is also the most computationally demanding [45]. The sliding mesh model must be used when transient rotor-stator interaction is desired. Figure 4.17 is an illustration of unsteady interaction in the sliding mesh model. One of the requirements of this method is that the stator and rotor interface should match (it must have fluid cells on both sides). However, in practice, the number of rotor and stator blades is usually different, so solving a single passage would violate the interface matching. An obvious solution is to solve all the passages for both rotor and stator which is computationally expensive and unfeasible in most cases. A way around this problem is to find a common denominator based on the number of rotor and stator blade, and then scale the rotor or stator for one passage accordingly. For example, if there are 36 stator vanes and 41 rotor blades, the computational domain can be approximated to 41 stator vanes and 41 rotor blades, making it possible to solve just one passage. The stator vanes are scaled by 36/41 (0.878) circumferentially to set up the simulation. When the mesh is rotating during analysis, node alignment along the grid interface is no longer required. In the SMM model, the grid interface and associated interface domains can be any shape, provided that the two interface boundaries are based on the same geometry [45]. To compute the flux in the SMM model, the intersection between the interface zones is determined every time step. The intersection can be interior (a zone with fluid cells on both sides) or periodic (if it is a periodic problem). The number of faces in these intersection zones will vary as the zones move relative to one another. Fluxes are calculated across the intersection of the interfaces. The open source CFD solver OpenFOAM [46] refers to the sliding mesh method as cyclic arbitrary meshing interface (AMI) or dynamic mesh model, where instead of adding the coriolis and centrifugal source terms to the governing equation to capture the rotation effects, the mesh is actually rotated. The rotation applied to the mesh gives it the name - dynamic mesh. The cyclic AMI in OpenFOAM is illustrated in Figure 4.18.

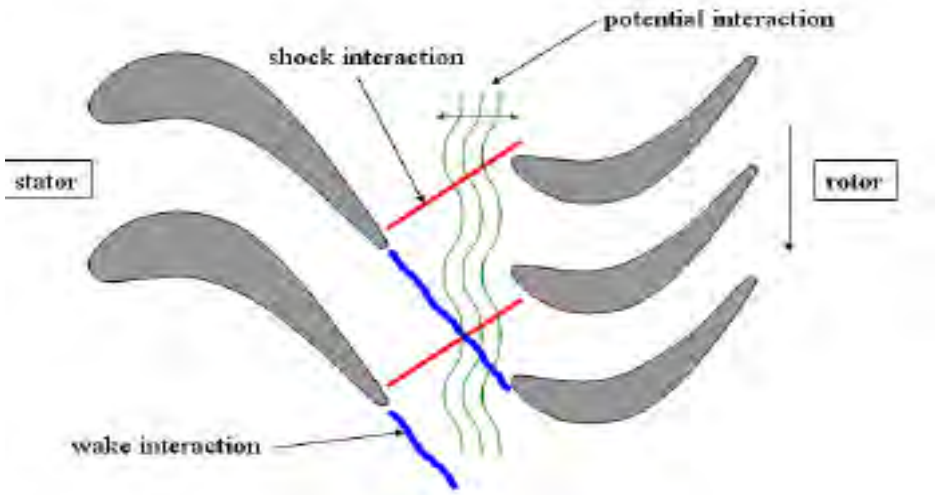

Figure 4.17 - Illustration of unsteady interaction. Source [45].

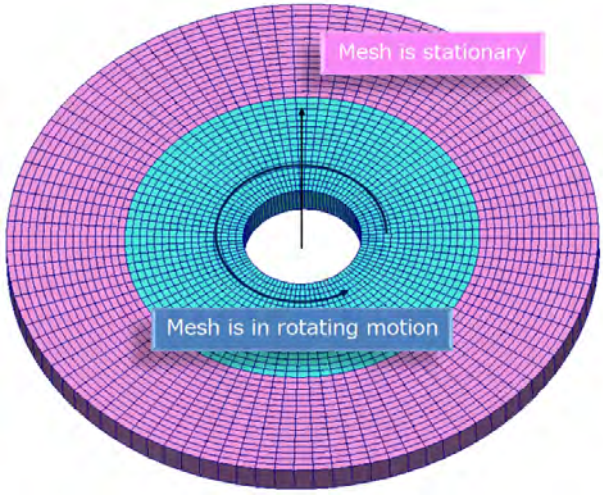

Figure 4.18 - Cyclic AMI showing rotating and stationary mesh regions. Source [46]

4.5 OPTIMISATION PROBLEM

Optimisation problems can be classed as either single objective or multi-objective depending on the number of objectives that need to be minimised. If only one objective is to be minimised, then it is considered as a single objective optimisation problem. If there is more than one objective to be minimised, then it is considered as a multi-objective problem [48].

4.5.1 Single Objective Optimisation

The single objective optimisation problem can be mathematically formulated as:

$$\text{Minimise:} \quad f(\vec{x}) \tag{4.22}$$

$$\text{Subject to:} \quad g_j(\vec{x}) \leq 0 \qquad j = 1 \ldots m \tag{4.23}$$

$$h_k(\vec{x}) = 0 \qquad k = 1 \ldots l \tag{4.24}$$

$$x_i^l(\vec{x}) \leq x_i \leq x_i^u(\vec{x}) \qquad i = 1 \ldots n \tag{4.25}$$

$$\text{where} \quad \vec{x} = \begin{Bmatrix} x_1 \\ x_2 \\ \vdots \\ x_n \end{Bmatrix} \tag{4.26}$$

The vector $\vec{x}$ is the vector of design variables representing the parameters of the design that can be modified e.g. blade thickness, blade angles etc. The function $f(\vec{x})$ is the objective function which is minimised. For example the weight is an objective function that can be minimised. To maximise an objective function such as efficiency, the inverse or negative value of the objective function is minimised instead. Equations 4.23 and 4.24 are the inequality and equality constraints that must be satisfied and can be used to reduce the number of design variables n. Equation 4.25 is the range of design variables which can be dependent on other variables [48].

4.5.2 Multi-Objective Optimisation

Some engineering applications require the minimisation or maximisation of several variables at the same time, e.g. minimise peak von Misses stress, while increasing total-to-static efficiency. This type of optimisation problem is called a multi-objective optimisation problem as defined by Equations 4.27 to 4.31

$$\text{Minimise:} \quad f_j(\vec{x}) \qquad i = 1 \ldots l \tag{4.27}$$

$$\text{Subject to:} \quad g_j(\vec{x}) \leq 0 \qquad j = 1 \ldots m \tag{4.28}$$

$$h_k(\vec{x}) = 0 \qquad k = 1 \ldots n \tag{4.29}$$

$$x_p^l(\vec{x}) \leq x_p \leq x_p^u(\vec{x}) \qquad i = 1 \ldots q \tag{4.30}$$

$$\text{where} \quad \vec{x} = \begin{Bmatrix} x_1 \\ x_2 \\ \vdots \\ x_n \end{Bmatrix} \tag{4.31}$$

In a multiple objective problem, the objectives often conflict, so no single optimal solution exists. A set of non-dominating solutions which forms a Pareto front are obtained. A best compromise design is chosen from the Pareto front. The Pareto front consists of designs for which one objective cannot be improved without worsening one or more other objectives [48]. Figure 4.19 is an example Pareto front of two non-dominated optimal solutions A and B i.e. design A dominates B in function f_1, while design B dominates A in function f_2. A multi-objective optimisation problem can be converted to a single-objective problem considering a weighted sum of each objective to form a single objective as illustrated in Equation 4.32 where w_i are the weights given to the i-th objective function. However, this is not a recommended practice because the different scales of the objective functions may bias the optimisation problem.

$$F(\vec{x}) = \sum_{i=1}^{l} w_i \cdot f_i(\vec{x}) \tag{4.32}$$

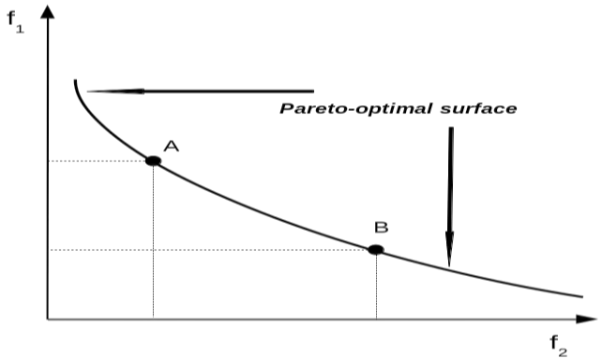

Figure 4.19 – A Pareto front for a two-objective optimisation problem

4.6 OPTIMISATION METHODS

Optimisation methods can be classified based on the order of derivatives of the objective function used. For example, zero order methods use only the function values for minimising the objective function. They are also referred to as derivative-free methods. First order and second order methods use the first and second order derivatives of the objective function $f(\vec{x})$ respectively. Turbomachinery design engineers have applied several optimisation methods in recent years to help improve performance. Some of the methods, notably zero order methods commonly used by turbomachinery design engineers are discussed in this Section. A common zero order (Differential Evolution) method use for turbomachinery optimisation problem is the Non-dominating Sorting Genetic Algorithm (NSGA). For example, Apurva Kumar *et al.* [49] used a NSGA-II algorithm in conjunction with a Gaussian stochastic method to search a compressor design space for robust designs. K. D. Wang *et al.* [50] also applied the NSGA-II to the

optimisation of NASA rotor 37. Jinya Zhang *et al.* [51] used the NSGA-II algorithm to optimise a helicon-axial multiphase pump impeller. Other popular algorithms are Strength Pareto Evolutionary Algorithm (SPEA) [52], Pareto Archived Evolution Strategy (PAES) [53], Vector Evaluated Genetic Algorithm (VEGA) [54].

In most optimisation methods a new design is computed from a previous one using Equation 2.33.

$$\vec{x}_{i+1} = \vec{x}_i + \alpha_i \cdot \vec{S}_i \tag{4.33}$$

where at the *i*-th iteration $\vec{x}_{i+1}$ is the new estimate of the optimum design based on the previous estimate $\vec{x}_i$, $\vec{S}_i$ is the search direction and α_i is a scalar defining the amplitude of the change in the $\vec{S}_i$ direction. The fundamental difference in the optimisation methods is determined by how $\vec{S}_i$ and α_i are computed based on information from the previous iteration.

4.6.1 Zero Order Methods

The following zero-order methods are described briefly - random search, random walk, simulated annealing and differential evolution.

Random Search

The random search involves randomly selecting and evaluating a large number of candidate vectors $\vec{x}$ from the design space. The $\vec{x}$ with the smallest $f(\vec{x})$ and satisfying all constraints is chosen as the optimum. This approach requires a large number of randomly selected candidates in order to obtain a precise solution; hence this method is not practicable and should be avoided at all cost.

Random Walk

A more practicable variation of random search is the random walk method. In this approach, each new design is based on a random perturbation of the previous random design by using Equation 4.33. In this case, the search direction $\vec{S}_i$ is a normalised randomly generated vector and the scalar α_i is set to a constant value. The main advantage of random walk over random search is that in random walk, the new design $\vec{x}_{i+1}$ replaces the current design $\vec{x}_i$ if it is considered as a better and otherwise if vice-versa. Whereas in the random search, time can be wasted computing several sub-standard designs to no avail. An important feature of random walk is that while evaluating dominance of candidates, priority is set towards achieving a feasible design, followed by an improvement of the design while maintaining feasibility. For example, if the current design has no constraint violations, the new design is better than

the current design only if it has no constraint violations and also has a better objective value. If the current design has constraints violations, the new design is considered better if the value of its constraints violation is lower than the current design, even if it has a worse objective value [48].

Simulated Annealing

Simulated annealing algorithm is analogous to the annealing process in materials science. The annealing process involves heating up a solid to a maximum temperature where the particles of the solid randomly move in the liquid phase, followed by slow cooling of the heated bath. The recombination of the molecules to form the solid is based on the difference in energy level of both molecules and the temperature of the bath [48]. In the simulated annealing algorithm, a random perturbation is made to an existing design $\vec{x}$ to create a new design which is evaluated. If the new design is better than the previous, it replaces it and the algorithm restarts. If the previous design is better than the new one, the new design may be accepted depending on a probability calculated using its 'virtual energy' and 'virtual temperature'. The 'virtual energy' is the difference between the performance of both designs, while the 'virtual temperature' is a number that decreases with iteration steps and reduces the probability of accepting a worse design [48]. The acceptance of a worse design in the early stages of a simulated annealing algorithm helps to expand the search area. This is beneficial for global optimisation and could potentially prevent the algorithm from getting trapped in a local optimum.

Evolutionary Algorithms

Evolutionary algorithms are based on Darwinian evolution, whereby populations of individuals evolve over a search space and adapt to the environment by the use of different mechanisms such as mutation, crossover and selection. Survival or a chance to reproduce in the population is based on the fitness of individuals [48]. In evolutionary algorithms, the entire population is evaluated at each iteration in contrast to random walk and simulated annealing where one individual is evaluated in each iteration. Also, the design vector $\vec{x}$ is called the individual, while the objective function is replaced by the fitness of an individual. Different evolutionary strategies can be used to evolve individuals in a population. Two popular methods will be discussed here in detail - Genetic Algorithms (GA) and Differential Evolution (DE).

To quickly understand genetic algorithms, let‟s take a hypothetical situation where a farmer decides to increase milk production from cows by interbreeding cows and keeping records of milk production from their offspring. After each generation, the farmer chooses cows to interbreed further based on their milk production rate. After a few generations, the farmer will achieve optimum milk production based on the

initial range of cow breeds from first generation. The downside to this is that the cows become too genetically similar from one generation to the next. From a genetic algorithm point of view, this can be resolved using a process called mutation, where genes are randomly altered to reduce similarity in parents and off springs. The breeding process is the exchange of genes (crossover) between parents to produce children. Differential evolution is similar to genetic algorithm except that it allows new children to have gene that is weighted from both parents‟ genes.

Genetic Algorithms

A genetic algorithm is a heuristic search technique this is inspired by Charles Darwin‟s theory of natural evolution [104]. Genetic algorithms are considered as a global search technique based on the mechanisms of natural selection and use of the survival of the fittest approach to obtain the optimum individual. At the start of the algorithm, a set of individuals called a population is randomly generated. An individual is characterised by a set of variables referred to as genes. A string of genes form a chromosome. This is depicted in Figure 4.20. For example, an individual could be a compressor design to be optimised with genes such as impeller back sweep angle, impeller hub radius, etc. A fitness function is defined and used to evaluate each individual in the population and the fittest individuals are selected and used to create new individuals for the next generation. A fitness function may compare candidates by efficiency and decide which is fitter. The creation of new individuals is achieved by crossover and mutation. A genetic algorithm process is depicted in Figure 4.21. Crossover is the reproduction process where a crossover point is randomly selected and the genes after the crossover point are swapped between two mating individuals. A crossover process is depicted in Figure 4.23. A mutation is a random tweak in the chromosome which promotes diversity in the population of individuals. A mutation process is depicted in Figure 4.24 where three genes are mutated in an individual. The algorithm stops when a stopping criterion is satisfied, for example there is no further improvement in the population or a pre-defined number of generations are reached. In a genetic algorithm, each population has a fixed number of individuals, each represented by a binary string containing all the parameter variables [48]. The number of bits per parameter determines the accuracy of representation of the parameter as illustrated in Figure 4.22. To ensure a constant population size from one generation to the next, each pair of parents can have two children. The population size must be even. To create a new pair of children from a generation, the fittest parents are selected for mating (cross-over); then the genes of the new children can be mutated before evaluating their fitness. If the child dominates the parent, it replaces the parent in the next generation. Several methods can be used to select parents, for example tournament selection and roulette wheel selection [48]. The

crossover process is illustrated in Figure 4.23 where the crossover point can vary from generation to generation. The last stage is mutation of the genes (bit-strings) as shown in Figure 4.24. The purpose of mutation is to prevent the algorithm from being trapped in a local minimum. It also prevents the population of chromosomes from becoming too similar to one another and stalling the evolution.

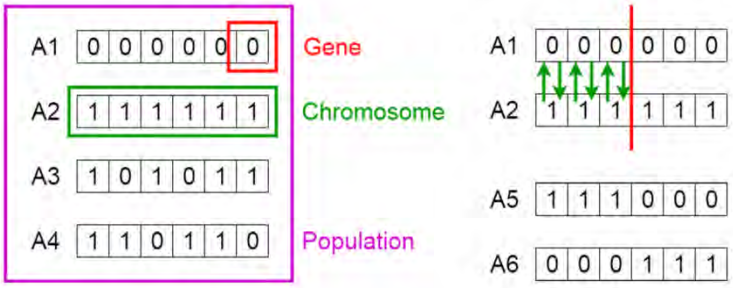

Figure 4.20 – Representation of gene, chromosome and population. Source [104]

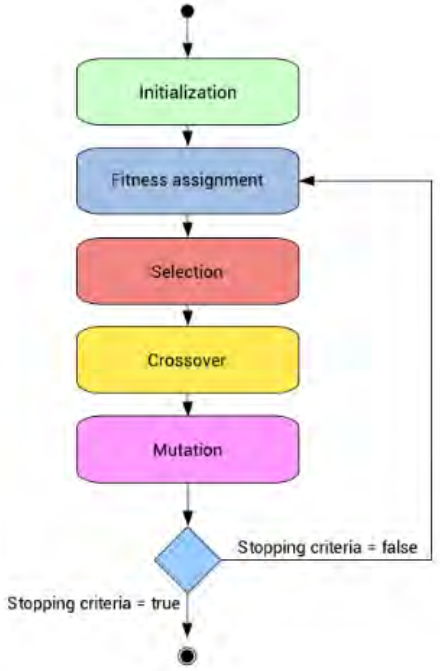

Figure 4.21 – Genetic algorithm process. Source [105]

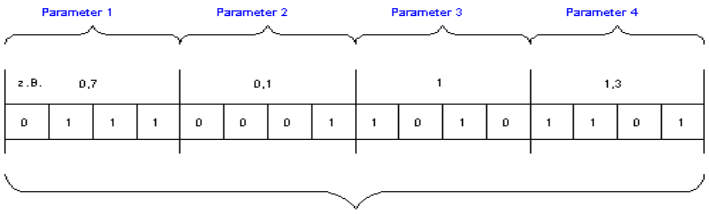

Figure 4.22 - Bitwise representation of parameters. Source [55]

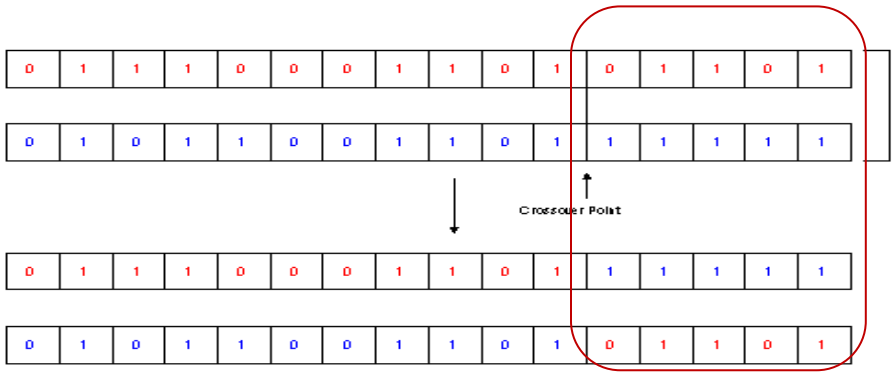

Figure 4.23 - Cross-over operation in genetic algorithms. Source [55]

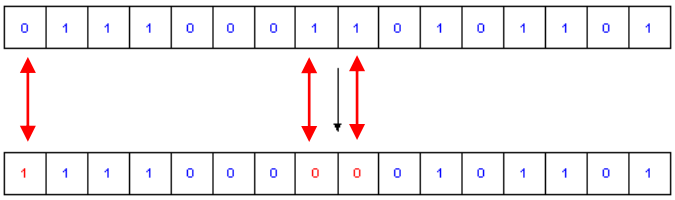

Figure 4.24 - Mutation operation in a genetic algorithm. Source [55]

Differential Evolution

The differential evolution (DE) method developed by Price and Storn [56] is similar to genetic algorithms except that it does not require the objective function to be continuous. Also, the method does not require the representation of the parameters with binary strings. In a single objective DE for example, each individual $\vec{x}_t$ contains n parameters as shown in Equation 4.34.

$$\vec{x}_t = (x_1, x_2, \dots\dots\dots\dots, x_n) \tag{4.34}$$

To evolve the parameter vector $\vec{x}_t$, three other parameter vectors a_t, b_t and c_t are randomly picked such that $a_t \neq b_t \neq c_t \neq \vec{x}_t$. A trial vector y_t is then defined as

$$y_i = a_i + F \cdot (b_i - c_i) \quad i = 1 \dots . n \tag{4.35}$$

where F is a user defined constant with values ranging from 0 to 1. Another vector z is obtained by a recombination operator involving $\vec{x}_t$ and $\vec{y}_t$ as show in Equation 4.36.

$$z_i = \begin{cases} y_i & if \quad r_i \leq C \\ x_i & if \quad r_i > C \end{cases} \quad i = 1 \dots \dots \dots n \tag{4.36}$$

where r_i is a uniformly distributed random variable ($0 \leq r_i < 1$) and C is a user defined constant with values ranging from 0 to 1 [48]. The final step of the differential evolution algorithm is the selection process and the minimization of the objective function $f(\vec{x}_t)$ using Equation 2.37.

$$\vec{x}_{t+1} = \begin{cases} z & if \ f(z) \leq f(\vec{x}_t) \\ \vec{x}_t & if \ f(z) > f(\vec{x}_t) \end{cases} \tag{4.37}$$

This final step is a selection process which is a simple replacement of the original vector $\vec{x}_t$ with the new vector z if the objective function decreases by such an action. In differential evolution, constraints are enforced such that the highest priority is given to achieve a feasible design, followed by improvement in the design while maintaining feasibility [48]. One problem that can occur in differential evolution, when a small population size is used, is stagnation - a situation whereby the population stops evolving.

4.6.2 First Order Methods

First order methods use the gradient of the objective function to compute the next iteration. This method is more efficient because less iteration is required to obtain a set of optimal solution. However, the main cost comes from computing the gradients for each iteration of designs [48]. Some common first order methods include steepest decent, finite difference method, algorithmic differentiation and adjoint methods.

Steepest Decent

The steepest decent method proposes a design in the direction where the objective function is decreasing the most. This can be illustrated using Equation 4.38.

$$\vec{S}_i = -\nabla f(\vec{x}_i) \tag{4.38}$$

In Equation 4.38, the search direction $\vec{S}_i$ is set to the opposite direction of the gradient of the objective function. An appropriate value of the amplitude α_i is chosen such that the method does not overshoot the descent of the objective function [48].

Finite Difference Method

The simplest finite difference method applicable to optimisation is a forward-difference first order method as shown in Equation 4.39.

$$\frac{\partial f}{\partial x_i}(\vec{x}) \approx \frac{f(\vec{x} + h \cdot \vec{e}_i) - f(\vec{x})}{h}, \quad i = 1 \dots n \tag{4.39}$$

where $\vec{e}_i$ is the *i*-th unit vector and *h* is a small scalar step size. Alternatively, a central difference second order numerical scheme can be used to compute the gradient and advance the iteration.

Algorithmic Differentiation

The algorithmic differentiation method is sometimes referred to as automatic differentiation. This method computes the gradient of each objective function using the chain rule [48]. Algorithmic differentiation is done at the programming level, whereby the derivative of a computed variable is computed when the variable is computed. Examples of algorithmic differentiation programs for C++ and FORTRAN respectively are ADIC [57] and ADIFOR [58].

Adjoint Methods

The adjoint method computes the gradient based on the concept of Lagrange multipliers [48]. For example in a CFD solver, the adjoint equations are solved next to the Navier-Stokes equations when an adjoint method is used. The computational cost of the adjoint method is similar to the partial differential equations being solved. As a result, the gradient is computed independent of the number of design variables. For this reason, the adjoint method has attracted a lot of research work in recent years. However, the major drawback of this method is that it is difficult to express the objective function as a function of global quantities such as mass flow, pressure ratio, etc.

CONCLUSION

In this Chapter, various geometry parameterisation and numerical modelling techniques used in turbomachinery design were presented. In addition, the various classes of optimisations algorithms applicable in the design of radial compressors were also discussed. The next Chapter will described the development of a parametric CAD algorithm and implementation of a high throughput computing (HTC) system for engineering design optimisation employed to speed up CFD calculations during this research.

CHAPTER 5

DEVELOPMENT OF A BESPOKE PARAMETRIC CAD ALGORITHM AND REALISATION OF A HIGH THROUGHPUT COMPUTING (HTC) SYSTEM

This Chapter presents the following:

- The development of a bespoke command-line parametric CAD algorithm for designing radial compressor impellers and vane-less diffusers
- Realisation of a high throughput computing (HTC) system to facilitate batch runs of multi-objective optimisation calculations

The contributions of this Chapter are as follows:

- A method of reducing the number of variables that define a radial compressor hub and shroud meridional profile without reducing the order of the Bezier curve
- A method of constraining control points that define the hub and shroud meridional profile of a radial compressor impeller to always move in the same direction. This ensures smooth distribution of meridional profile curvature.
- Use of a mid control point between the first two and last two control points at the shroud to improve local control of shroud profile curvature
- A mapping algorithm for calculating operating points on a radial compressor map that ensures the surge point is a valid solution. This was used to predict accurate compressor map width in Chapter 6.

The parametric CAD algorithm developed during this thesis has been used to design the HP stage of a two-stage turbocharger at Napier. The algorithm has been extended to include vaned diffusers and is now been used to design a range of radial compressors for the low pressure stage of a two-stage turbocharger at Napier. The HTC system realised during this research has also been embedded into Napier and is being used to facilitate automated multi-objective optimisation calculations and design of experiments studies.

5.1 INTRODUCTION

The motivation for the work carried out in this Chapter is one of the central themes of this thesis, which is to implement a low cost design environment for multi-objective optimisation of turbo machines such as radial compressors. The system should shorten the time to carry out batch CFD/FEA analysis. The high license cost of commercial Computer Aided Engineering (CAE) tools, and the need for multiple licenses for batch computing makes commercial codes uneconomical for use in this research. As a result, a decision was made to use free or open-source codes, or develop bespoke code to minimise cost. If commercial software is used, it should provide additional benefits such as, no additional license cost for running multiple instances simultaneously. The next Sections in this Chapter describes a bespoke parametric CAD algorithm developed during this research and the implementation high throughput computing (HTC) system based HTCondor [28] employed to speed up CFD calculations.

5.2 DEVELOPMENT OF A BESPOKE RADIAL COMRESSOR CAD PROGRAM – RC_CAD

5.2.1 Background

Most commercial turbo-machinery CAD packages provide a GUI which makes them user friendly. ANSYS BladeModeler [29] is a CAD tool for the rapid 3-D design of rotating machinery components. It is used to design axial, mixed-flow, and radial blade components in applications such as pumps, compressors, fans, blowers, turbines, expanders, turbochargers, inducers and more. The design is defined in a number of 2-D sketches, either at span-wise positions or at user-defined positions, to immediately and interactively generate the full 3-D design, as well as provide quantitative information such as blade angles and throat area. A meridional view is used to define flow paths, and two modes are available for defining blade shapes. An angle/thickness mode can be used to specify blade wrap and thickness distribution, as is typically used in radial machine design. Alternatively, a pressure side/suction side mode can be employed to independently describe the blade pressure side and suction side curves, as is common in axial machine design.

ANSYS BladeGen [30] turbo-machinery blade design software is used in the design of radial compressors and turbines. It allows the user to define blade profile in two modes – angle/thickness or pressure side/suction side. The angle/thickness mode allows the user to specify blade angle and thickness

distribution when designing a new blade. The pressure side/suction side mode gives the user the option of designing the pressure and suction side independently as is the case in most axial machines.

TURBOdesign CAD [31] turbo-machinery design software is developed by Advanced Design Technology to considerably speed up the blade design process and integration with existing design environments. The code includes a Quasi-3D module for blade loading analysis of existing designs, direct blade design capabilities and major import/export functions to/from other TURBO design software.

AutoBlade™ [32] is a 3D parametric blade modeller developed by Numeca International and it includes an advanced fitting module to start designs either from scratch or from an existing geometry. It is fully parametric with advanced dependencies between parameters and bounds associated to free parameters. 3D blades are defined by several sections and stacked together to ensure continuity of curves and surfaces.

AxCent [33] turbo-machinery software developed by Concepts NREC is used for detailed 3D geometric design and for rapid flow analysis of multi-stage axial and radial turbo-machinery through streamline curvature. AxCent employs powerful features for axial, mixed-flow, and radial geometries that can be combined to design various types of turbomachinery. It allows for blade stacking in 2D cross sections and blade re-staggering around an arbitrary axis. It allows the user to define variable tip clearance on either end of the blade and swept leading/trailing edges. The user can also define the splitter blade independent of main blade.

In addition to using the GUI for turbomachinery design, most CAD systems also offer methods of defining geometry, for example, via a text input file or scripting, such that they can be modified automatically during an optimisation process. In this thesis, a bespoke parametric CAD algorithm that allows the user to define geometric parameters for a radial compressor via an input text file is implemented to facilitate automatic generation of radial compressor geometries during multi-objective optimisation. The CAD algorithm is low cost (only development cost measured in time), compared to commercial alternatives, as it allows multiple instances of the algorithm to be executed simultaneously at no additional license cost. The bespoke CAD algorithm is called “rc_cad”.

5.2.2 RC_CAD Algorithm

Without a robust and efficient blade modeller, the optimisation chain‟s fidelity and robustness can be severely compromised [59]. The description of geometry is the most important step in the shape optimisation process [60]. A bespoke parametric CAD algorithm was developed during the optimisation phase of this research to facilitate the creation of a radial compressor impeller blade and vane-less diffuser region using parameters specified in an input text file. The algorithm is implemented in the C++ programming language, and employs object oriented design and memory management techniques [61] for easy upgrade in the future and improve execution speed (creates geometries in less than 5 seconds on an Intel Core i5, 2.5GHz, 8GB RAM laptop computer). Geometric features of CAD models created can be visualized using the free Matplotlib library [62] called from custom python scripts or using Paraview [63]. The geometry of the impeller, including splitter blades and vane-less diffuser is defined using 23 parameters specified in an input file called „optParam_in.dat‟. Figure 5.1 shows the hub and shroud curve parameterisation using 5 Bezier control points each. The direction of movement of the Bezier control points are indicated by arrows.

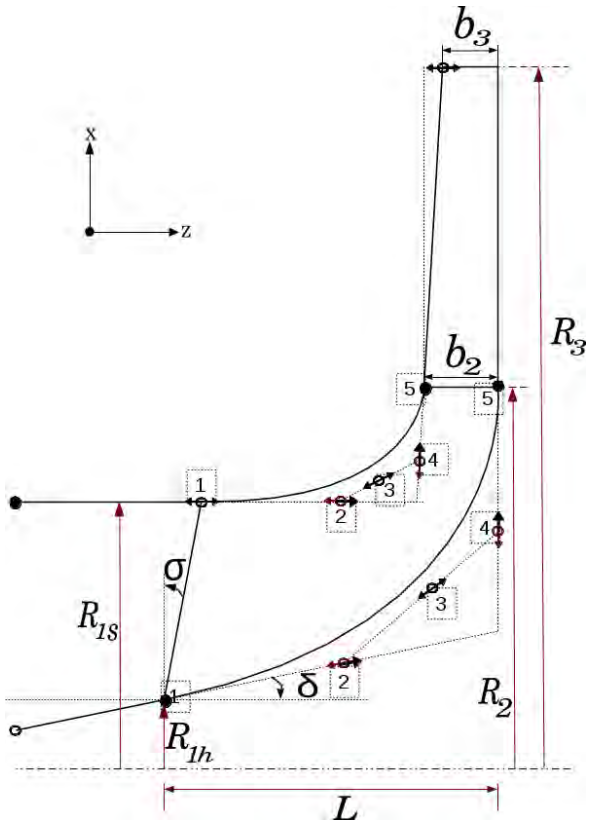

Figure 5.1 – Meridional parameterisation of compressor geometry

The steps in the geometry creation algorithm are as follows:

Step 1 – Create meridional profile

A blade meridional hub and shroud profile is created on the X-Z plane using fourth order Bezier curves with five control points as shown in Figure 5.1. The curvature of hub and shroud meridional profile is controlled by three internal points. The 2nd and 4th control points are controlled by one parameter to reduce the number of optimisation variables. This approach was used because according to Bonaiuti *et al.* [64], the shape of the curve in front of the blade has a much greater influence on the performance than that of the rear part of the blade. So it was decided to adjust the 2nd and 4th Bezier control points with one variable. Also, the 2nd and 4th control points were restricted to move in the same direction by the same fraction of the sliding path to keep the rate of change of radius of curvature in control. The 3rd (middle) control point is allowed to slide in any direction along the straight line joining the 2nd and 4th control points. The Z position of the 4th control point at the shroud is influenced by the ratio (b_3/b_2), while the Z position of the 4th and 5th control point is the same at the hub. Continuity of curvature is enforced between the inlet section and the impeller at hub and shroud by ensuring control points are on a straight line across each section. Continuity of curvature is also enforced between the impeller and diffuser using the same method.

Step 2 – Generate impeller blade thickness distribution

The blade thickness is defined using 3 parameters – leading edge (LE) thickness, maximum blade thickness at mid section and trailing edge (TE) thickness at hub and shroud. The blade thickness distribution is then generated by cubic spline interpolation across the three thickness control points. This is illustrated in Figure 5.2.

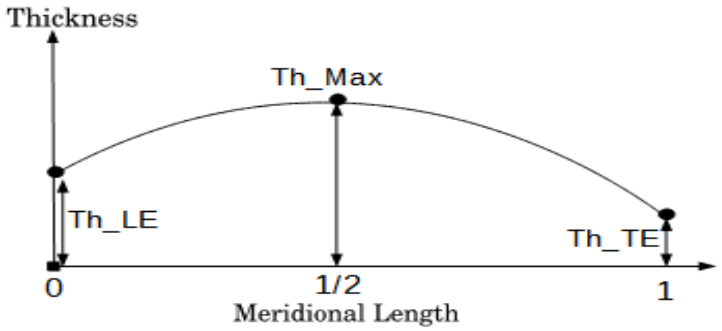

Figure 5.2 - Blade thickness definition curve

Step 3 – Calculate blade angle distribution at the shroud

The blade angle β distribution at the shroud is calculated by fitting a cubic spline across four control point angles (β_0, β_1, β_2, β_3) at the LE, 33% and 67% of meridional length; and at the TE as illustrated in Figure 5.3. Blade angle is illustrated in 3D in Figure 5.4.

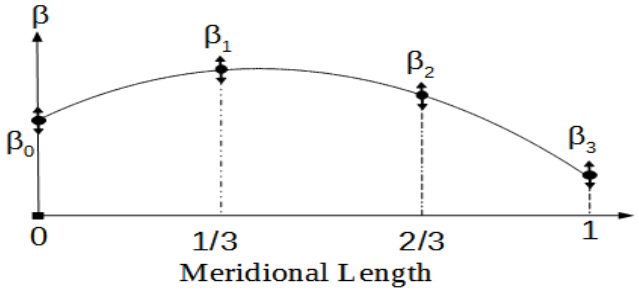

Figure 5.3 - Blade angle β definition

Step 4 – Calculate blade wrap angle or theta distribution at the shroud

The camber line circumferential position at the shroud is then defined by calculating wrap angle θ along the meridional line using Equation 5.1.

$$R \times d\theta = dm \times tan(\beta) \tag{5.1}$$

Equation 5.1 allows transformation from beta angle β distribution to the coordinates of the camber line by integrating and calculating the change in wrap angle θ along the meridional profile using Equation 5.2. Figure 5.4 illustrates the meridional and camber line directions. Wrap angle is used to transform the impeller profile from 2D meridional view to 3D. The circumferential position of the shroud is then achieved by rotating the points defining the shroud profile in meridional view to 3D using the wrap angle distribution calculated.

$$d\theta = \frac{1}{R} \times tan(\beta) \int dm \tag{5.2}$$

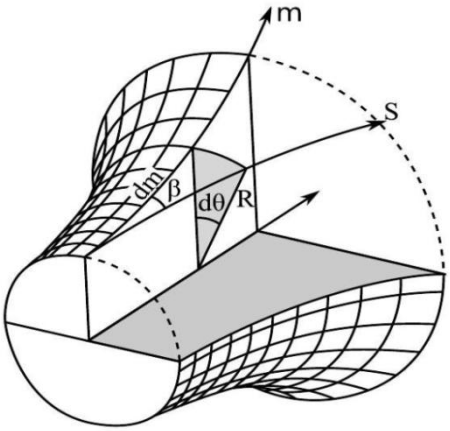

Figure 5.4a - Diagram of the meridional direction (m) and camber line (S) [48]

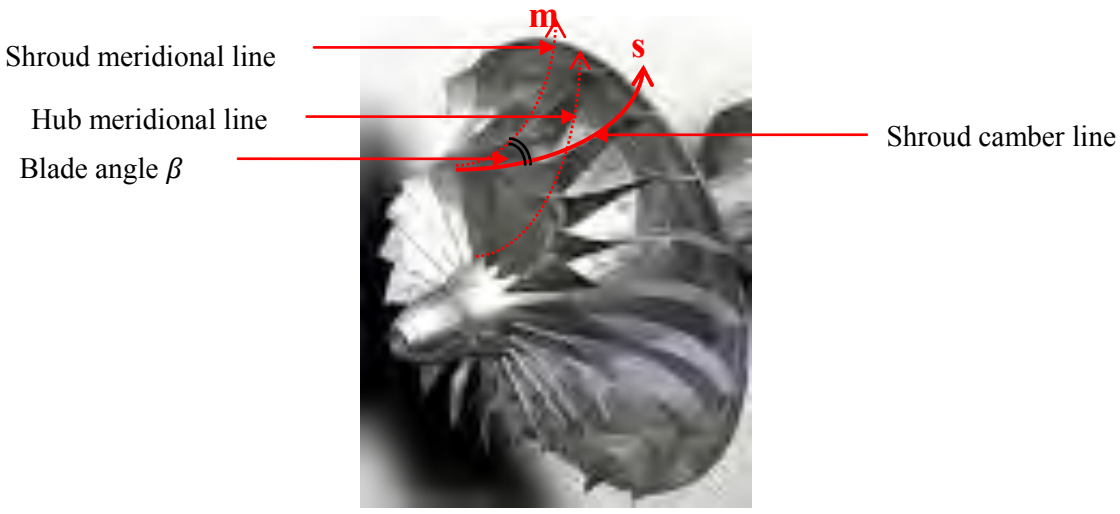

Figure 5.4b – 3D Diagram of an impeller

Step 5 – Calculate hub wrap angle distribution

The wrap angle distribution at the hub is then calculated by applying a correction to the shroud wrap angle distribution. This correction is calculated by cubic spline interpolation of wrap correction angles θ^C defined at the LE, mid span of the meridional length and TE as shown in Figure 5.5.

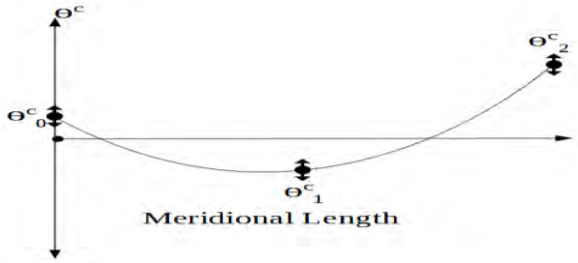

Figure 5.5 - Picture of correction cubic spline on hub

The TE wrap angle correction θ_2^C is calculated from the rake angle which is specified by the user. A rake angle of zero means ($\theta_2^C = 0\ at\ TE$). Rake angle (Ψ) is converted to TE wrap angle correction using Equations 5.5 to 5.5 and Figure 5.6.

$$l = b_2 \times tan\Psi \tag{5.3}$$

$$l = 2r \times sin\left(\frac{\theta_2^c}{2}\right) \equiv b_2 \times tan\Psi = 2r \times sin\left(\frac{\theta_2^c}{2}\right) \tag{5.4}$$

$$\theta_2^c = 2 \times sin^{-1}\left(\frac{b_2 \times tan\Psi}{2r}\right) \tag{5.5}$$

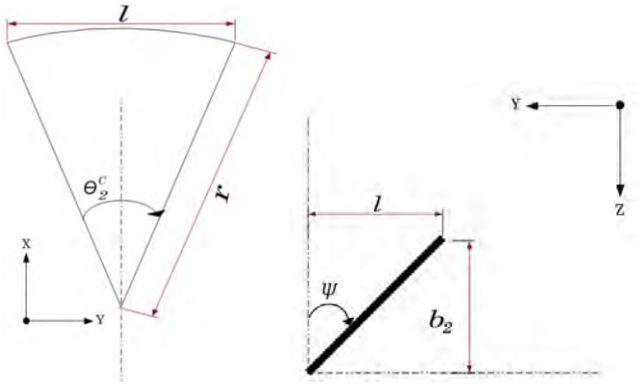

(a) (b)

Figure 5.6 - Illustration of rake angle Ψ conversion to wrap angle correction θ^C at the hub

The array of correction angles is then added to the array of wrap angles θ at shroud to obtain hub wrap angle distribution. This approach gives the designer direct control over blade twist which has an impact on mechanical stresses.

Step 6 – Calculate blade angle distribution at the hub

The blade angle β distribution at the hub is then re-calculated from the wrap angle distribution using a re-formulation of Equation 5.1 now written as Equation 5.6

$$\beta = tan^{-1}\left(R\frac{d\theta}{dm}\right) \tag{5.6}$$

Equation 5.6 is solved using forward and backward finite difference method at the LE and TE boundary; and central difference scheme in the remaining section to calculate blade angle distribution along the hub meridional profile. The finite difference formulations are illustrated in Equations 5.7 to 5.9.

$$LE: \quad \beta_i = tan^{-1}\left(R\frac{\theta_{i+1} - \theta_i}{m_{i+1} - m_i}\right) \tag{5.7}$$

$$Mid - section: \quad \beta_i = tan^{-1}\left(R\frac{\theta_{i+1} - \theta_{i-1}}{m_{i+1} - m_{i-1}}\right) \tag{5.8}$$

$$TE: \quad \beta_i = tan^{-1}\left(R\frac{\theta_i - \theta_{i-1}}{m_i - m_{i-1}}\right) \tag{5.9}$$

Step 7 – Correct blade thickness at hub and shroud using blade angle distribution

The blade thickness at hub and shroud is then corrected using blade angle distribution as shown in Equation 5.10, where t_i is the blade thickness on the meridional plane (X – Z) and ${t_i}^C$ is the corrected thickness. This will ensure consistency of blade thickness when the pressure and suction sides are rotated to create a 3D geometry of the impeller.

$${t_i}^C = \frac{t_i}{cos\beta_i} \tag{5.10}$$

Step 8 – Construct hub and shroud pressure and suction side

The pressure and suction sides of the main blade at hub and shroud are constructed using the corrected thickness distribution. This is carried out by rotating the hub and shroud curves on the meridional plane clockwise and anti-clockwise, half the corrected thickness of the blade measured from the axis of rotation as illustrated in Figure 5.7. At this point, the pressure and suction side of the blade at hub and shroud have been created on the meridional plane.

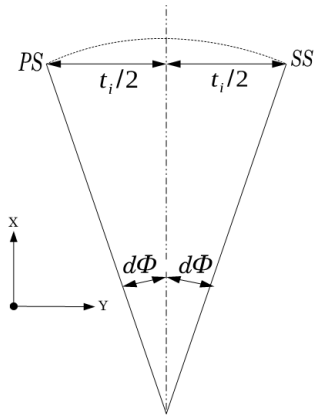

Figure 5.7 - Picture of rotation angle on both sides

Step 9 – Construct impeller blade trailing edge

The TE line at hub and shroud is created by joining the TE of the pressure and suction side at hub and shroud. Five points are used to create the TE lines using linear interpolation.

Step 10 – Create splitter blade from main blade

The splitter blade is created from the main blade by copying sections of main blade points into a new array defining the splitter blade. The splitter blade position at the hub and shroud is defined as fraction of meridional distances on the main blade. These are two separate optimisation parameters which enables the creation of leaning splitter blade leading edge. Values range from 0 to 75% of meridional length as show in Figure 5.8. A combination of low value and high value could lead to an invalid blade or high stress at the hub leading edge. A rule of thumb is that % locations should not differ by more than 30% (e.g. 20% at hub and 50% at shroud).

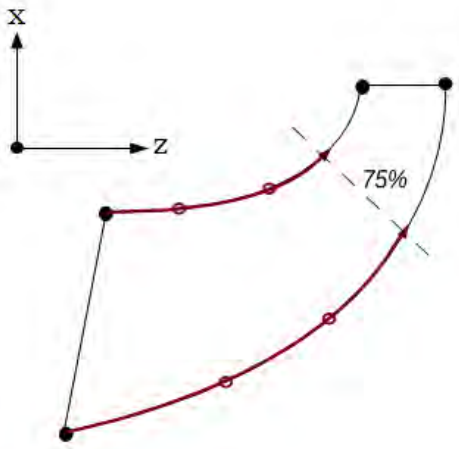

Figure 5.8 - Splitter possible positions at hub and shroud

Step 11 – Fit leading edge to splitter blade

A leading edge is fitted to the splitter blade profile at hub and shroud on the meridional plane using an ellipse approximately the size of the blade thickness as shown in Figure 5.9. TE lines at hub and shroud are also fitted to the splitter blade. As the position of splitter blade at hub and shroud profile are independent and may vary largely, the numbers of points defining the hub and shroud profile are re-interpolated to match the profile with more points. This allows for flank milling so there are equal number of equidistant points on the hub and shroud profiles of the splitter blade.

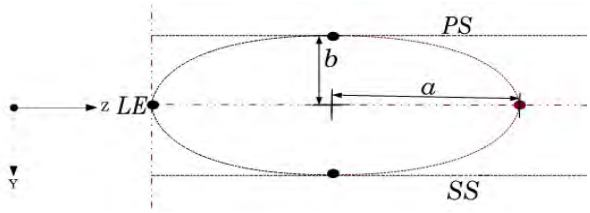

Figure 5.9 - Picture of elliptical leading edge on meridional plane

Step 12 – Rotate blade profiles to actual 3-D positions

The main and splitter blade profile on the meridional plane is rotated clockwise to their actual position in 3-D using the wrap angle distributions at the hub and shroud. Since the main and splitter blade have the same wrap angle distribution they will be in the same location in 3D. The splitter blade profile is then rotated to its actual position by further rotating each data point on the profile by a uniform angle calculated using Equation 5.11 where n_b is the number of main blades.

$$\partial\theta_i = \frac{360}{2 \times n_b} \tag{5.11}$$

Step 13 – Fit leading edge to main blade

The next step is to fit the main blade LE at hub and shroud. This is done using two Bezier curves of third order with 4 control points on either side – pressure side (PS) and suction side (SS). The first control point (which is shared by the PS and SS Bezier curves) is the LE point at hub and shroud and the last control point is defined by choosing a point approximately the local thickness of the blade while traversing from the LE point along the centre of the blade. The second point is chosen to enforce smooth curvature across the pressure and suction side leading edge of the

blade. The third control point is chosen to ensure the blade thickness is sufficient closer to the leading edge. This is illustrated in Figure 5.10.

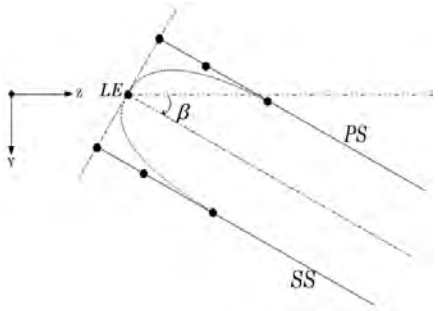

Figure 5.10 - Leading edge Bezier fitting control points

Step 14 – Construct mid layers between hub and shroud profile

At this stage the hub and shroud profile of the main and splitter blade have been created. The layers joining the hub and shroud profile are then created by straight line interpolation of the profiles from hub to shroud. This ensures radial elements of points define the profile from hub to shroud and this helps to reduce manufacturing cost as the blades can be simply generated in only one continuous sweep of a 5-axis flank milling machine.

"RC_CAD" is built using Object Oriented Programming (OOP) techniques. Classes are created for the basic geometric entities, polynomial interpolation functions and CAD transformations. Lines are defined as vector of points (vertices) in the form of straight lines or curves using a Lagrange interpolation or cubic spline interpolation or Bezier curve. The program contains 10 classes and 2 implementation files as shown in Table 5.1. The class dependency structure is illustrated in Figure 5.11 where the orange boxes are the implementation files only and classes are in blue.

Class Name /File Name	Header file	Implementation file
Bezier	20	146
CAD_Operation	103	4580
CubicSplineInterpolator	45	561
curveFilesWriter.cpp	N/A	2229
DynamicTable	61	499
LagrangeInterpolator	35	665
main.cpp	N/A	100
Matrix	35	158
Matrix_Operation	25	127
MatrixVector	45	282
OptimisationParameters	164	1000
Vertice	25	88
Sub Total	*558*	*10435*
Total		**10993**

Table 5.1 - Classes and files in the CAD program showing number of lines of code

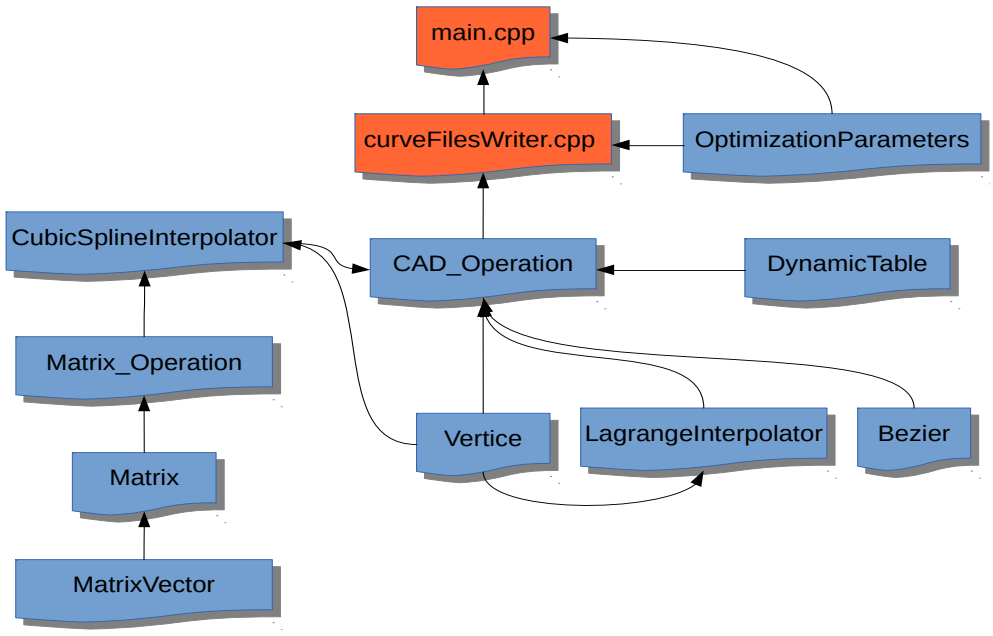

Figure 5.11 - Class dependency diagram

The class names in "RC_CAD" describe their functionality except the *DynamicTable* class which is used to read and write numeric data in a tabular format. The CAD_Operation, Lagrange Interpolator, Bezier, Cubic Spline Interpolator and Matrix_Operation classes contain only static member functions, so an object of the class is not required to use the classes. Sections of the Bezier class is shown in Figure 5.12

bezier.h

```
#ifndef BEZIER_H
#define BEZIER_H

using namespace std;

class Bezier
{
        public:
        Bezier();       //default constructor
        static double bernstineDegree2(int index, double u, double* iCtrlVerticeWeight);
        static double bernstineDegree3(int index, double u, double* iCtrlVerticeWeight);
        static double bernstineDegree4(int index, double u, double* iCtrlVerticeWeight);
        static double bernstineDegree5(int index, double u, double* iCtrlVerticeWeight);
        static double bernstineDegree6(int index, double u, double* iCtrlVerticeWeight);
};
#endif
```

bezier.cpp

```
double Bezier::bernstineDegree6(int index, double u, double* iCtrlPointWeight)
{
        double bernstine;
        switch (index)
        {
                case 0:
                        bernstine = iCtrlPointWeight[index]*pow((1-u),6);
                        break;
                case 1:
                        bernstine = iCtrlPointWeight[index]*6*u*pow((1-u),5);
                        break;
                case 2:
                        bernstine = iCtrlPointWeight[index]*15*u*u*pow((1-u),4);
                        break;
                case 3:
                        bernstine = iCtrlPointWeight[index]*20*u*u*u*pow((1-u),3);
                        break;
                case 4:
                        bernstine = iCtrlPointWeight[index]*15*u*u*u*u*pow((1-u),2);
                        break;
                case 5:
                        bernstine = iCtrlPointWeight[index]*6*u*u*u*u*u*(1-u);
                        break;
                case 6:
                        bernstine = iCtrlPointWeight[index]*pow(u,6);
                        break;
                default:
                        cout<<"Invalid choice of polynomial degree in bernstine degree 6
calculation"<<endl;
        }

        return bernstine;
}
```

Figure 5.12 – Snippet of the Bezier class code

5.2.3 Comparison of RC_CAD with literature

In this sub-section, the parameterisation technique employed in "rc_cad" is compared with common practice in literature as presented under the following sub-headings:

Number of parameters for parametric CAD design

Literature:

Full 3D design of turbomachinery blades can be defined using Bezier Curves, B-Splines construction, Bezier-patches representation or Tensor-product Bezier surface. In all of these approaches, at least 20 parameters are needed for accurate description of each span wise section. As a result up to 100 parameters could be involved in fully 3-D geometric representation [65]. A detailed definition of centrifugal compressor impeller geometry in 2D will require at least 7 parameters and 27 parameters in 3D [34]. The meridional profile parameterisation proposed by R. A. Van den Braembussche [34] uses 16 parameters to define the impeller geometry without a splitter blade and diffuser, increasing to 26 when splitter blades are introduced. M. Casey *et al.* [66] used 52 free parameters to define the 3D geometry of an impeller with splitter vanes; however some of the parameters were fixed during the optimisation. They used 5 and 7 Bezier control points to define the hub and shroud meridional curves respectively, modified by a total of 6 variable parameters. Verstraete, T. *et al.* [67] used 23 optimisation parameters for optimisation which includes stress parameters. However, some geometric dimensions such as number of blades were fixed due to manufacturing constraints. Bosman Botha van der Merwe [68] used a total of 88 parameters to define the impeller of a centrifugal compressor for aerodynamic and stress optimisation.

"RC_CAD":

The 3-D parametric CAD algorithm developed during this research defines the impeller with splitter vanes and vane-less diffuser of a centrifugal compressor for aerodynamic optimisation using 23 parameters. This number of parameters was shown to be sufficient during the optimisation phase of this thesis.

Blade Thickness Distribution

Literature:

M. Casey *et al.* [66] defined the hub and shroud blade thickness with a third order Bezier polynomial with two internal points whereby the roundness of the elliptical leading and trailing edges are defined by separate parameters. Bosman Botha van der Merwe [68] and Verstraete, T. *et al.* [67] defined blade thickness using a combination of ellipse at leading edge section, a constant thickness section and a parabolic profile towards the trailing edge. The blade thickness was distributed normal to the camber line as a function of the non-dimensionalised camber length. R.A. Van den Braembussche *et al.* [69]

defined blade thickness as constant except at leading edge where it is defined by an ellipse.

"RC_CAD":

The CAD algorithm developed during this thesis uses a cubic spline interpolation across three control points defining the leading edge blade thickness, maximum blade thickness specified at 50% of the meridional length and a trailing edge thickness to define the blade thickness distribution. A Bezier curve is then used to fit the main and splitter blade leading edges.

Blade Manufacturability

Literature:

M. Casey *et al.* [66] defined the impeller blade as a ruled surface of straight lines joining hub and shroud contours which are equidistant along the meridional channel of the impeller between the leading edge and trailing edge. This leads to simpler manufacture through flank milling. Leonid Moroz *et al.* [70] also considered manufacturability in their design process by having radial elements of points define the profile from hub to shroud. Duccio Bonaiuti *et al.* [64] defined blade surface profile as ruled surface to reduce manufacturing cost as the blades can be simply generated in only one continuous sweep of a 5-axis flank milling machine. Impeller geometries where the surfaces are not ruled will require point milling, a more time consuming manufacturing method compared to flank milling.

"RC_CAD":

The CAD algorithm developed during this research generates the impeller profile by a linear interpolation between the hub and shroud meridional profiles to produce ruled surfaces of the pressure and suction side of the blade. This approach makes geometries generated using "RC_CAD" suitable for 5-axis flank milling.

Blade Angle Definition

Literature:

M. Casey *et al.* [66] defined the impeller blade angle β distribution using a fourth order Bezier curve with five control points at the hub and shroud. Their code then modifies the specified hub blade angle distribution by applying a small correction to each internal Bezier point at the hub until it matches the leading edge lean and rake angle specified by the user while taking into account the importance of the shroud streamlines in the diffusion process of the impeller. R. A. Van den Braembussche *et al.* [34] defined beta angle at hub and shroud using third order Bezier polynomials with 4 control points each. In his approach, the circumferential extend of the blade (difference between wrap angle θ at leading and trailing edge) at hub and shroud are related by the maximum lean that is allowed at leading and

trailing edge and constitute a limitation on the blade angle distribution. Bosman Botha van der Merwe [68] defined the blade angle distribution using a third order Bezier polynomial at hub and shroud and also ensured curvature continuity between sections of the compressor geometry.

"RC_CAD":

In the CAD algorithm developed during this thesis, the blade angle at the shroud is defined by interpolating across four control points using a cubic spline. The wrap angle distribution at the shroud is then calculated from the blade angle. The program does not allow the user to specify blade angle distribution at the hub; instead, the wrap angle at the shroud is modified by a correction distribution to get the hub wrap angle distribution. The hub blade angle distribution is then calculated from the hub wrap angle distribution. This approach helped to reduce the number of control blade angle control points at the hub by 1.

Splitter Blade Definition

Literature:

Verstraete, T. *et al.* [67] defined the stream wise position of splitter blade leading edge as a fraction of blade camber length and can vary between 20% and 35%. They did not state whether the splitter location at hub and shroud are defined independently or not. The same camber line distribution on the main blade is applied to the splitter blade. In other words, the splitter blade is a cut-off section of the main blade. Unlike the method used by Verstraete, T. *et al.* [67], the approach used by Leonid Moroz *et al.* [70] allows the designer to modify the splitter blade camber line independent of the main blade. Their method also allows the splitter blade circumferential position to be at an arbitrary angle offset between the main blades. M. Casey *et al.* [66] have also defined the splitter blade as a shortened version of the main blade just as Verstraete, T. *et al.* [67] did. However, they defined the hub and shroud leading edge location relative to axial length of the impeller instead of the camber length. Bosman Botha van der Merwe [68] also defined the splitter blade location as a fraction of camber line location.

"RC_CAD":

In the CAD algorithm developed during this thesis, the splitter blade is defined as a shortened version of the main blade except that the leading edge position at hub and shroud are defined independently as a fraction of the blade meridional length and not axial distance as in [66] or camber line as in [68] and [67]. Position values of 0 to 75% are possible at the hub and shroud giving the designer reasonable flexibility. This parameterisation approach was chosen as the rate of change of impeller radius with respect to impeller axial length is too large towards the exit of the impeller. This could make the effective flow area too sensitive to splitter blade position if splitter blade location is defined as a

fraction of the axial length.

Meridional Profile

Literature:

Verstraete, T. *et al.* [67] defined the hub and shroud meridional contour by third order Bezier curve from leading edge to trailing edge. The two internal control points at the hub can be adjusted while all four control points at the shroud are adjustable during optimisation. Continuity of curvature is enforced between the sections of the impeller using Bezier control points on a straight line tangential to the curve. Leonid Moroz *et al.* [70] defined the meridional profile at hub and shroud by a third order Bezier curve with four control points using linear extensions to the inlet and outlet sections of the impeller. S. Ramamurthy and K. Murugesan [71] used an analytical equation with the form of an ellipse to describe the hub and shroud meridional profiles with some modifications to the hub slope at impeller inlet and outlet. Duccio Bonaiuti *et al*. [64] defined the meridional profile at hub and shroud using second order Bezier curves with three control points having both end points fixed. The fewer variables used by Duccio Benaiut *et al.* imposed some limitations on the curve flexibility. S. Kim *et al*. [72] defined the meridional profile by a third order Bezier curve with four control points where only one of the control points is movable at hub and shroud respectively. The other control points are fixed and defined by the impeller exit tangential on which the profile lies. R.A. Van den Braembussche *et al.* [73] defined the meridional profile at hub and shroud with a third order Bezier curve of 4 control points. The literature survey shows Bezier curve is the most popular method of defining an impeller hub and shroud curve on the meridional plane.

"RC_CAD":

The CAD algorithm developed during this thesis uses fourth order Bezier curve with five control points to define the hub and shroud meridional profiles. The 2nd and 4th control points are adjusted by the same variable. Instead of specifying X, Z coordinates of the three mid control points, the points are calculated as fraction of tangent lengths on which they slide as shown in Figure 5.13. This reduces the number of optimisation variables from 6 to 3 at hub and shroud, respectively. Any reduction in the number of variables is a gain in terms of computing time during multi-objective optimisation. Also, the 2nd and 4th control points move in the same direction all the time as shown in Figure 5.13. This helps to keep the rate of change of curvature under control, compared to when both points move independently which could result in very large or small radius of curvature around the middle section of the meridional profile as shown in Figure 5.14a and 5.14b, respectively. The 3rd control point helps to further tune the curvature between the 2nd and 4th control points. This added flexibility allows for detailed curvature variation to improve compressor performance.

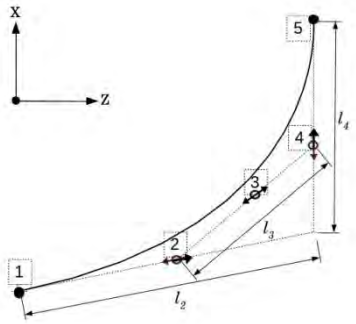

Figure 5.13 – Meridional profile definition

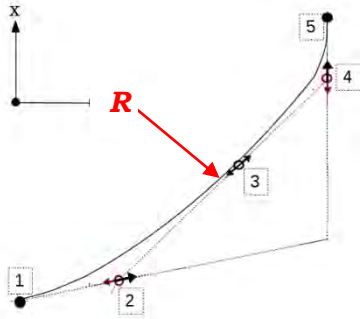

Figure 5.14a – Meridional profile for very large radius of curvature

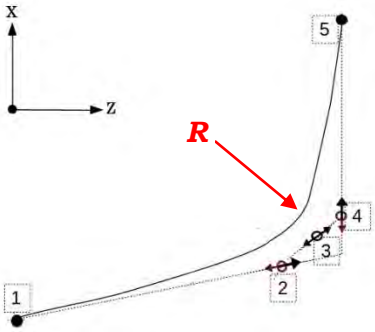

Figure 5.14b – Meridional profile for very small radius of curvature

5.3 REALISATION OF A HIGH THROUGHPUT COMPUTING SYSTEM

In contrast to High Performance Computing (HPC) which concerns speeding up individual programs, High Throughput Computing (HTC) allows many copies of the same program to run concurrently. The benefit of HTC is in its ability to use different input data for each program copy, referred to as jobs [74].

The HTC software HTCondor [28], offer further benefit to HTC as it enables exploitation of commodity hardware such as desktop PCs for computing tasks, at virtually no extra cost. The following sub-sections describe the HTCondor enabled HTC system implemented during this research to facilitate running batch jobs concurrently. The sub-programs that constitute the job work flow are also described as part of the HTC system.

5.3.1 Choice of CAE Tools for the HTC System

Every Computational Fluid Dynamics (CFD)/Computational Structural Mechanics (CSM) design process starts with the creation of the physical geometry using Computer Aided Design (CAD) software. The physical geometry is then discretised/meshed into smaller cells using meshing software so the problem can be numerically analysed using CFD/CSM software. The final process is the analysis of results using post-processing software. During the optimisation phase of this research, it was decided to use free or open-source codes, or develop bespoke code to minimise license cost associated with commercial softwares.

In the early stages of this research, a feasibility study of available open source CAE programs was carried out. Gmsh [75] and SALOME [76] were considered for use as CAD and/or meshing programs respectively, while TBLOCK [6], OpenFOAM [46] and Turbostream [77] were considered for use as the CFD solver. Turbostream is a re-implementation of TBLOCK on GPU‟s and is optimised for speed. Due to the high cost per seat of Turbostream licence, it was not a feasible option. OpenFOAM is a widely used open-source CFD solver with a lot of online support. However, a turbomachinery specific solver was not part of the standard solvers supplied with the publicly available version of OpenFOAM at the time of the feasibility study, so it was ruled out also. TBLOCK is widely used and reliable turbomachinery specific software, but it is not free. However, it was already being used at Napier and also considerably cheaper than most commercial turbomachinery CFD solvers. For this reason, TBLOCK was chosen as the solver. The choice of CFD solver then influenced the choice of CAD and meshing programs. In-house meshing software from Napier compatible with TBLOCK is used. The in-house meshing software reads in CAD files in *.curve* format specific to ANSYS BladeGen [30]. ANSYS BladeGen would have been the obvious choice of CAD program; however, it is expensive due to additional licence costs, particularly when multiple instances of the software are required during batch optimisation calculations. For this reasons, ANSYS BladeGen was not a feasible option for the CAD stage of the CAE process. Hence, there was a need to develop a bespoke parametric CAD algorithm to output *.curve* file format and complete the

design loop. Also a post-processing program called "tb_to_vtk" was developed to convert TBLOCK CFD data to VTK (Visualisation Tool Kit) format for visualisation in ParaView [7].

After the CAD, meshing and CFD solver program were in place, the next task is then to link them all together to run automatically and independently. A "mapping" algorithm is developed to perform this task. The mapping algorithm also collates target objective functions from each CFD run of a compressor CAD model for the optimisation algorithm - DEMO to evolve the CAD model. DEMO is a multi-objective implementation of Differential Evolution (DE) by Storn and Price [56]. At this point, the multi-objective optimisation system can run locally on one machine. The next challenge is to deploy the system on a low cost cluster to speed up the calculations. Low cost in this context means using already available desktop computers to run multiple concurrent jobs when they are idle. HTCondor [28] job management software is then deployed on the clusters to manage job execution.

The High Throughput Computing (HTC) system implemented consist of the following CAE tools - a bespoke parametric CAD algorithm, an in-house meshing program, TBLOCK CFD solver, the developed post-processing program, an open-source optimisation algorithm called DEMO, a mapping algorithm to link the CAD, mesh and solver programs together called "Mapper", and the open-source HTC software HTCondor. An illustration of the HTC system is shown in Figure 5.15. The next Section will discuss the programs/algorithms in the HTC system, excluding the CAD algorithm already described in Section 5.2.

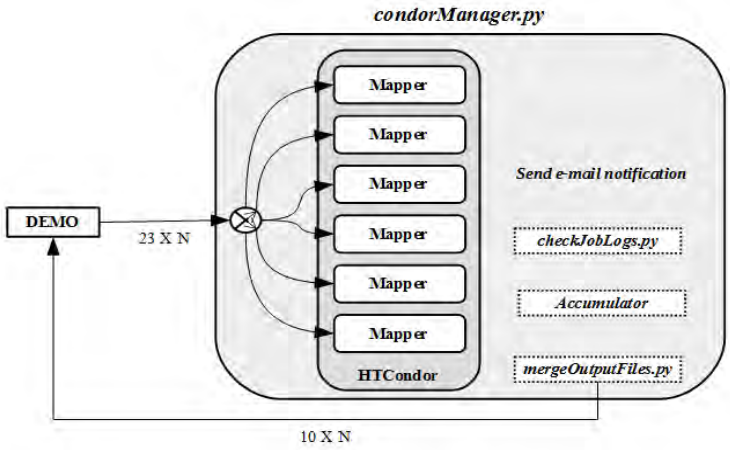

Figure 5.15 - Full Illustration of the HTC System

Meshing Program

In-house meshing software at Napier is used to generate computational grid for the geometry created by the bespoke CAD algorithm. The meshing program is written in FORTRAN and it creates blocks of

structured hexahedral mesh in the inlet, inducer, flow passages and diffuser of radial compressor geometry. It takes less than 4 seconds on an Intel Core i5, 2.5GHz, 8GB RAM Laptop computer to create a mesh of about 300000 cells. The meshing software creates 7 blocks of structured mesh of the impeller and vane-less diffuser region as shown in Figure 5.16. The program allows the user to specify the number of cells in the pitch-wise (circumferential), span-wise (hub to shroud) and stream-wise (inlet to outlet) directions in each block. The same pitch-wise and span-wise number of cells is used for blocks 1, 2, 3, 4 and 7. Blocks 5 and 6 are the shroud gap of the main and splitter blade respectively. The number of cells in the pitch-wise and span-wise of blocks 5 and 6 are set differently. The cell growth rate from the wall can also be set for each block. A sample meridional mesh distribution created using the meshing program is shown in Figure 5.17.

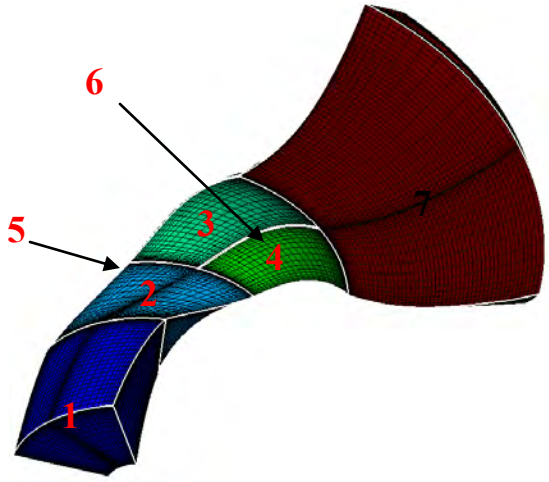

Figure 5.16 - 7 Blocks in the computational domain

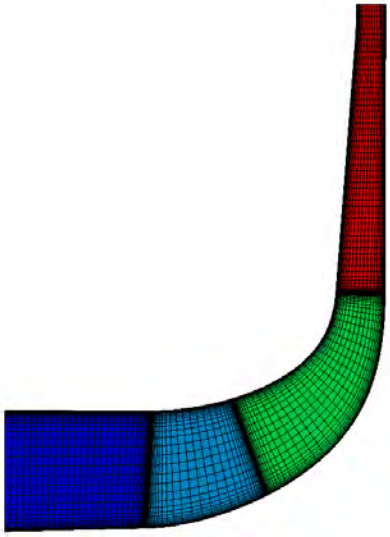

Figure 5.17 - Meridional view of mesh distribution

CFD Solver

TBLOCK [6] is a multi-block flow solver aimed at predicting both main blade path and secondary gas path flows in turbomachinery, although it is also applicable to many other types of flow. The program is written in FORTRAN 77 and the development started in the early 70's by Prof. John Denton [6]. The code is now widely used in academia and industry to design different types of turbo machines. It solves the Reynolds-averaged Navier-Stokes equations on multi-block structured grids of the inlet, passages and diffuser of a radial compressor. TBLOCK version 6.3 uses a mixing plane model to exchange flow properties between the stationary and rotating reference frame. To facilitate use for turbomachinery blades the program is written in cylindrical $(x, r\theta, r)$ coordinates. The coordinates and I, J, K directions must satisfy the following convention as illustrated in Figure 5.18. The geometry of every block must be cuboid with 6 faces and 12 edges as illustrated in Figure 5.19a. TBLOCK treats the interface between the blocks as patches. It also treats the interface between the blocks and inlet and outlet flow surfaces as patches. A block with surface patches is illustrated in Figure 5.19b. There is no limit to number of patches a block can have. Various patch types can be specified, for example, inlet boundary, exit boundary, mixing plane, etc.

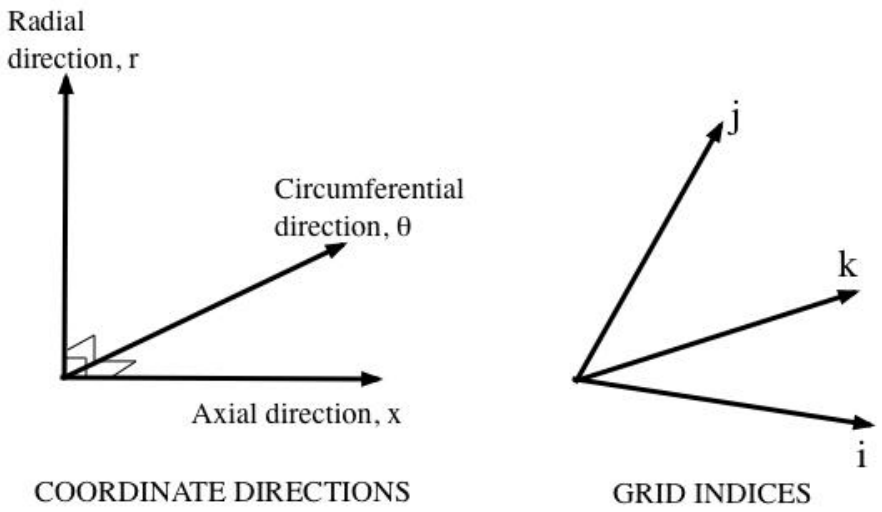

Figure – 5.18 Coordinates and grid indices in TBLOCK

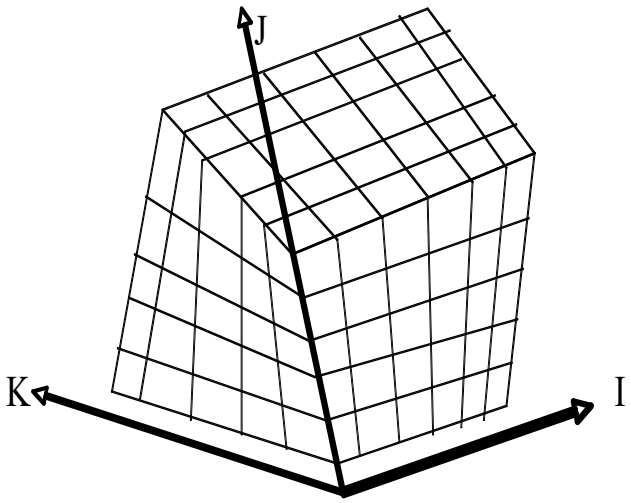

Figure 5.19a - Block and structured grid example for TBLOCK

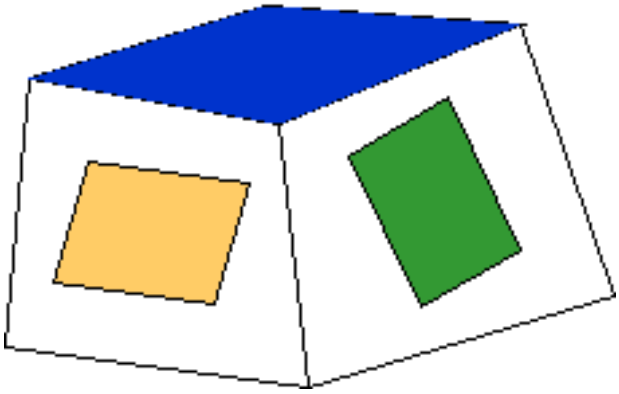

Figure 5.19b – A block with surface patches

TBLOCK version 6.3 [6] uses a very simple and fast single step explicit scheme with minimal artificial viscosity as shown in Equation 5.12

$$\Delta F = \left\{ 2\left(\frac{dF}{dt}\right)^{n} - \left(\frac{dF}{dt}\right)^{n-1} \right\} \Delta t \tag{5.12}$$

where n is the time step index and F is the flow property vector $[\rho,\ \rho V_x, \rho V_r,\ \rho r V_\tau,\ \rho E]$ being solved for. The viscous terms in TBLOCK are full Navier-Stokes equations. The turbulence model is a simple mixing length model. The mixing length is set up to a maximum value which is input as data and is proportional to the distance from the nearest solid wall [6]. Different mixing length values can be set for each block in the computational domain.

Post-processing Program

The open-source post-processing software ParaView [7] was used for post-processing the CFD results. A bespoke computer program is used to convert TBLOCK data to ParaView compatible format. The program reads flow results and grid output files from TBLOCK and converts it to legacy Visualization Tool Kit (VTK) [63] format compatible with ParaView. The computer program calculates summary performance parameters from the results data and some important mesh quality measurement parameters such as Y+, aspect ratio and mesh skewness. Figure 5.20 is an example plot of velocity vectors on the blade surface and hub surface in ParaView.

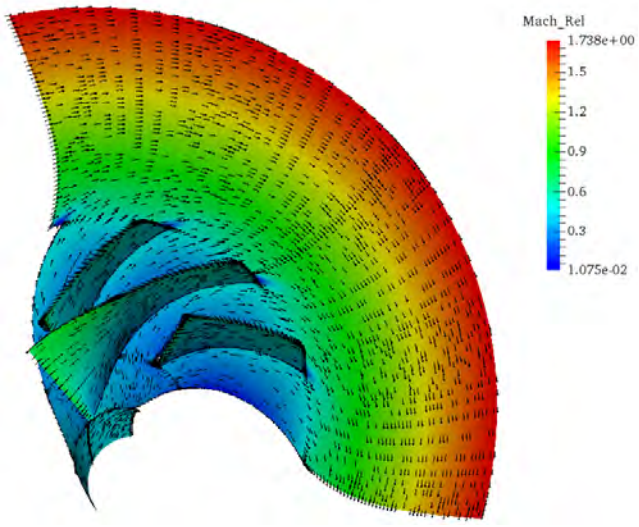

Figure 5.20 - Vector plots on blade and hub profile

Optimisation Algorithm

A modified version [8] of DEMO for batch computing was used in this project to generate candidate geometries (CAD models) in batches so that HTCondor can dispatch multiple jobs to the cluster of 8 desktop machines running Linux CentOS 6.4. DEMO is a multi-objective implementation of Differential Evolution (DE) by Storn and Price [56]. It combines the advantages of differential evolution with the mechanisms of Pareto-based ranking and crowding distance sorting used by state-of-the-art evolutionary algorithms for multi-objective optimisation [9]. Differential Evolution [56] has attained much popularity in the optimisation community.

As batch computing was a key requirement of this project, the modified version of DEMO [8] which supports batch computing was chosen. Also, compared to genetic algorithms, differential evolution

algorithms allows creation of new genes that is a weighted average of two parents genes, instead of using only either of both parents genes. More so, the variant of differential evolution algorithm used during this research, DEMO, was found to have comparable performance to other state-of-the-art optimisation algorithms [56]. Figure 5.21 illustrates the DEMO optimisation algorithm.

---

*1. Evaluate the initial population **P** of random individuals*

2. While stopping criteria is not met, do:

*2.1 For each individual **Pi** (i = 1,…., popSize) from **P** repeat:*

*(a) Create candidate **C** from parent **Pi** -> (mutation)*

*(b) Evaluate the candidate **C***

*(c) If **C** dominates **Pi**, replace **Pi** with **C***

*If **Pi** dominates **C**, discard **C***

*Otherwise, add **C** to population*

2.2 If population > popSize, truncate population

*2.3 Randomly enumerate individuals in **P***

Figure 5.21 – Pseudo code of the DEMO algorithm

Mapping Algorithm

A mapping algorithm is developed to automate the CFD workflow. It calls the CAD and meshing programs and then run the flow solver for different operating conditions to produce radial compressor performance data of each CAD model over a range of mass flows at constant rotor speed to produce the speed line of the compressor. The mapping algorithm then calculates 8 objective functions based on the 23 CAD input parameters for DEMO to evolve new CAD models to meet the target objectives. The mapping algorithm is illustrated in Figure 5.22 where the star is the target design point, and points 1 to 6 are calculated operating points. After calling the CAD and meshing programs, the compressor mapping process starts by running TBLOCK to calculate the performance at the design pressure (point 1). It then continues to reduce the outlet pressure by a set percentage and calculates performance at different outlet pressures until choke is predicted. The percentage reduction is defined as a function of the speed line slope. The program uses the previous solution from the last point to restart the next point in each case to

speed up the process. When choke is predicted, surge prediction is started using the solution from point 1. In this case, the outlet pressure is increased until surge is predicted. The original percentage increase in outlet pressure is reduced by the program during surge prediction and is defined as a function of percentage drop in mass flow from the previous point (i.e. as the slope of the speed line reduces towards surge, smaller increase in outlet pressure is used to calculate the next point). At the end of the algorithm, the compressor speed line is obtained. A speed line is a collection of operating points with values for mass flow, pressure ratio and efficiency at each point.

After obtaining the speed line, the algorithm then computes 8 objectives to be optimised using an optimisation algorithm. The objectives for the optimisation calculations carried out in Chapter 6 of this thesis can be described using Figure 5.22. In Figure 5.22, points 1 to 6 are calculated operating points. The broken line is a hypothetical target speed line. Assuming the target design point is „start" in Figure 5.22 (this is known by the designer), every valid compressor CAD geometry evaluated should have a speed line crossing the target design points. The eight objectives are described as follows:

1. Reduce distance from 1 to „star" (in mass flow). In other words, the new optimised design should deliver the target mass flow at the design speed.
2. Reduce distance from „star" to the calculated speed line (in pressure ratio)
3. Assuming the peak efficiency on the speed line is at operating point 5, the distance between 1 and 5 (in mass flow) should be reduced.
4. Similar to objective 3, reduce distance between 1 and 5 (in pressure ratio)
5. Centralise peak efficiency. Mass flow at 5 should be approximately the average of choke (point 4) and surge (point 6) mass flow
6. Design point sufficiently clear from surge mass flow. Mass flow at point 1 greater than mass flow at point 6. The larger the better.
7. Peak efficiency at operating point 5 should be as high as possible
8. Map width (choke mass flow – surge mass flow) should be as large as possible.

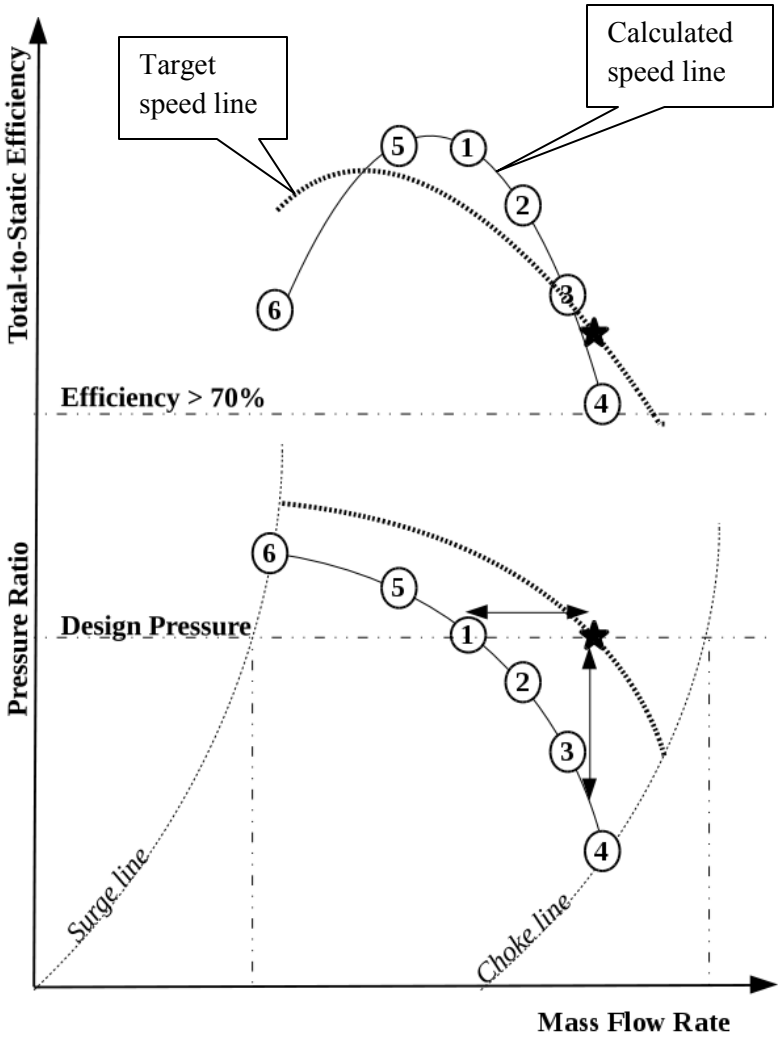

Figure 5.22 - Illustration of the mapping algorithm

Choke is determined if the slope of the performance curve (change in mass flow with change in pressure) is less than a set value or the calculated efficiency is below a set value e.g. 70%, depending on which situation occurs first. Surge is an unsteady phenomenon and is characterised by longer calculation time and large variance in mass flow and efficiency. Surge is determined to have occurred if the number of solver time steps at a point during surge prediction exceeds a particular value typically 25000 or the average efficiency in the last 1000 iterations is less than 70%. The mapping program then outputs a „sim_out.dat" file that contains the calculated non-dimensionalised objective functions and „operatingPoints_sorted.dat" file containing the compressor speed line performance data.

HTCondor

HTCondor [28] is a specialized workload management system developed at the University of Wisconsin Madison for computer-intensive jobs. HTCondor provides a job queuing mechanism, scheduling policy, priority scheme, resource monitoring, and resource management. Users submit their serial or parallel jobs to HTCondor. HTCondor places the jobs into a queue, chooses when and where to run the jobs based upon a policy, carefully monitors their progress, and ultimately informs the user upon completion [28]. The HTCondor pool set up for this project consist of 8 desktop computers running Linux CentOS 6.4 operating system. Each machine has 4GB of RAM and 4 cores. This means 32 instances of TBLOCK can run on the desktop cluster to speed up the calculations. The decision to use CAE tools without Graphical User Interface (GUI) was informed by the need to use cluster job management software such as HTCondor. This is due to the fact that commercial applications with GUI"s are more difficult to set up in a cluster of desktop computers running HTCondor software and often require multiple licences which can be very expensive [78]. A typical HTCondor pool with six machines is show in Figure 5.23. The central manager is identified by the presence of „negotiator" and „collector" daemons. Submit and execute nodes are identified by the presence of „schedd" and „startd" daemons respectively.

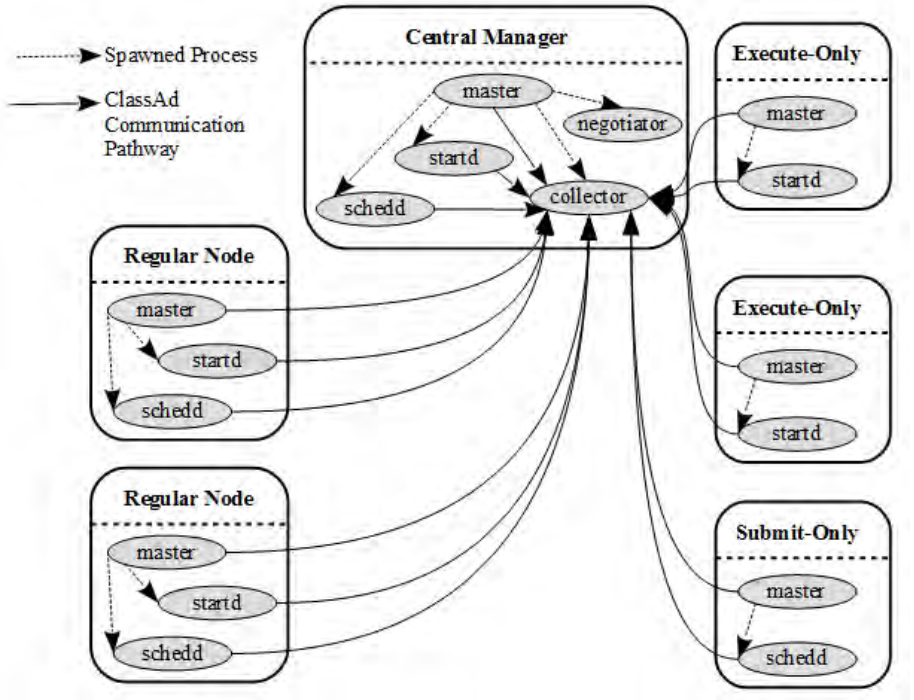

Figure 5.23 - A typical condor pool with 6 machines

5.4.2 The Complete HTC System

The HTC system implemented during this thesis includes the components described in the previous Section and a python script - *„condorManager.py"* that manages the communication between HTCondor running jobs and DEMO. As described earlier, the mapping algorithm runs the CAD and meshing programs and then runs the CFD solver at various outlet pressures to obtain the compressor speed line. The mapping algorithm workflow is illustrated in Figure 5.24.

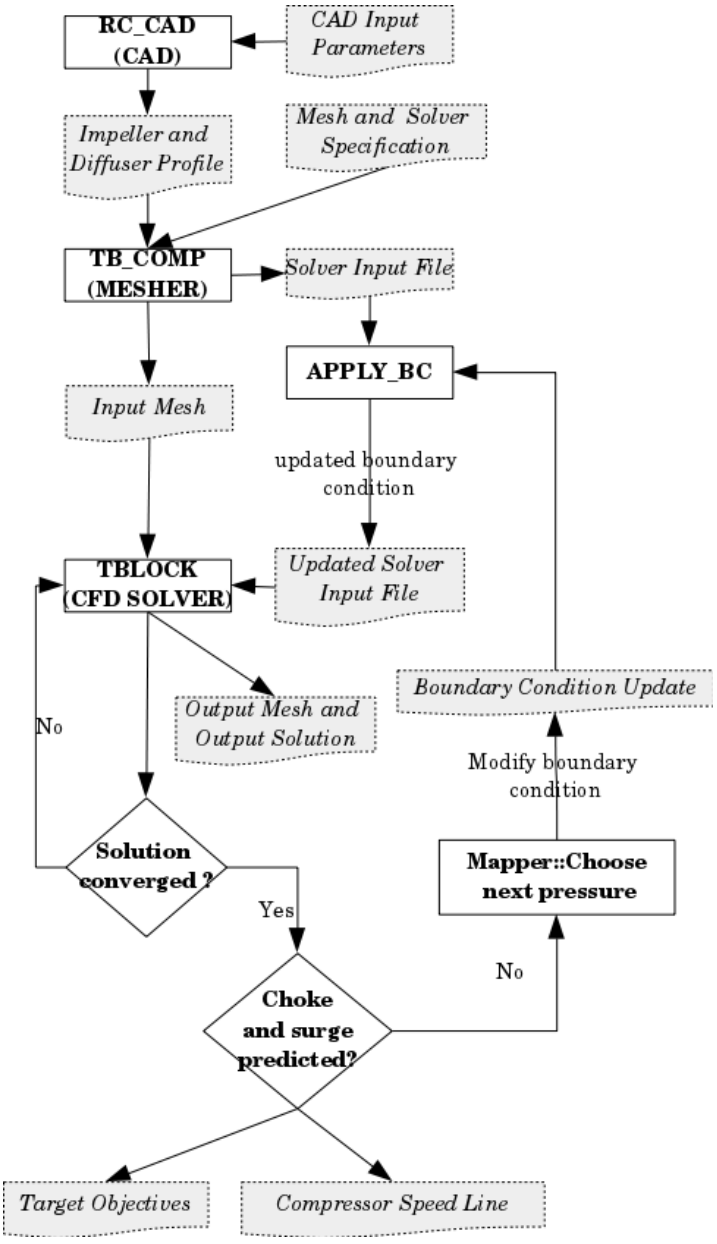

Figure 5.24 - Detailed view of Mapper work flow

The number of candidates per generation was approximated to 180 (23 X 8 = 184). A batch size of 45 candidates was chosen to run on the 8 desktop machines (32 processors) so that most of the processors are utilised all the time. The batch version of DEMO was then configured to optimise the CAD models in batches of 45. Hence 45 directories were created in the central manager machine in the condor pool for each candidate CAD model to be solved. The full system works as follows:

1. DEMO generates 45 CAD model input parameters.
2. *„condorManager.py"* splits the 45 input parameters into 45 separate directories.
3. *„condorManager.py"* instructs HTCondor to dispatch the jobs to the cluster.
4. *„condorManager.py"* delivers to DEMO the completed batch of results and DEMO produces another batch of 45 candidates and the process continues.

This process is illustrated again Figure 5.25 where N is the batch size and 23 represents the number of parameters input for the CAD algorithm.

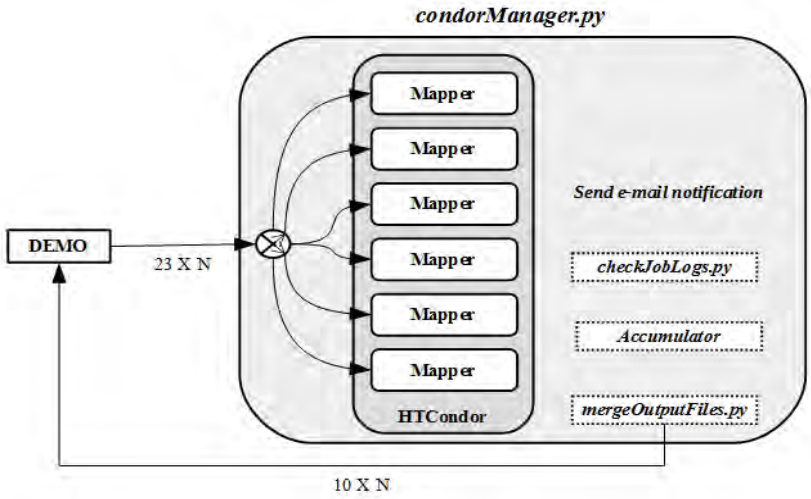

Figure 5.25 - Full Illustration of the HTC System

„condorManager.py" also calls the following sub programs – *„checkJobsLog.py"*, *„mergeOutputFiles.py"* and *„Accumulator"*. *„condorManager.py"* calls *„checkJobsLog.py"* at defined intervals set by the user (e.g. every 5 seconds) to check the job logs in each of 45 folders for completion status and notifies *„condorManager.py"* when all jobs are finished. When all jobs are finished, *„condorManager.py"* calls *„mergeOutputFiles.py"* to merge the „sim_out.dat" file (i.e. calculated objectives) of each CAD model in the different folders into a single file for DEMO to read in. *„condorManager.py"* then calls *„Accumulator"* which collates relevant input and output parameters for each valid CAD model in each set up folder (45 folders that make up a batch) into separate log files with a unique column (the first column – „Job ID") identifying each candidate geometry. This accumulation takes place when a batch is completed so all the

information required to recreate evaluated compressor geometry are stored. Three log files of each valid CAD model are maintained as described below:

1. „paremetersLog.dat" containing logs of CAD input parameters
2. „objectivesLog.dat" containing logs of calculated objectives
3. speedLineLog.dat" containing logs of each compressor operating speed line

„condorManager.py" then sends an e-mail with statistics of valid designs along with an attachment of log files to relevant project team members. A sample e-mail notification is show in Figure 5.26 and a picture of the 8 desktop machines in the condor pool is shown in Figure 5.27.

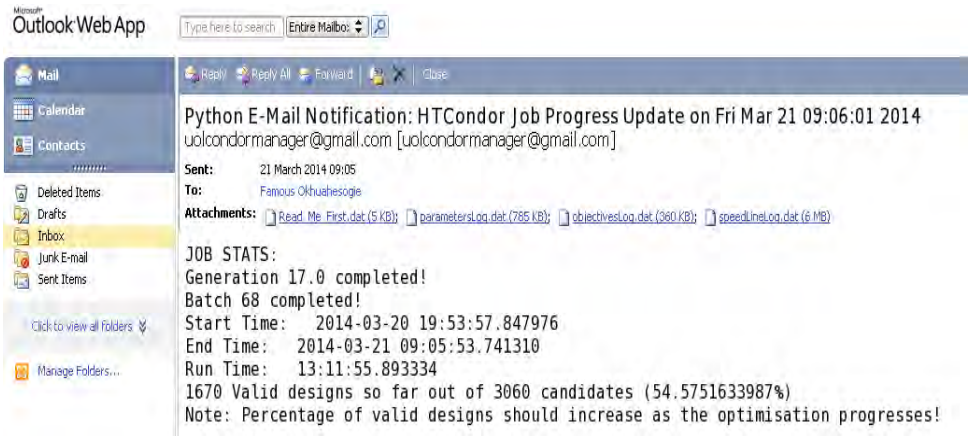

Figure 5.26 - Sample e-mail notification from „condorManager.py"

Figure 5.27 - Picture of computers in the condor pool

CONCLUSION

This Chapter detailed the bespoke parametric CAD algorithm developed during this thesis to facilitate multi-objective optimisation of radial compressors. It also details the implementation of an HTCondor enabled HTC system and work flow of sub-programs within the HTC system. In the next Chapter, multi-objective optimisation of an existing HP compressor of a two-stage turbocharger using the HTC system will be presented.

CHAPTER 6

AERODYNAMIC OPTIMISATION OF A RADIAL COMPRESSOR IN THE HP STAGE OF A TWO-STAGE TURBOCHARGER

This Chapter presents the multi-objective aerodynamic optimisation of a radial compressor in the high pressure (HP) stage of a two-stage turbocharger facilitated by the HTC system realised in Chapter 5. A new optimised compressor design with significant improvement in efficiency (up to 1.6 points) and 20% increase in map width across three speed lines was achieved, compared to a reference compressor that was designed incrementally. Compressor map width is the difference between the largest and smallest mass flow on a compressor speed line. A speed line is a collection of operating points, each containing information about mass flow, pressure ratio and efficiency.

The contributions of this Chapter are as follows:

- A demonstration of multi-objective optimisation of a radial compressor with up to 8 conflicting objectives, including map width enhancement
- The discovery of new impeller blade design topology with large blade angles at the exit (or back sweep angle). The large blade angle impeller designs showed higher efficiency, but lower pressure ratio. However, since the HP stage compressor pressure ratio is merely around 2:1, the low pressure ratio of large back sweep impeller is not a disadvantage

6.1 MESH CONVERGENCE STUDY

A mesh convergence study on an existing geometry is carried out to find the optimum mesh settings (in terms of accuracy and run-time) for the optimisation calculations. The mesh details for the three levels of mesh investigated are detailed in Table 6.1 and illustrated Figure 6.1. The compressor consists of 6 impeller main blades and 6 splitter blades, with a tip gap of 0.5%.

	Parameter	Coarse	Medium	Fine
1	Span wise mesh cells on blade	28	34	42
2	Span wise mesh cells on tip clearance	4	4	4
3	Upstream meridional mesh cells	26	34	38
4	Inducer meridional mesh cells	26	34	50
5	Passage meridional mesh cells	30	45	65
6	Diffuser meridional mesh cells	45	60	65
7	Pitch wise cells	14	18	27
8	Pitch wise cells on leading edges	4	4	5
9	Mesh growth rate from boundaries	1.3	1.3	1.3
	Total number of cells	**136672**	**272393**	**603992**

Table 6.1 - Mesh details for mesh sensitivity study

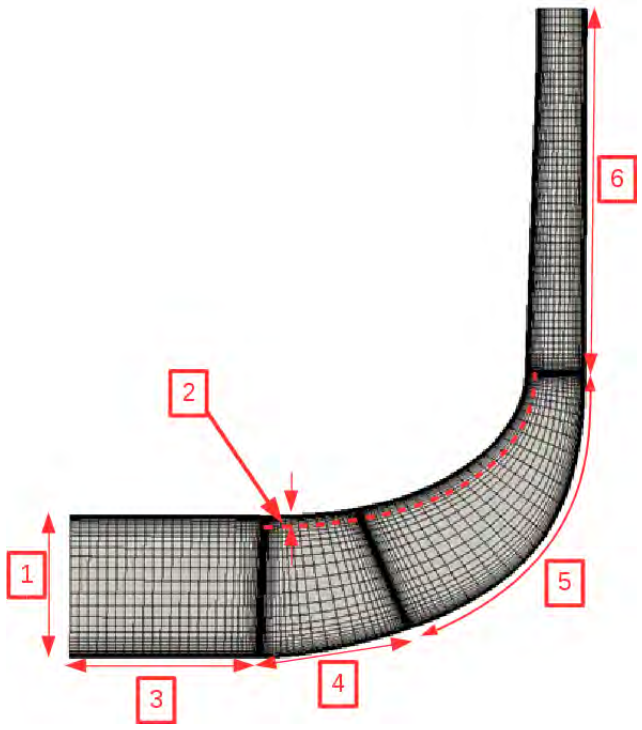

Figure 6.1a – Meridional mesh description

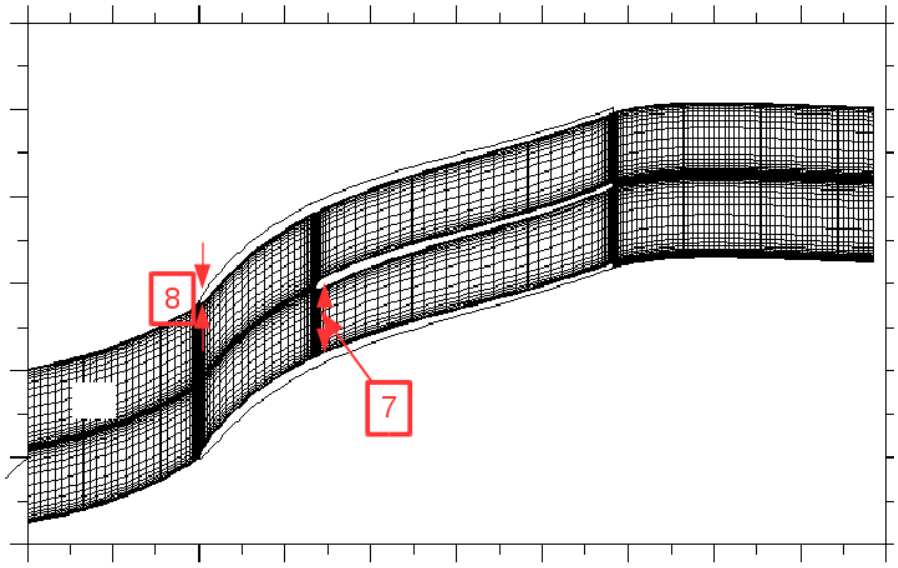

Figure 6.1b – Blade-to-blade mesh description

The CFD settings for the mesh convergence study case are shown in Table 6.2. The geometry is a high pressure (HP) compressor with inlet stagnation pressure of 350000 Pa and inlet temperature of 60^{o}C (333K). The pressure ratio of the HP compressor is 2:1, resulting in an outlet static pressure ratio of 700000 at the design speed of 25000 rpm. CFL number is set to a TBLOCK [6] recommended value of 0.4. CFL number sets the solver time steps i.e. how quickly it iterates to find a solution. Smaller values result in a more stable iteration, but longer run time. Smoothing factor is used to scale the CFL number within the solver. A recommended value is chosen for this study. The plot of speed line for the three mesh levels is shown in Figure 6.2. The Figure shows that the target mass flow for all three mesh levels was within 1% of each other at the design pressure ratio of 2:1 as illustrated in Figure 6.2. Overall, the result shows there is no significant difference between the medium and fine mesh in terms of mass flow and efficiency prediction. As a result, the medium mesh is chosen for use in the optimisation calculations.

Parameter	**Value**
Design Operating speed (rpm)	25000
Inlet stagnation pressure (Pa)	350000
Inlet stagnation temperature (Kelvin)	333
Outlet static Pressure at design point (Pa)	700000
CFL number	0.4
Smoothing factor	0.03

Table 6.2 – CFD settings for mesh convergence case

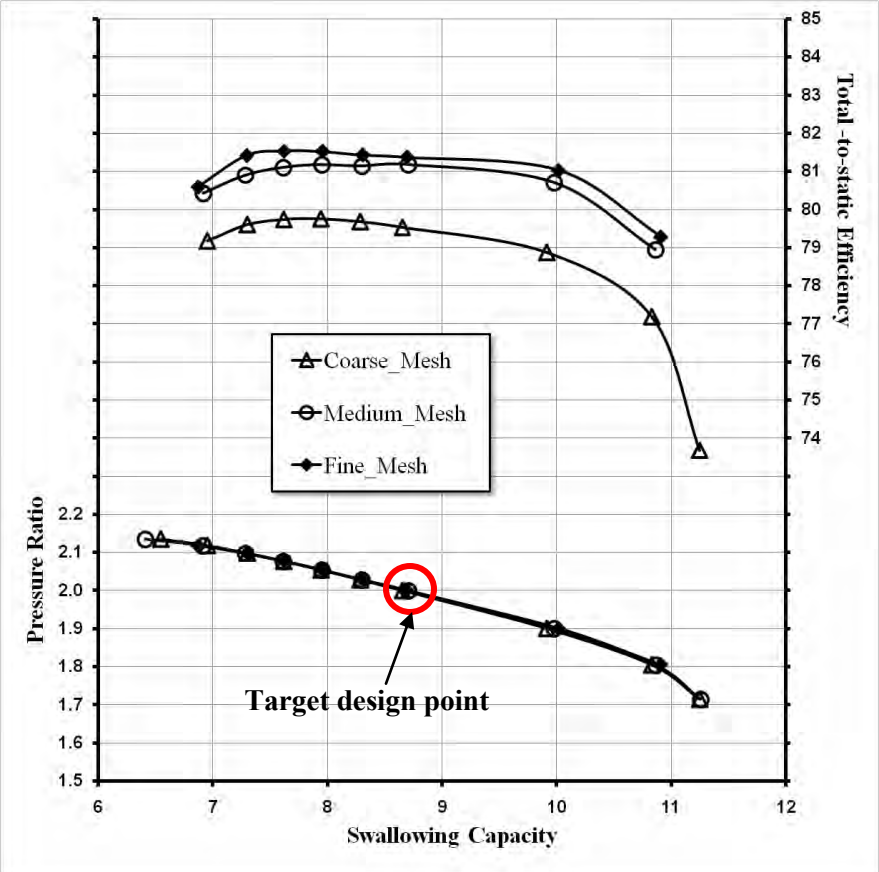

Figure 6.2 – Convergence study of sample compressor geometry

Mesh topology and quality for each mesh density level is depicted in Figures 6.3 to 6.5. Figures 6.3a, 6.4a and 6.5a show the aspect ratio of cells in the main passage is about 1, except near walls or leading edges where it goes up to 20. Aspect ratio is a measure of how „square" a 2D mesh cells is. A perfect square has an aspect ratio of 1. Aspect ratios close to 1 are ideal. Aspect ratios up to 40 may be permissible for structured meshes particularly near boundary layers where fluid properties changes rapidly in the direction normal to the surface and less so in the tangential direction. Figures 6.3b, 6.4b and 6.5b depict mesh skewness for each mesh level to be between 0 and 0.2. A perfect square or cube has a skewness of zero, while a rhombus has a skewness greater than 0 but less than 1. An almost flat rhombus will have skewness approximately 1. Skeweness value close to 1 is very bad for CFD. Figures 6.3 to 6.5 show that the mesh settings used for mesh convergence study produced meshes with very good aspect ratios and skewness values. Figures 6.3c, 6.4c and 6.5c depict mesh topology at the hub for the coarse, medium and fine mesh respectively.

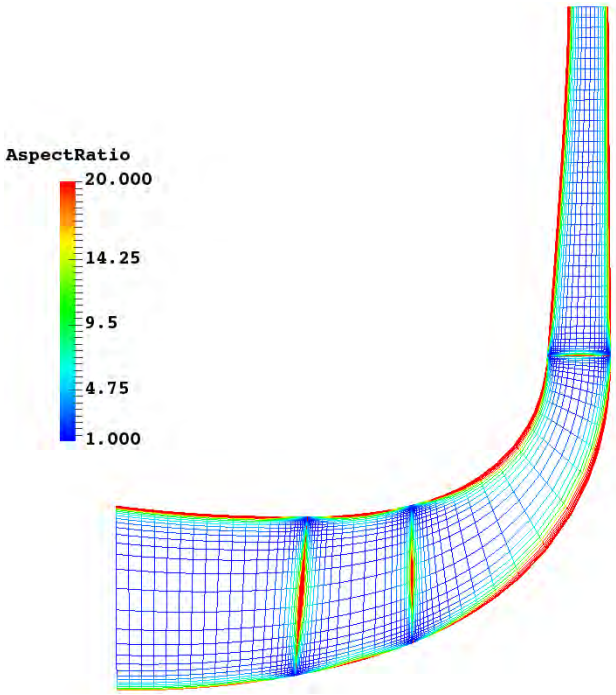

Figure 6.3a – Meridional view of coarse mesh showing mesh aspect ratio

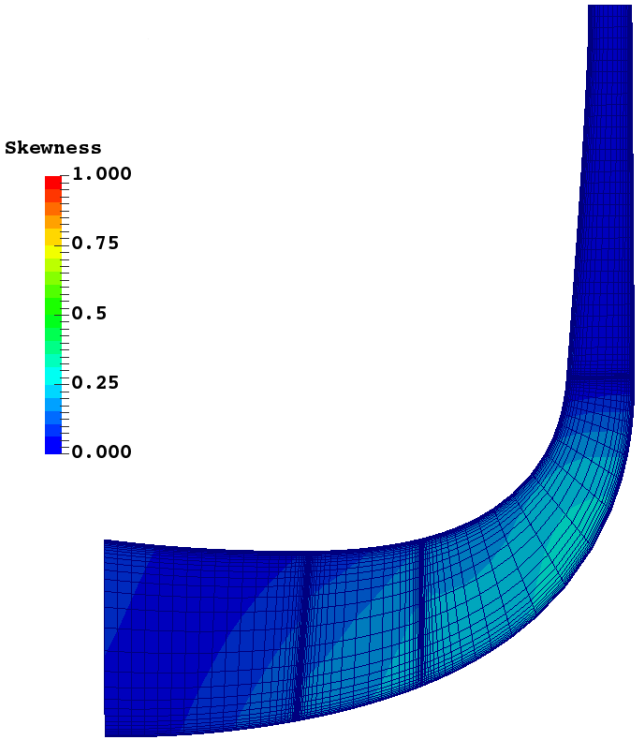

Figure 6.3b – Meridional view of coarse mesh showing mesh skewness

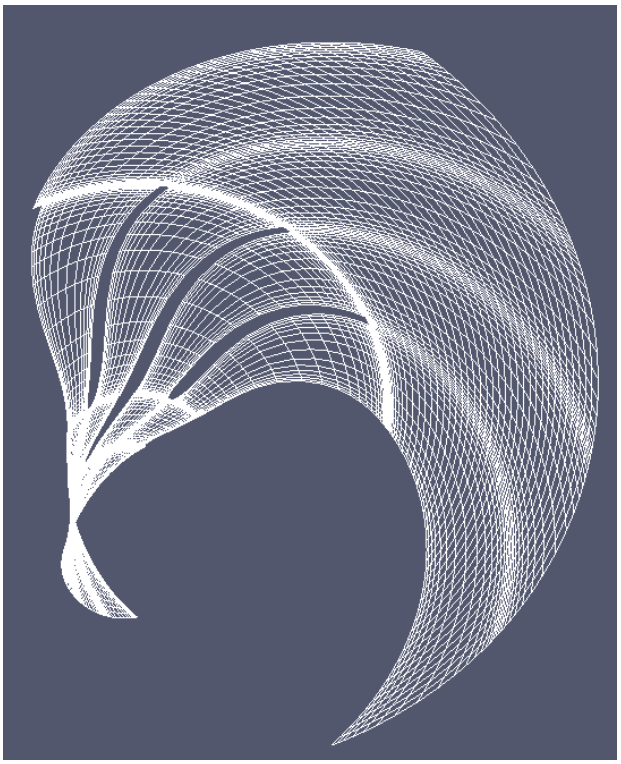

Figure 6.3c – Hub view of coarse mesh topology

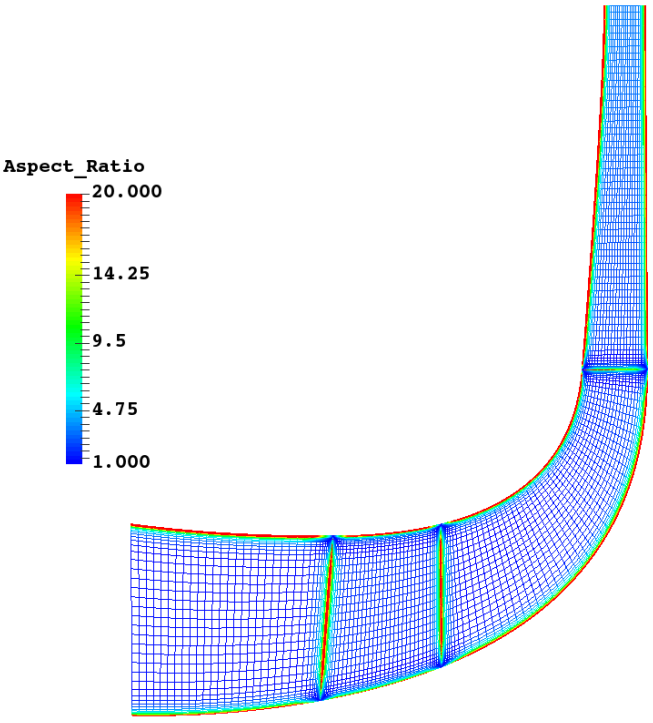

Figure 6.4a – Meridional view of medium mesh showing mesh aspect ratio

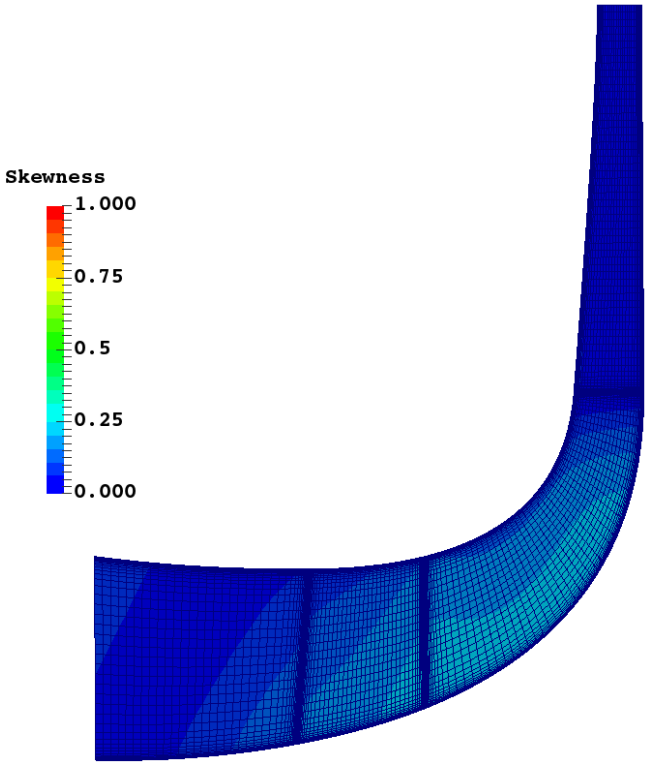

Figure 6.4b – Meridional view of medium mesh showing mesh skewness

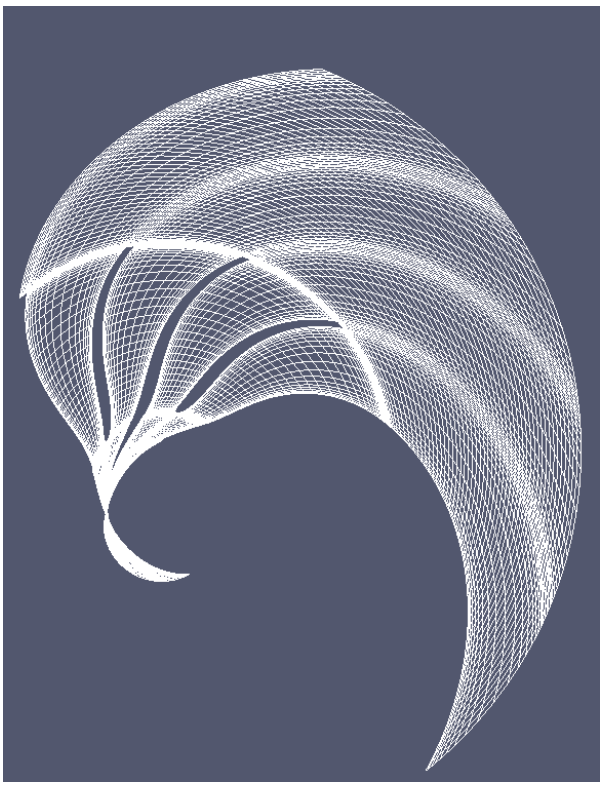

Figure 6.4c – Hub view of medium mesh topology

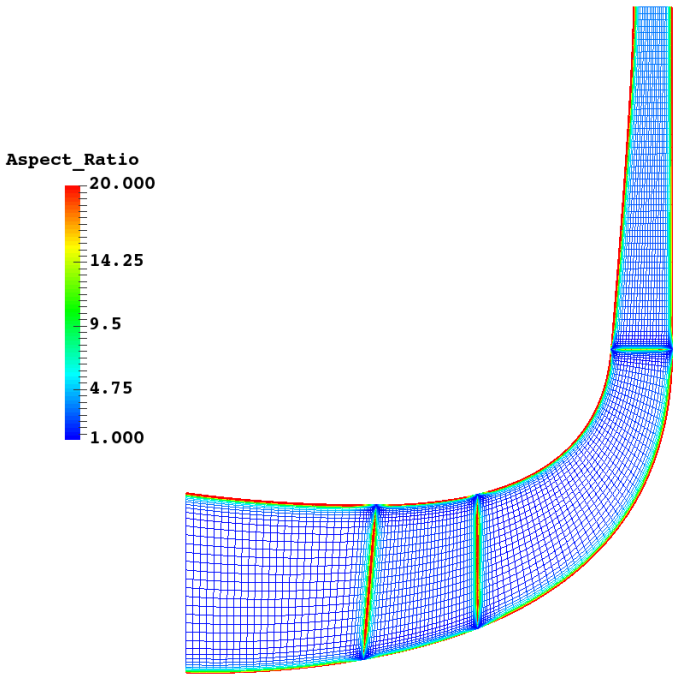

Figure 6.5a – Meridional view of fine mesh showing mesh aspect ratio

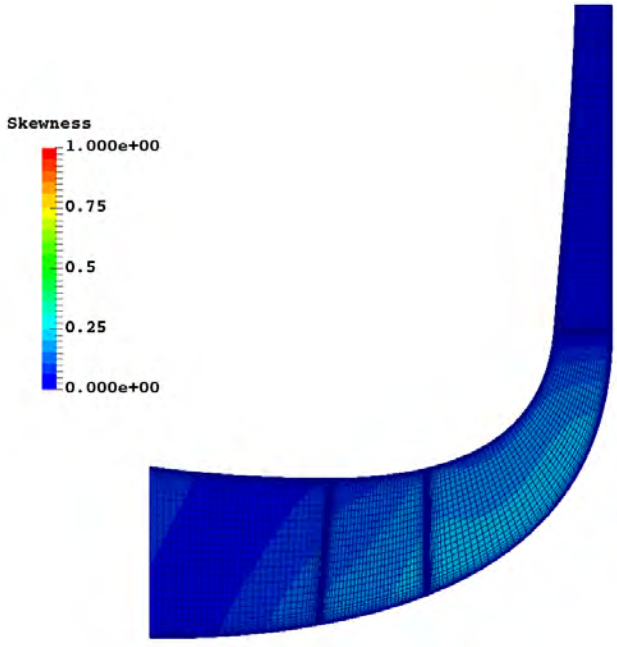

Figure 6.5b – Meridional view of fine mesh showing mesh skewness

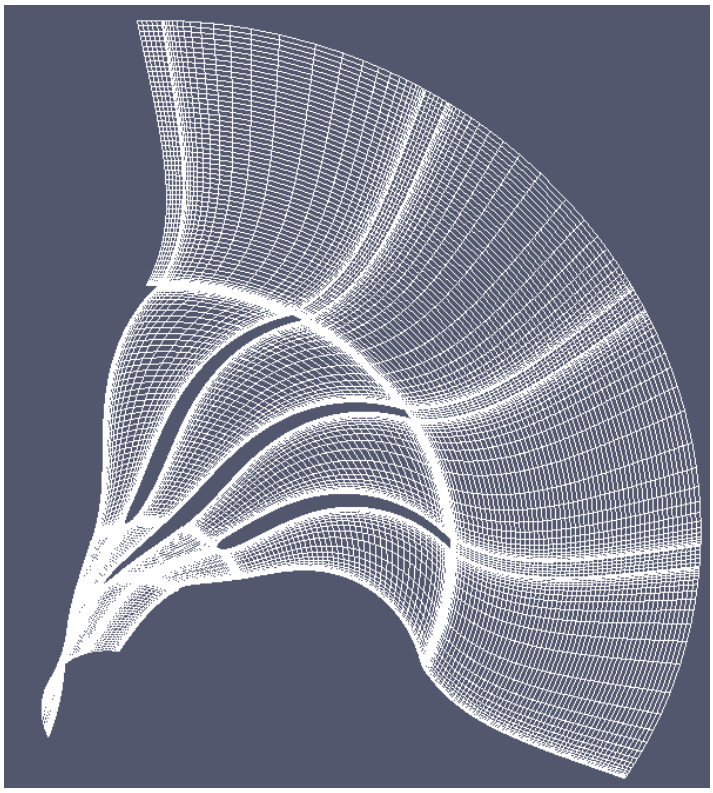

Figure 6.5c – Hub view of fine mesh topology

6.2 VALIDATION OF CFD SOLVER

TBLOCK and experimental results for sample compressor geometry are compared for validation purposes. Mesh details for the TBLOCK analysis is shown in Table 6.3. The medium mesh from the mesh convergence study was used for the validation study. TBLOCK boundary conditions and settings are outlined in Table 6.4. Normalised values of speed and capacity are presented in Figure 6.6 which compares experimental and TBLOCK CFD compressor maps. It shows good agreement in terms of width and height of map for the range of speed lines compared as indicated. Also, the peak efficiency of 84% is in the same region in the experimental and CFD results. Figure 6.7 also show good agreement in pressure ratio, mass flow and efficiency across three speedlines – 1400, 1500 and 1600. Choke and surge mass flow computed using TBLOCK compare well with experimental data.

Parameter	**Value**
Number of main blades	6
Number of splitter blades	6

Parameter	Value
Shroud tip clearance	0.5%
Span wise mesh cells on blade	34
Span wise mesh cells on tip clearance	4
Upstream meridional mesh cells	34
Inducer meridional mesh cells	34
Passage meridional mesh cells	45
Diffuser meridional mesh cells	60
Pitch wise cells	18
Pitch wise cells on leading edges	4
Mesh growth rate from boundaries	1.3

Table 6.3 – Mesh settings for TBLOCK

Parameter	Value
Design Operating speed (rpm)	25000
Inlet stagnation pressure (Pa)	350000
Inlet stagnation temperature (Kelvin)	333
Outlet static Pressure at design point (Pa)	700000
CFL number	0.4
Smoothing factor	0.03

Table 6.4 – CFD solver setting for TBLOCK

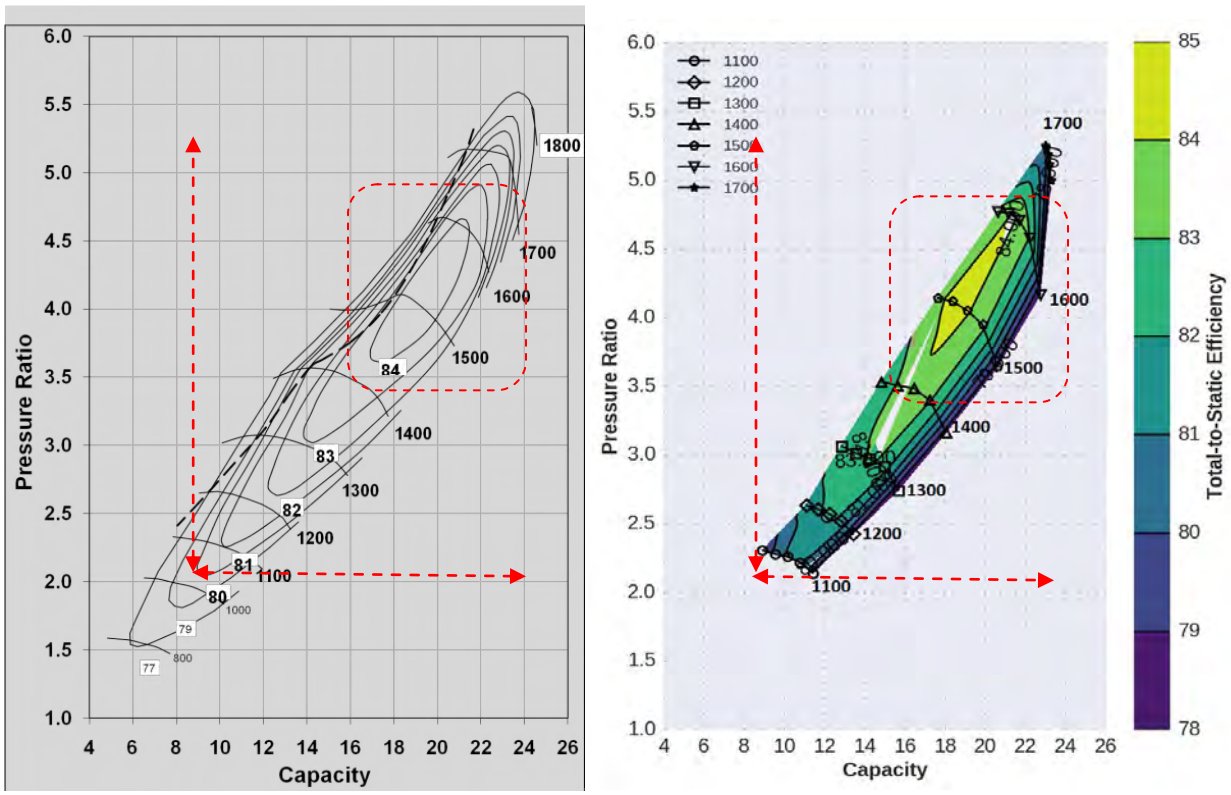

(a) Experiment **(b) TBLOCK CFD**

Figure 6.6 – Comparison of experiment and TBLOCK compressor maps

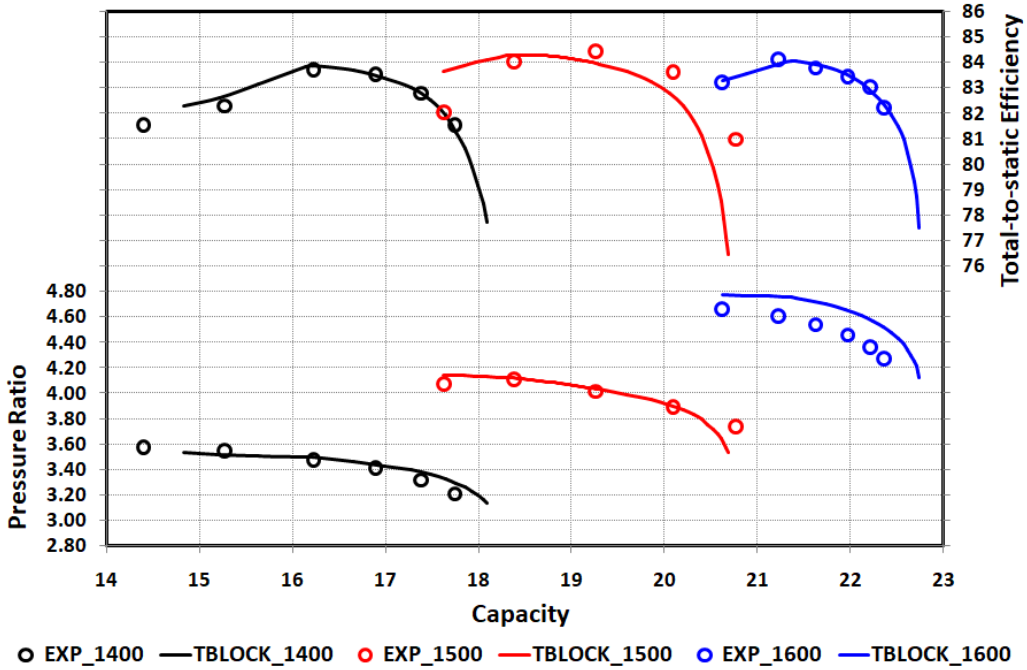

Figure 6.7 – Comparison of experiment and TBLOCK across three speed lines

6.3 MULTI-OBJECTIVE OPTIMISATION

The current or baseline design of the compressor in the HP stage of a two-stage turbocharger is designed at an operating speed of 25000 rpm and total-to-static pressure ratio of 2:1 at a mass flow rate of 11.4kg/s. The intent of the optimisation task is to improve on the performance of a very good baseline design of a HP compressor. The parameter bounds for the optimisation task are based around the baseline design. Also, there are physical geometric constraints for the HP compressor such as outer radius of the diffuser; so the optimisation started from a design space that contained good designs without needing an initial Design of Experiments (DoE). Hence, the optimiser, DEMO was set up to search the design space around the design parameters of the baseline HP compressor.

6.3.1 Optimisation 1

In the first run of optimisation calculations, the configuration settings for the 23 optimisation parameters are illustrated in Table 6.5. Each parameter was specified with bounds in which DEMO can generate values. The step parameter sets how values are generated within the range of each parameter. For example, low value of 5 and high value of 7 with step 1 means possible values are 5, 6 and 7. If step is set to 0, any number between low value and high, including fractions is possible.

S/N	Parameter	Low Value	High Value	Step*	Description
1	N_b	5	7	1	Number of main blades or splitter blades
2	R_{1h}	0.0295	0.0300	0	Radius of the impeller hub at the leading edge
3	R_{1s}/R_{1h}	2.950	3.000	0	Ratio of shroud radius to hub radius at impeller leading edge
4	R_{1s}/R_2	0.600	0.650	0	Ratio of impeller trailing edge radius to impeller leading edge shroud radius
5	b_2/R_2	0.140	0.180	0	Ratio of impeller exit blade height to impeller exit radius
6	L/R_2	0.800	1.000	0	Ratio of impeller axial length to impeller exit radius
7	R_3/R_2	1.850	1.891	0	Ratio of diffuser exit radius to impeller exit radius
8	b_3/b_2	0.5000	0.8000	0	Ratio of diffuser exit height to impeller exit blade height
9	β_0	60.000	68.0000	0	Shroud leading edge blade angle. See Figure 5.3
10	β_3	45.000	55.000	0	Shroud backsweep angle. See Figure 5.3
11	σ	2	10	0	Leading edge sweep angle. See Figure 5.1

S/N	Parameter	Low Value	High Value	Step*	Description
12	δ	0	12	0	Axial sweep angle. See Figure 5.1
13	θ_0	-10	10	0	Hub wrap angle correction at leading edge. See Figure 5.5
14	θ_1	-20	20	0	Hub wrap angle correction at mid-meridional profile. See Figure 5.5
15	ψ	20	60	0	Rake angle. See Figure 5.6
16	H_P(1,4)	0.05	0.95	0	Location of 1st and 4th hub Bezier control point as fraction of the lines on which they slide . See Figure 5.1
17	H_P(3)	0.05	0.95	0	Location of 3rd hub Bezier control point as a fraction of the lines on which they slide . See Figure 5.1
18	S_P(1,4)	0.05	0.95	0	Location of 1st and 4th shroud Bezier control point as fraction of the lines on which they slide. See Figure 5.1
19	S_P(3)	0.05	0.95	0	Location of 3rd shroud Bezier control point as a fraction of the lines on which they slide . See Figure 5.1
20	β_1	35	50	0	Shroud blade angle at 33% of shroud meridional length . See Figure 5.3
21	β_2	40	60	0	Shroud blade angle at 67% of shroud meridional length . See Figure 5.3
22	Split_Hub	0.2	0.5	0	Splitter leading edge position at the hub as a fraction of main blade hub meridional length . See Figure 5.1
23	Split_Shr	0.2	0.5	0	Splitter leading edge position at the shroud as a fraction of main blade shroud meridional length . See Figure 5.1

Table 6.5 – Parameters limits set in DEMO

The objectives for the optimisation calculations carried out in this Chapter can be described using Figure 6.8. In Figure 6.8, points 1 to 6 are calculated operating points. The broken line is a hypothetical target speed line. Assuming the target design point is „star" (this is known by the designer), every valid compressor CAD geometry evaluated should have a speedline crossing the target design points. The eight objectives are therefore described as follows:

1. Reduce distance from 1 to „star" (in mass flow). In other words, the new optimised design should deliver the target mass flow at the design speed.
2. Reduce distance from „star" to the calculated speed line (in pressure ratio)
3. Assuming the peak efficiency on the speed line is at operating point 5, the distance between 1 and 5 (in mass flow) should be reduced.
4. Similar to objective 3, reduce distance between 1 and 5 (in pressure ratio)
5. Centralise peak efficiency. Mass flow at 5 should be approximately the average of choke (point 4) and surge (point 6) mass flow.

6. Design point sufficiently clear from surge mass flow. Mass flow at point 1 greater than mass flow at point 6. The larger the better.
7. Peak efficiency at operating point 5 should be as high as possible
8. Map width (choke mass flow – surge mass flow) should be as large as possible.

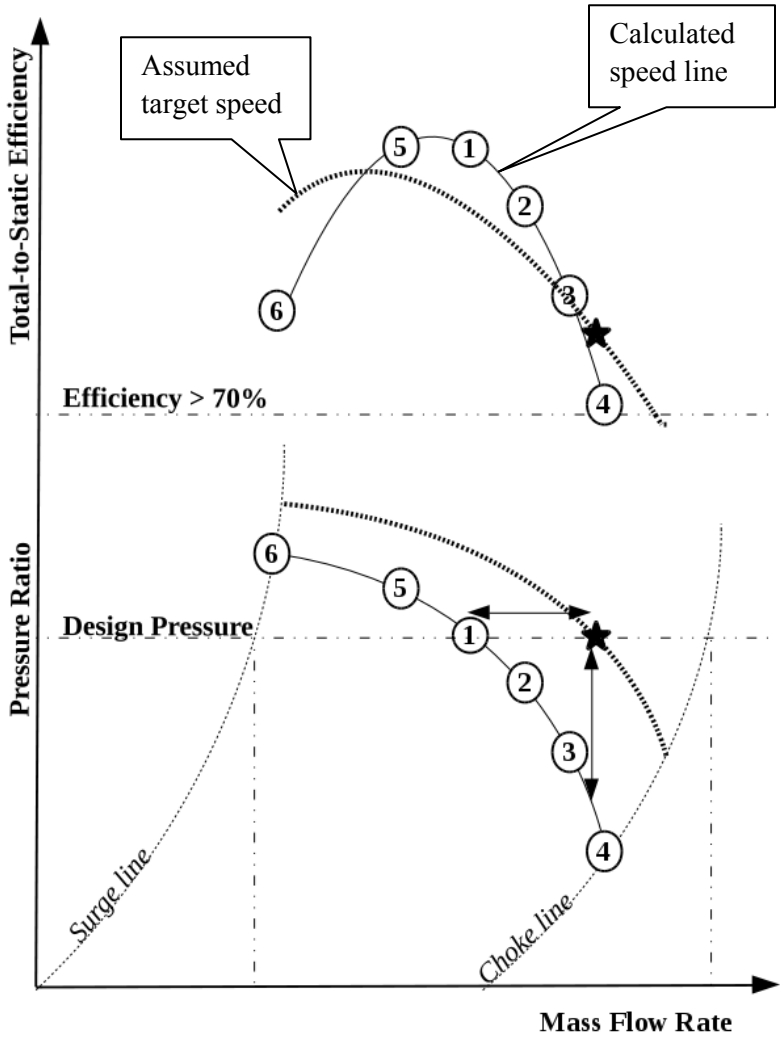

Figure 6.8 - Illustration of the mapping algorithm

The number of candidates per generation is approximated to 180 ~ (23 X 8 = 184). A batch size of 45 candidates is chosen to run on the 8 desktop machines (32 processors) so that most of the processors are utilised all the time. The batch version of DEMO is then configured to optimise the CAD models in batches of 45. The calculations took about 6 weeks to run on the cluster running 24 hours every day.

Optimisation Results

After 32 generations, the objective parameters are observed to be converged as shown in Figure 6.9 which shows averaged values of each parameter for all candidates in each generation. It shows that peak efficiency and map width are improved to an optimum level and the other six objectives are minimised to a suitable level. Also, DEMO logs shows that there are no further improvements in the design objectives so the optimisation is manually halted at this point.

Figure 6.10 is a Pareto front of the optimisation calculation showing the progression of peak efficiency and map width. The Pareto front does not show an obvious front, however, there is a clear trend to improve map width and efficiency from one generation to the next as depicted in Figure 6.10. This is because 8 objectives is quite a high number of target objectives, so plotting just two may not show a clear Pareto front. Figure 6.11 is a plot of the closeness of the calculated design point to the target point in terms of mass flow on the x-axis versus the closeness of the design point to the peak efficiency point in terms of mass flow on the y-axis. Just as in Figure 6.10, Figure 6.11 does not show a clear Pareto front. However, it is clear from the plot that the objectives plotted are been improved from one generation to the next as indicated by the arrow.

Choosing the best candidate(s) is not an easy task because of the conflicting objectives. Based on the number of objectives, in order to confidently choose a set of best candidate(s) visually, it will require combination of 3D plots of several generations, however, that approach would be very tedious. The more efficient way of choosing a best design is to filter and sort the log files based on objectives of high interest. In this case, objective 1 - which measures how close a design is to the target mass flow, objective 7 - peak efficiency and objective 8 – map width are used to filter the „objectivesLog.dat" file to get the best candidates. The final choice of design, further analysed and presented here also required checking the „speedLineLog.dat" for the range of mass flow rate of the promising candidates to ensure it covers the current design mass flow range. In the end, candidate No. 3862 in the 32nd generation is chosen as the best compromise design as indicated by a circle in Figure 6.10. The new design compressor impeller has 7 blades compared to the baseline design with 6 blades.

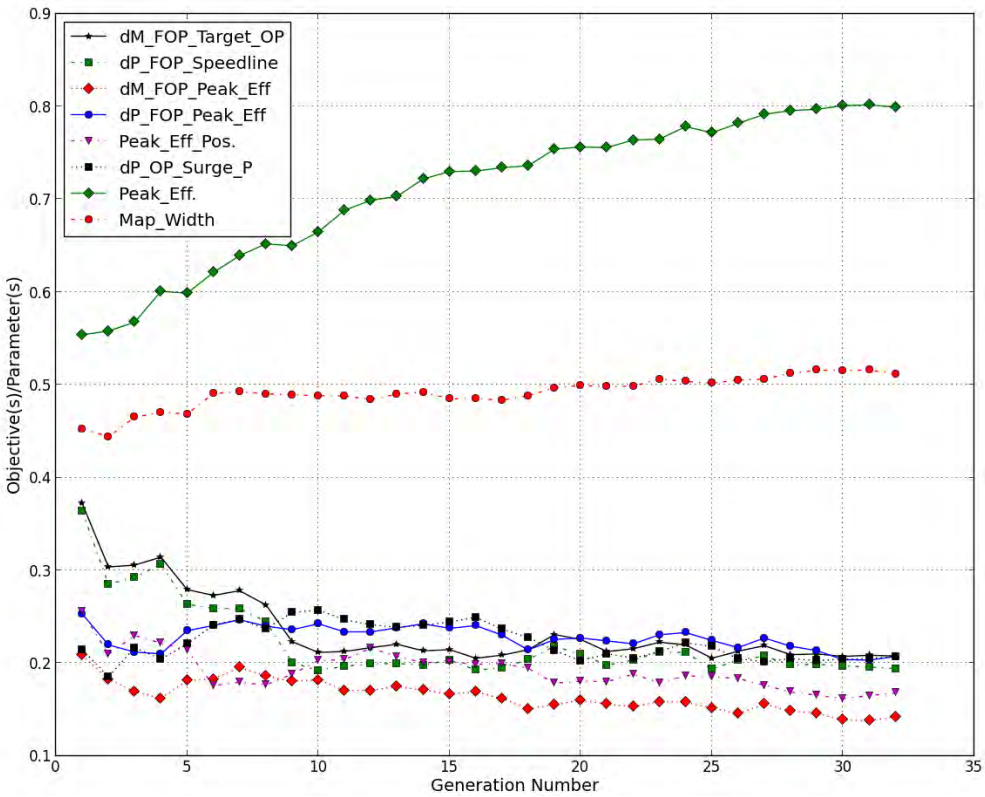

Figure 6.9 – Convergence plot showing average of objective functions per generation

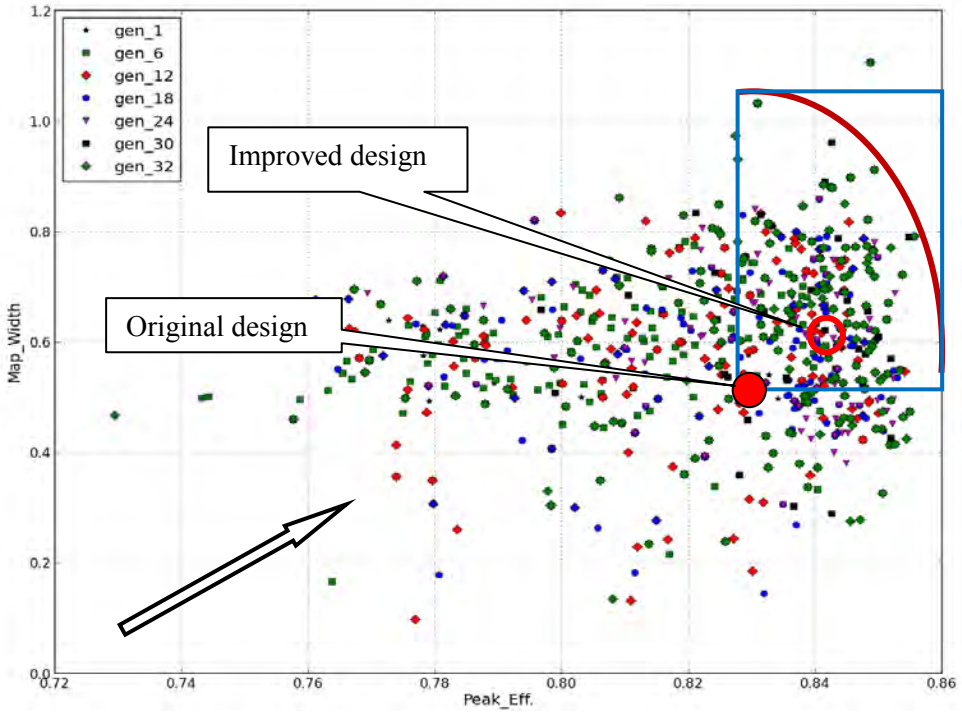

Figure 6.10 – Pareto front plot of peak efficiency vs map width

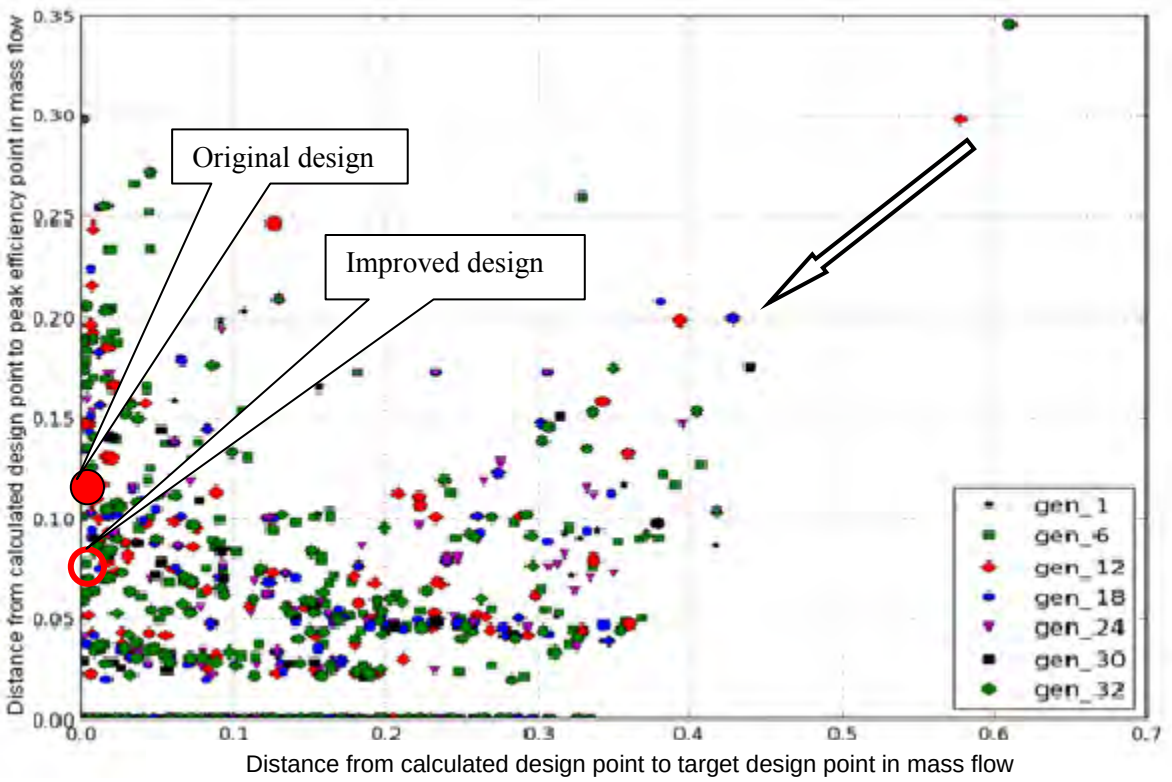

Figure 6.11 – Pareto plot of dM_FOP_Peak_Eff vs dM_FOP_Target_OP

A comparison of the calculated objective functions for the old and new design is illustrated in Table 6.6. The optimised design is better than the current design in 5 out of the 8 objectives. Objectives 1 and 2 are impossible to match exactly (i.e. achieving the exact design point mass flow) but the values calculated here gives a mass flow within 1.4% of the target value which is considered a satisfactory deviation. Table 6.6 also shows up to 1.6 points increase in peak efficiency from the old design which is substantial in the current application. In Table 6.6, the parameters for which the new design dominates the baseline design are highlighted in bold. The meridional view of old and new designs is show in Figure 6.12. The new design is longer than the previous design, but the impeller radius is kept constant so that both designs can be tested on the same test rig. The performance map of the old and new design is compared in Figure 6.13. The new design shows a significant increase in swallowing capacity on speed lines 15000 rpm, 25000 rpm, 30000 rpm and 35000 rpm. The new design also maintained the surge and choke margin on all the speed lines. At the design point of 11.4kg/s and pressure ratio of 2:1 on the 25000 speed line, there is an increase in efficiency by about 1.6 points. There is also an average of 10% increase in map width across all the speed lines. The new design improves on the old design in terms of efficiency across all speed lines. Figures 6.14 and 6.15 are plots of Mach number and velocity vectors on the blade surface for

the current design and design 3862H at the design speed of 25000 rpm and pressure ratio of 2:1. The plots show overall similarity in Mach number distribution on the blade surfaces except around main blade leading edge shroud where the current design has a larger region of higher Mach number. There is no significant difference in Mach number and velocity vector distribution in both designs. Figure 6.16 shows the 3-D shape of the baseline design and design 3862H blades. Figure 6.17 shows the model of the new design 3862H created for manufacturing purpose.

Objective No.	Description	Current Design	Improved Design
1	Distance from calculated design point to target design point measured in mass flow.	0	0.0038
2	Distance from target design point to calculated speed line measured in pressure	0	0.0037
3	Distance from calculated design point to peak efficiency point on calculated speed line measured in mass flow.	0.1163	**0.0792**
4	Distance from calculated design point to peak efficiency point on calculated speed line measured in pressure.	0.1000	**0.0752**
5	A measure of how centralised the peak efficiency is. Ideal value is 0.5	0.1000	0.0927
6	Surge safety margin	0.0476	**0.0615**
7*	Peak efficiency normalised	0.9766	**1.0000**
8	Compressor map width	0.5349	**0.6852**

Table 6.6 - Comparison of objectives

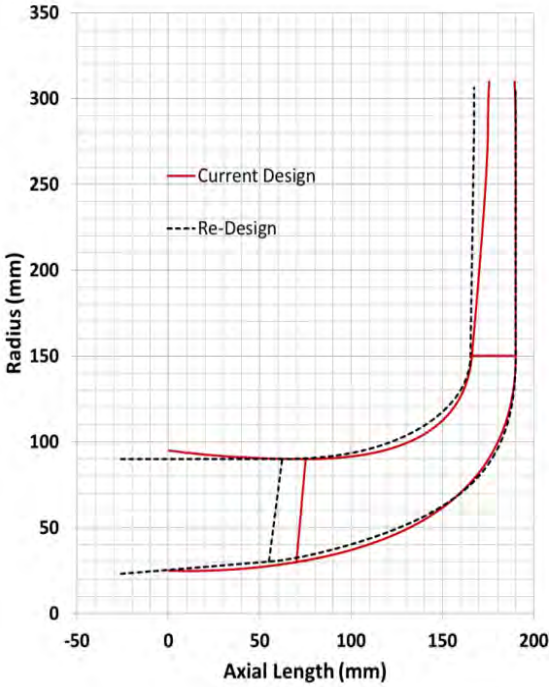

Figure 6.12 - Meridional view of current and new design

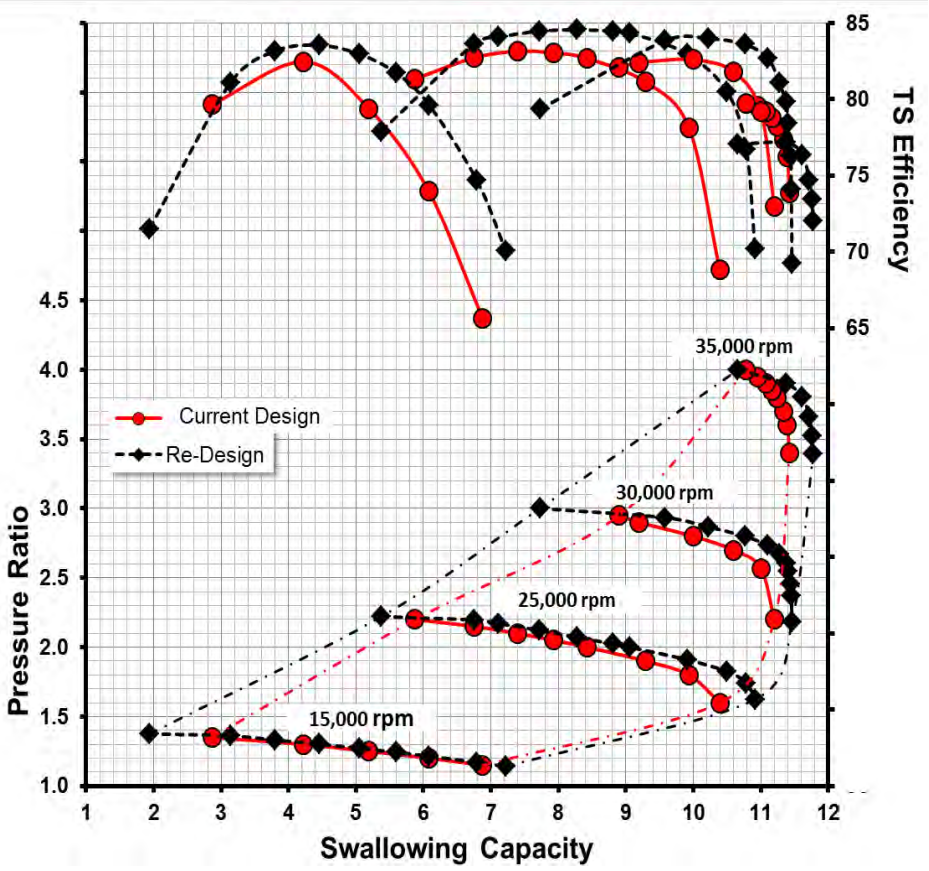

Figure 6.13 - Comparison of performance maps

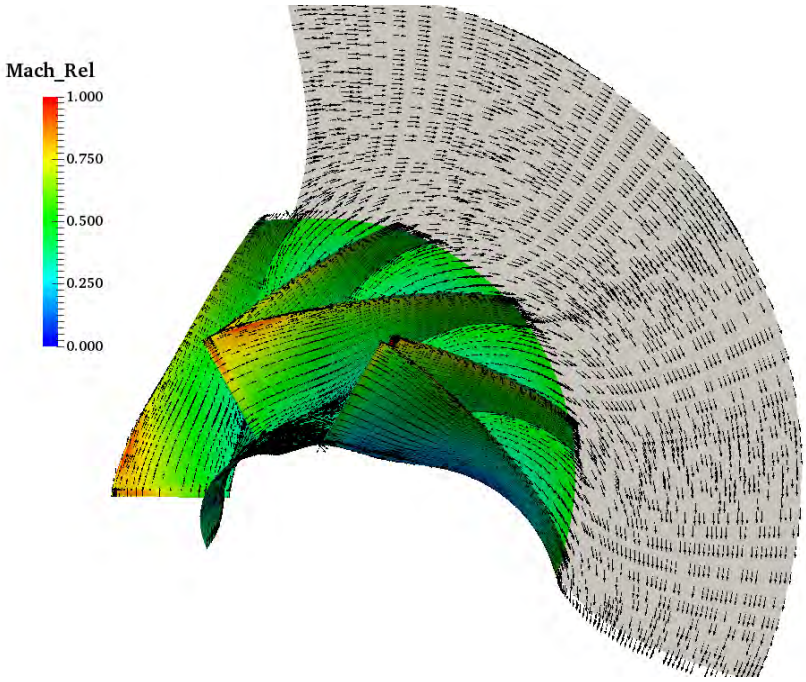

Figure 6.14 – Flow visualisation of blade and 5% span profile for the current design

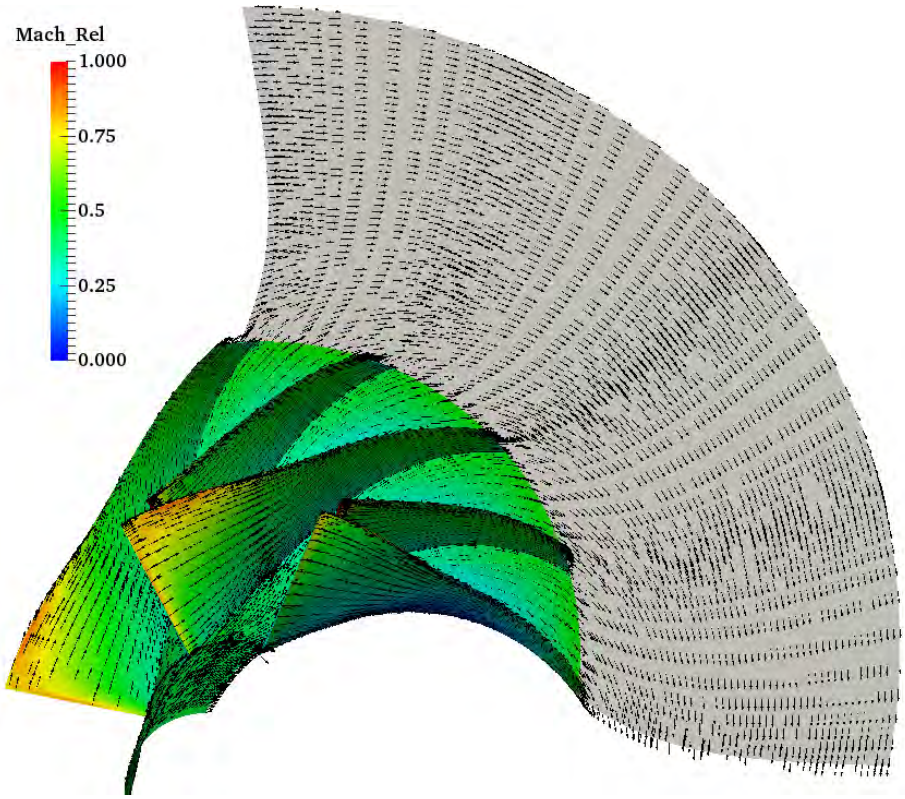

Figure 6.15 – Flow visualisation of blade and 5% span profile for design 3862H

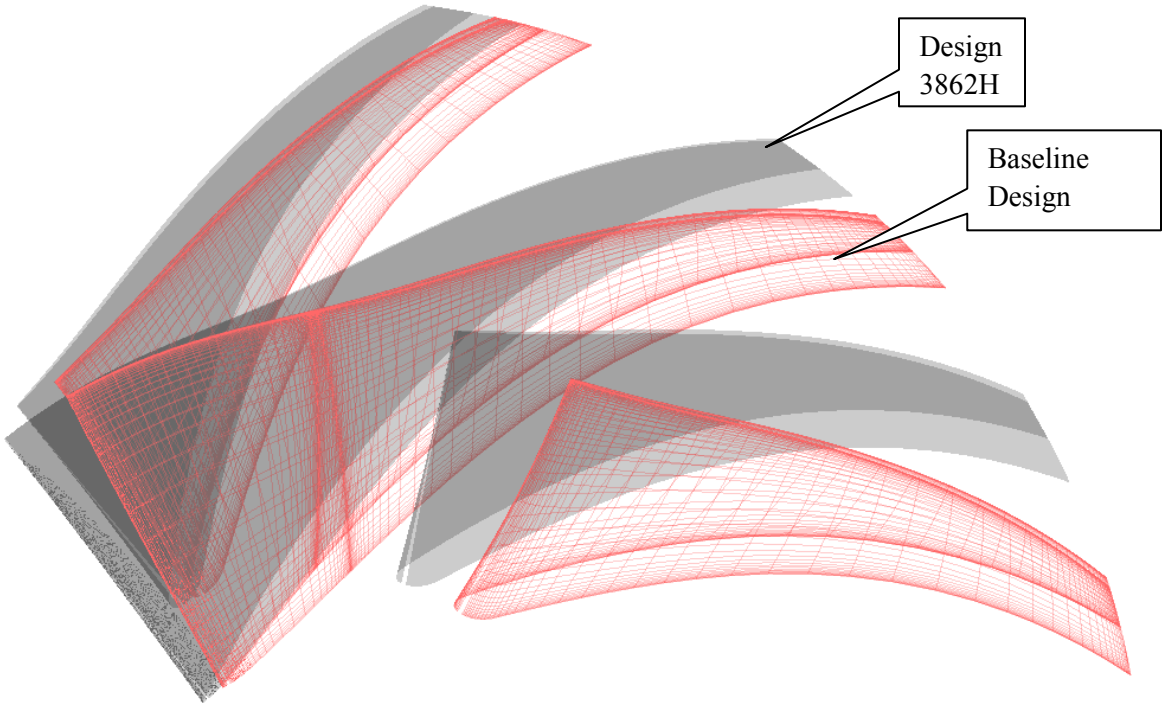

Figure 6.16 – Comparison of current design and design 3862H blades

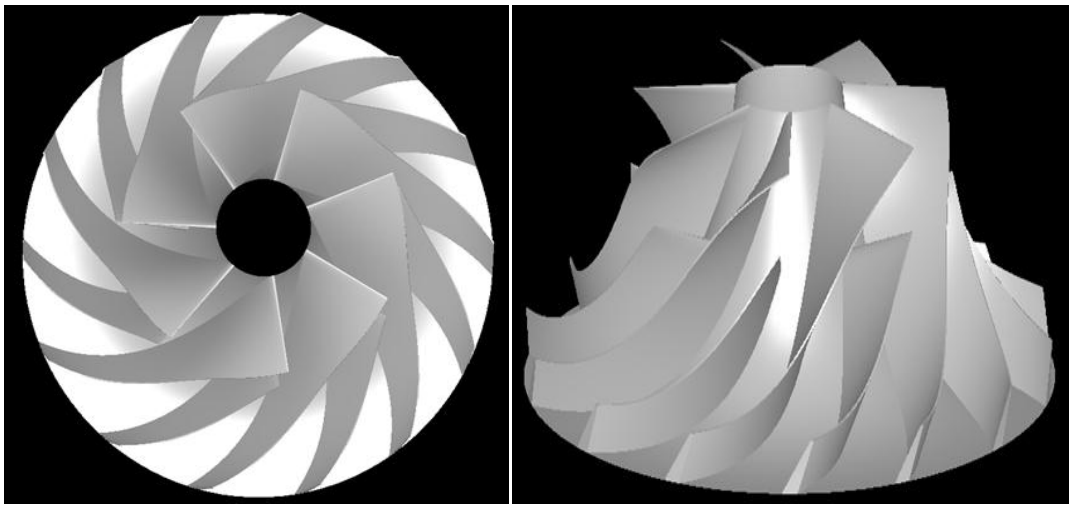

Figure 6.17 - Manufacturing model of new design

6.4.2 Optimisation 2

In the second run of optimisation calculations, the configuration settings for the 23 optimisation parameters are shown in Table 6.7. The knowledge gained from analysing log data of first optimisation calculation was used to update the parameter limits. All the parameter bounds in this optimisation run are different from optimisation 1 run.

S/N	Parameter	Low Value	High Value	Step*	Description
1	N_b	5	6	1	Number of main blades or splitter blades
2	R_{1h}	0.0299	0.030	0	Radius of the impeller hub at the leading edge
3	R_{1s}/R_{1h}	2.990	3.000	0	Ratio of shroud radius to hub radius at impeller leading edge
4	R_{1s}/R_2	0.600	0.6005	0	Ratio of impeller trailing edge radius to impeller leading edge shroud radius
5	b_2/R_2	0.165	0.168	0	Ratio of impeller exit blade height to impeller exit radius
6	L/R_2	0.799	0.800	0	Ratio of impeller axial length to impeller exit radius
7	R_3/R_2	1.890	1.891	0	Ratio of diffuser exit radius to impeller exit radius
8	b_3/b_2	0.650	0.900	0	Ratio of diffuser exit height to impeller exit blade height
9	β_0	62	66	0	Shroud leading edge blade angle. See Figure 5.3
10	β_3	50	57	0	Shroud backsweep angle. See Figure 5.3
11	σ	0	5	0	Leading edge sweep angle. See Figure 5.1
12	δ	0	10	0	Axial sweep angle. See Figure 5.1
13	θ_0	-10	0	0	Hub wrap angle correction at leading edge. See Figure 5.5
14	θ_1	0	5	0	Hub wrap angle correction at mid-meridional profile. See Figure 5.5
15	ψ	35	40	0	Rake angle. See Figure 5.6
16	H_P(1,4)	0.25	0.50	0	Location of 1st and 4th hub Bezier control point as fraction of the lines on which they slide . See Figure 5.1
17	H_P(3)	0.50	0.70	0	Location of 3rd hub Bezier control point as a fraction of the lines on which they slide . See Figure 5.1
18	S_P(1,4)	0.35	0.65	0	Location of 1st and 4th shroud Bezier control point as fraction of the lines on which they slide . See Figure 5.1
19	S_P(3)	0.35	0.65	0	Location of 3rd shroud Bezier control point as a fraction of the lines on which they slide . See Figure 5.1
20	β_1	35	48	0	Shroud blade angle at 33% of shroud meridional length . See Figure 5.3
21	β_2	38	50	0	Shroud blade angle at 67% of shroud meridional length . See Figure 5.3
22	Split_Hub	0.28	0.40	0	Splitter leading edge position at the hub as a fraction of main blade hub meridional length . See Figure 5.1
23	Split_Shr	0.32	0.40	0	Splitter leading edge position at the shroud as a fraction of main blade shroud meridional length . See Figure 5.1

Table 6.7 – Parameters limits set in DEMO for second optimisation

Step 0 means no step

Objective Functions

In the second optimisation calculations, the 8 objectives in the first optimisation are averaged to two objectives. Also, an analytical estimation of stress was introduced. It was decided to use weighted sum for the second run to make the optimisation quicker. Although there is a risk of unwanted bias of optimisation parameters associated with weighted sum, the previous optimisation run was used to narrow the search domain to reduce this risk. The estimated stress criterion was established based on wrap angle at hub and shroud near impeller trailing edge. The wrap angle of the blade at the shroud relative to the hub at the trailing edge of the impeller has a significant influence on the peak von-misses stress at the hub close to the trailing edge. The ideal case is to have the difference between the wrap angles at the hub and shroud to be less than 20 degrees. It was decided to set an ideal range of between 18 and 20 degrees (shroud wrap > hub wrap angle). This constraint was used as the stress criteria. Designs with values between 18 and 20 are assigned a stress objective of 0 (good). For designs with values outside this range, the stress objective is measured as absolute distance to the range. One of the goals of the optimisation algorithm is to find designs with stress criteria close to zero.

Based on analysis of previous optimisation run, sufficient mass flow range was achieved, so mass width was not prioritised in the weighting. A large weight is attached to previous objective 1 – closeness to target mass flow and the new stress criteria. High importance is also attached to peak efficiency as it‟s the main driver for turbomachinery design. The new objectives were split into two groups – efficiency and mass flow/stress related as outlined below. Please refer to Table 6.6 for description of objectives 1 to 8.

1) New_Objective 1 = (4 × objective 1 + 4 × stress criteria + objective 3 + objective 5 + objective 6)/11
2) New_Objective 2 = (19 × objective 7 + objective 8)/20

Optimisation Results

The optimisation is set up with 45 candidates per generation. The optimisation calculations are allowed to run for 87 generations until a Pareto front was achieved as shown in Figure 6.20. About 3700 valid compressor designs were analysed using the HTCondor cluster over 8 weeks. The normalised average of the objectives per generation is shown in Figure 6.21. It shows both objectives reduced together until about generation 50 when objective 2 start to diverge, while objective 1 continued to converge. This may be due to the weighted optimisation problem. The log file from 50th generation to 87th generation is then sorted in order to choose a compromise design. The log file is sorted by peak efficiency, compressor map

with and closeness of calculated design mass flow to target design mass flow. A compromise design (No. 2301) is chosen from generation 55 as shown in Figure 6.20. Figures 6.18 and 6.19 are 3D and meridional comparison of design 2301 and the baseline design - impeller 39. In both Figures, the current design is coloured in red. The meridional mesh distributions are overlaid in Figure 6.19.

The performance curve of the new design is compared with the existing design (referred to as impeller 39) at a rotor speed of 25000 rpm as shown in Figure 6.22. All plots in Figure 6.22 are for geometries with 1% tip gap except for „Imp_39_TBLOCK_0.5" which is a 0.5% tip gap case of the existing design. Two tip gap cases are plotted just to see the impact of tip gap on performance at the design speed using TBLOCK. The plot shows that TBLOCK captures up to 1% drop in efficiency across the speed line when the tip gap is increased from 0.5% to 1%. An interesting observation is that the performance calculated using TBLOCK with a tip gap of 0.5% closely matches the CFX case with a 1% tip gap. This could be interpreted as either TBLOCK over estimating the impact of tip clearance or CFX underestimating tip clearance impact. In all 3 cases of the current compressor design analysed, the solvers predicted the same choke mass flow. The new design 2301 shows an improvement in efficiency mostly on the right half of the performance curve when compared to the three cases of impeller 39 analysed. At least 0.3 points gain and up to 2 points gain in efficiency is observed at a given pressure ratio. Like-for-like comparison of design 2301 and Impeller 39, both analysed using TBLOCK with a 1% tip gap show about 1.4 points improvement in efficiency at the design pressure ratio of 2:1. The new design clearly offers an improvement in choke mass flow (corrected to inlet stagnation conditions) from 10.34 to 10.75. The lower peak pressure ratio of design 2301 is caused by larger slip at the impeller trailing edge. The larger slip is due to the larger backsweep angle of design 2301 compared to impeller 39, resulting in lower efficiency at high pressure ratios.

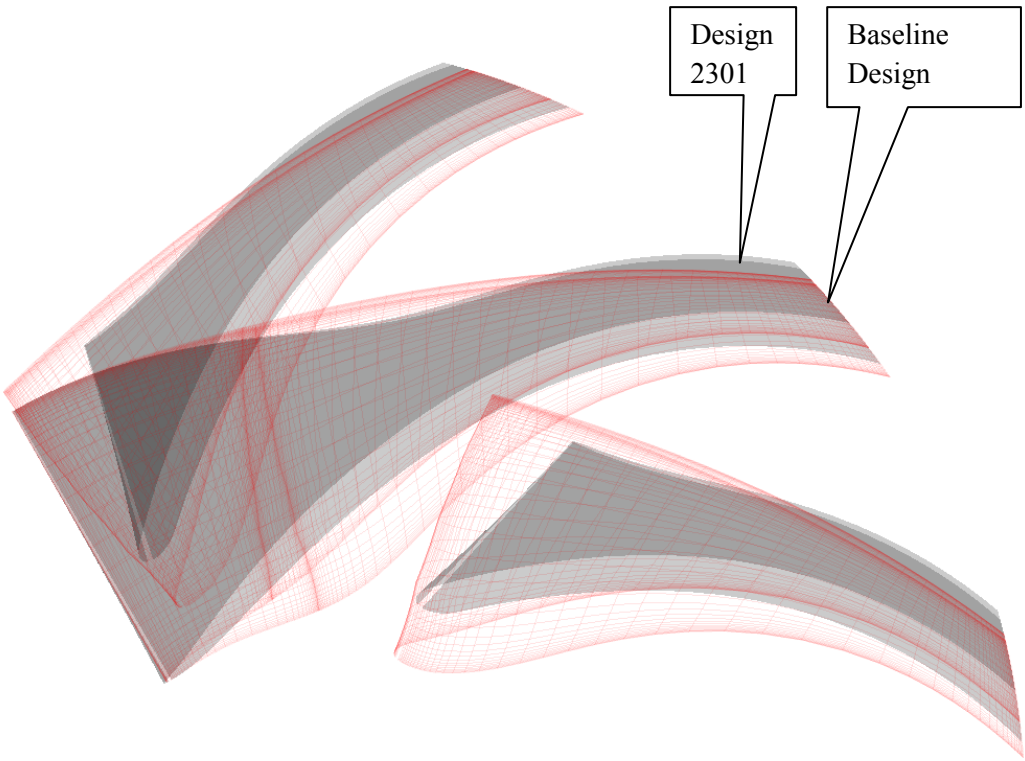

Figure 6.18 – Geometric differences between design 2301 and Impeller 39

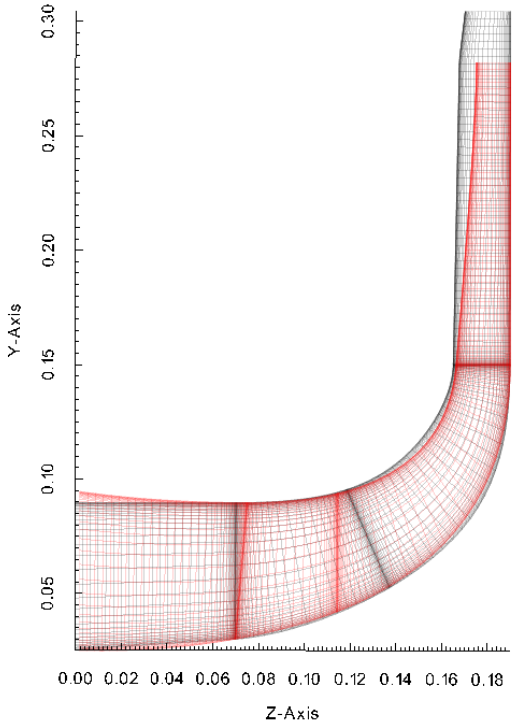

Figure 6.19 – Meridional view comparison of Impeller39 and Design 2301 with mesh overlay

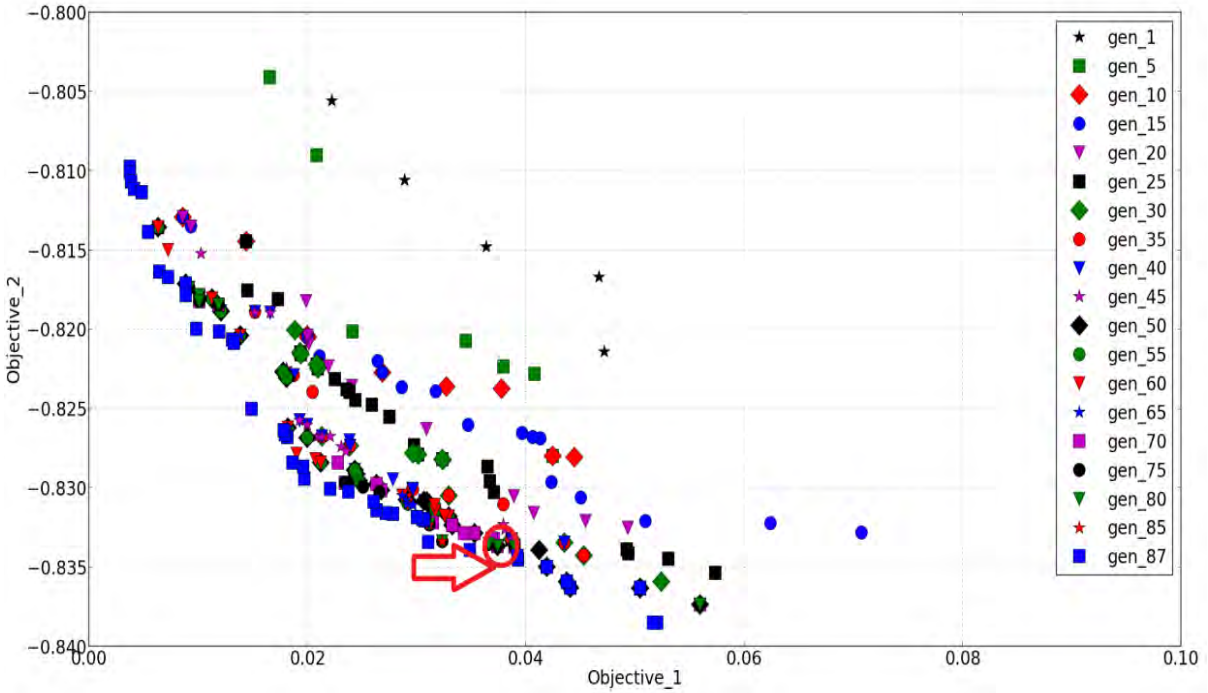

Figure 6.20 – Pareto front of the optimisation calculations

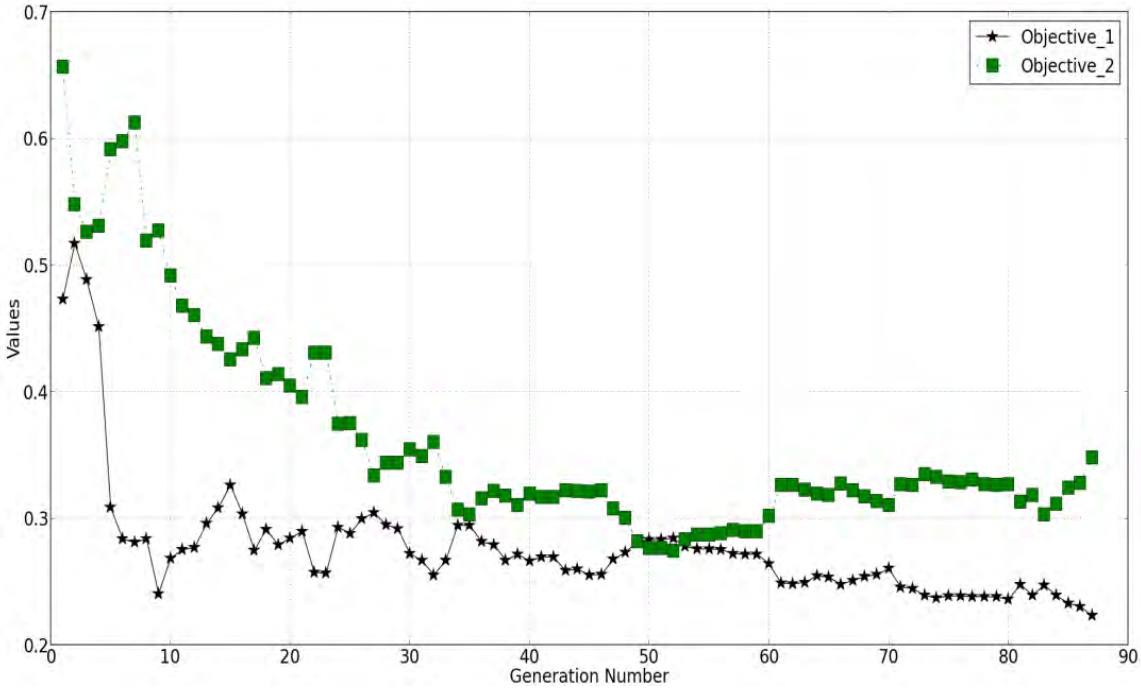

Figure 6.21 – Normalised average of objectives per generation

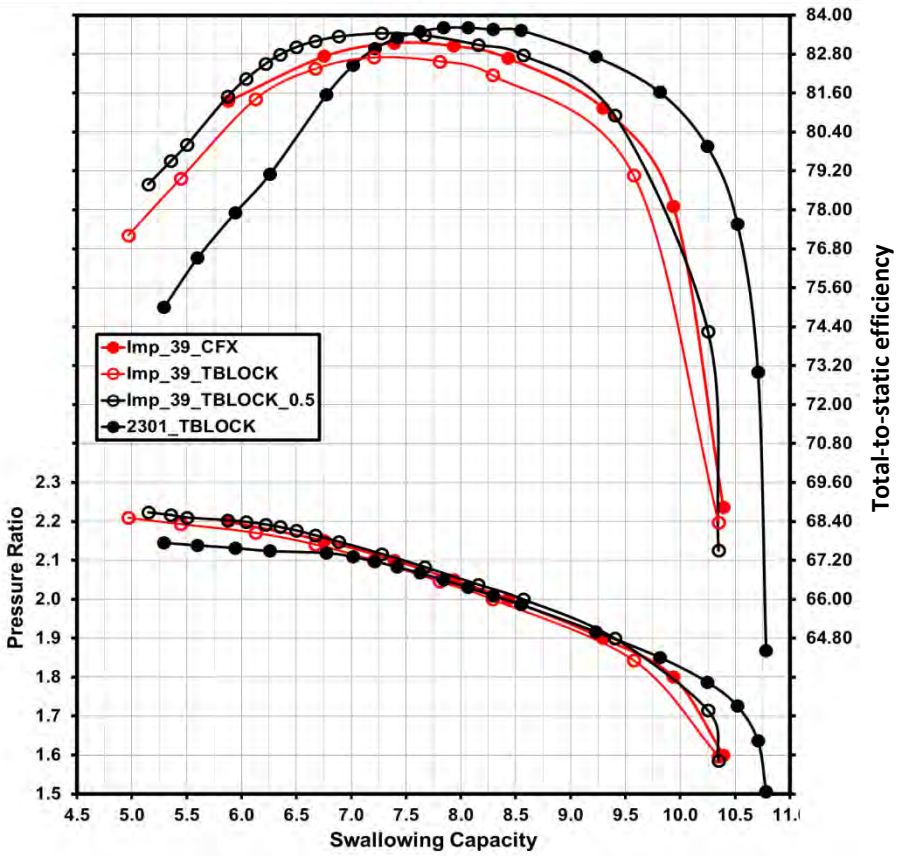

Figure 6.22 – Comparison of performance of new design with existing design

Figures 6.23 and 6.24 are relative Mach number plots on blade surface and at 5% span of design 2301 and impeller 39 (the current design) respectively. The plots show overall similarity in Mach number distribution on the blade surfaces except around at the hub of the current design where there is a larger region of low Mach number. This is an indication of separation, resulting in lower performance of the current design at the design point compared to design 2301

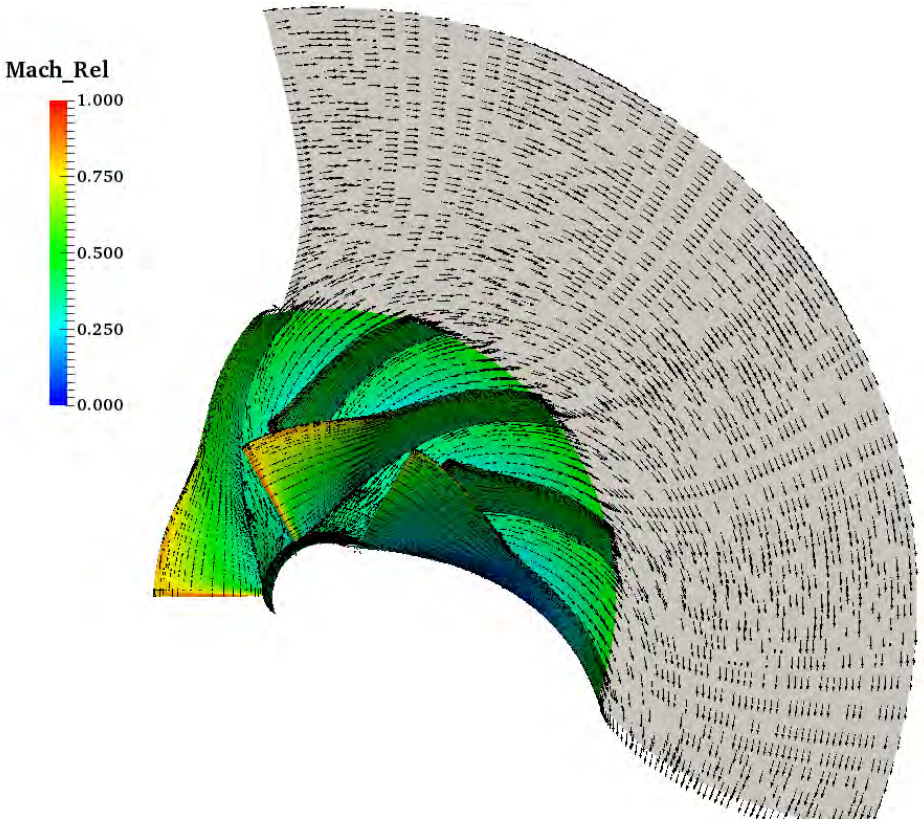

Figure 6.23 – Flow visualisation of blade and 5% span profile for design 2301

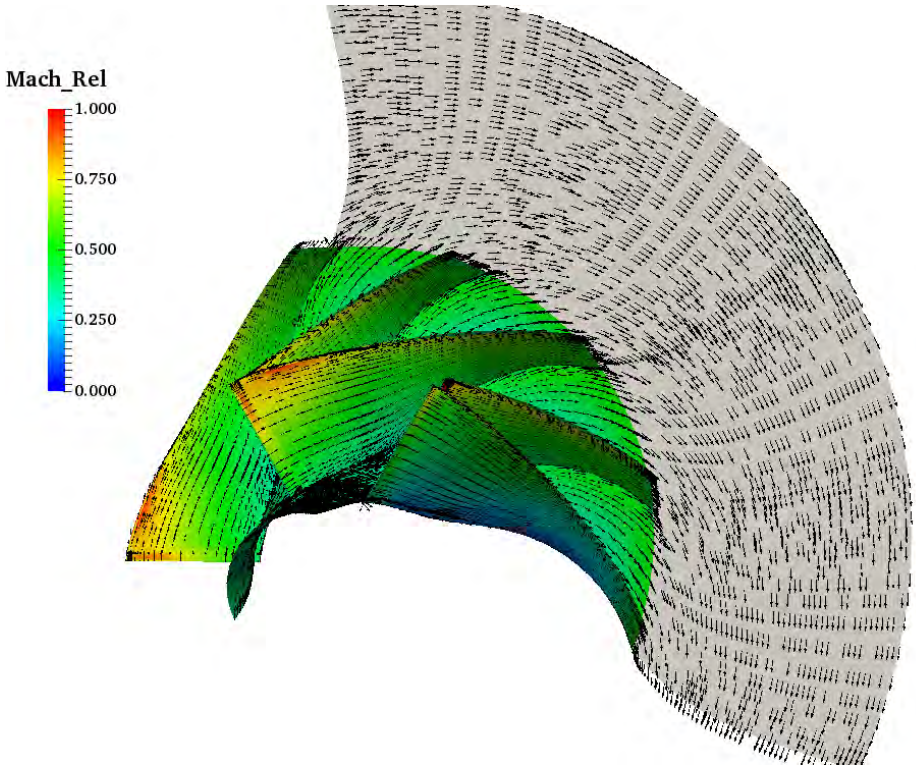

Figure 6.24 – Flow visualisation of blade and 5% span profile for impeller 39

CONCLUSION

This Chapter detailed the optimisation of the compressor in the HP stage of a two-stage turbo charger. The HTC system described in Chapter 5 was used to carry out the calculations. Two new designs were found with improvement in total-to-static efficiency up to 1.6 points and average increase in map width of 10% across all speed lines. One of the new designs has been drawn up using CAM software in preparation for manufacture. In the next Chapter, a study of the effect of impeller manufacturing undercut on compressor performance will be presented.

CHAPTER 7

EFFECT OF IMPELLER MANUFACTURING UNDERCUT ON RADIAL COMPRESSOR AERODYNAMIC PERFORMANCE

This Chapter presents a novel study on the impact of impeller manufacturing undercut on the aerodynamic performance of a radial compressor. An undercut is formed when excess material is left on the machined surface during manufacture. The radial compressors used for the study are fitted with a vane-less diffuser. The effect of undercut on the compressor flow features is analysed using detailed 3D CFD modelling and the impact on performance is quantified using a variety of statistical techniques. Various undercut height and width levels at 13 different locations on the blade surface are analysed for three choices of compressor designs. A unique sensitivity distribution for each compressor impeller is calculated and used to create a variable tolerance map on the impeller surface. Instead of using a fixed tolerance across the whole impeller surface and scrapping impeller based on a fixed tolerance limit, this approach could lead to potential savings in manufacturing cost due to relaxation of tolerance limits in certain sections of the impeller surface.

7.1 RESEARCH CONTRIBUTIONS

The following are research contributions to knowledge from the work carried out in this Chapter:

- A novel variable tolerance limit plot on the impeller surface ("heat map") is developed for the impeller designs evaluated. This template could serve as a guideline to manufacturing engineers to decide if a machined surface defect such as an undercut could result in significant deviation from design performance. This could reduce scrap rate and result in cost savings. To the author"s knowledge, this is the first 3D CFD analysis of undercut on a radial compressor impeller surface.
- Performance parameters such as peak efficiency, design point mass flow, etc was found to be more sensitive to undercut height, than to undercut width.
- The study shows that as undercut height increases, design point efficiency and target mass flow (or design point mass flow) will reduce for any impeller design. Also, the average mass flow along the speed line will reduce.

- Placing an undercut on the splitter blade may increase peak efficiency and average speed line efficiency.
- For all three cases of designs investigated, surge mass flow was determined to be the most sensitive to undercut, irrespective of the location, width and height level of the undercut. This is not so surprising because surge is an unsteady phenomenon in turbo-machinery where the flow separates rapidly.
- The study shows that a highly optimised design is more sensitive to undercut, as in the case of the optimised design investigated,
- Every compressor impeller design has its own unique sensitivity distribution depending on its shape and operating conditions, hence it is important to have unique screening template for each new compressor design.

7.2. INTRODUCTION

During flank milling of centrifugal compressor impellers, it is important to avoid errors due to tool trajectory or tool geometry that can reduce the quality of surface finishing. Tool trajectory errors due to a power cut can result in an undercut or an overcut. Tool geometry errors due to using a blunt cutter can result in an undercut. Also, a newly fitted cutter may initially remove excess material, resulting in an overcut. More so, overheating of the CNC machine cabinet can result in a sudden stop, causing localised deep cuts on the impeller surface. Errors during 5-axis milling can be due to many factors such as tool deflection, tool wear, feed drives vibration, tool path programming error and so on [10]. Examples of errors common during 5-axis milling include undercut, overcut and surface roughness [10].

Undercuts were chosen for study in this research because it results from flank milling which is widely used to manufacture turbocharger compressor impellers. In addition, flank milling is used to machine impellers at Napier, and undercut accounts for about 55% [Internal QA Audit estimate] of manufacturing defects encountered. More so, an undercut is much easier to represent on an impeller surface by modifying the CAD file, compared to, for example a dent on the hub profile. Scrapping impellers due to a manufacturing error during 5-axis flank milling can represent a significant cost. The current practice in industry is to scrap impellers where the designed surface deviates from the machines surface by a fixed tolerance limit. This thesis presents a technique for reducing impeller scrap rate by quantifying sensitivity of compressor performance to undercuts on various locations on the impeller surface after the design phase but before manufacture, and passing impellers below an average sensitivity threshold, leading to potential reduction in manufacturing costs.

Five-axis flank milling computer numerical controlled (CNC) machines are commonly used during the manufacture of aerospace parts and turbo-machinery parts such as turbine impellers and compressor impellers. Compared to 3-axis CNC machines where a collision between the cutting tool and impeller is common, 5-axis milling provides better control of the cutting tool there by reducing collisions [11]. Flank milling type errors can be categorised into two groups – error due to tool trajectory (e.g. overcut, undercut, surface roughness) and error due to tool geometry (e.g. tool deflections, tool energy, flank forces) [10]. 5-axis flank milling of centrifugal compressor impeller blade can introduce geometric variability to the blade. This variability can lead to reduction in performance or sometimes rejection of the manufactured impeller if the variability is outside of the tolerance limit for the design [12]. It is therefore necessary to make "robust" compressor designs - where there is no significant change in compressor performance due to deviation between the designed surface and machined surface. Taguchi [80] defined a robust design as a product or design whose performance is minimally sensitive to factors causing variability, for example design input parameters or environmental factors affecting the designed product when in use. This variability must be at the lowest possible cost for the design to be robust.

Designing compressors to be robust to manufacturing variability during the design phase will require several thousands of CFD calculations to model the effect of geometric variations. Due to the computational cost of this approach, it is not explored further. Instead, a methodology for quantifying the sensitivity of designed compressors to the presence of an undercut is presented. Undercut parameters are chosen to be below and above the existing tolerance limit for the scale of compressors being investigated. The tolerance limit for the size of compressor investigated is 0.1 mm; while undercut height levels of 0.075, 0.1, 0.25 and 0.6 mm are investigated.

7.3. LITERATURE SURVEY

Several researchers have developed methods for quantifying the sensitivity of centrifugal compressors to manufacturing variability and designing them for robustness to manufacturing variability. A review of literature in this subject showed that previous researchers have studied manufacturing variability in centrifugal compressors as either geometric deviations [12, 81, 82, 83, 84] or surface roughness variation [83, 85, 86] due to the manufacturing method employed.

Eric A. Dow and Qiqi Wang [12] developed a sensitivity analysis methodology for finding an optimal blade design and distributing the manufacturing tolerances across the blade surface. They used a gradient based optimisation scheme to determine the optimal geometry. They modelled the manufacturing

variability as a Gaussian random field with non-stationary variance. The statistical performance of the compressor blade system taking into account the manufacturing variability was evaluated using the Monte Carlo method. They found out that enforcing strict tolerance near the leading edge helps to reduce the mean loss in performance. This finding is consistent with standard practice in industry [12].

A Javed *et al.* [81] carried out a sensitivity analysis on a micro turbine centrifugal compressor using a 1-D model and a detailed CFD analysis by varying 8 geometric parameters individually within specific limits to understand their influence on efficiency and pressure ratio. They also performed a Monte Carlo simulation using the 1-D model to access the variability of efficiency and pressure ratio to simultaneous random deviations in input geometric parameters from the nominal values. They identified blade thickness, impeller radius, impeller exit blade height, tip clearance, back sweep angle and shroud radius as the main contributors to sensitivity.

A Javed *et al.* [82] used a 1-D analysis model to develop a simple methodology to study the effects of geometric variations on the performance of a micro turbine centrifugal compressor. They extracted geometric information and tolerances to carry out the performance analysis within the permissible limits for manufacturing. Their analysis showed that increasing impeller tip clearance results in a drop in efficiency, increasing back sweep angle increases efficiency and stresses, but reduces the pressure ratio. They also found that increasing the blade height leads to a significant increase in blade bending stress, while increasing the impeller exit radius increases the pressure ratio and stresses, but drops the design point efficiency. Their methodology helped to specify allowable geometrical parameters and variations permissible based on the effect on performance.

Andrae Panizza *et al.* [83] used a sparse grid polynomial chaos expansion approach to quantify the variations in a centrifugal compressor performance due to changes in design parameters. They compared the results with a Monte Carlo simulation approach and achieved similar results with much lower computational effort. A 1-D model and a 2-D blade-to-blade and through flow code was used to analyse the compressor geometry. They varied 13 independent variables (including surface roughness) at the same time to quantify the uncertainty of the compressor performance in the presence of geometric variability.

A. Javed *et al.* [84] used a response surface method (RSM) surrogate model based on a space-filling Latin hypercube set of designs to identifying critical geometric parameters that affect the performance of a centrifugal compressor impeller with a view to optimising it for robustness to manufacturing uncertainties. They used Monte Carlo simulation to quantify uncertainties propagated by changing geometric

parameters such as back sweep angle, blade thickness, blade height, tip clearance etc. Their results reveal four parameters that have the largest influence on performance – tip clearance at the inlet and outlet of the impeller, blade thickness and impeller exit radius. They then used a multi-objective optimisation approach based on a multi-objective optimisation algorithm (MOGA) to attain a compromise between performance and robustness of the design.

A. Javed and E. Kamphues [85] performed a sensitivity analysis study to evaluate the impact of surface roughness on performance and manufacturability of a mass produced turbocharger centrifugal compressor for automotive application. They carried out the sensitivity analysis study in three stages by varying the surface roughness. The first study looked into the impact of roughness over a speed line, while the second study investigated the compressor components (impeller, diffuser and volute) roughness separately with a view to identify which component has the most impact on performance. The third study then looked at surface roughness at various sections of the volute geometry. Their result shows that the impeller and vane-less diffuser carry the most sensitivity to deviations in surface roughness and therefore require more regulation during manufacture to prevent unnecessary performance variability. Their study also showed that the volute has the smallest impact on performance deterioration.

William T. Cousins *et al.* [86] used experimental and CFD techniques to investigate the effect of surface roughness on the performance of a shrouded centrifugal impeller. They compared the performance of cast impellers and machined impellers with smoother surface. Their result showed that the rougher cast impeller had a lower peak efficiency compared to the machined impeller; about 1.8% drop.

Nathan Pash *et al.* [87] applied the Taguchi Method [80] to evaluate the impact of centrifugal impeller manufacturing methods, manufacturing tolerances, and quality control on impeller efficiency and overall compressor performance. They evaluated two compressor rotors manufactured using different techniques. The first using two-piece welded impellers and the second with one piece impeller via Electrical Discharge Machining (EDM) [87] and Electrochemical Machining (ECM) [87, 88]. They used EDM and ECM techniques to improve quality where a 5-axis mill machine could not be used due to practical limitations of machine tool head accessibility, for example impellers with very narrow tip width. Their findings suggest a significant improvement in individual impeller performance as well as overall performance for the single piece impeller compared to the two-piece impeller. They found out that blade angle distribution is a key parameter to be controlled to avoid performance discrepancies. They also found out that blade height, welding distortion and blade thickness affected only the pressure coefficient. Surface roughness was not investigated in their study.

Tomoki Kawakubo *et al.* [89] applied experimental and CFD techniques to investigate the effect of surface roughness on the performance of a centrifugal compressor. They roughened the surface of the impeller by sand-blasting it. They carried out the CFD calculation with FLUENT 6.3, using a high Reynolds number turbulence model with wall function correction to model surface roughness. Their results showed good agreement in performance degradation at design and off-design point between the experimental and CFD results.

Shin-Hyoung Kang *et al.* [90] investigated the effect of surface roughness on the performance of an axial compressor and an axial turbine. They did not employ any sensitivity analysis methodology in their calculations, but did a comparison between a smooth geometry and different levels of roughness on a compressor blade. They modelled roughness in the compressor and turbine using the wall function option in the CFD code TascFlow. They found that surface roughness in the multi-stage axial compressor reduced the efficiency and increased pressure loss. They also found that work transfer increased in the turbine as surface roughness was introduced, while efficiency also drops with increase in surface roughness. It is worth mentioning that this author did not carry out his analysis from a manufacturing point of view.

Dirk Buche *et al.* [91] carried out multi-uncertainty analysis of the impact of surface roughness on different components on the performance of a centrifugal compressor. The goal of their study was to verify the robustness of new compressor designs towards operational and geometric uncertainties. They used a response surface method in combination with the i-optimal design approach to generate sample cases which are simulated with a commercial CFD RANS solver. Their analysis showed a decrease in efficiency by about 2% for the given operating point on the rough impeller surface for roughness values above the limit of a hydraulically smooth surface.

R. Spence *et al.* [92] carried out a CFD parametric study of geometric variations on the pressure pulsations and performance characteristics of a centrifugal pump using the Taguchi method to reduce the number of transient analysis to 27. They also used Taguchi's post-processing analysis methods to rank the relative importance of four geometric parameters varied at 15 different locations and at 3 flow rates. The four geometric parameters investigated are - the cutaway gap, vane arrangement, scrubber gap and side wall clearance. Their result showed that the cutaway gap and vane arrangement are the two strongest influences on the pressure pulsations.

Victor E. Garzon *et al.* [93] used a probabilistic methodology based on principal-component analysis (PCA) of blade surface measurements to quantify the impact of geometric variability on axial compressor performance. The probabilistic blade geometry model was then solved using a compressible CFD solver and the impact of passage loss and blade turning on performance was estimated using a Monte Carlo simulation. They also developed a 1-D model based on results from the CFD analysis to quantify the impact of blade variability on compressor efficiency and pressure ratio. Their methodology was applied to a flank-milled integrally bladed rotor. Their study showed that compressor efficiency can reduce by up to 1% due to manufacturing variability in the blade passage.

Apurva Kumar *et al.* [94] applied a Bayesian Monte Carlo technique to the robust design of a compressor blade in the presence of manufacturing variability. To model manufacturing uncertainties, they used a parametric geometry model to describe geometry variations within a given tolerance band around the nominal geometry. They used surrogate model training initialised with a Latin hypercube (LHC) sample of 100 candidates which was analysed using CFD and a Gaussian stochastic process emulator trained using the initial 100 data sets. A Non-dominated Sorting Genetic Algorithm-II (NSGA-II) was then employed in conjunction with the trained Gaussian stochastic method to search the entire design space. They then used a Bayesian Monte Carlo technique for populations in each generation to evaluate the performance statistics. Their result showed that the robust blade has substantial improvement in robustness against manufacturing variations in comparison with the deterministic optimal blade.

Apurva Kurma *et al.* [49] used a novel geometric parameterisation technique to represent manufacturing variations within tolerance bands. They used a LHC DOE technique to generate the initial training data set. The initial geometry data set was then meshed and solved using CFD and Gaussian stochastic process models were used as computational surrogates based on the high-fidelity CFD results. They then used a Bayesian Monte Carlo system based on the surrogate model to obtain the statistics of the performance at each design point. A multi-objective optimiser was then used to search the design space for robust designs. A robust design was found to be considerably less sensitive to manufacturing variations as compared to the deterministic optimal design.

The study presented in this Chapter concerns the impact of an undercut on the surface of a radial compressor impeller on its performance. The literature survey showed that previous research to understand the effect of manufacturing variability on the centrifugal compressor performance treated manufacturing variability as either deviations in geometric parameters or surface roughness and did not address the effect of undercuts. More so, some of the research in this area have used less accurate 1-D

models to evaluate the effect of manufacturing variability on centrifugal compressor performance. This Chapter presents a study that quantifies the sensitivity of radial compressors to impeller undercut using more accurate 3-D CFD simulations. To the author‟s knowledge, this is the first time a study on the effect of impeller undercut on radial compressor performance has been carried out using 3-D CFD analysis.

7.4 PROBLEM STATEMENT

The study on the effect of undercut on compressor performance presented in this Chapter is not aimed at designing the compressor (impeller) to be robust i.e. studying the effects of undercut during the automatic optimisation process, as this will be too expensive computationally. Instead the work in this Chapter focuses on developing a tolerance template of the impeller surface, unique for each compressor design. Compared to current practice in the industry where a fixed tolerance limit is set for a range of compressor designs irrespective of location of manufacturing defect on the blade surface – leading edge, suction side, pressure side, etc., this Chapter contributes a variable tolerance limits distribution at different locations on impeller surface unique to every compressor design. The manufacturing error presented in this Chapter focuses on undercuts – where there is excess metal on the machined surface compared to the design surface. This type of manufacturing error can occur during 5-axis flank milling of centrifugal compressor impellers [10] and accounts for about 55% of manufacturing defects at Napier. During flank milling, the long surface of the cutter is used to remove material from a block of metal to form the blade passages. This is different from point milling where the circular tip of the cutter is used to remove material. Flank milling of an impeller blade is depicted in Figure 7.1, while Figure 7.2 depicts an undercut and overcut, and tool path trajectory during flank milling.

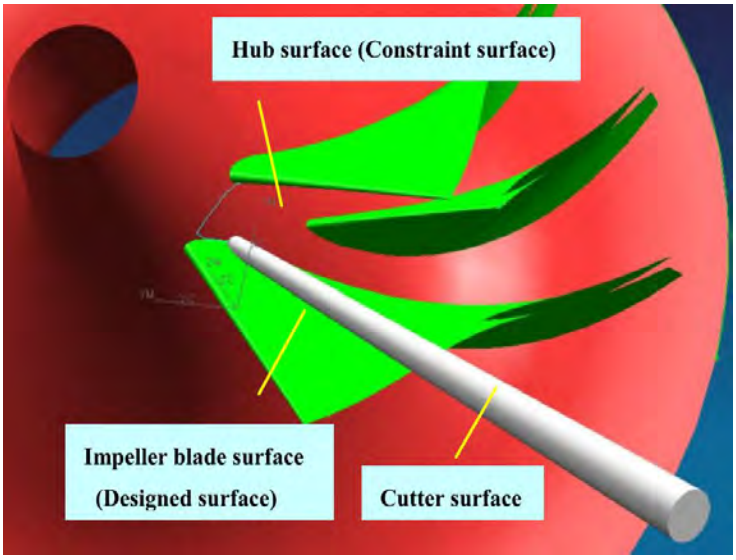

Figure 7.1 - Flank milling of an impeller [95]

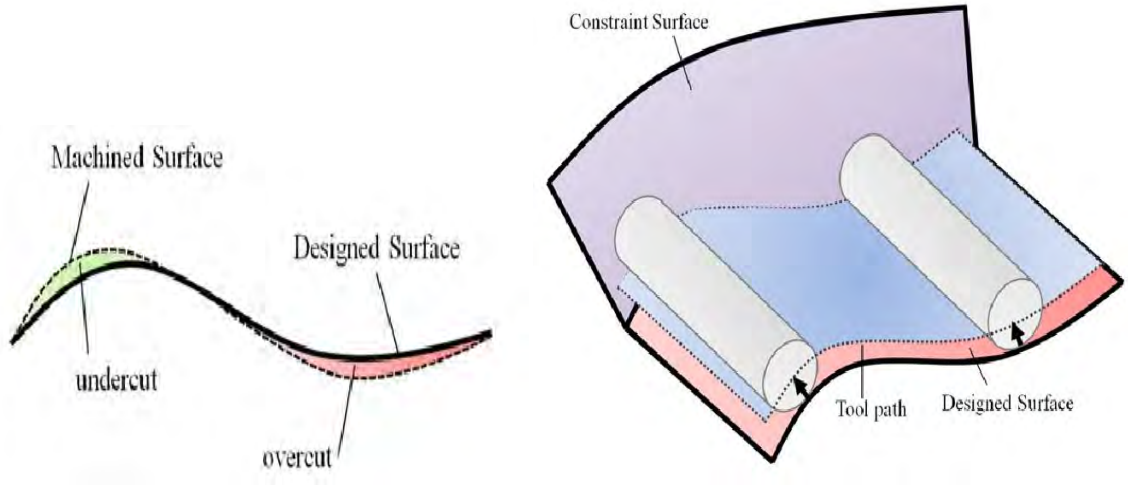

Figure 7.2 - (a) Example undercut and an overcut (b) illustration of tool path trajectory [10]

7.5 METHODOLOGY

Practical replica of impeller undercut is created on an impeller blade by modifying the CAD geometry file to include an undercut. An existing in-house computer program at Napier is used to create an undercut on the impeller surface by modifying the CAD geometry file. Percentage deviation of compressor performance parameters such as peak efficiency, design mass flow, compressor map width, etc due to an undercut is calculated using CFD analysis. The compressors analysed in this study are fitted with vane-less diffusers. The range of values for the undercut parameters were carefully chosen so that an existing tolerance limit of 0.1 mm is within the range of undercut height levels investigated. Figure 7.3 depicts an undercut width and height on an impeller blade surface. Tables 7.1 to 7.3 show the range of values for the undercut parameters. Table 7.1 shows undercut height levels measured in mm. An undercut of height 0.075 mm was chosen to have a value below the set tolerance limit of 0.1 mm and large enough to be visible in the geometry. It can be classed as a localised poor surface finish. The shroud blade thickness for the range of impellers studied during this research is about 2 mm. This imposes a limit of maximum size of undercut feasible at the shroud to be less than half of the blade thickness at shroud. Also, to capture a reasonable change in sensitivity, it was decided to have height levels of at least twice the previous step. For these reasons, the height levels of 0.075, 0.1, 0.25 and 0.6 mm are investigated. Table 7.2 shows undercut locations described as fraction of impeller meridional length measured from leading edge to trailing edge. For example 0.1 refers to 10% of meridional length measured from leading edge. Locations on pressure side of the blade are represented as negative values. More undercuts are placed towards the

leading edge of the impeller because of higher Mach numbers in that area. Table 7.3 shows undercut widths described as fraction of impeller meridional length. Undercut width are chosen based on typical widths encountered in industry. The impact of undercut on the compressor performance is quantified for various combinations of undercut width and height levels. The data is then used to generate an undercut tolerance map at different locations on the blade surface.

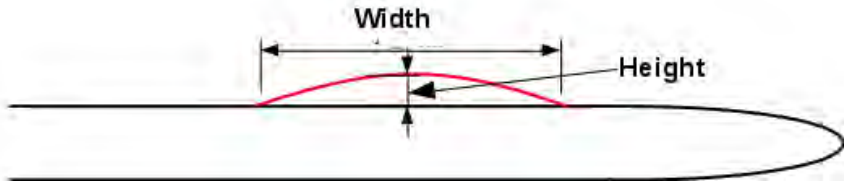

Figure 7.3 – Illustration of an undercut

Level 1	0.075 mm
Level 2	0.10* mm
Level 3	0.25 mm
Level 4	0.60 mm

Table 7.1 - Undercut heights (in mm)
current tolerance limit at Napier

Pressure Side Locations (as fraction of impeller meridional length*)						LE	Suction Side Locations (as fraction of impeller meridional length*)					
-0.8	-0.6	-0.4	-0.3	-0.2	-0.1	0	0.1	0.2	0.3	0.4	0.6	0.8

Table 7.2 - Undercut location positions
PS: Pressure side, LE: Leading edge, SS: Suction side
**Measured from leading edge to trailing edge*

Level 1	0.01
Level 2	0.02
Level 3	0.5
Level 4	0.1

Table 7.3 - Undercut widths as fraction of imepeller meridional length

7.5.1 Choice of Candidate Compressors

Three compressor geometries are evaluated during the study as detailed in Table 7.4. An existing HP compressor design at Napier – NAP and an optimised HP compressor design 3862H obtained from the optimisation phase of this research are selected. Both compressors are designed for the HP stage of a two stage turbocharger with an inlet stagnation pressure of 350000 Pa. A third design, ADT [96], which is geometrically dissimilar to designs NAP and 3862H is selected from available literature. The ADT compressor is a mixed flow compressor (the diffuser is inclined away from the radial direction) as depicted in Figure 7.4. In addition, the ADT compressor is not a HP compressor and it has an inlet stagnation pressure of 100000 Pa. A tolerance limit of 0.1mm is used to access the quality of compressor impellers about the same size of the chosen designs. Design mass flow, pressure ratio and operating speed of the selected designs is summarised in Table 7.5. The meridional view of all three designs is shown in Figure 7.4. The overarching idea of using reference geometry from the literature is to apply the undercut study on a geometrically different compressor designs to establish robustness of the method.

Design Name	Description
NAP	Napier‟s current HP compressor design modelled using ANSYS BladeGen
3862H	Optimised design. Geometry modelled using in-house CAD program
ADT	Advanced Design Technologies (ADT) compressor design obtained from literature.

Table 7.4 - Description of compressors analysed.

Design Name	Design Mass Flow (kg/s)	Design Pressure Ratio	Operating Speed (RPM)
NAP	10.7	2:1	25000
3862H	11.4	2:1	25000
ADT	2.3	2.2:1	40000

Table 7.5 – Design conditions of compressors analysed

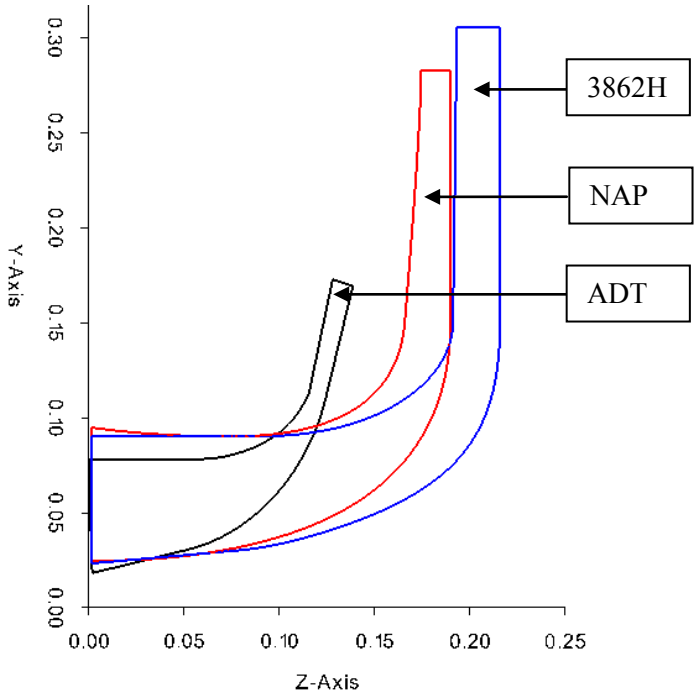

Figure 7.4 - Meridional view of the three compressors

7.5.2 ADT Geometry Validation

The geometry data for the ADT design obtained required significant pre-processing before it was usable. A program was written in C++ to create hub to shroud .curve files compatible with ANSYS BladeGen. The output points file for ADT design did not have the-same number of points at different layers from hub to shroud, so a cubic spline interpolation is used to create equal number of points at the various layers. The points at the layers are then joined together to form the profile curve that defines the blade in 3D. The newly created geometry is analysed using a fine mesh settings with 600000 cells. A uniform tip clearance of 4% is used for the calculated geometry, while the reference geometry has a variable tip clearance varying from 3% to 5% from inlet to outlet. The calculated geometry showed similar trend with the reference geometry as shown in Figure 7.5. The differences in mass flow and efficiency at the rotor speed of 40000 rpm can be attributed to the geometric differences introduced while cleaning the raw data file. Also, different solvers were used to analyse the geometries. The reference design was analysed using the TurboDesign suite [96] on a 880000 cells mesh, while the calculated geometry was solved using TBLOCK [6]. Since the overarching idea of using reference geometry from the literature is to apply the undercut study on a geometrically different compressor design to establish robustness of the method, the difference between the designs shown in Figure 7.5 is not a source of concern.

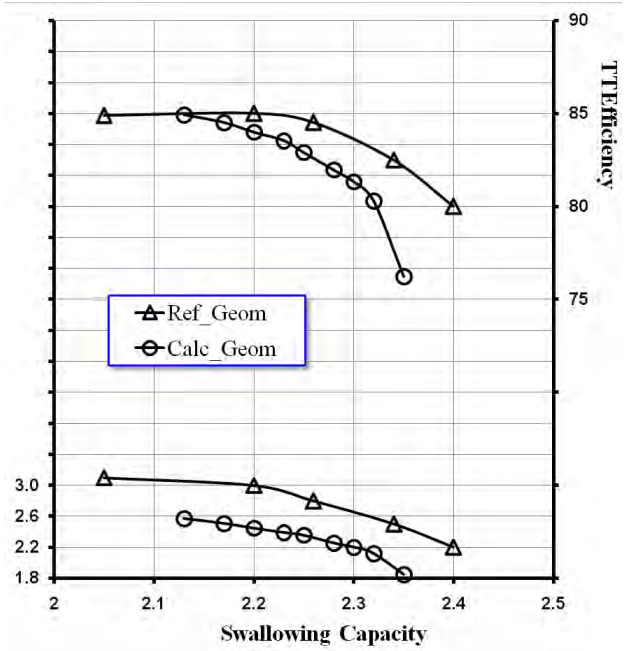

Figure 7.5 – Validation of calculated geometry

7.6 CAE TOOLS

In this study, the engineering design optimisation system used in the optimisation phase is also used but with a slight modification. A computer program for creating an undercut on the surface of a compressor impeller by modifying the CAD geometry file is included in the system. The program is used to modify the CAD geometry before meshing. Also DEMO is removed from the new set-up as automatic optimisation is not required. TBLOCK CFD solver [6] and ParaView [7] are also used to calculate the flow and post-process the results respectively. The mapping algorithm is modified to run the undercut creation program, and to not run the CAD program in instances where an external geometry file is being investigated. The approach used to achieve the objectives of fast, low-cost and reliable computing system in the optimisation phase also applies to this phase. All tools used in the undercut study are command line driven, hence easy to deploy on the HTCondor cluster. The HTCondor cluster is expanded from 8 machines (32 cores) to 17 machines (44 cores) for the undercut study. The undercut creation algorithm is used to place undercuts of various height and width at different locations on the impeller blade surface. 3D CFD calculation is used to calculate percentage change in eight performance parameters and compared to the same compressor geometry without an undercut on the impeller.

7.6.1 CAD Program

The CAD program used for this analysis depends on the source of the compressor geometry being analysed. For example the geometry file for design NAP is already created before this study using ANSYS BladeGen [30], while the geometry file for design ADT is obtained from literature with further pre-processing. The geometry of the ADT design was extracted from the CFD result file of an ANSYS simulation of the design and further processed. Design 3862H geometry is created using the CAD algorithm developed during the multi-objective optimisation phase of this research [13].

7.6.2 Undercut Creation Program

The undercut analysed in this study is described in Figure 7.2 as illustrated by [10], the type of manufacturing error that is due to tool deflection, tool wear or error in tool trajectory. The undercut height is specified normal to the blade surface at the location of choice. The width of the undercut is calculated tangential to the blade surface, 50% in both directions from the centre of the undercut as shown in Figure 7.3. A cubic spline is used to connect the base points of the undercut with the tip of the undercut to form the complete undercut surface as shown in Figure 7.3. The undercut creation algorithm allows the user to specify the meridional position of the undercut at the hub and shroud independently. It also allows the user to place one undercut on the main and splitter blade at the same time.

7.6.3 Mesh and Solver Settings

The fluid computational domain is meshed using Napier‟s in-house meshing code described in Section 5.3. The mesh used for the undercut sensitivity study consists of 600000 computational cells as detailed in Table 7.6. Figure 7.6 shows example representation of undercut features by the mesh used. The blue outline represents the geometry without and undercut, while the red mesh outline represents the undercut geometry. Figure 7.6a and 7.6b show undercut at the leading edge at hub and shroud respectively. Figure 7.6c shows an undercut on the pressure side of an impeller near the shroud.

Parameter	Value
Span wise mesh cells on blade	42
Span wise mesh cells on tip clearance	4

Parameter	Value
Upstream meridional mesh cells	38
Inducer meridional mesh cells	50
Passage meridional mesh cells	65
Diffuser meridional mesh cells	65
Pitch wise cells	27
Pitch wise cells on leading edges	5
Mesh growth rate from boundaries	1.3

Table 7.6 – Mesh settings for undercut study

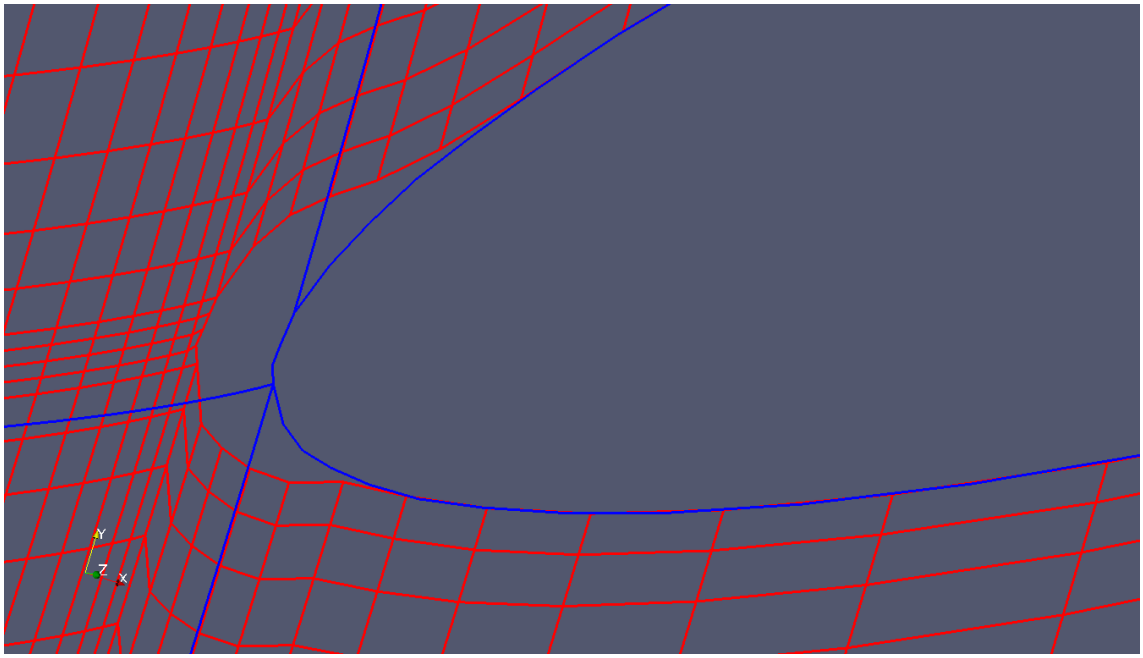

Figure 7.6a – Undercut height 0.6mm, width level .01 at hub leading edge

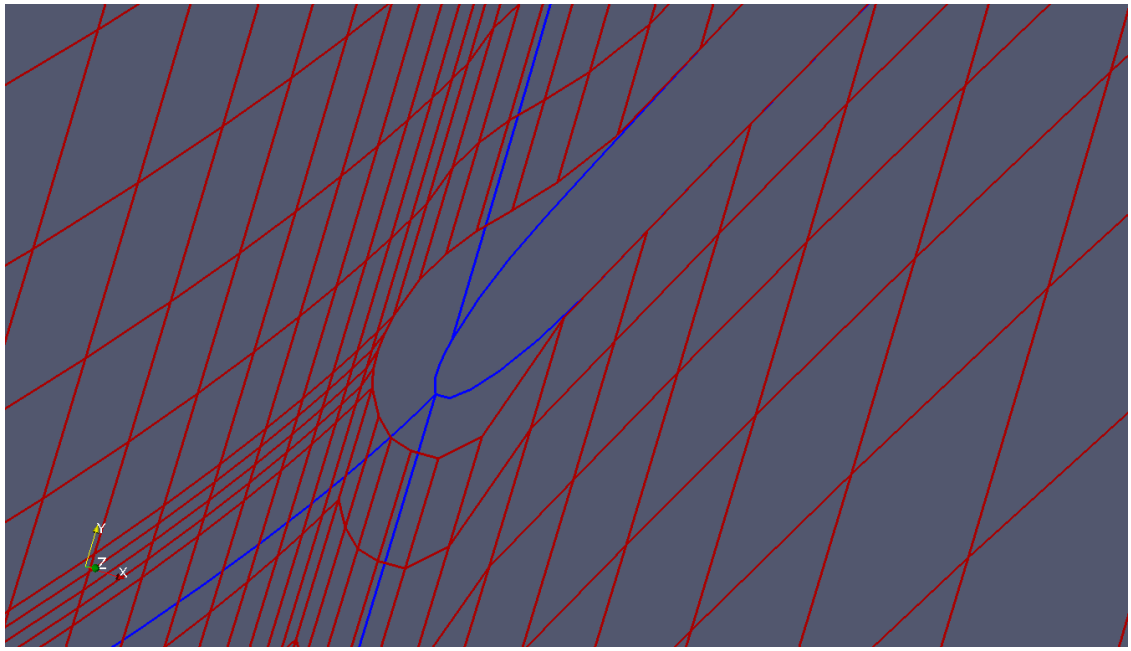

Figure 7.6b – Undercut height 0.6mm, width level .01 at shroud leading edge

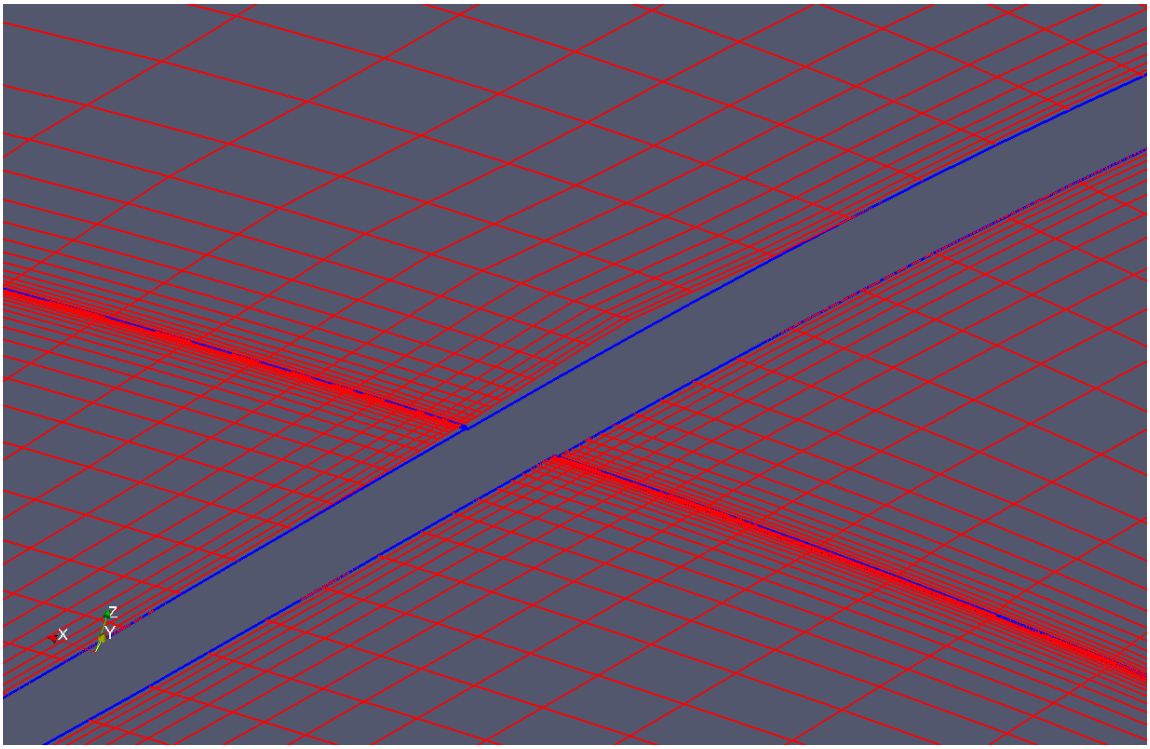

Figure 7.6c – Undercut height 0.25mm, width level 0.1 at shroud pressure side location -0.2

CFD solver settings in TBLOCK used for the undercut study are shown in Table 7.7. The mixing length turbulence model is used for all three design analysis. CFL number and smoothing factor is set to 0.4 and 0.03 respectively for all three designs analysed.

Parameter	NAP	3862H	ADT
Design Operating speed (rpm)	25000	25000	40000
Inlet stagnation pressure (Pa)	350000	350000	100000
Inlet stagnation temperature (Kelvin)	333	333	288
Outlet static Pressure at design point (Pa)	700000	700000	220000
Shroud tip clearance	0.5%	0.5%	0.4%
Number of main blades	6	7	13
Number of splitter blades	6	7	13

Table 7.7 – Solver settings for undercut study

7.6.4 Sensitivity Calculation Programs

In order to calculate the sensitivity of a compressor performance to an undercut on the impeller blade surface, the performance of the compressor is first obtained without an undercut, and then re-calculated with an undercut. The sensitivity of the compressor to undercut is calculated as percentage change in performance of the undercut impeller relative to an impeller without an undercut. To compute the compressor speed line for an undercut impeller, the mapping algorithm used in the optimisation phase of this thesis was modified to call the undercut creation program before meshing the geometry. Performance parameters are calculated as in the optimisation phase. Sensitivity to undercut is calculated for 8 performance parameters. Three sub-programs are developed to calculate percentage changes in performance parameters due to the undercut and also to accumulate the result for geometries evaluated. The programs are discussed below

a) *Sensitivity Calculator:* This C++ algorithm compares the performance speed line in a compressor – with and without an undercut, and calculates 8 percentage changes in performance parameters as listed below and illustrated in Figure 7.7.
    1. Change in target mass flow

2. Change in choke mass flow
3. Change in surge mass flow
4. Change in efficiency at design point
5. Change in peak efficiency along the speed line
6. Average change in mass flow along the speed line (averaged for all operating points)
7. Average change in efficiency along the speed line (averaged for all operating points)
8. Global average of 1 to 7

b) *Sensitivity Accumulator:* This C++ algorithm is used to collate the undercut parameters and sensitivity calculation results for each compressor geometry evaluated.

c) A python script is developed to carry out a signal-to-noise (S/N) ratio analysis on the sensitivity analysis data obtained. Signal-to-noise ratio is the ratio of standard deviation (σ) to mean (μ) for a given data set as shown in Equation 7.1

$$SNR = \frac{\sigma}{\mu} \tag{7.1}$$

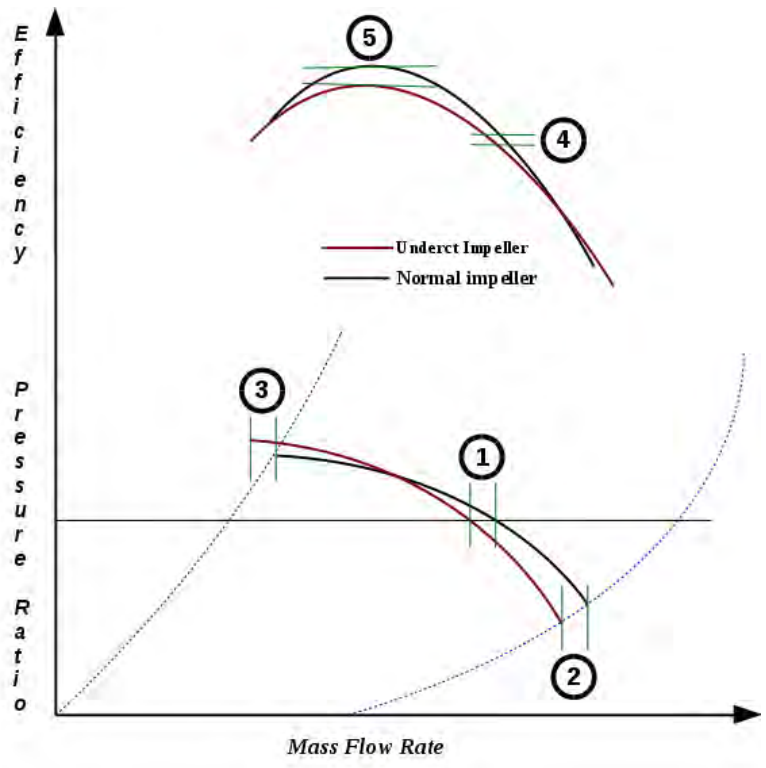

Figure 7.7 - illustration of sensitivity calculations

7.7 SENSITIVITY CALCULATIONS

The following assumptions are used to set up the problem;

1. One undercut is placed on the blade surface at a time
2. The undercut can be on the main blade or splitter blade
3. The undercut is placed at the same merdional position at the hub and shroud of the blade. This is illustrated in Figure 7.8.
4. All locations are to be evaluated using CFD

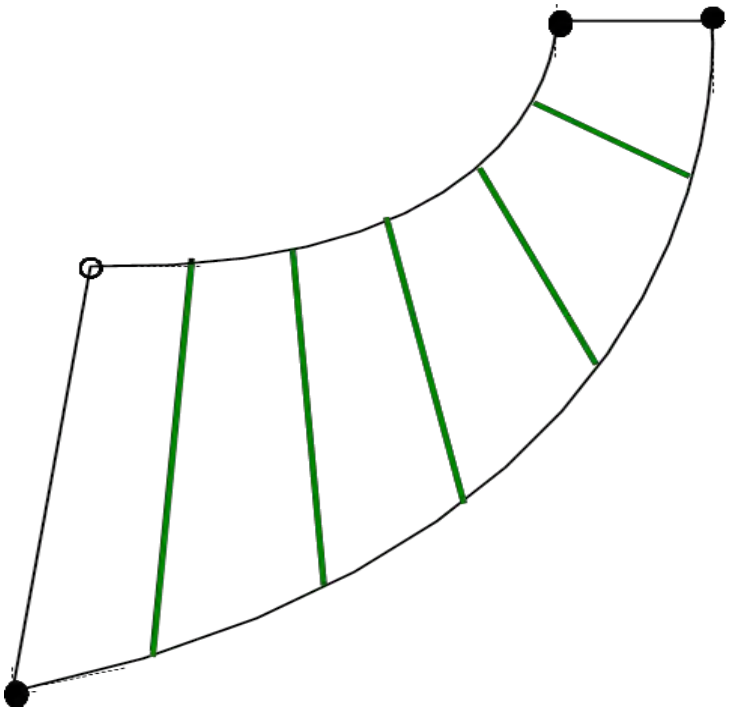

Figure 7.8 – Illustration of undercut meridional location

Tables 7.1 to 7.3 shows there are 4 undercut height levels, 13 locations and 4 width levels. Based on assumptions 1 to 3, the number of CFD analysis required for a full factorial analysis for each blade (main or splitter) is 4 * 13 * 4 = 208. Therefore, for each compressor design, 416 CFD analyses are required for both the main and splitter blade undercuts. A full factorial analysis is generally considered unfeasible if the number of combinations of parameter levels is high as is the case in this study. However, the use of a low cost HTC cluster implemented during this research makes a full factorial study possible. As a result, a full factorial study is carried out.

7.7.1 Updated HTC System

The HTC system work flow used in the multi-objective optimisation phase is modified for the undercut study. The modified mapping flow chart is shown in Figure 7.9a. The undercut creation program reads in the „bump.dat" file containing specifications for the undercut and adds an undercut to the profile data of the blade. The geometry is then meshed and solved at different pressure ratios at the same rotor speed. Figure 7.9b is a schematic of the updated HTC system used to run the sensitivity analysis calculations. A python script „run_mapper_bump.py" is written to call the Mapping program, then the sensitivity calculator and sensitivity accumulator programs for each undercut parameter evaluated. The sensitivity calculator creates the file „sim_out_bump" containing the calculated sensitivities. The sensitivity accumulator program collates the sensitivity data for each case into a single file – „sensitivityLog.dat". Figure 7.10 is a picture of the expanded cluster showing the increased number of workstations in the HTCondor cluster pool.

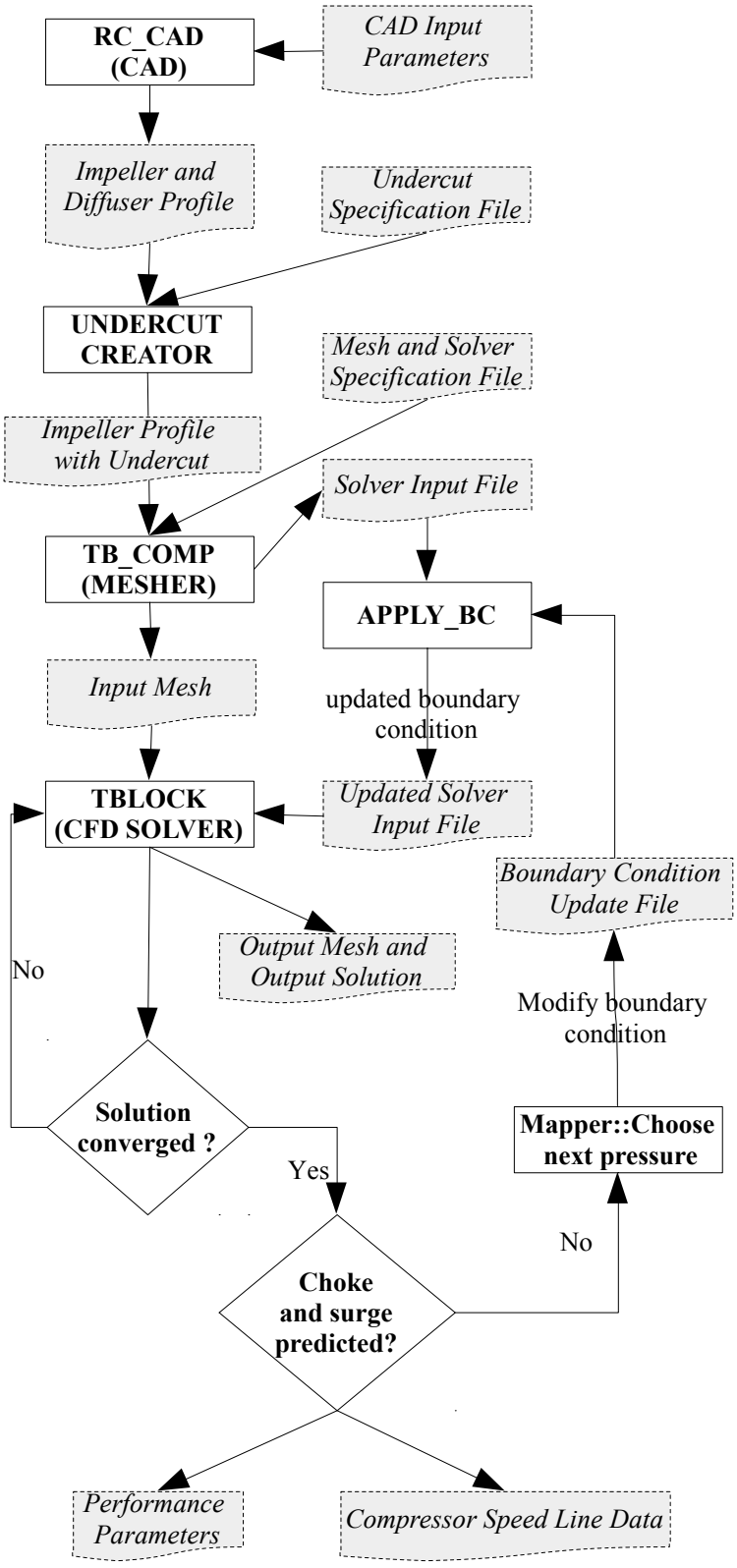

Figure 7.9a – Updated mapping work flow

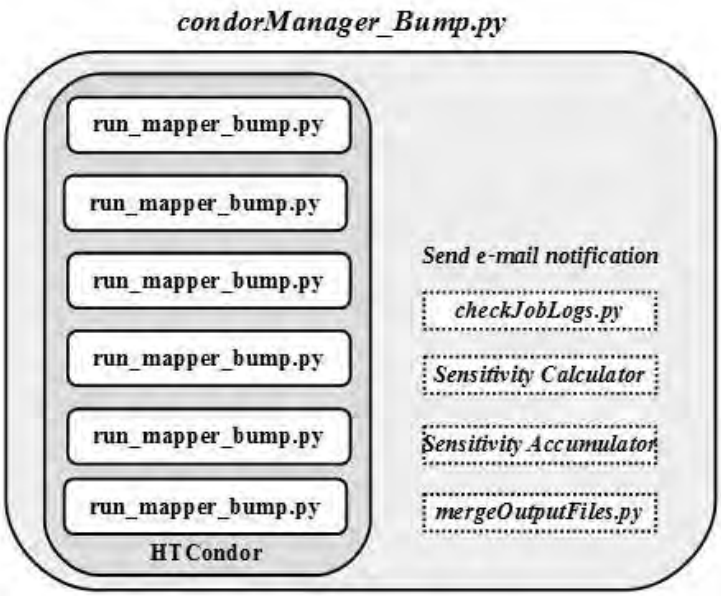

Figure 7.9b – Updated HTC system

Figure 7.10 – Computers in the condor pool

7.8 RESULTS AND ANALYSIS

The result of the undercut study is presented under the following sub-headings:

- Rank of designs by sensitivity
- Rank of performance parameter by sensitivity
- Sensitivity of blade locations
- Impact of undercut height or width level on performance parameters

7.8.1 Rank of Designs by Sensitivity

The sensitivity of the designs is calculated using the total absolute averaged value of parameter sensitivities, measured in percentage deviation. This value is computed for the main and splitter blade as shown in Figure 7.11 where the existing Napier design (NAP) is the least sensitive to undercut, and the optimised design (3862H) is the most sensitive. This is a reasonable outcome due to the fact that, during optimisation, the optimisation algorithm pushes the design to improve performance, and in most cases reduce the robustness of the design, resulting in a design more sensitive to manufacturing deviations.

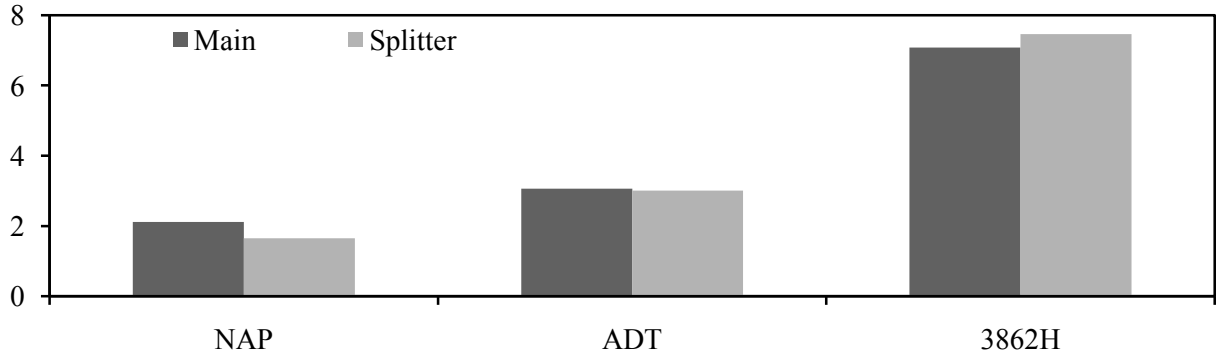

Figure 7.11 – Sum of averaged absolute sensitivities for each design

7.8.2 Rank of Performance Parameters by Sensitivity

It is important to understand the performance parameter most sensitive to undercut in order to make better judgement on passing an undercut using the screening template (or "heat map") discussed later in this thesis. Two graphs are used to rank the performance parameter sensitivities. The first graph depicted in Figure 7.12, is based on combined data of all three designs, and ranks the performance parameters based on absolute averaged sensitivity. Names of some sensitivity parameters presented in Figures 7.12, 7.13, and other subsequent plots, are shortened for brevity as follows:

- Eff_Avg_SL Absolute averaged total-to-static efficiency sensitivity along the speed line.
- Mf_Avg_SL Absolute averaged mass flow sensitivity along the speed line.

These are subsequently referred to as speed line efficiency sensitivity and speed line mass flow sensitivity in subsequent Sections. Other performance parameter names are self descriptive.

Figure 7.12 shows that surge mass flow is the most sensitive to undercut, while the least sensitive is the average mass flow deviation along the speed line. The graph also suggests that peak efficiency and choke mass flow will be more impacted by an undercut compared to design point efficiency.

Figure 7.13 shows the sensitivities of performance parameters for each compressor design. As in Figure 7.12, surge mass flow is observed to be the most sensitive parameter for all three designs. This is not surprising due to the fact that surge is an unsteady phenomenon characterised by separating and reversed flows, easily triggered by a high curvature change on a blade surface. However, the order of sensitivity of other performance parameters differs across the three designs. For example, peak efficiency is more sensitive in design 3862H compared to Napier design. Also, target mass flow in the ADT design is more sensitive compared to the other two designs. These variations further emphasise the importance of developing unique tolerance limits for every new compressor design. A typical centrifugal compressor impeller blade consists of high curvature sections required to turn the flow in the axial and radial direction. It is therefore necessary to control the rate of change of curvature through the blade passage. A manufacturing defect such as an undercut on the blade surface changes the local curvature, resulting in instability in the flow. For this reason, it is important to take into consideration the most suitable manufacturing process while optimising a compressor design. For example, during machining of an impeller blade surface with high curvature; the cutter is programmed to cut in small steps in order to capture the curvature. This increases the time required to machine the impeller. More so, aerodynamic performance of a high curvature blade impeller is more sensitive to an undercut on the blade surface, compared to a blade with lower curvature.

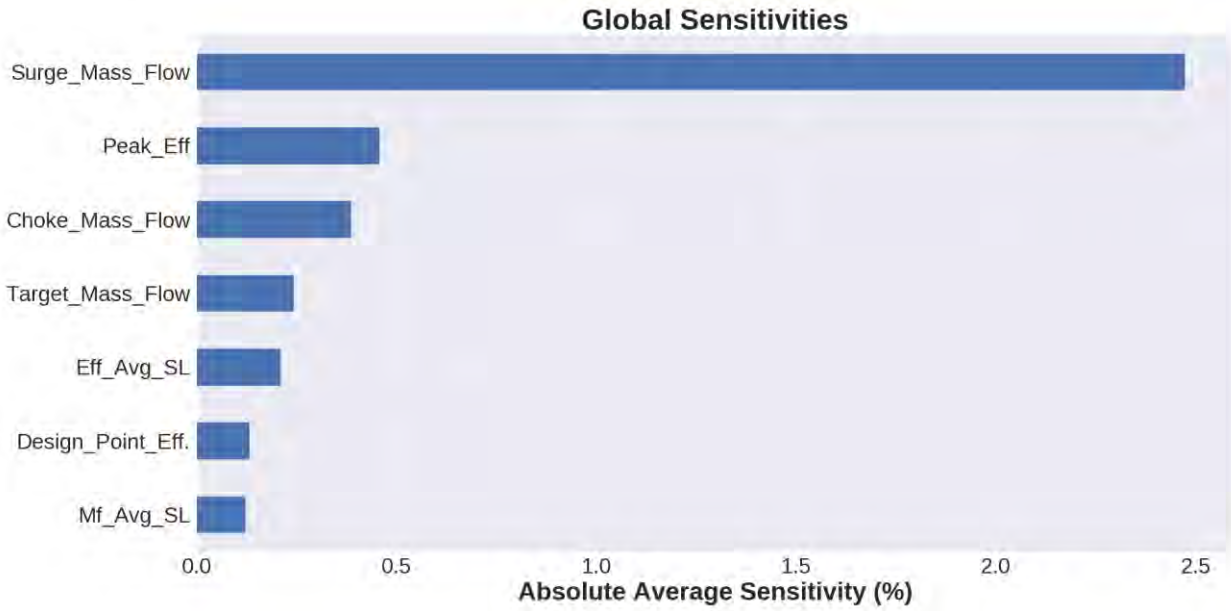

Figure 7.12 – Sum of absolute averaged sensitivity per performance parameter

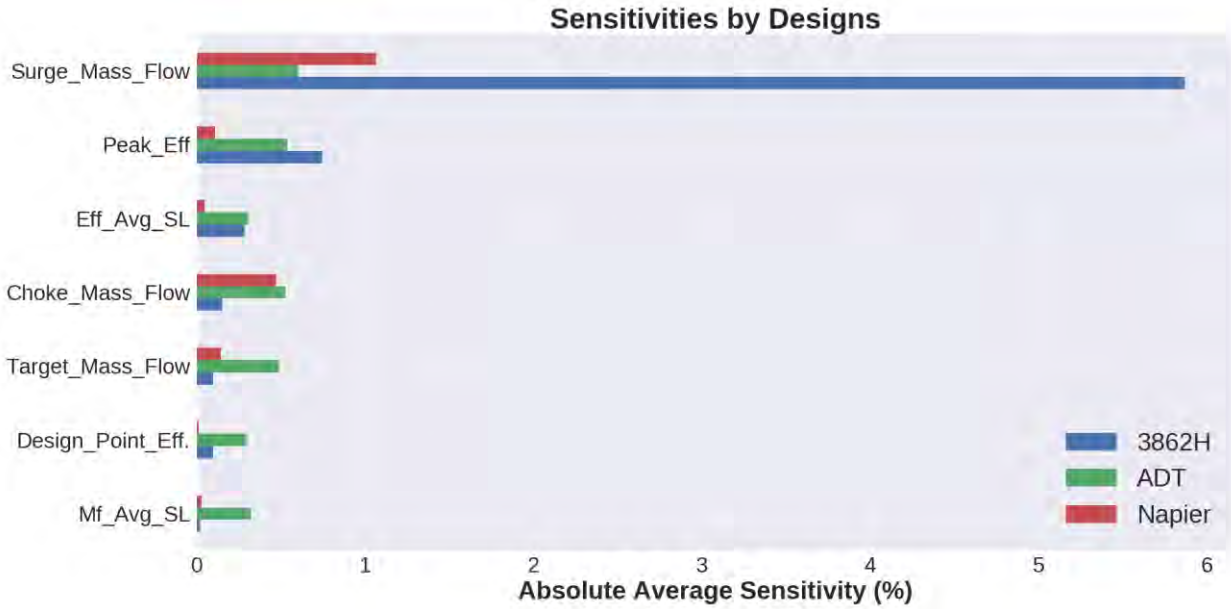

Figure 7.13 - Sum of absolute averaged sensitivity per performance parameter per compressor design

7.8.3 Sensitivity of Locations

It is important for manufacturing engineers to know the most sensitive location on an impeller blade, so careful attention is provided when machining that area. Also, stricter tolerance may be applied to most sensitive locations on an impeller blade. Figure 7.14 shows the absolute averaged sensitivity for each blade location (main or splitter) for all three designs. It shows the leading edge is the most sensitive location (whether main or splitter blade), and that surge mass flow is the most sensitive parameter. It is hard to tell the variation of the other parameters along the blade surface using this plot.

Figures 7.15 to 7.20 depict sensitivities at different locations on the main and splitter blade for all three designs. This is calculated as a signal-to-noise ratio of performance deviations at each location on the impeller blade surface. Signal-to-noise ratio is the ratio of standard deviation to mean for a given data set.

Figures 7.15 and 7.16 shows that the leading edge is the most sensitive location on the main and splitter blade of Napier design. It is hard to tell any difference in sensitivity between the pressure and suction side.

In the ADT design plots shown in Figures 7.17 and 7.18, the pattern is different from the Napier design. The main blade is not the most sensitive location. Instead, the location 30% along the meridional, starting from the leading edge, and on the pressure side is the most sensitive. High sensitivity is also observed on 40% length on the suction side. These locations on the main blade coincide with the location of the splitter blade leading edge. This may be the reason for high sensitivity. The location 40% along the suction side will be visualised in CFD to further improve understanding. However, on the splitter blade, the leading edge is the most sensitive location, while the suction side appears to be more sensitive than the pressure side.

In Figure 7.19 which depicts the sensitivity of design 3862H main blade, no data is presented for the leading edge due to the fact that the solution diverged for all cases of undercut parameters. This suggests the main blade leading edge of this design is too sensitive and no undercut is permissible there. By visual inspection of Figure 7.19, the pressure side appears to be more sensitive than the suction side. On the splitter blade sensitivity depicted in Figure 7.20, the leading edge is the most sensitive location. There appears to be no difference in sensitivity between the pressure and suction side.

Based on Figures 7.14 to 7.20, it is clear the leading edge is the most sensitive location for each impeller design. Figures 7.14 to .20 also show the distribution in sensitivity at different location on the pressure and suction sides of the blade is unique to each impeller design.

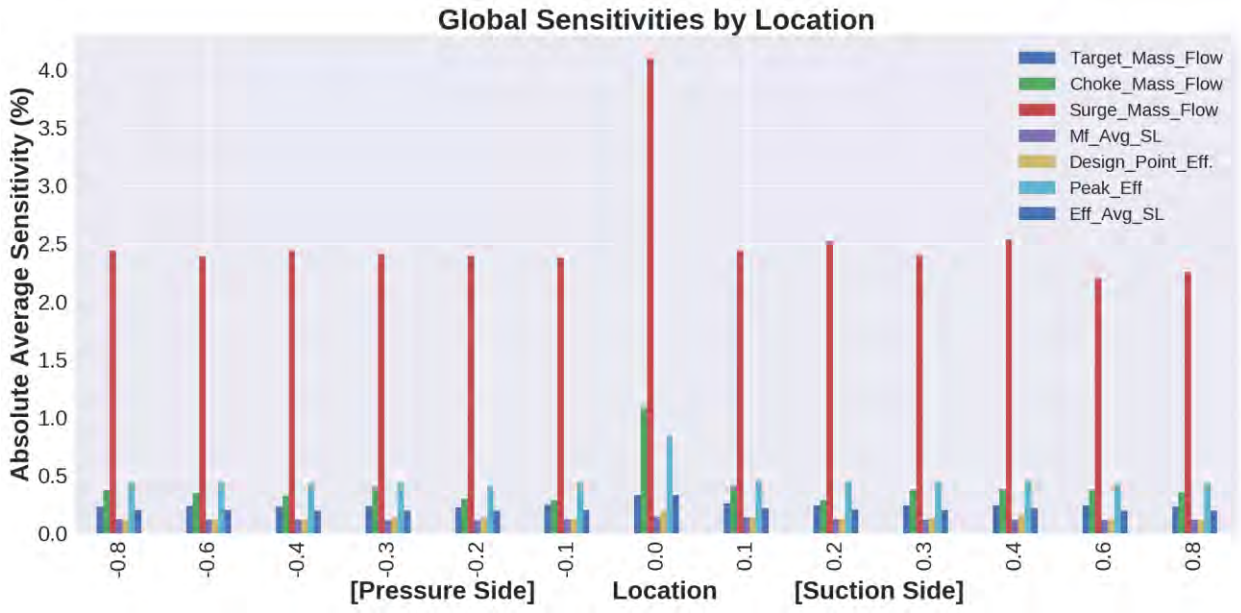

Figure 7.14 – Sum of absolute averaged sensitivity per location

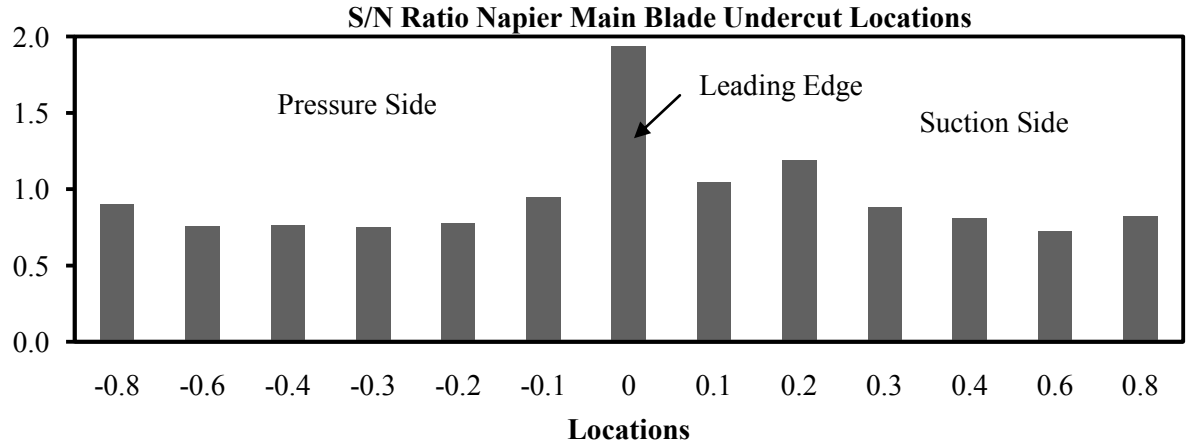

Figure 7.15 – Signal-to-noise ratio of undercut locations (Napier Main Blade)

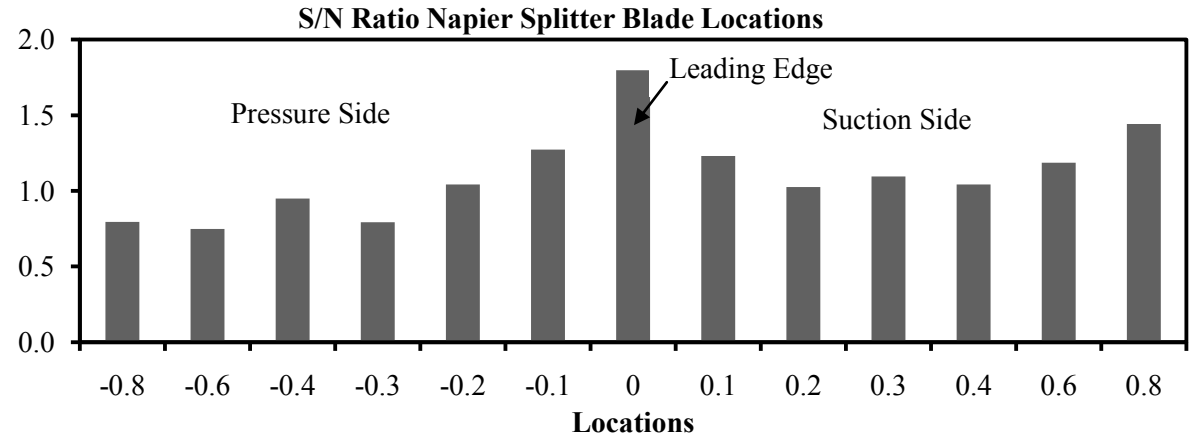

Figure 7.16 – Signal-to-noise ratio of undercut locations (Napier Splitter Blade)

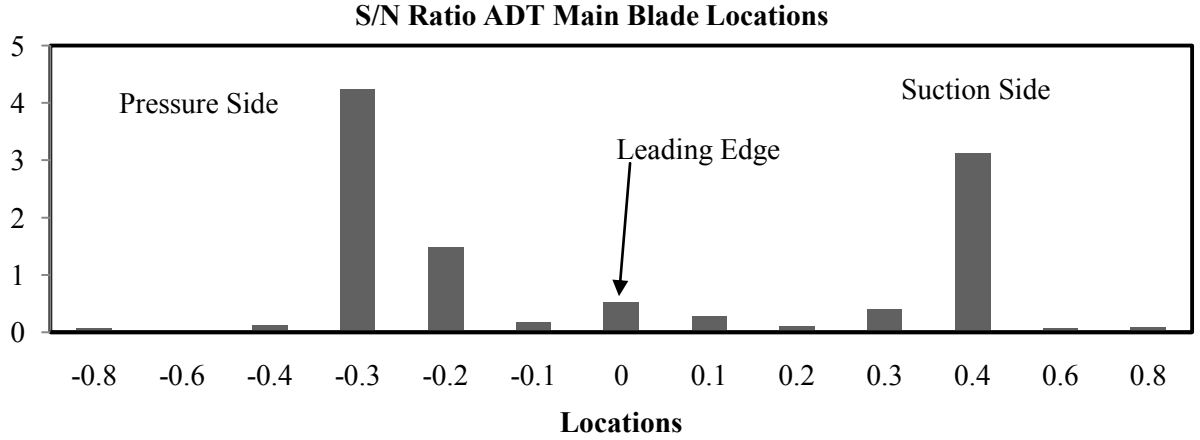

Figure 7.17 – Signal-to-noise ratio of undercut locations (ADT Main Blade)

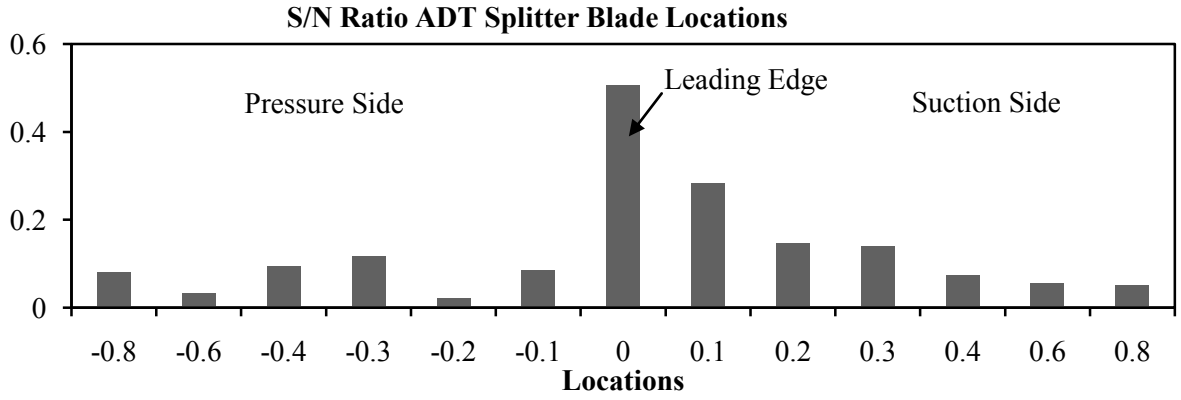

Figure 7.18 – Signal-to-noise ratio of undercut locations (ADT Splitter Blade)

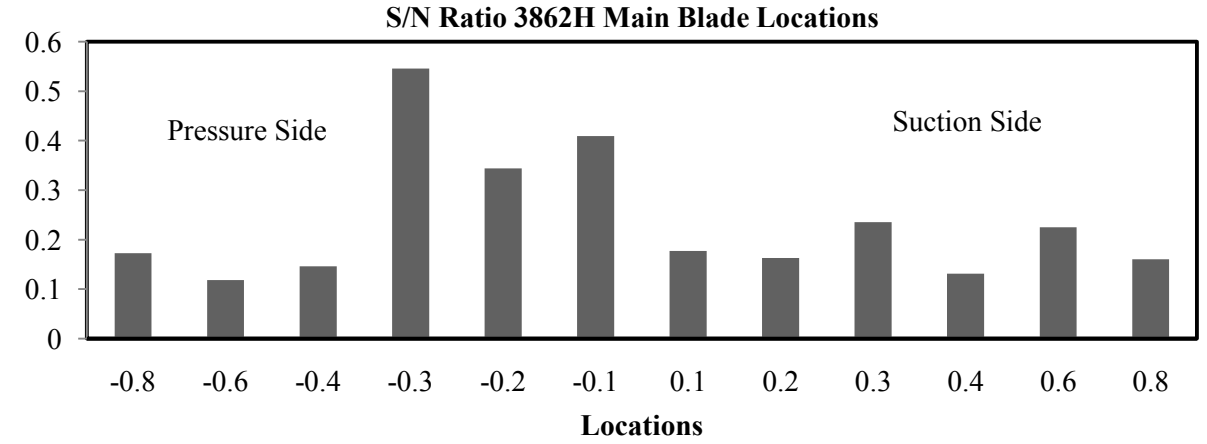

Figure 7.19 – Signal-to-noise ratio of undercut locations (3862H Main Blade)

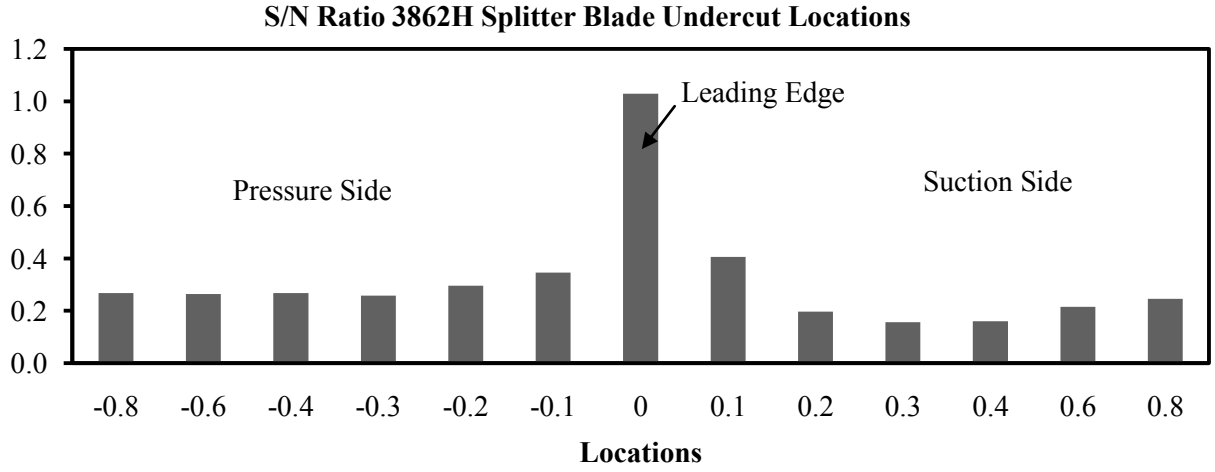

Figure 7.20 – Signal-to-noise ratio of undercut locations (3862H Splitter Blade)

7.8.4 Impact of Undercut Height and Width Levels on Performance Parameters

The impact of undercut height and width levels on performance parameters is determined by calculating the correlations between height and width, and the performance parameter. To facilitate the calculations, the python data analysis library – Pandas [97] is utilised to calculate the standard Pearson correlation coefficient. Pearson correlation coefficient is the ratio of covariance of two sets of data to the product of their standard deviation. Given two data sets $x(x_i \ldots\ldots x_n)$ and $y(y_i \ldots\ldots y_n)$, Pearson's correlation coefficient can be calculated using Equation 7.2, where n is the population size, $x_i \; and \; y_i$ are individual points in the data set, and $\bar{x} \; and \; \bar{y}$ are the mean of each data set.

$$r = \frac{\sum_{i=0}^{n}(x_i - \bar{x})(y_i - \bar{y})}{\sqrt{\sum_{i=0}^{n}(x_i - \bar{x})^2}\sqrt{\sum_{i=0}^{n}(y_i - y)^2}} \tag{7.2}$$

Correlation values are unit-less, and range from -1 to 1, with -1 indicating very strong negative correlation, while 1 indicates very strong positive correlation. Values between -0.2 and 0.2 are generally regarded as weak correlations. The correlation values should also determine whether undercut height or width has more impact on performance parameters.

Figures 7.21 to 7.23 show correlations between undercut height and width, and all performance parameters for all the designs. In Figure 7.21, the main and splitter blade data for all designs is put together, and correlation values are computed globally. Overall, weak positive and negative correlations are observed in Figure 7.21. For example, undercut height levels are negatively correlated with target mass flow (or design point mass flow), meaning that, as undercut height increases, target mass flow reduces. Visual inspection of Figure 7.21 shows that undercut height levels appear to be more strongly correlated with the performance parameters, compared to undercut width levels. This suggests performance parameters are more sensitive to undercut height levels, than to undercut width levels.

Figures 7.22 and 7.23 show global correlations between undercut height and width, and all performance parameters for the main and splitter blades respectively for all three compressor designs. Both Figures also reveal the superior significance of undercut height levels compared to undercut width levels. Similar directions of correlation (positive or negative) on the main and splitter blades is observed, except for surge and choke mass flow. On the main blade, choke mass flow reduces with increase in undercut width or height, but increase on the splitter blade. This is easy to explain on the main blade, since an undercut there would likely reduce the impeller throat area, and result in a lower choke mass flow. On the splitter blade however, depending on location of the undercut – pressure or suction side, it may be insignificant. On the other hand, surge mass flow increases with increase in undercut height or width levels on the main blade, but shows a very weak negative correlation with undercut width on the splitter blade. Overall, correlations plotted in Figures 7.22 and 7.23 are classed as weak.

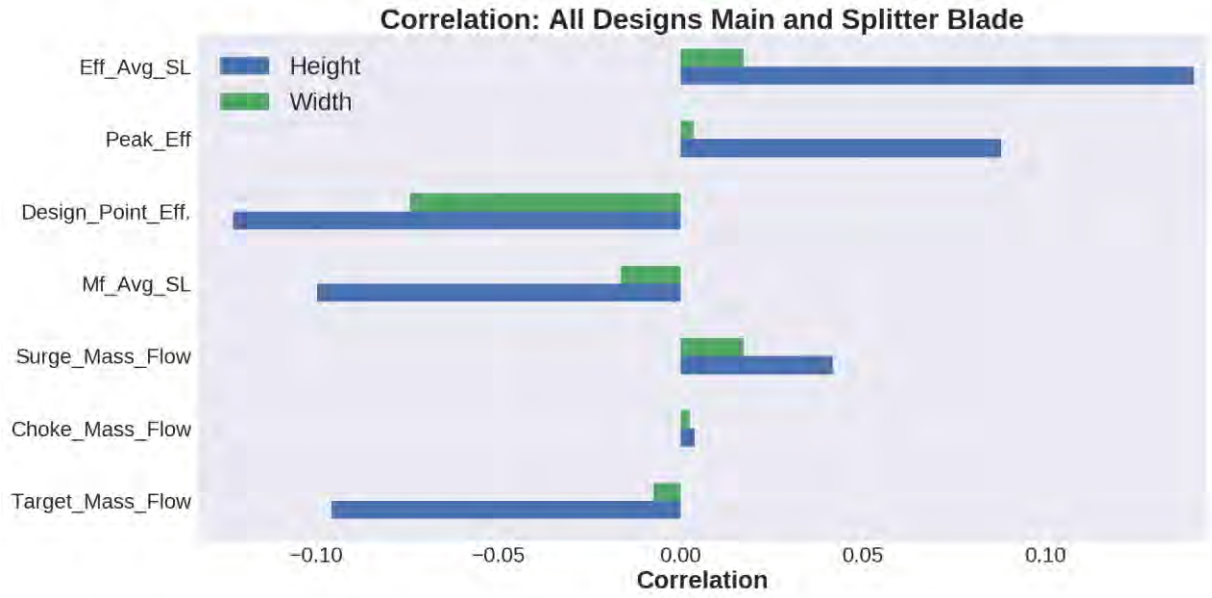

Figure 7.21 – Correlation of all designs (main and splitter blade combined)

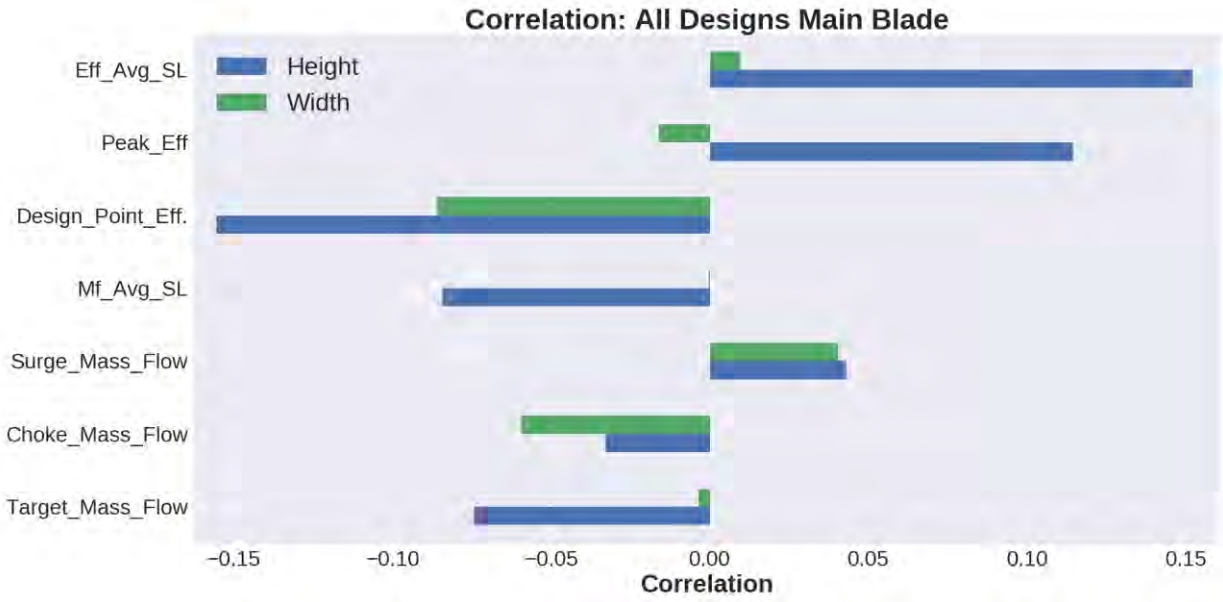

Figure 7.22 – Correlation of all designs main blade

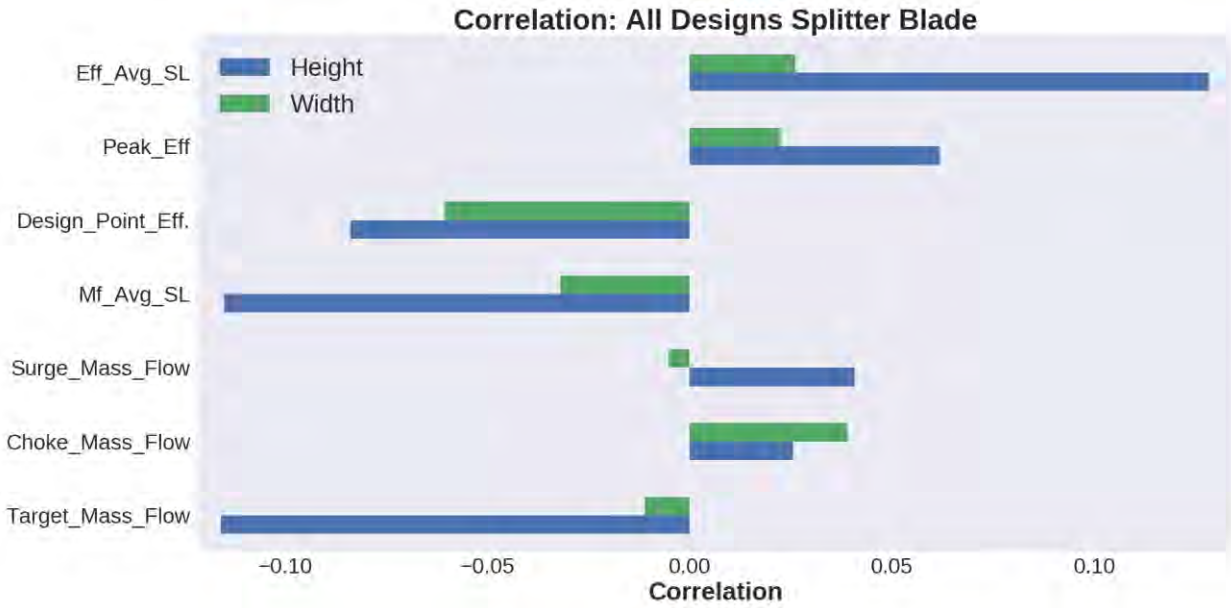

Figure 7.23 – Correlation of all designs splitter blade

Figures 7.24 and 7.25 show correlations between undercut height and width; and all performance parameters using sensitivity data for design 3862H. Figures 7.24 and 7.25 shows some strong correlations on the main and splitter blade respectively, between undercut height and width levels, and performance parameter. Significant correlations are observed for speed line efficiency sensitivity, design point efficiency, speed line mass flow sensitivity and target mass flow sensitivity. For example, there is a strong negative correlation between undercut height levels and design point efficiency, speed line mass flow and target mass flow on the main blade as shown in Figure 7.24. These strong correlations also indicate high sensitivity of design 3862H to undercut. On the splitter blade plot shown in Figure 7.25, significant negative correlation is observed between undercut height levels, and design point efficiency and speed line mass flow. Significant negative correlation is also observed between undercut width and speed line mass flow.

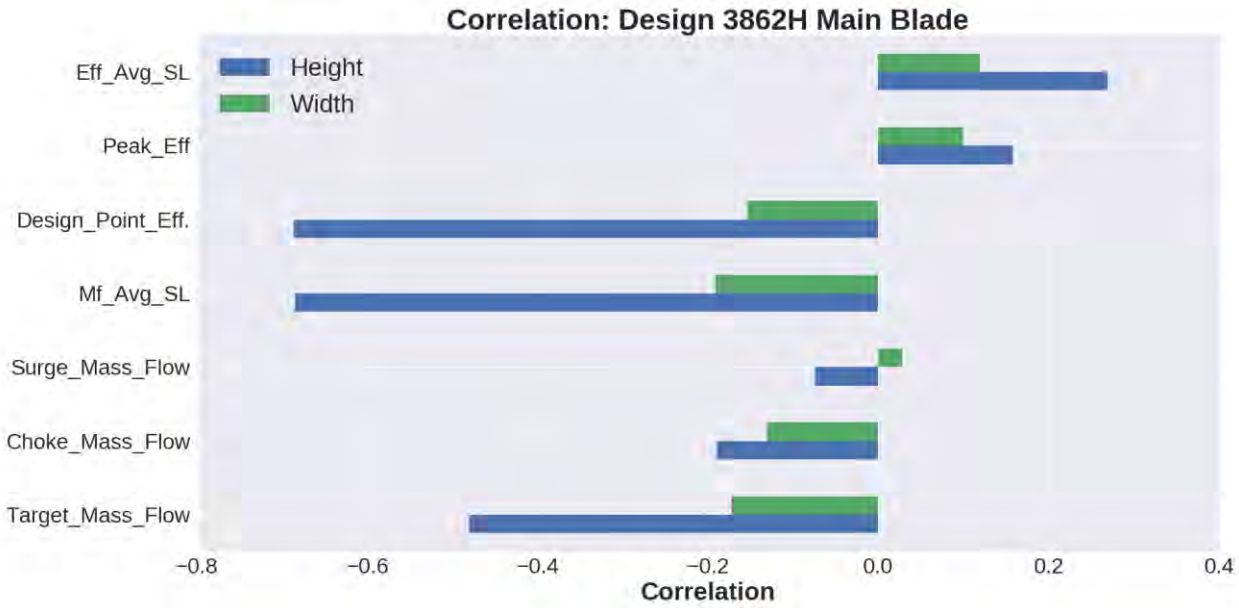

Figure 7.24 Correlation on main blade of design 3862H

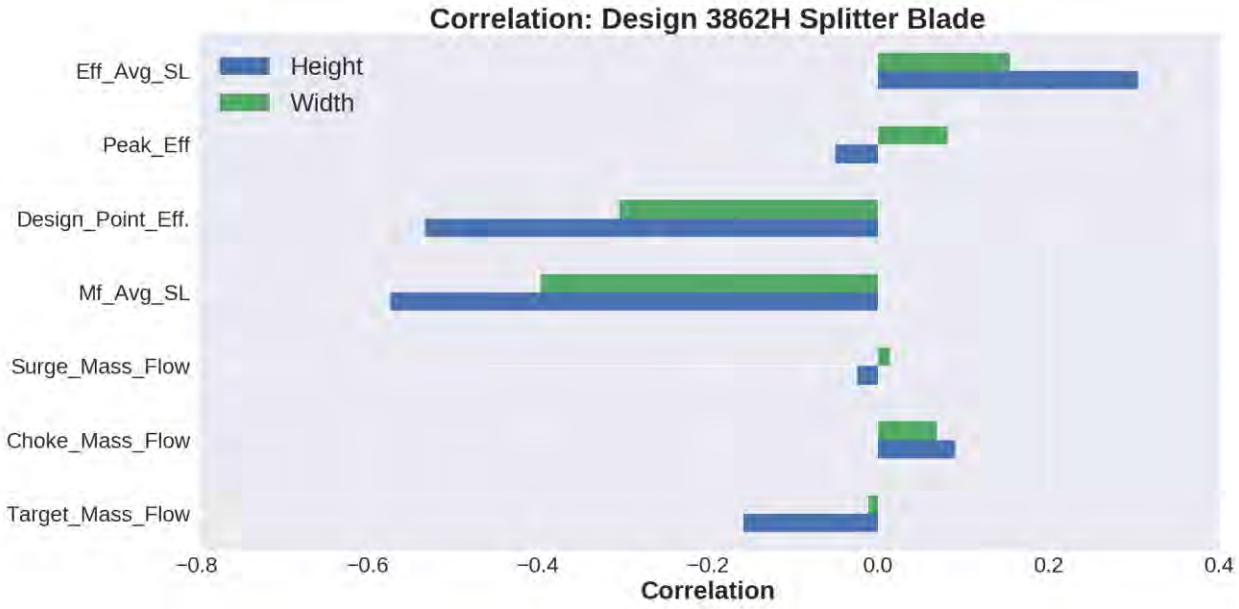

Figure 7.25 Correlation on splitter blade of design 3862H

Figures 7.26 and 7.27 show weak correlation between undercut width and performance parameters on the main and splitter blade of Napier design. Significant negative correlation between undercut height levels and design point efficiency, speed line mass flow and target mass flow is observed on the main and splitter blade. Significant positive correlation is observed between undercut height levels, and speed line efficiency and peak efficiency, suggesting an undercut on a splitter blade may improve peak efficiency.

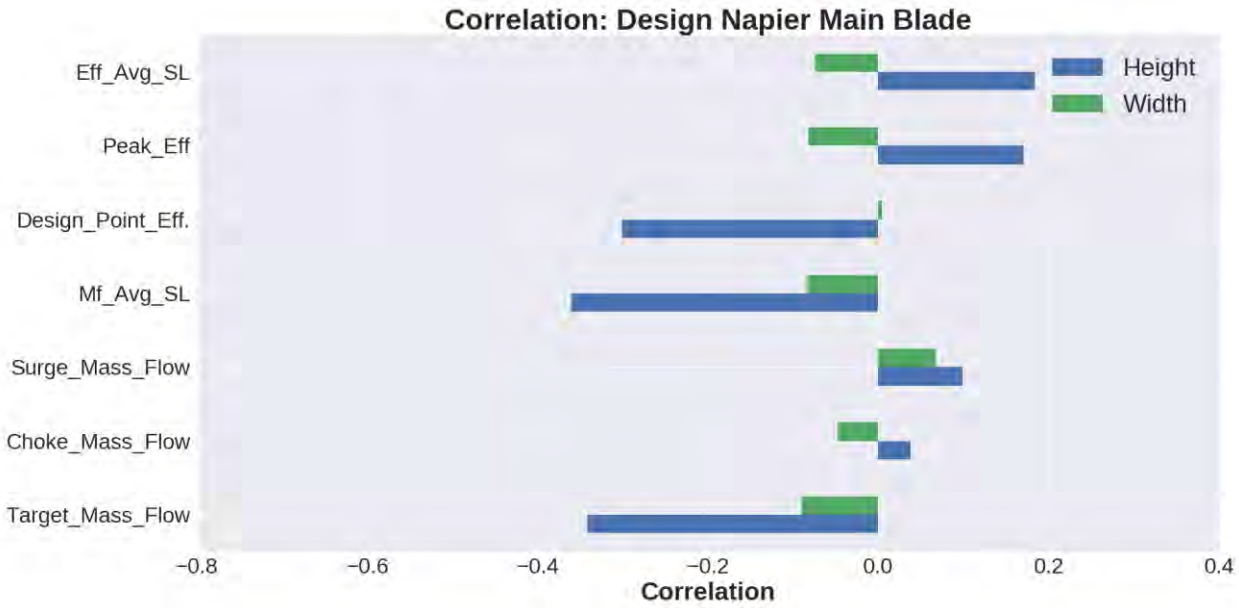

Figure 7.26 Correlation on main blade of Napier design

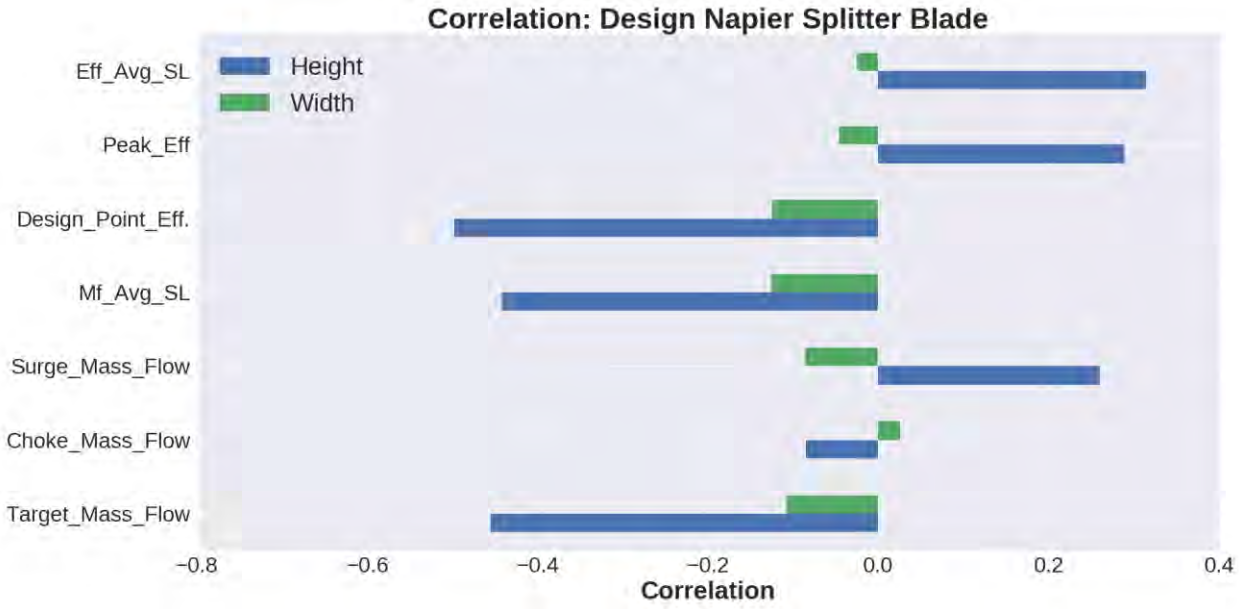

Figure 7.27 Correlation on splitter blade of Napier design

Figures 7.28 and 7.29 show weak correlation between undercut width and performance parameters on the main and splitter blade of ADT design. Significant negative correlation is observed between undercut height levels and speed line mass flow on the main blade as shown in Figure 7.28. On the splitter blade, significant negative correlation is observed between undercut height levels, and speed line mass flow and target mass flow as shown in Figure 7.29

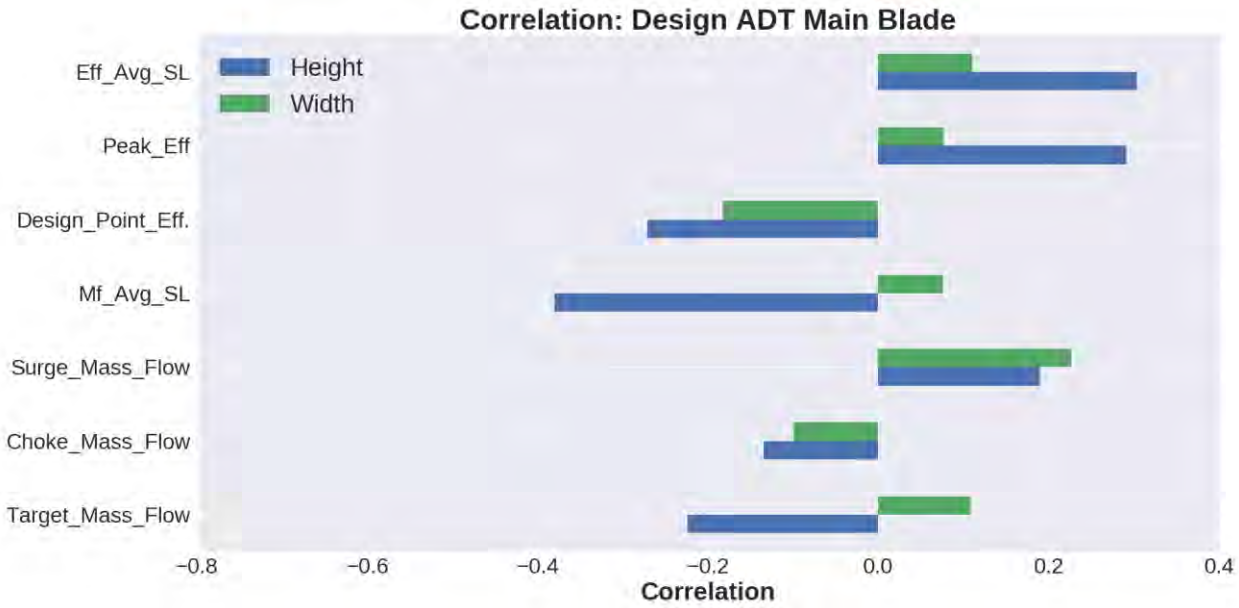

Figure 7.28 Correlation on main blade of design ADT

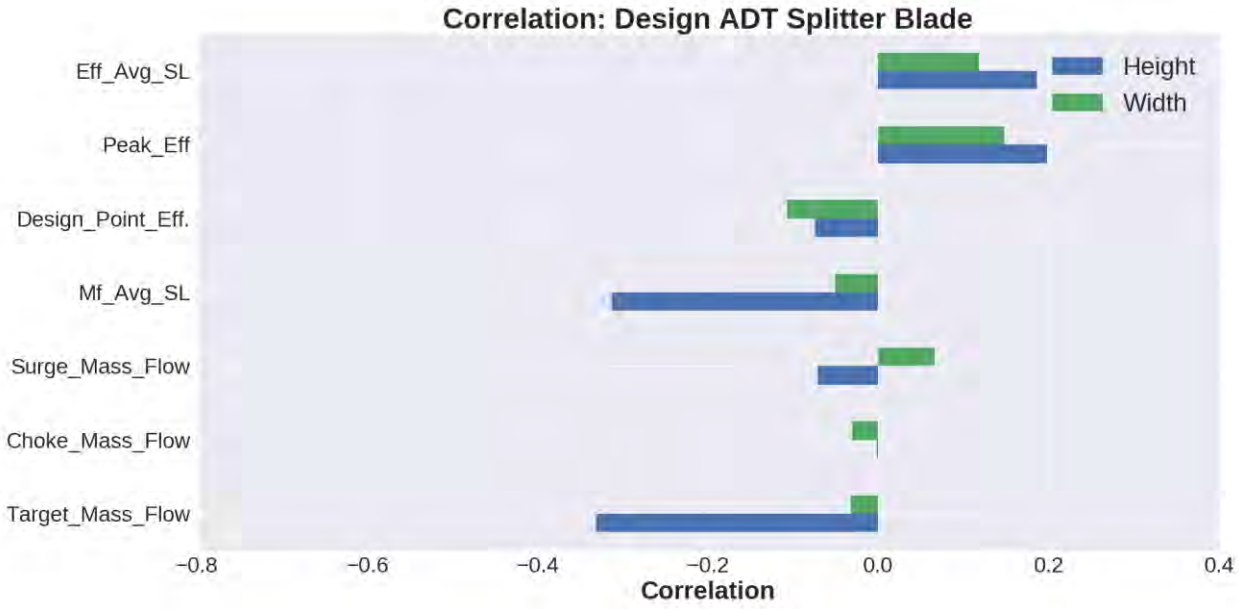

Figure 7.29 Correlation on splitter blade of design ADT

In summary, Figures 7.21 to 7.29 reveal some interesting findings:

- There is a stronger correlation between undercut height levels and performance parameters, than there is with undercut width levels. This means, performance parameters are more sensitive to undercut height, than to undercut width.

- Only negative correlations exist between undercut heights levels, and design point efficiency, speed line mass flow and target mass flow on the main and splitter blades for all three designs.
- Only positive correlations exist between undercut height levels, and peak efficiency and speed line efficiency on the main and splitter blade for all three designs, except for design 3862H splitter blade where there is a weak negative correlation.
- Surge and choke mass flows do not show consistent correlation with undercut height and width levels across all three designs.
- There is no clear pattern of correlation between undercut width levels and performance parameters. All correlations are weak except on design 3862H splitter blade.

In the next Section, 3D flow visualisations will be presented for selected cases of undercut height and width levels, and location.

7.9 3D FLOW VISUALISATIONS

This Section presents CFD visualisations of the effect of undercut on the flow features. Several plots are presented to explain how the undercut parameter resulted in the sensitivities observed. Four cases are chosen for visualisation in 3D based on impact of the undercut on performance parameters and variety of undercut parameters. The cases to be investigated in detail are summarized in Table 7.10.

	Case 1	**Case 2**	**Case 3**	**Case 4**
Design	Napier	Napier	3862H	ADT
Main blade		√	√	√
Splitter blade	√			
Undercut Height (mm)	0.6	0.075	0.6	0.6
Undercut Location	0	0	-0.3	0.4
Undercut Width	0.02	0.1	0.1	0.1
Target Mass Flow*	-0.70	0.11	-0.18	-0.6
Choke Mass Flow*	-0.096	-1.12	-2.96	-1.27

	Case 1	Case 2	Case 3	Case 4
Surge Mass Flow*	15.25	4.25	5.93	6.83
Speed Line Mass Flow*	2.47	0.23	0.87	2.14
Target Efficiency*	-0.31	0.006	-0.04	-0.28
Peak Efficiency*	-0.23	-0.005	-0.13	-4.17
Speed line Efficiency*	0.98	0.1	0.33	2.12
Average Sensitivity	2.86	0.83	1.49	2.49

Table 7.10 - Undercut cases visualised with CFD
***% sensitivity**

7.9.1 Case 1 Flow Visualisation

In this design, the undercut is located at the leading edge of the splitter blade with a width 2% of the meridional length and the highest height level of 0.6 mm. Since the undercut is located on the leading edge of the blade, the pressure and suction sides of the blade contain flow features influenced by the undercut. The reference model without an undercut is compared side by side with the undercut geometry in order to understand the effect of undercut on the flow features. Focus is placed on design point data; although choke and surge point data/plots may be shown also. The undercut profile at the hub and shroud of this case is shown in Figure 7.30.

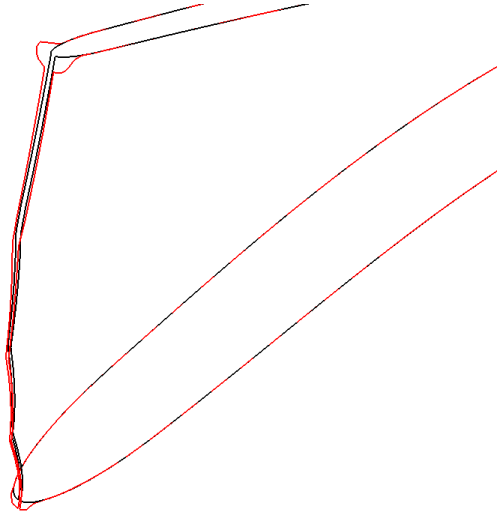

Figure 7.30 - Illustration of undercut at leading edge of the splitter blade of NAP design. The reference geometry is the black line

DESIGN POINT

Splitter blade pressure side plots

Figure 7.31 shows a reduction in relative Mach number on the leading edge of the splitter blade due to the flow detaching from the pressure side of the blade surface as it flows around the undercut. The breakaway of the fluid particles results in a lower meridional velocity around the shroud region of the blade as shown in Figure 7.32; eventually lowering the target mass flow by 0.7% at the design point. On the pressure side of the blade, the undercut represents a reduction in blade angle around the surface leading to a lower relative swirl angle around the shroud of the splitter blade as shown in Figure 7.33. The vector plots in Figure 7.34 shows a change in the velocity vectors around the shroud of the leading edge. This unsteadiness introduced by the undercut resulted in an early inception of surge resulting in about 15% increase in surge mass flow, leading to a narrower performance curve.

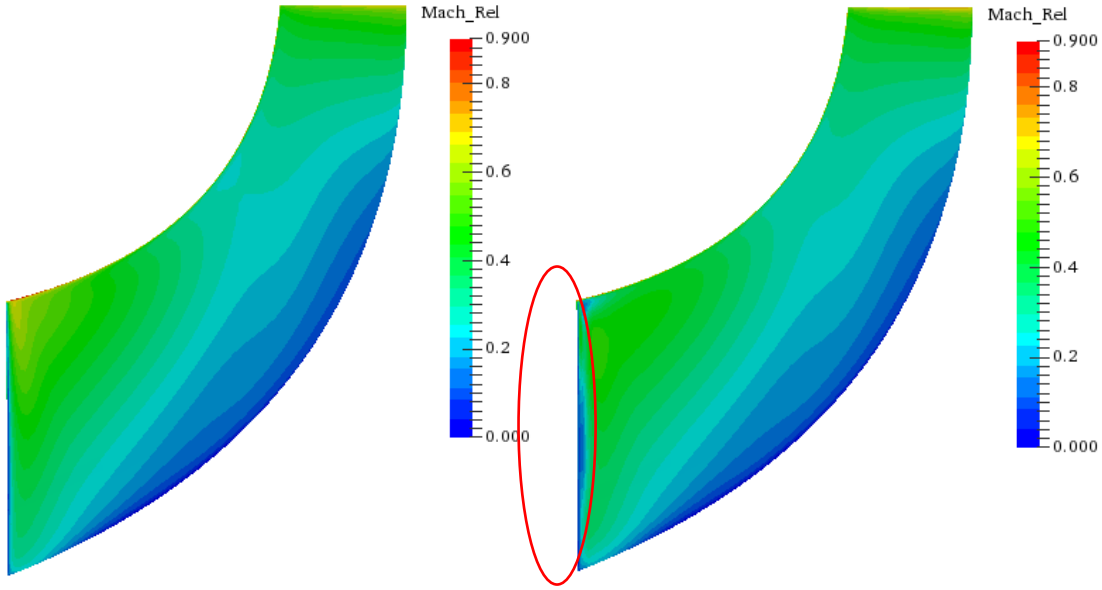

Fig 7.31a Fig 7.31b

Figure 7.31 (a) Relative Mach number plot on pressure side of splitter blade without undercut (b) Relative Mach number plot on pressure side of splitter blade with undercut at the leading edge.

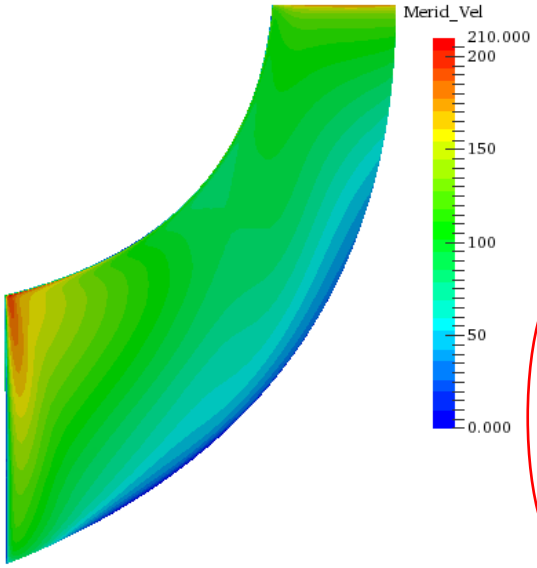

Fig 7.32a

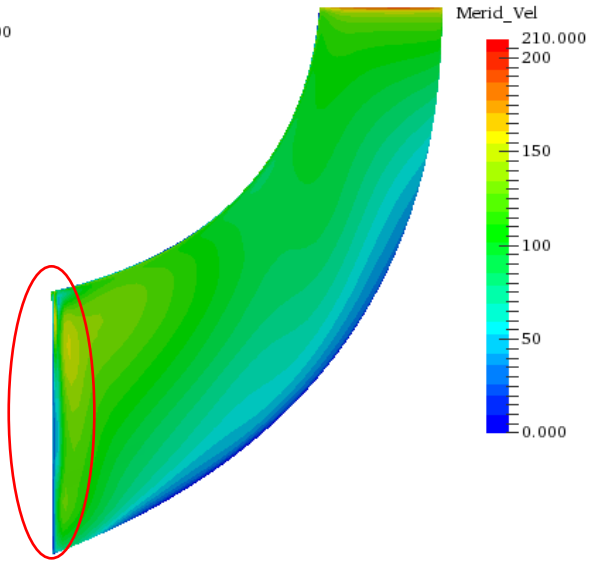

Fig 7.32b

Figure 7.32 (a) Meridional velocity plot on pressure side of splitter blade without undercut (b) Meridional velocity plot on pressure side of splitter blade with undercut at the leading edge.

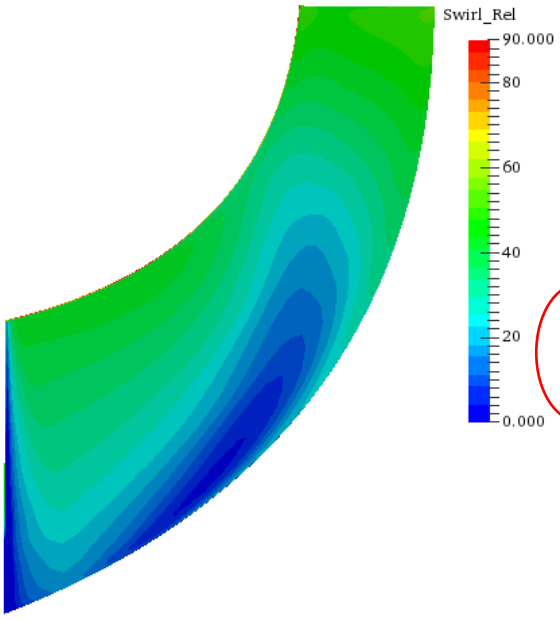

Fig 7.33a

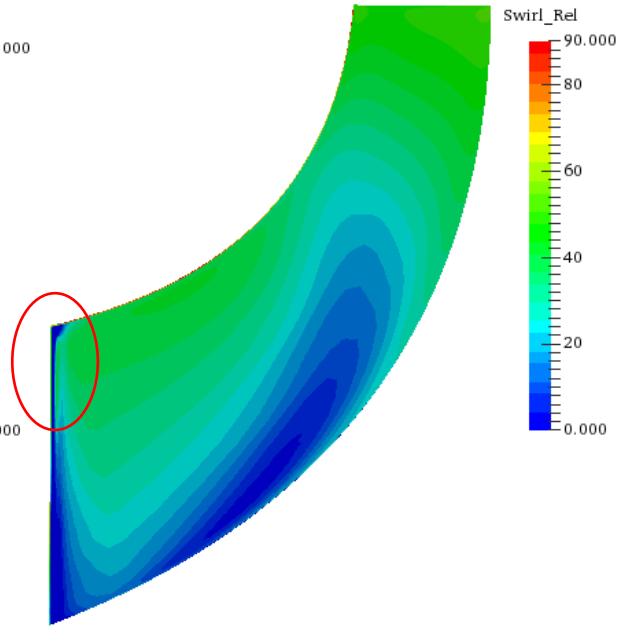

Fig 7.33b

Figure7.33 (a) Relative swirl angle plot on pressure side of splitter blade without undercut (b) Relative swirl angle plot on pressure side of splitter blade with undercut at the leading edge.

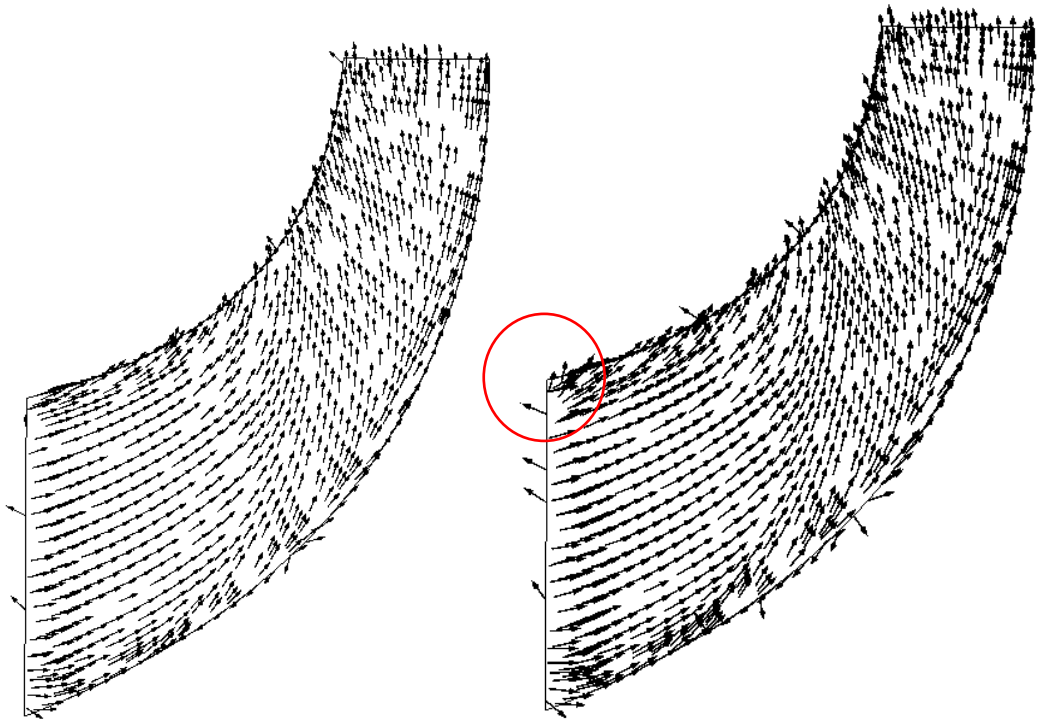

Fig 7.34a Fig .34b

Figure 7.34 (a) Vectors on pressure side of splitter blade without undercut (b) vectors on pressure side of splitter blade with undercut at the leading edge.

Splitter blade suction side plots

Figures 7.35 and 7.36 shows the region of low Mach number and meridional velocity around the leading edge of the splitter blade due to the undercut. The low Mach number and meridional velocity results in a lower mass flow at the design point. Negative swirling flow angle shown in Figures 7.37 and 7.38 is also observed due to the flow detaching from the blade surface as the flow goes around the blade surface at the leading edge. The swirling flow reduces the effective flow area and contributes to the reduced mass flow at the design point.

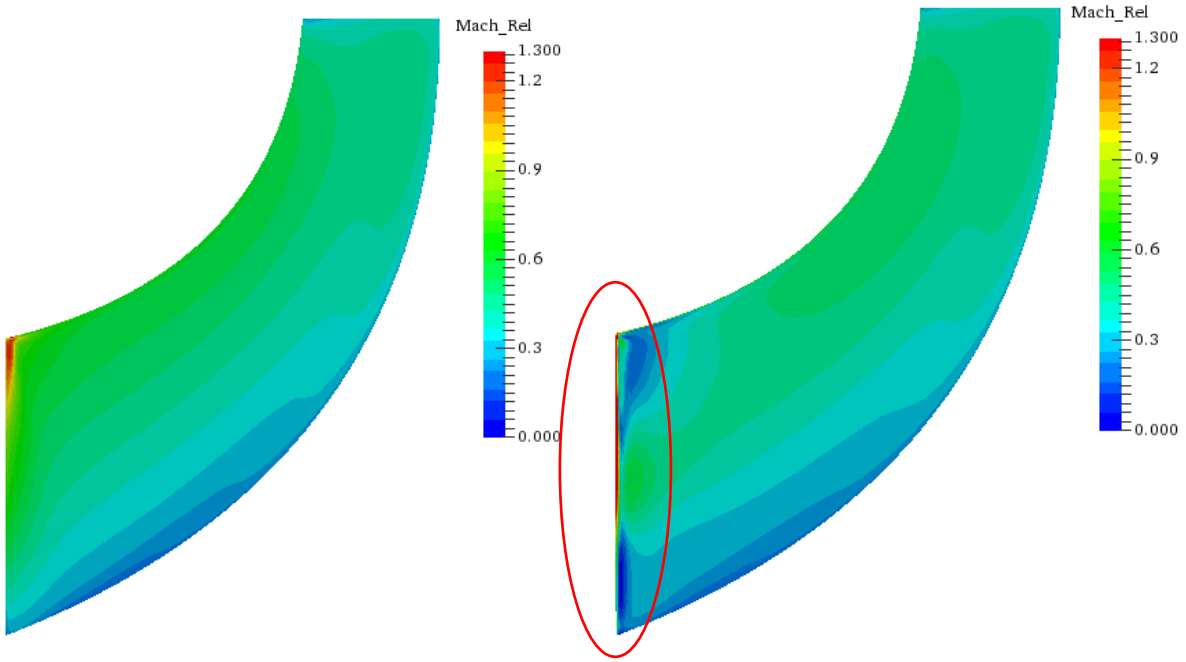

Fig 7.35a Fig 7.35b

Figure 7.35 (a) Relative Mach number on suction side of splitter blade without undercut (b) Relative Mach number on suction side of splitter blade with undercut at the leading edge.

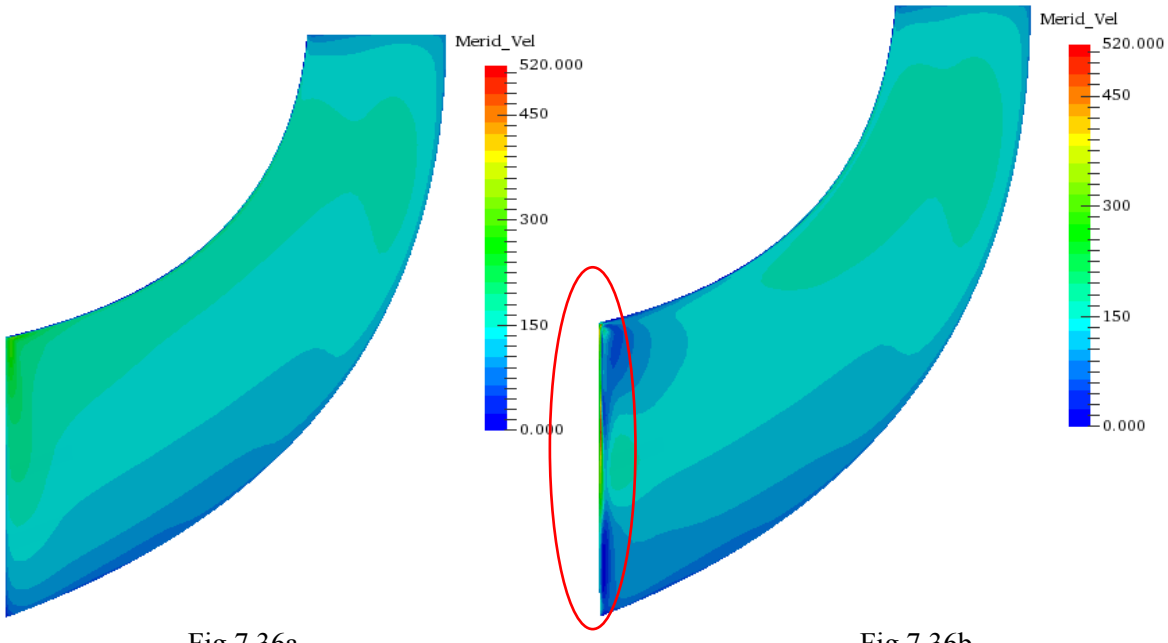

Fig 7.36a Fig 7.36b

Figure 7.36 (a) Meridional velocity on suction side of splitter blade without undercut (b) Meridional velocity on suction side of splitter blade with undercut at the leading edge.

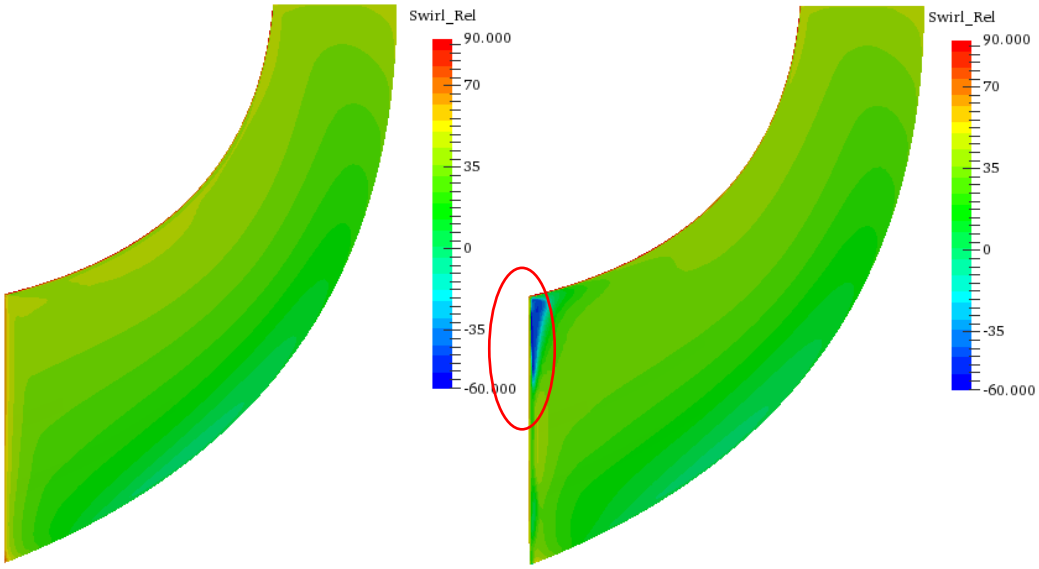

Fig 7.37a Fig 7.37b

Figure 7.37 (a) Relative swirl angle on suction side of splitter blade without undercut (b) Relative swirl angle on suction side of splitter blade with undercut at the leading edge.

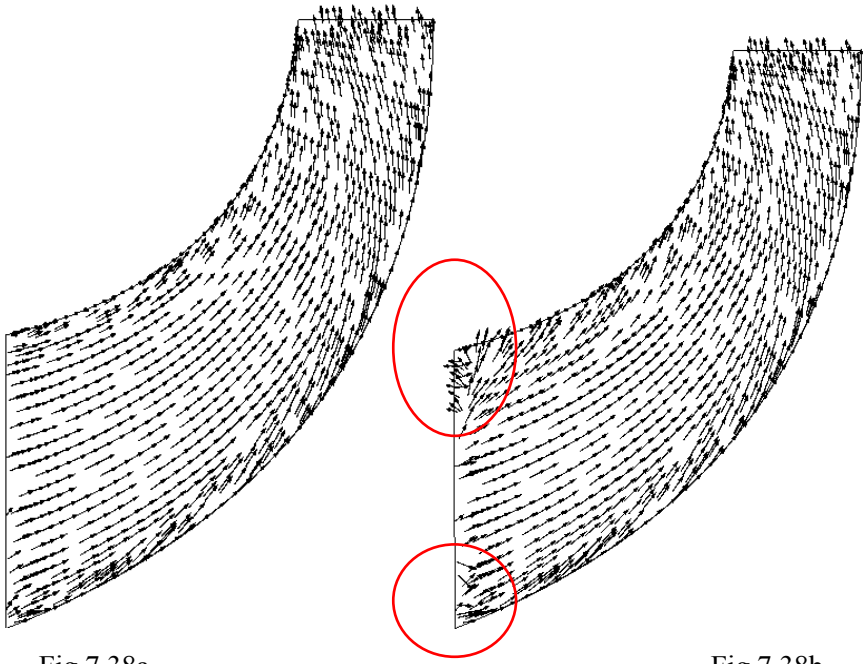

Fig 7.38a Fig 7.38b

Figure 7.38 (a) Velocity vectors on suction side of splitter blade without undercut (b) Velocity vectors on suction side of splitter blade with undercut at the leading edge.

CHOKE POINT

Although the undercut on the leading edge of the splitter blade did not have any impact on choke mass flow, high Mach number at choke reveal the location of the undercut in the Figures 7.39 to 7.43.

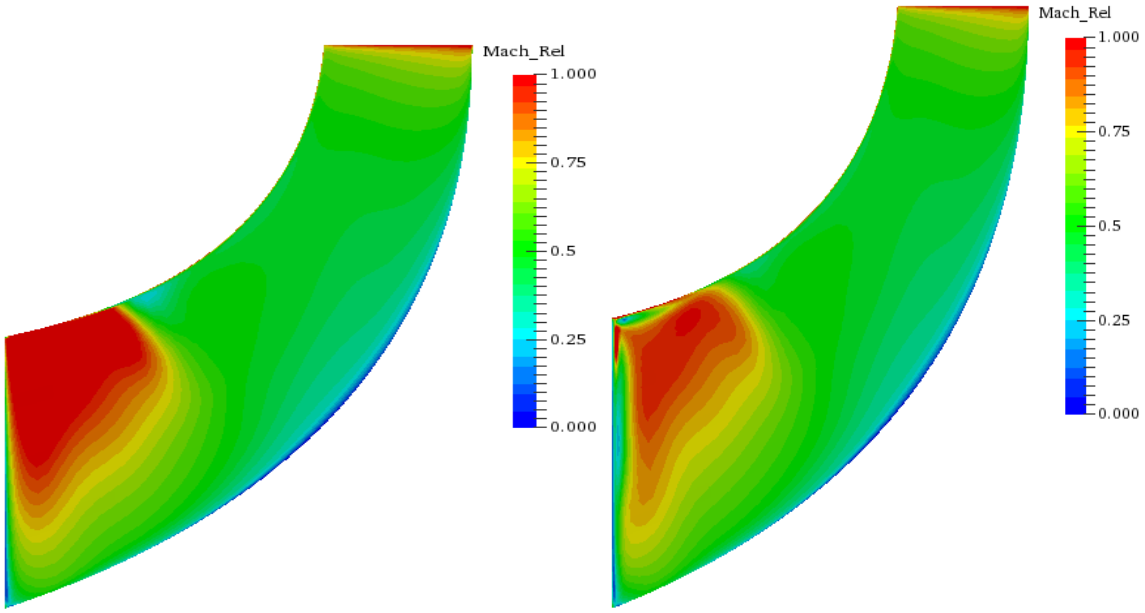

Fig 7.39a Fig 7.39b

Figure 7.39 (a) Relative Mach number plot on pressure side of splitter blade without undercut (b) Relative Mach number plot on pressure side of splitter blade with undercut at the leading edge.

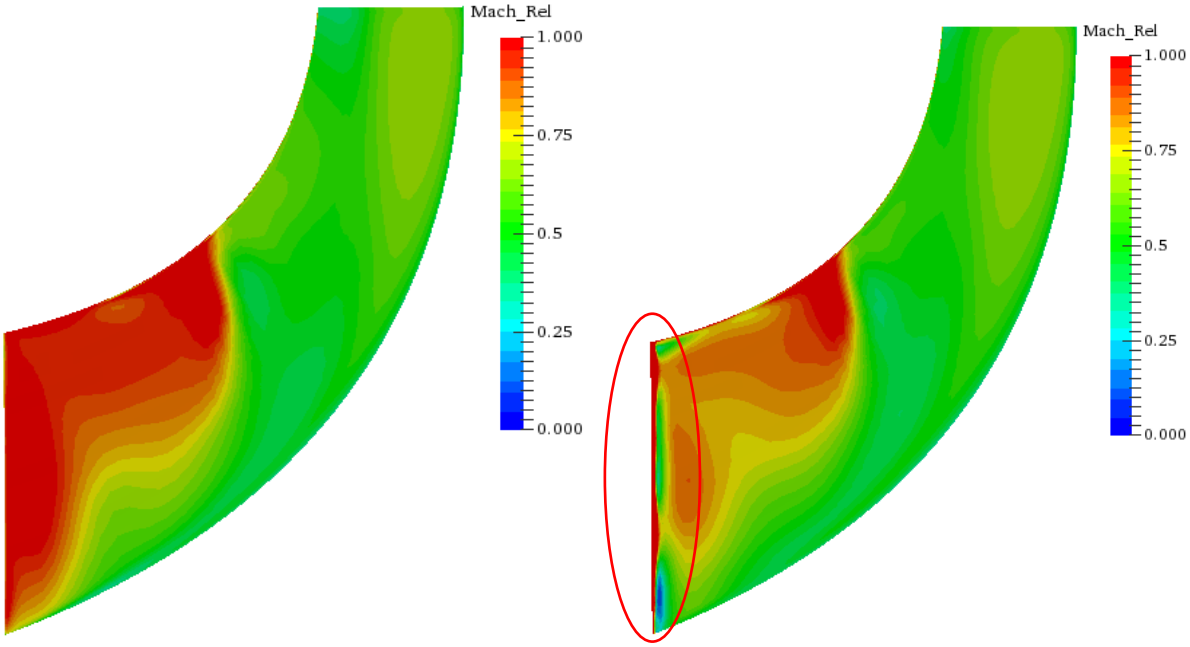

Fig 7.40a Fig 7.40b

Figure 7.40 (a) Relative Mach number plot on suction side of splitter blade without undercut (b) Relative Mach number plot on suction side of splitter blade with undercut at the leading edge.

SURGE POINT

Figure 7.41 plot of Mach number at surge for the reference and undercut geometry shows that the reference geometry has more features of surge flow compared to the undercut geometry. The undercut at the leading edge triggered an early inception of surge, thereby increasing the surge mass flow and lowering the surge pressure ratio. Figure 7.42 also shows more reverse flow at the leading edge and trailing edge in the reference design compared to the undercut design indicating that the surge condition of the undercut design is more stable. Figure 7.43 shows an overall lower meridional velocity for the reference design, the reason for its lower surge mass flow compared to the undercut design.

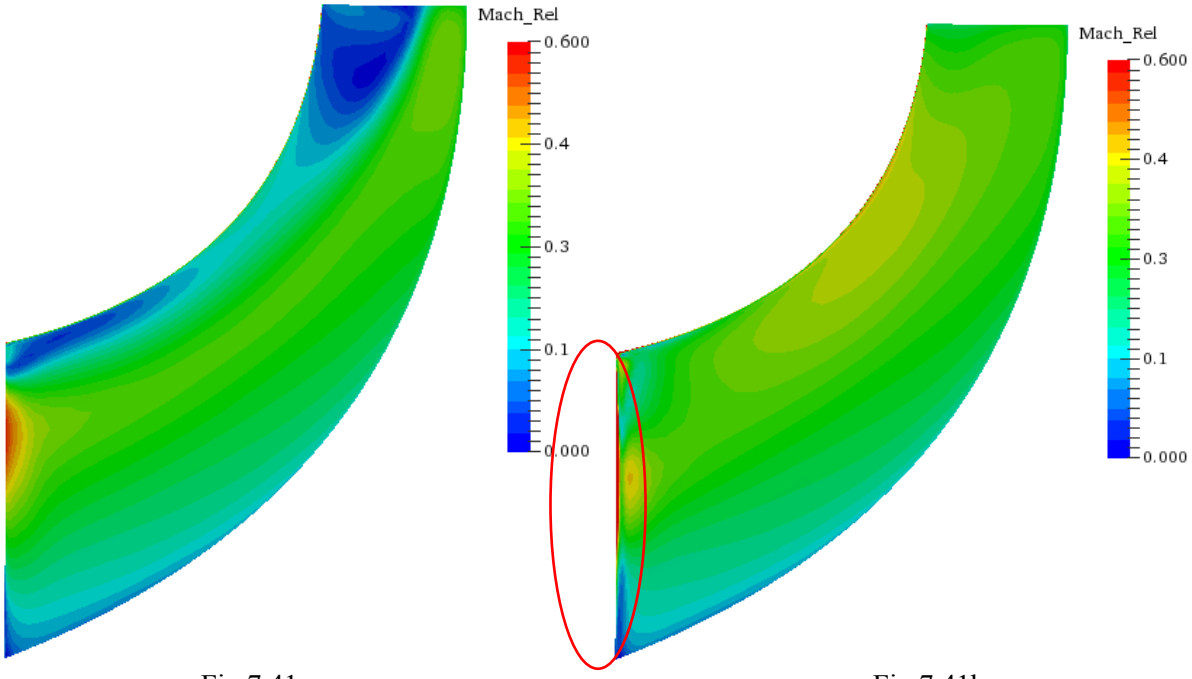

Fig 7.41a Fig 7.41b

Figure 7.41 (a) Relative Mach number plot on suction side of splitter blade without undercut (b) Relative Mach number plot on suction side of splitter blade with undercut at the leading edge.

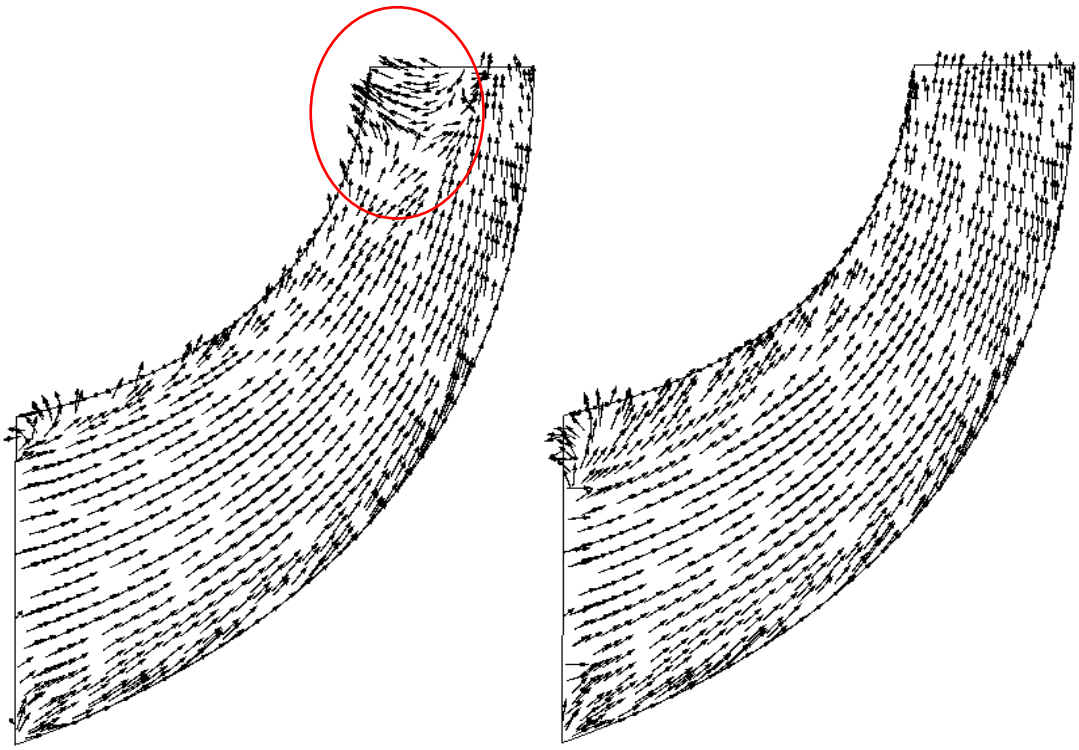

Fig 7.42a Fig 7.42b

Figure 7.42 (a) Velocity vectors on suction side of splitter blade without undercut (b) Velocity vectors on suction side of splitter blade with undercut at the leading edge.

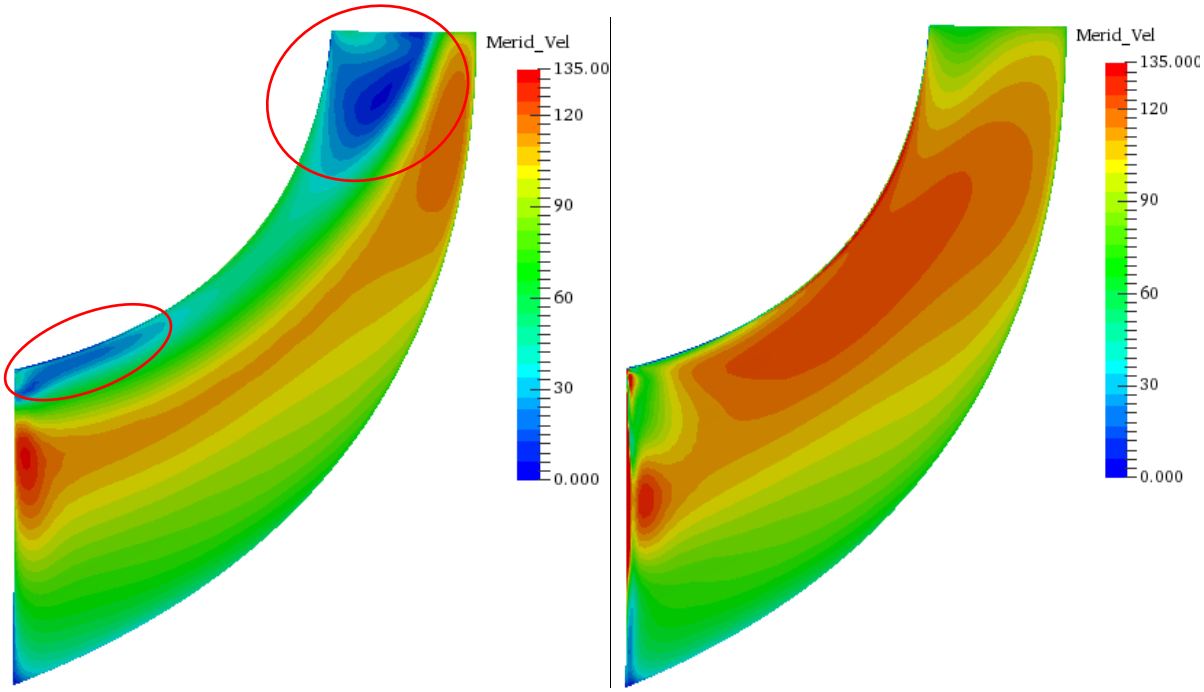

Fig 7.43a Fig 7.43b

Figure 7.43 (a) Meridional velocity on suction side of splitter blade without undercut (b) Meridional velocity on suction side of splitter blade with undercut at the leading edge.

Since surge occurred at a lower pressure ratio in the undercut geometry compared to the reference design, 2.2 and 2.19 in the reference and undercut design respectively, it is necessary to compare CFD results data at the same surge pressure ratio for both cases. The reference geometry was analysed at a pressure ratio of 2.19 and the results are presented side by side with the undercut geometry in Figures 7.44 to 7.49.

The surge mass flow for the reference and undercut design at a total-to-static pressure ratio of 2.19 was 7.85 kg/s and 7.36 kg/s respectively. Figure 7.44 shows lower Mach number around the splitter blade leading edge due to the undercut compared to the reference design. Also, there is larger separation mid-length of the blade along the shroud line in the undercut design compared to the reference design. These flow features explains the lower surge mass flow in the undercut design. Similarly, Figure 7.45 shows overall lower meridional velocity in the undercut design compared to the reference design. This also explains the lower surge mass flow in the undercut design. On the suction side of the blade, the difference in Mach number is more obvious as shown in Figure 7.46. The undercut makes the flow to detach from the blade surface resulting in very low Mach number particularly near the shroud region of the leading edge. The higher Mach number in the reference design also explains the larger surge mass flow in the design. The meridional velocity plot on the suction side of the blade in Figure 7.47 shows a reduction in the meridional velocity just after the undercut due to the flow detaching from the blade surface. Flow separation is effectively a blockage which lowers the surge mass flow in the undercut case. The flow separation is seen in Figure 7.48 where a negative swirl gas angle up to -50 degrees is observed around the shroud of the leading edge. The negative swirl reduces the effective flow area thereby lowering the surge mass flow in the undercut geometry. Figure 7.49 shows the velocity vectors on the suction side of the blade. On the reference design, the vectors are well aligned with the blade profile and mostly uniform. On the undercut design, the some vectors around the leading edge are in the radial/reverse direction indicating instability and inception of surge. Comparing both designs at the same pressure ratio clearly shows that the undercut at the leading edge triggers an early inception of surge by forcing the flow to detach from the blade surface.

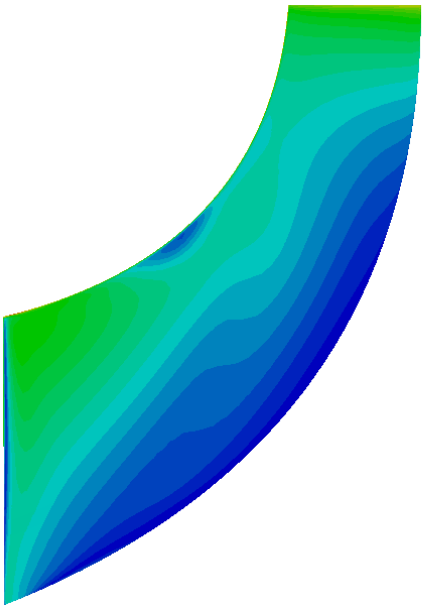

Fig 7.44a

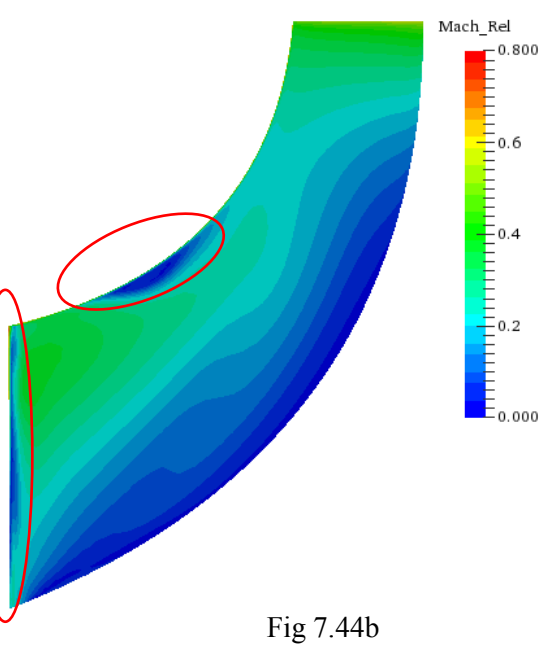

Fig 7.44b

Figure 7.44 (a) Relative Mach number plot on pressure side of splitter blade without undercut (b) Relative Mach number plot on pressure side of splitter blade with undercut at the leading edge.

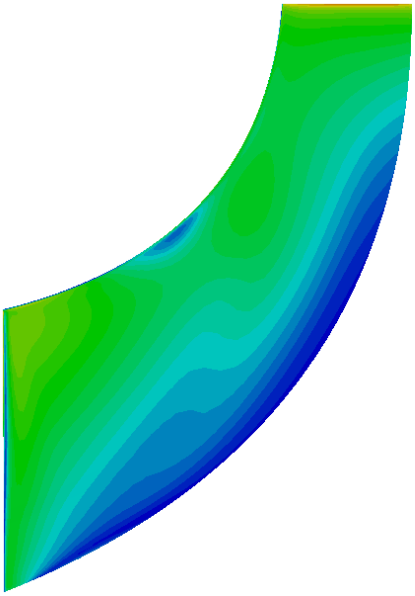

Fig 7.45a

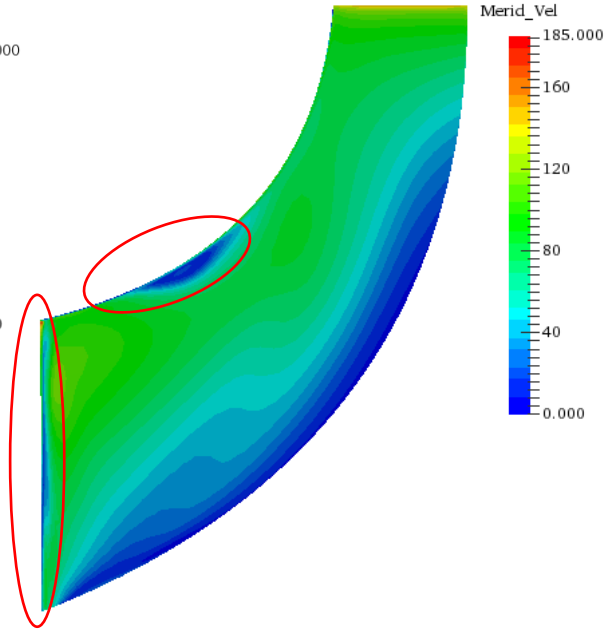

Fig 7.45b

Figure 7.45(a) Meridional velocity on pressure side of splitter blade without undercut (b) Meridional velocity on pressure side of splitter blade with undercut at the leading edge.

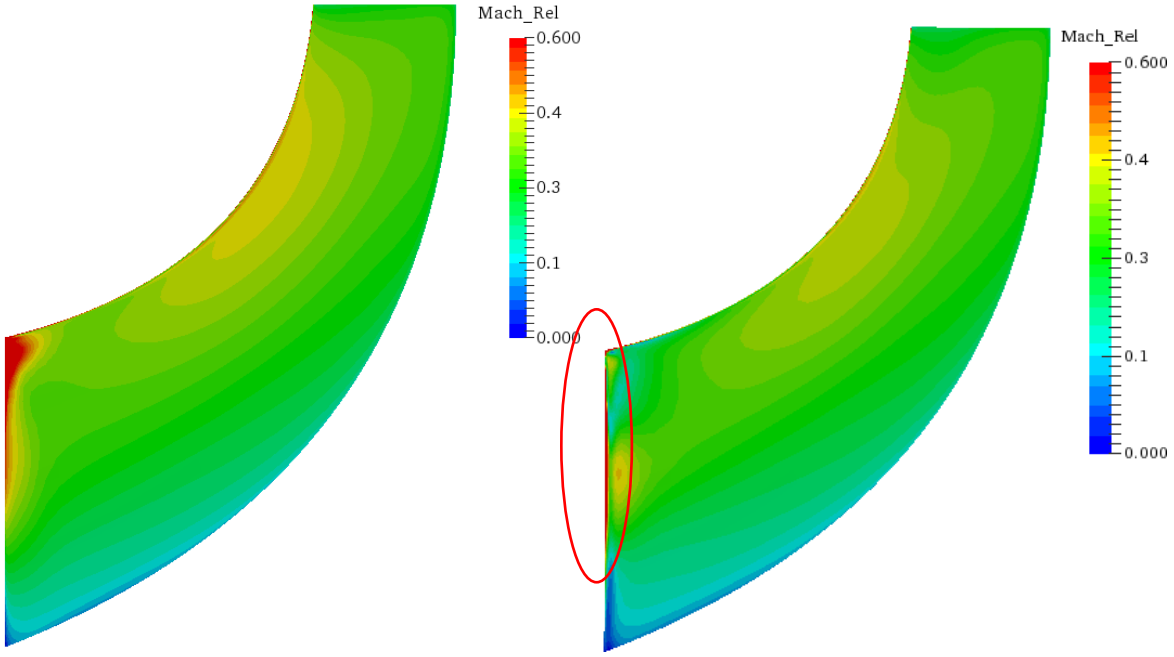

Fig 7.46a Fig 7.46b

Figure 7.46 (a) Relative Mach number plot on suction side of splitter blade without undercut (b) Relative Mach number plot on suction side of splitter blade with undercut at the leading edge.

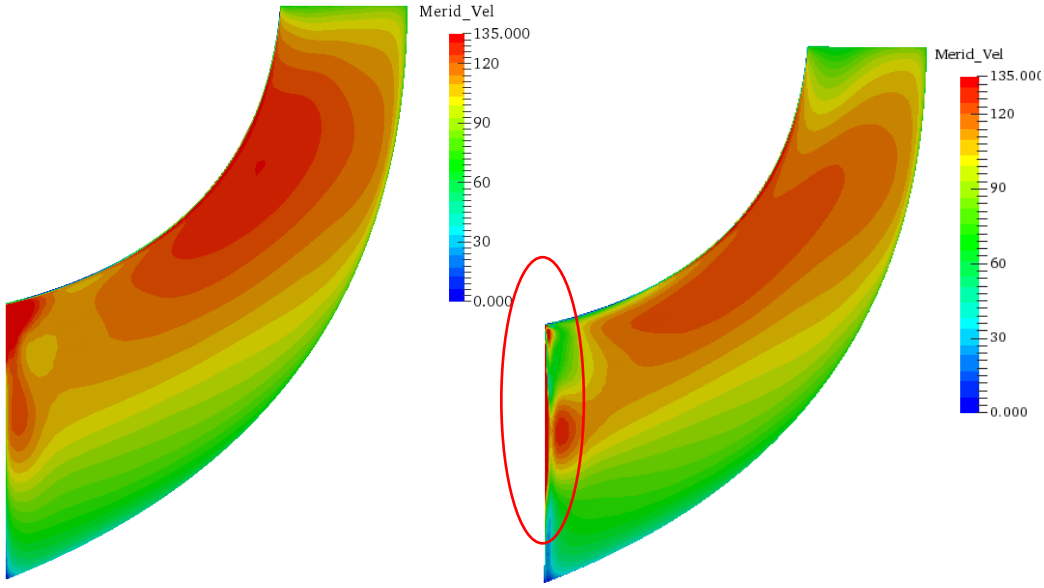

Fig 7.47a Fig 7.47b

Figure 7.47(a) Meridional velocity on suction side of splitter blade without undercut (b) Meridional velocity on suction side of splitter blade with undercut at the leading edge.

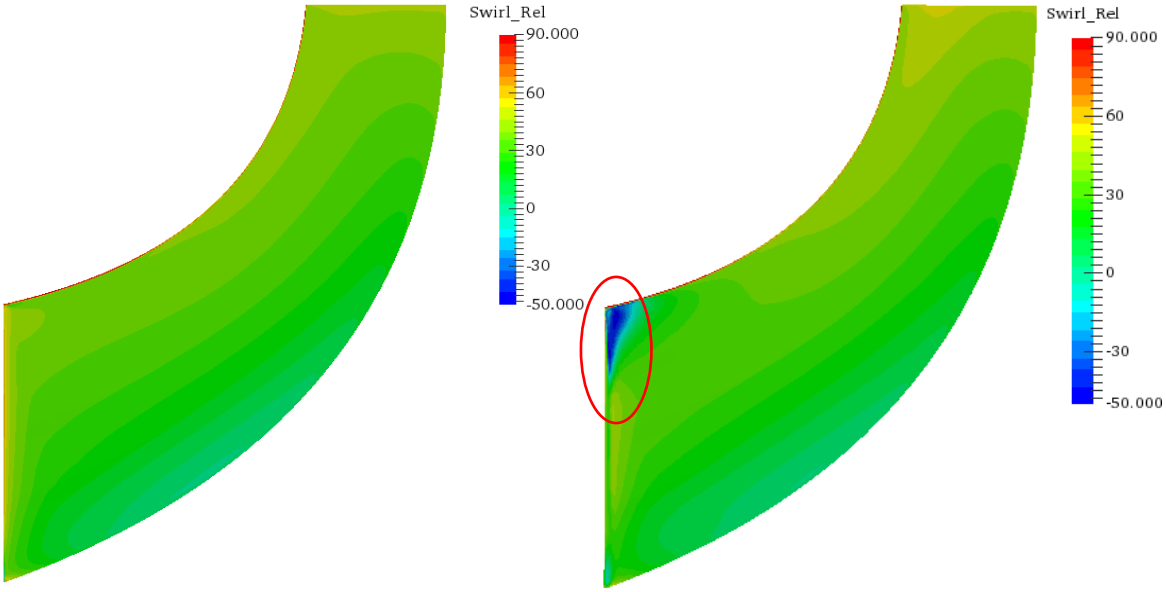

Fig 7.48a Fig 7.48b

Figure 7.48(a) Relative swirl angle on suction side of splitter blade without undercut (b) Relative swirl angle on suction side of splitter blade with undercut at the leading edge.

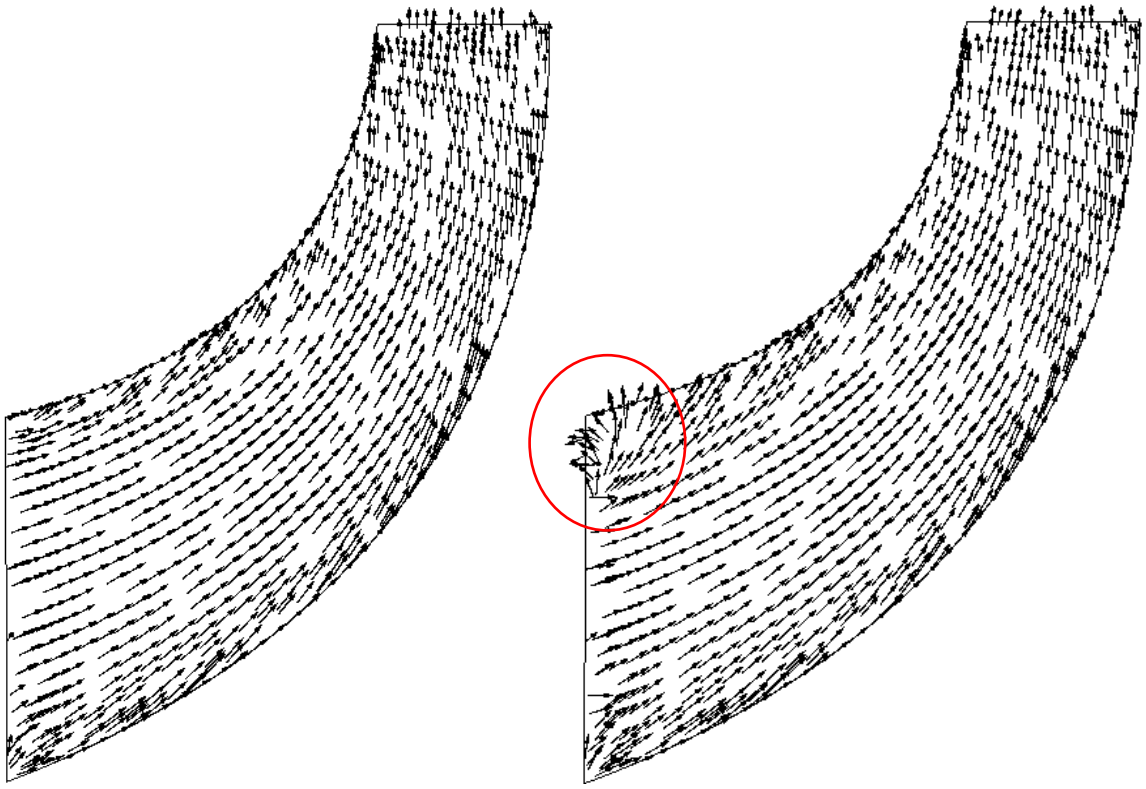

Fig 7.49a Fig 7.49b

Figure 7.49(a) Velocity vectors on suction side of splitter blade without undercut (b) Velocity vectors on suction side of splitter blade with undercut at the leading edge.

7.9.2 Case 2 Flow Visualisation

In this design, the undercut is located at the leading edge of the main blade with a width 1% of the meridional length and the lowest height level of 0.075 mm. Since the undercut is very small in this case, only the few plots that show the impact of undercut on flow features are presented. The reference model without an undercut is compared side by side with the undercut geometry in order to understand the effect of undercut on the flow features. The undercut profile at the hub and shroud of this case is shown in Figure 7.50.

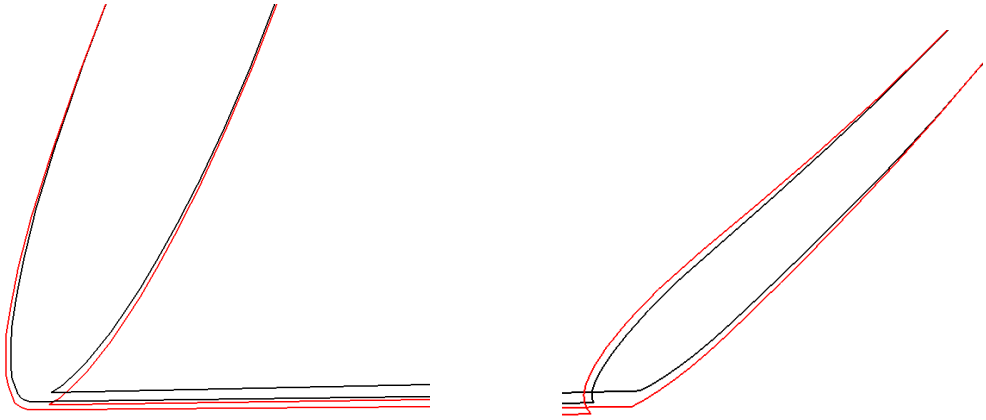

Fig 7.50 (a) Fig 7.50(b)

Figure 7.50 (a) undercut at leading edge of main blade at hub (b) undercut at leading edge of main blade at shroud

DESIGN POINT

The undercut at the leading edge of the main blade had an insignificant (0.11%) change in the design point mass flow. Figure 7.51 shows there is no significant difference in flow features between the undercut design and the reference geometry at the design point.

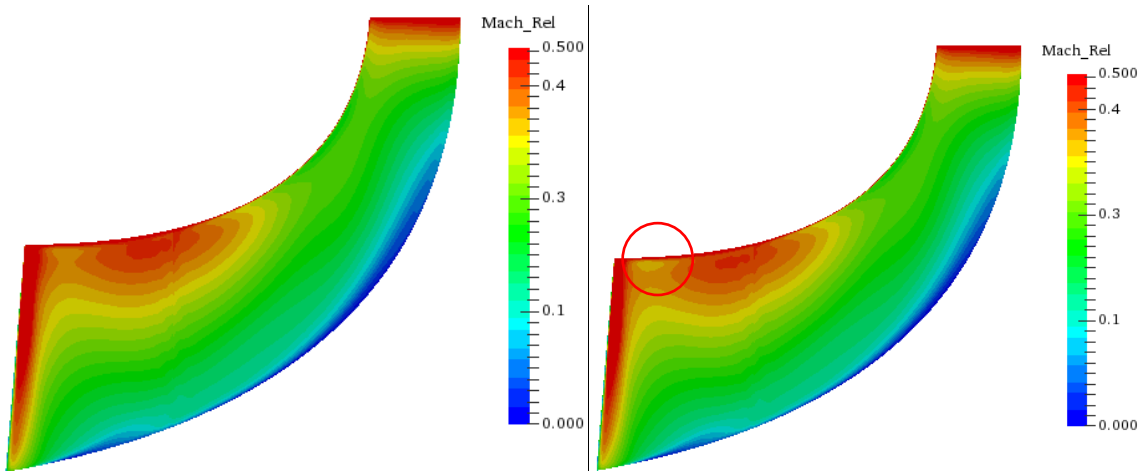

Fig 7.51a Fig 7.51b

Figure 7.51 (a) Relative Mach number plot on pressure side of main blade without undercut (b) Relative Mach number plot on pressure side of main blade with undercut at the leading edge.

CHOKE POINT

The undercut in this case resulted in a significant 1.1% reduction in the choke mass flow compared to the reference design. Figures 7.52 and .53 show an overall lower relative Mach number and meridional velocity in the undercut design case compared to the reference design. The undercut triggers a region of low Mach number, effectively blocking the impeller throat and resulting in reduced impeller capacity. On the suction side of the blade shown in Figure 7.54, the reference geometry shows flow features of a fully choked flow indicated by regions of high Mach number around the splitter blade passage compared to the undercut design.

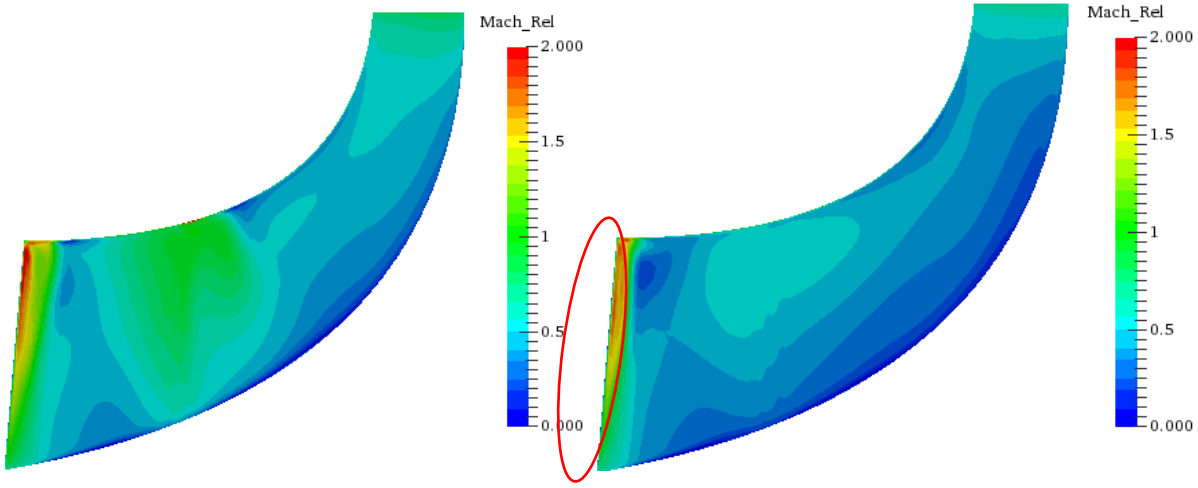

Fig 7.52a Fig 7.52b

Figure 7.52 (a) Relative Mach number plot on pressure side of main blade without undercut (b) Relative Mach number plot on pressure side of main blade with undercut at the leading edge.

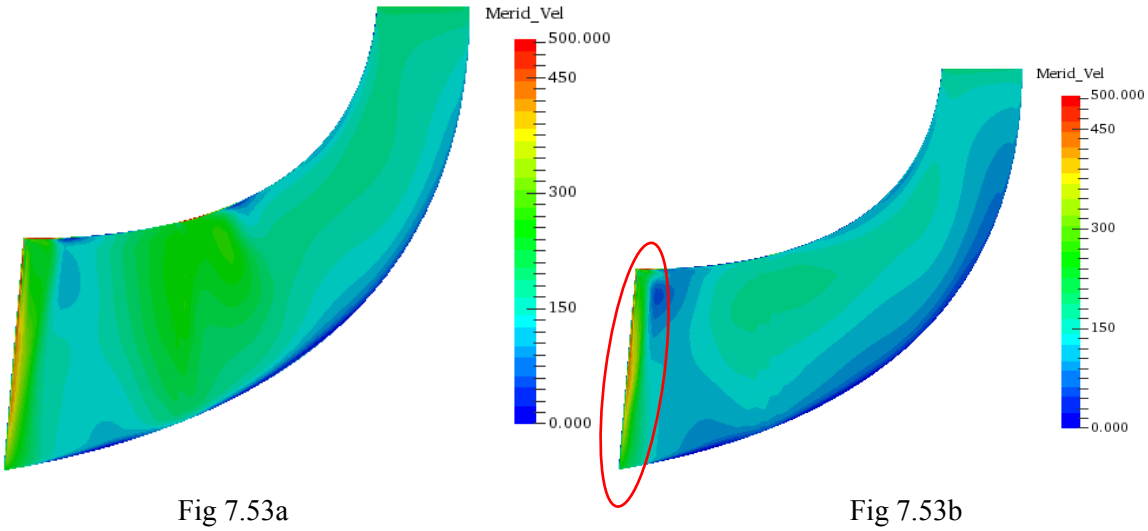

Fig 7.53a Fig 7.53b

Figure 7.53 (a) Meridional velocity plot on pressure side of main blade without undercut (b) Meridional velocity plot on pressure side of main blade with undercut at the leading edge.

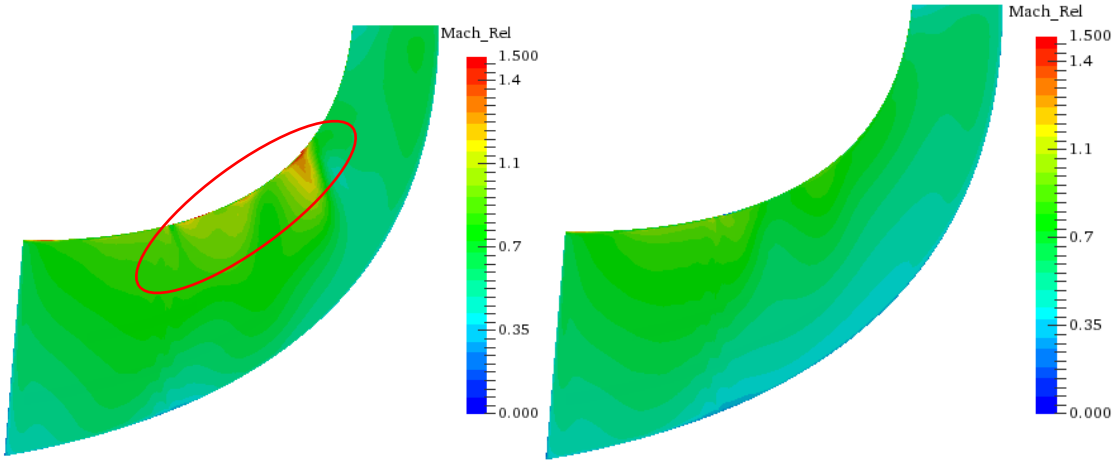

Fig 7.54a Fig 7.54b

Figure 7.54 (a) Relative Mach number plot suction side of main blade without undercut (b) Relative Mach number plot on suction side of main blade with undercut at the leading edge.

SURGE POINT

The undercut at the leading edge in this case resulted in a significant 4.25% increase in the surge mass flow. This means the undercut triggered an early inception of surge by causing the flow to detach from the blade surface. A careful look at Figure 7.55 shows a few of the undercut vectors (red) point slightly upwards around the leading edge compared to the reference black vectors. In this case the surge pressure ratio of the reference geometry and the undercut geometry were the same.

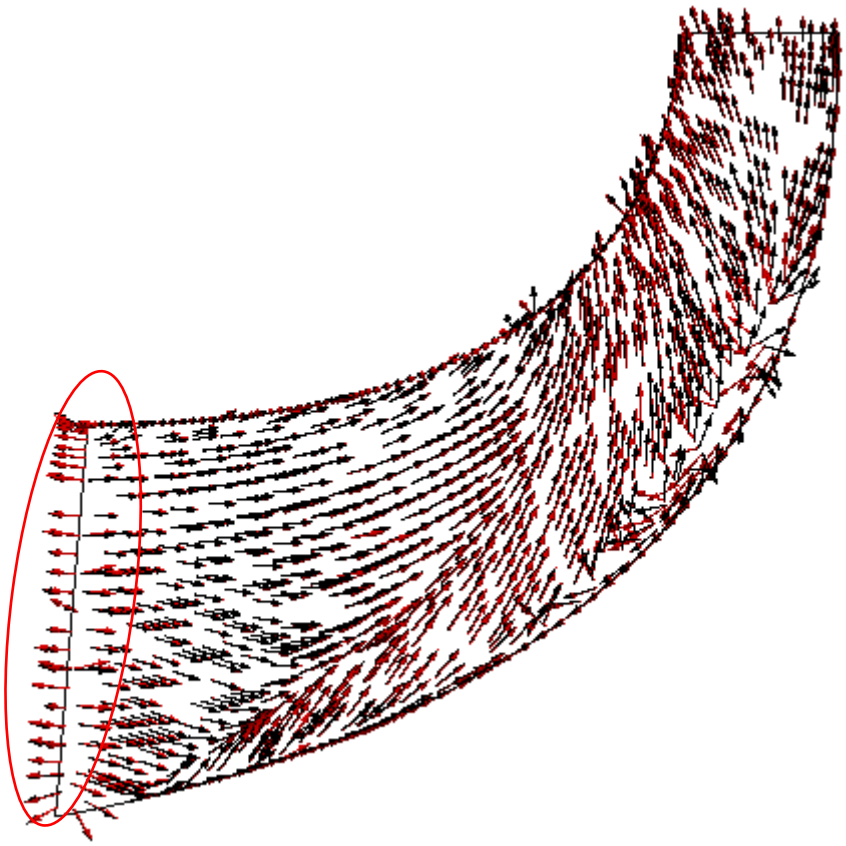

Figure 7.55 Vector plot pressure side of main blade (black) without undercut (red) with undercut

7.9.3 Case 3 Flow Visualisation

In this design, the undercut is located on the pressure side of the main blade with a width 1% of the meridional length and the highest height level of 0.6 mm. Since the undercut is located on the pressure side of the blade, only suction side plots will be presented. The reference model without an undercut is compared side by side with the undercut geometry in order to understand the effect of undercut on the flow features. The undercut profile at the hub and shroud of this case is shown in Figure 7.56.

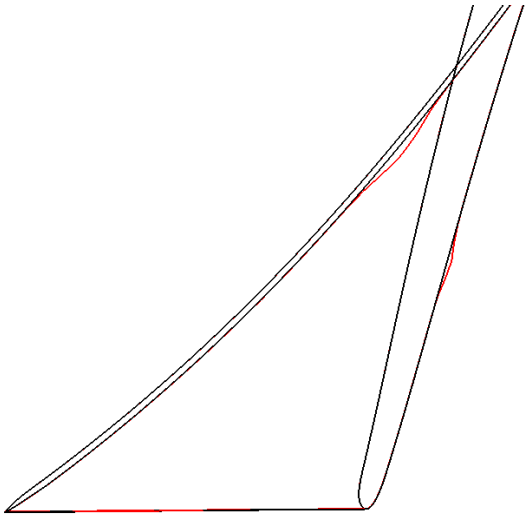

Figure 7.56 - Undercut at the hub and shroud profile

DESIGN POINT

The undercut on the pressure side of the leading edge resulted in an insignificant change of -0.18% in the design point mass flow. Although the impact of the undercut on design point mass flow is insignificant, Figures 7.57 and 7.58 shows the location of the undercut and its impact on relative Mach number and relative swirl angle respectively.

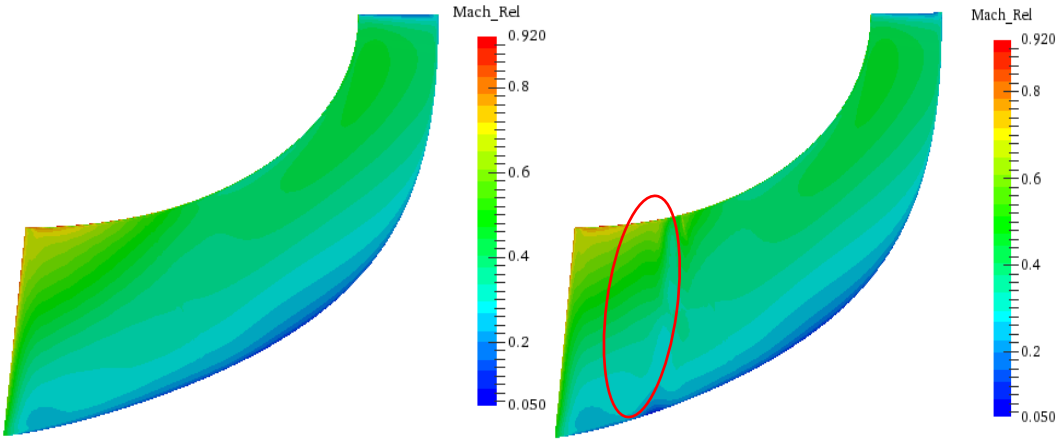

Fig 7.57a Fig 7.57b

Figure 7.57 (a) Relative Mach number on pressure side of main blade without undercut (b) Relative Mach number on pressure side of main blade with undercut

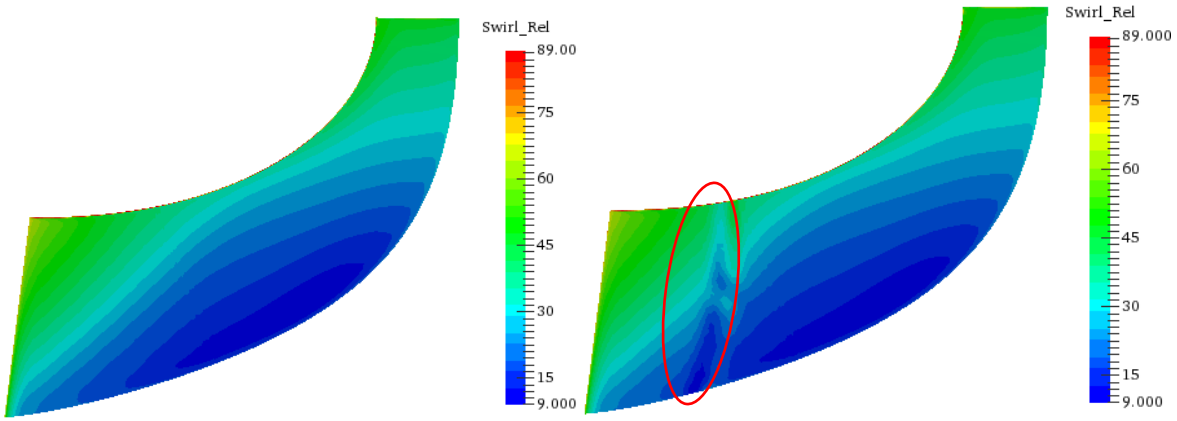

Fig 7.58a Fig 7.58b

Figure 7.58 (a) Relative swirl angle on pressure side of main blade without undercut (b) Relative swirl angle on pressure side of main blade with undercut

CHOKE POINT

The undercut on the pressure side of the blade resulted in a significant reduction in choke mass flow by 2.96%. Figure 7.59 shows the location of the undercut indicated by lower Mach number as the flow goes over the undercut. The undercut effectively reduces the throat area and lowers the choke mass flow. The lower Mach number on the undercut blade surface explains the reduction in choke mass flow due to the undercut. Figure 7.60 shows how the location of the undercut indicated by the change in swirl angle of the flow.

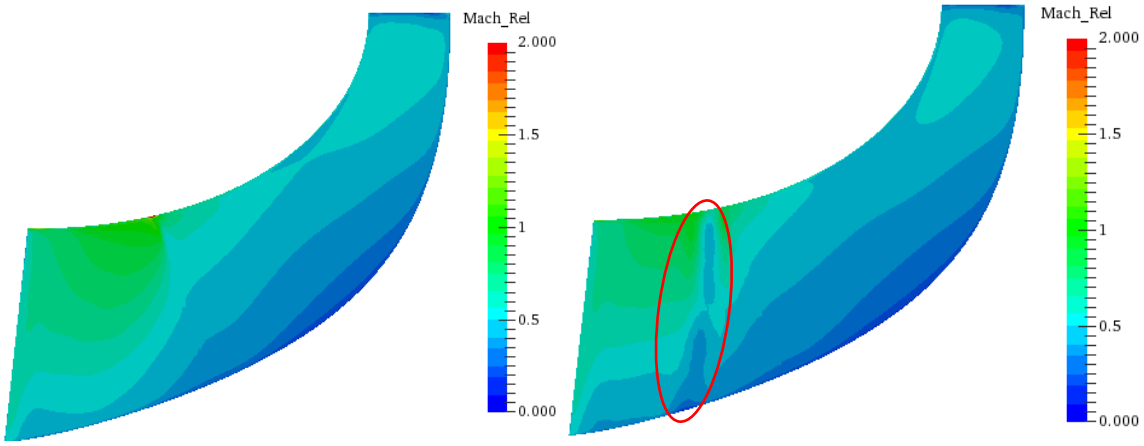

Fig 7.59a Fig 7.59b

Figure 7.59 (a) Relative Mach number on pressure side of main blade without undercut (b) Relative Mach number on pressure side of main blade with undercut

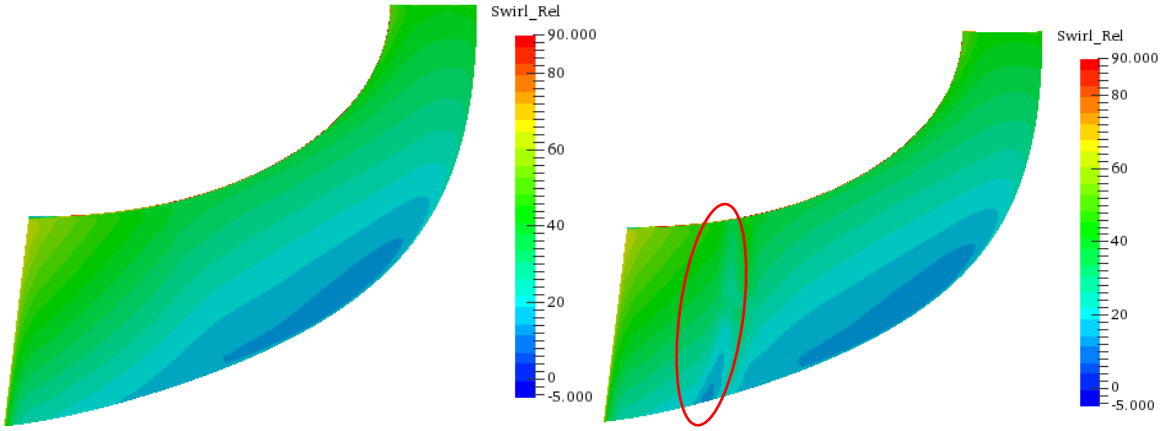

Fig 7.60a Fig 7.60b

Figure 7.60 (a) Relative swirl angle on pressure side of main blade without undercut (b) Relative swirl angle on pressure side of main blade with undercut

SURGE POINT

The undercut at the pressure side of the blade resulted in an increase in surge mass flow by 5.93% compared to the reference geometry without an undercut. Figure 7.61 demonstrates that the reference design show more surge flow features indicated by lower Mach number around the shroud compared to the undercut design. The reference and undercut geometries surged at pressure ratios of 2.125 and 2.109 respectively. The undercut design may have triggered an early inception of stall by causing the flow to separate from the blade surface at a lower pressure ratio. Figure 7.62 shows the instability in the flow introduced by the undercut on the blade.

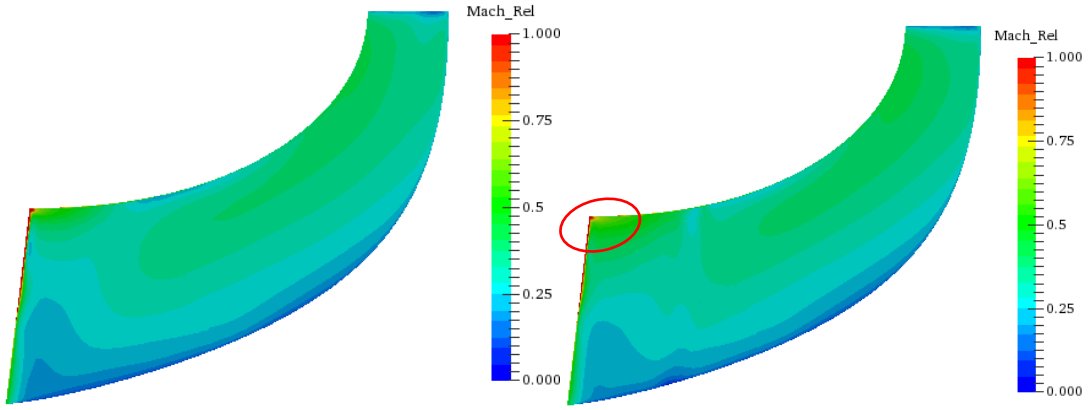

Fig 7.61a Fig 7.61b

Figure 7.61 (a) Relative Mach number on pressure side of main blade without undercut (b) Relative Mach number on pressure side of main blade with undercut

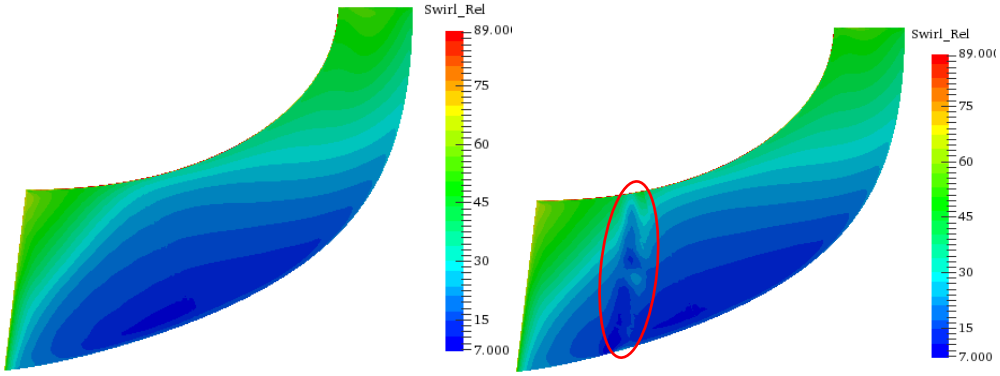

Fig 7.62a Fig 7.62b

Figure 7.62 (a) Relative swirl angle on pressure side of main blade without undercut (b) Relative swirl angle on pressure side of main blade with undercut

Since surge occurred at a lower pressure ratio in the undercut design compared to the reference design, at 2.125 and 2.109 in the reference and undercut design respectively, it is necessary to compare CFD results data at the same surge pressure ratio for both cases. The reference geometry was analysed at a pressure ratio of 2.109 and the results are presented side by side with the undercut geometry in Figures 7.63 and 7.64. The surge mass flow for the reference and undercut design at a total-to-static pressure ratio of 2.109 is 7.17 kg/s and 7.11 kg/s respectively. Figures 7.63 and 7.64 shows the relative Mach number and relative swirl angle respectively of the reference and undercut designs. There is no significant difference in flow features between the reference and undercut cases except at the location of the undercut. This explains the insignificant difference in mass flow rate in both cases. The instability introduced to the flow field by the undercut makes the design to surge at a pressure ratio greater than 2.109, while the reference geometry remains stable at a higher pressure ratio.

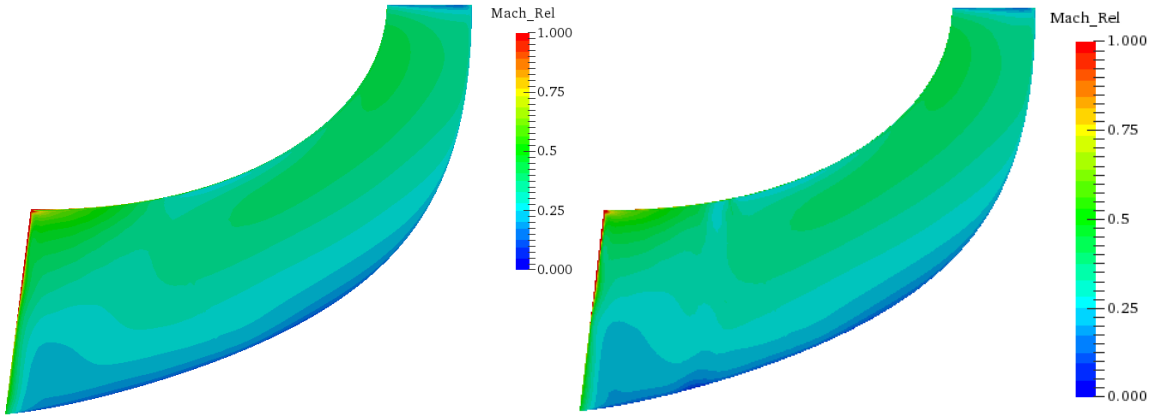

Fig 7.63a Fig 763b

Figure 763 (a) Relative Mach number on pressure side of main blade without undercut (b) Relative Mach number on pressure side of main blade with undercut

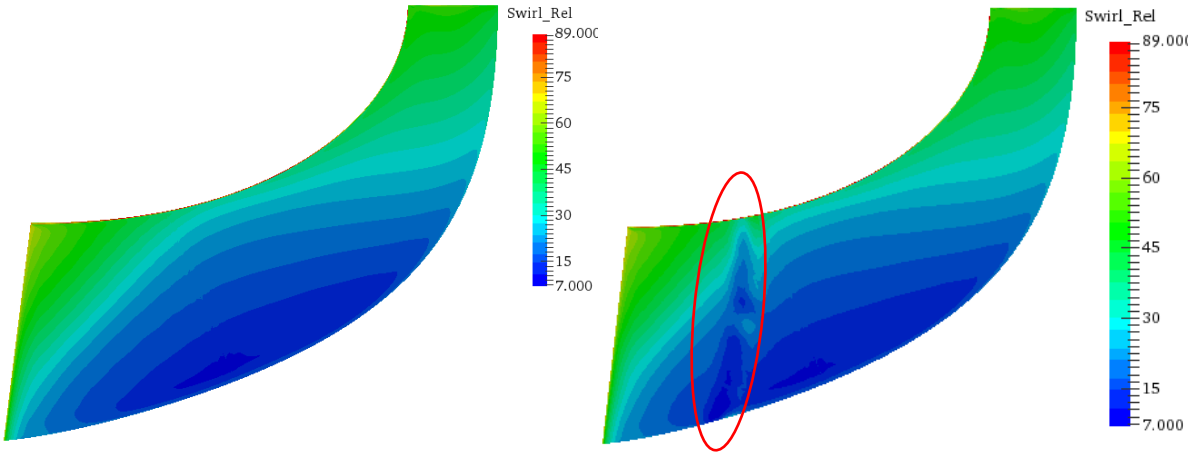

Fig 7.64a Fig 7.64b

Figure 7.64 (a) Relative swirl angle on pressure side of main blade without undercut (b) Relative swirl angle on pressure side of main blade with undercut

7.9.4 Case 4 Flow Visualisation

In this design, the undercut is located on the suction side of the main blade with a width 1% of the meridional length and the highest height level of 0.6 mm. Since the undercut located on the pressure side of the blade, only pressure side plots will be presented. The reference model without an undercut will be compared side by side with the undercut geometry in order to understand the effect of undercut on the flow features. The undercut profile at the hub and shroud of this case is shown in Figure 7.65.

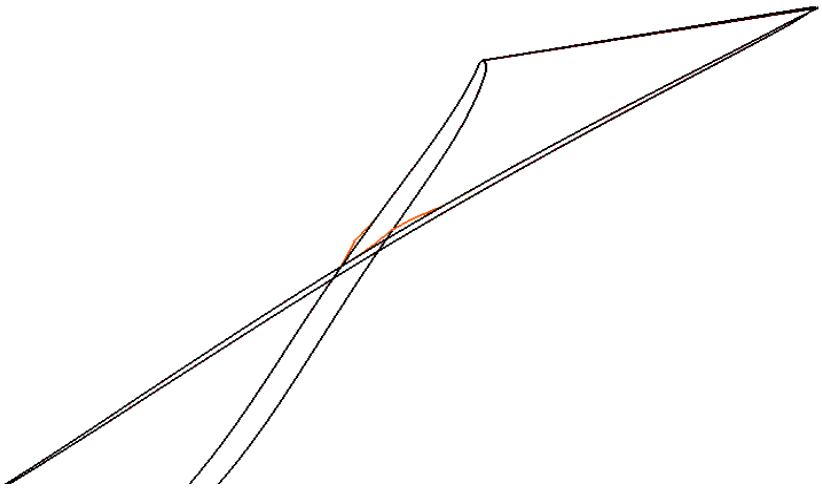

Figure 7.65 - Undercut at hub and shroud of ADT design

DESIGN POINT

The impact of the undercut on the design point mass flow was an insignificant reduction by 0.6%. The flow features on the reference and undercut geometry were exactly the same except around the location of the undercut as shown in Figure 7.66. Also, in Figure 7.67, there is no difference between the reference geometry and the undercut geometry. These observations explain the insignificant change in design mass flow due to the undercut on the pressure side of the blade. The undercut, however, may have triggered an early inception of stall.

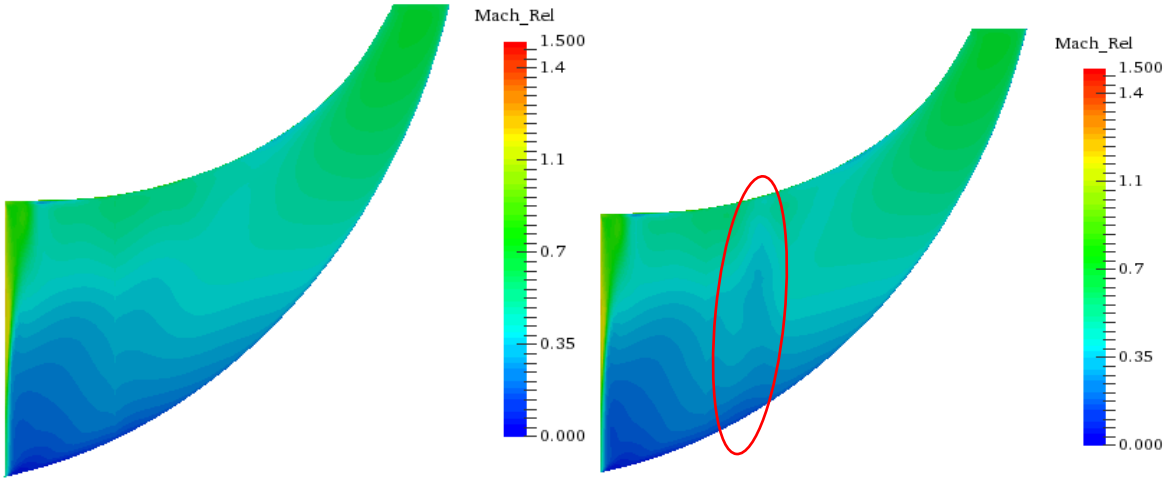

Fig 7.66a Fig 7.66b

Figure 7.66 (a) Relative Mach number on pressure side of main blade without undercut (b) Relative Mach number on pressure side of main blade with undercut

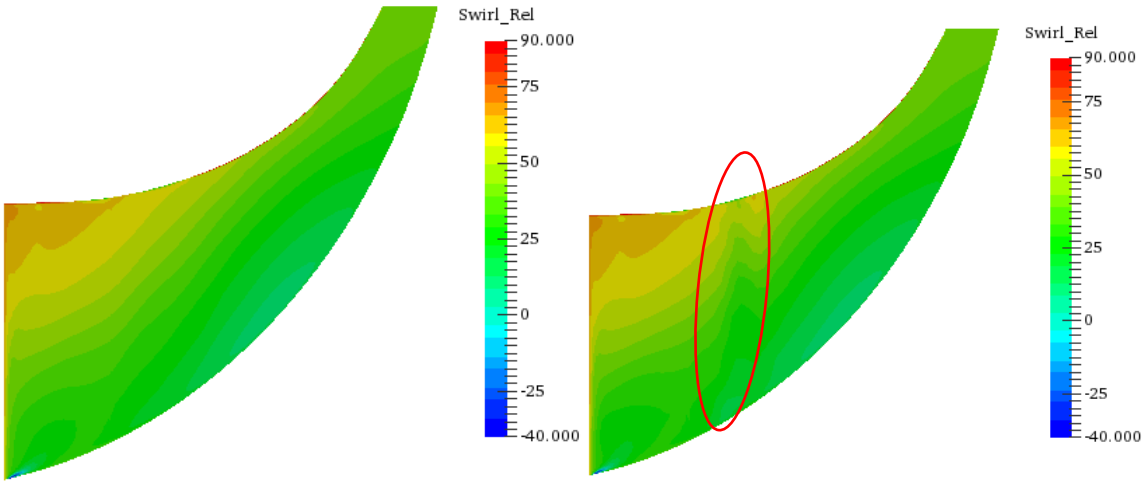

Fig 7.67a Fig 7.67b

Figure 7.67 (a) Relative swirl angle on suction side of main blade without undercut (b) Relative swirl angle on suction side of main blade with undercut

CHOKE POINT

The undercut on the pressure side of the blade resulted in a reduction in choke mass flow by 1.27%. Figures 7.68 and 7.69 shows there is no significant difference in flow features between the reference and undercut designs. The undercut does not seem to influence the flow field upstream and downstream of the undercut.

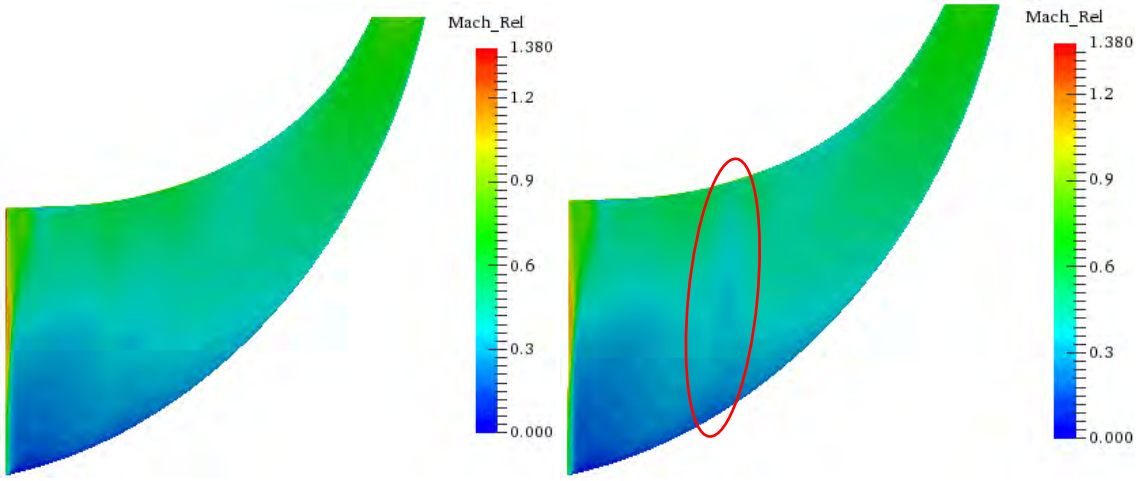

Fig 7.68a Fig 7.68b

Figure 7.68 (a) Relative Mach number on pressure side of main blade without undercut (b) Relative Mach number on pressure side of main blade with undercut

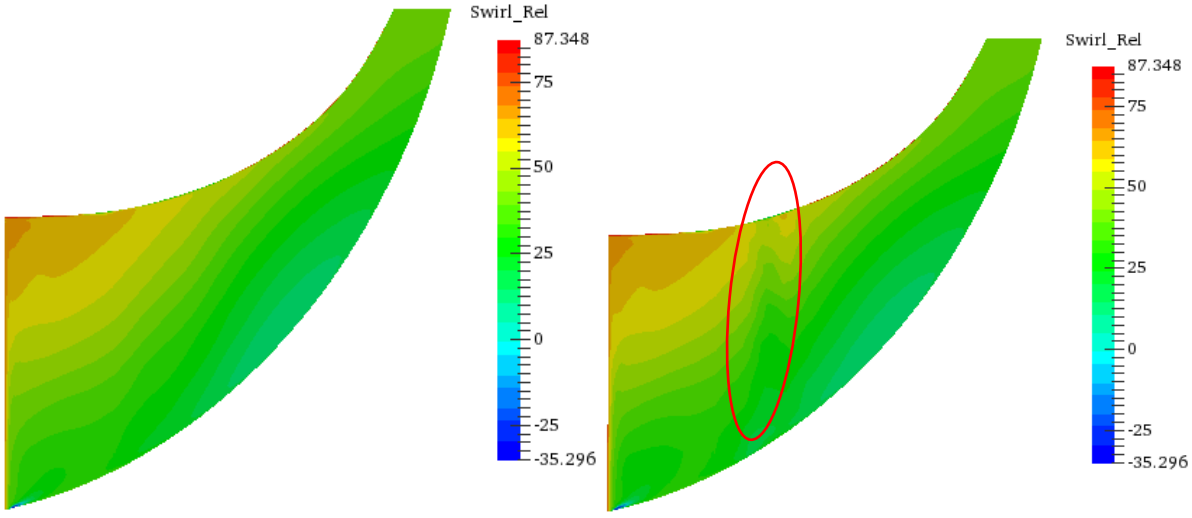

Fig 7.69a Fig 7.69b

Figure 7.69 (a) Relative swirl angle on suction side of main blade without undercut (b) Relative swirl angle on suction side of main blade with undercut

SURGE POINT

The undercut on the pressure side of the blade resulted in an increase in surge mass flow by 6.83%. The undercut on the blade surface caused the design to surge at a lower pressure compared to the reference design. The surge pressure ratio for the reference and undercut design is 2.57 and 2.23 respectively, while the peak efficiency reduced by 4.18% compared to the reference design. The lower peak efficiency compared to the reference design is due to higher efficiency in the reference design towards surge, while the undercut design had narrower characteristic and lower efficiencies. Figure 7.70 shows lower relative Mach number on the blade surface of the reference design indicative of its lower surge mass flow. Figure 7.71 does not say much about the impact of the undercut on surge mass flow, but it shows the location of the undercut. Figure 7.72 shows the vector plot of the reference design (black vectors) and undercut design (red vectors). A close look at the undercut vectors in the inducer region up to the location of the undercut shows the reference design vectors points more in the radial direction indicating it is further in surge.

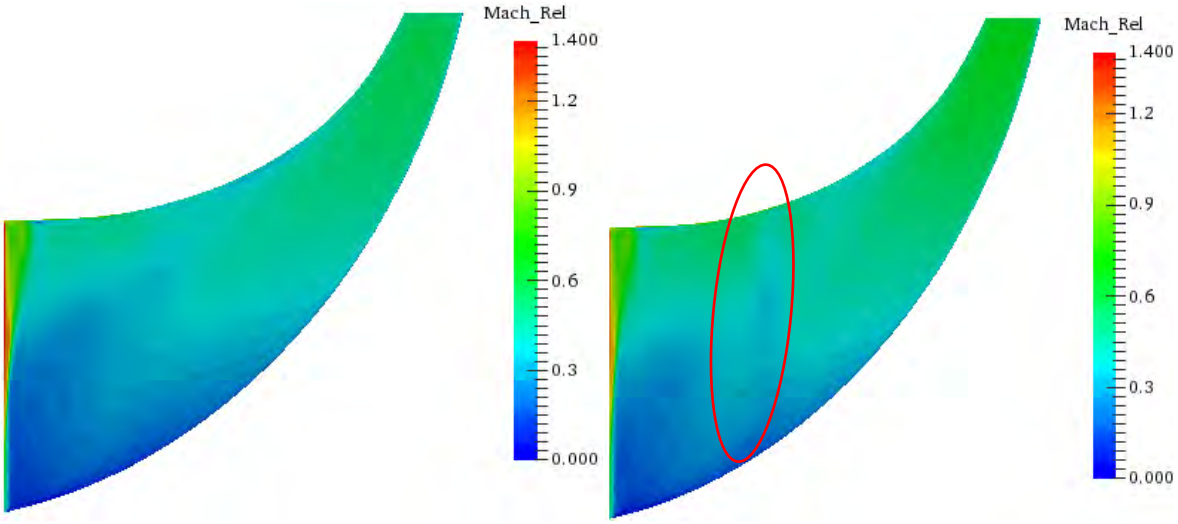

Fig 7.70a Fig 7.70b

Figure 7.70 (a) Relative Mach number on pressure side of main blade without undercut (b) Relative Mach number on pressure side of main blade with undercut

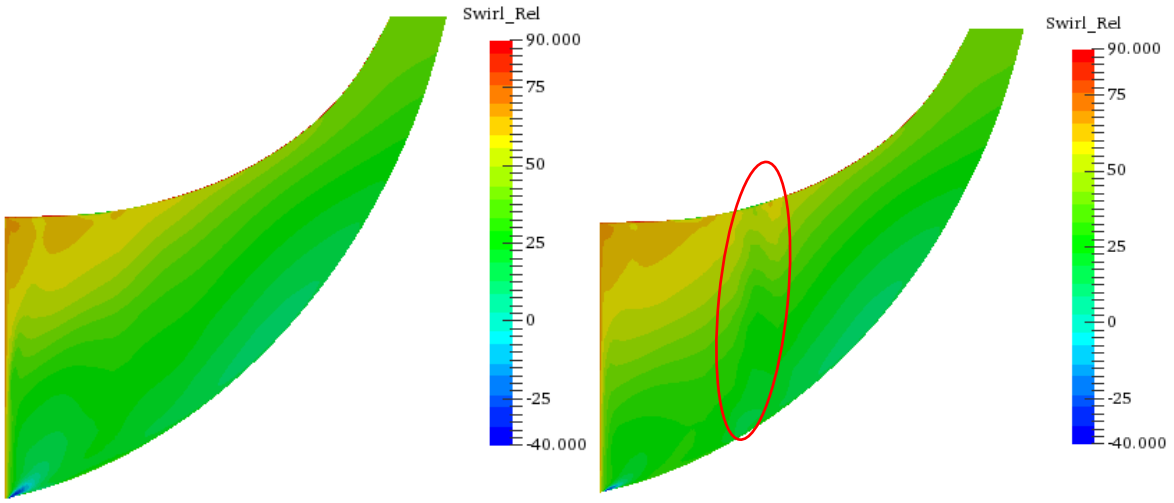

Fig 7.71a Fig 7.71b

Figure 7.71 (a) Relative swirl angle on pressure side of main blade without undercut (b) Relative swirl angle on pressure side of main blade with undercut

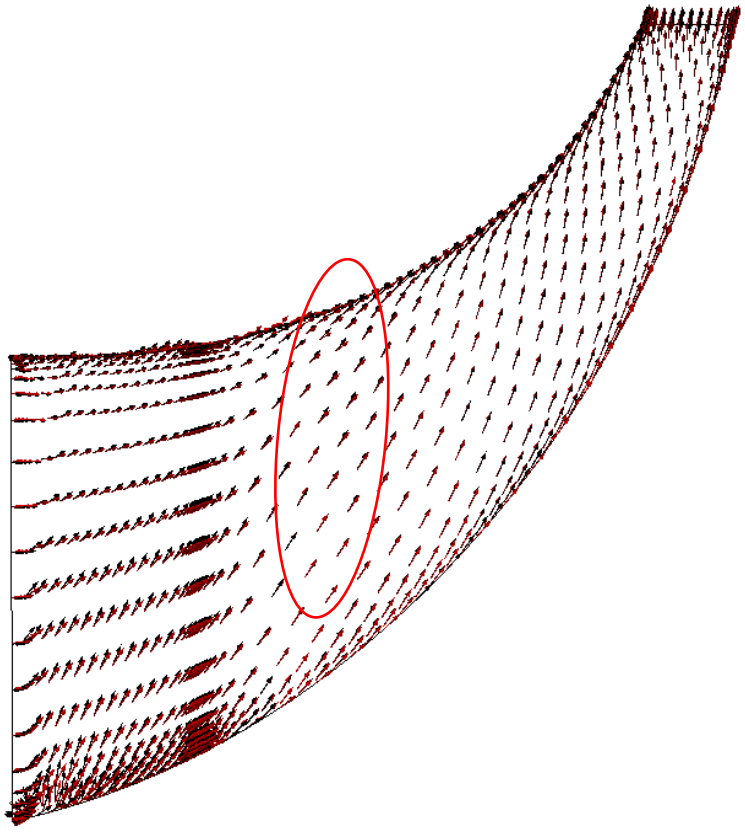

Figure 7.72 – Vector plots of reference (black) and undercut (red) designs

The surge pressure ratio for the reference and undercut design was 2.57 and 2.23. It is important to compare the flow features of both designs at the same pressure ratio, so the reference design is analysed at

the same surge pressure ratio of 2.23 as the undercut design. Figures 7.73 and 7.74 show relative Mach number and relative swirl angle plots respectively for both designs at a pressure ratio of 2.23. The mass flow at this pressure ratio is 2.288 kg/s and 2.275 kg/s for the reference and undercut designs respectively. Figure 7.73 shows the relative Mach number on the blade surface is the same on both cases except around the region of the undercut due to a change in direction of the flow. The lower Mach number explains the lower mass flow rate in the undercut design compared to the reference design at this pressure ratio. Figure 7.74 shows the change in relative swirl angle due to the undercut. There is no difference in the swirl angle distribution between the reference and undercut design, except at the undercut location. Although Figures 7.73 and 7.74 do not show clear difference in flow features between the reference and undercut design, it does indicate the presence of an undercut may have introduced instability that developed into surge at a slightly higher pressure ratio. Also at the same pressure ratio of 2.23, the undercut design mass flow is lower compared to the reference design indicating the inception of stall.

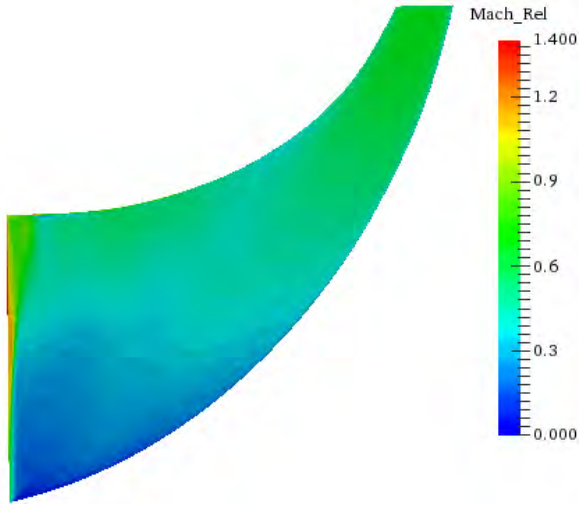

Fig 7.73a

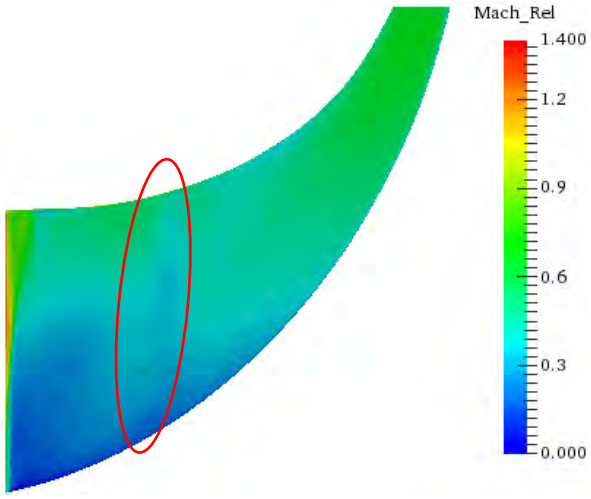

Fig 7.73b

Figure 7.73 (a) Relative Mach number on pressure side of main blade without undercut (b) Relative Mach number on pressure side of main blade with undercut

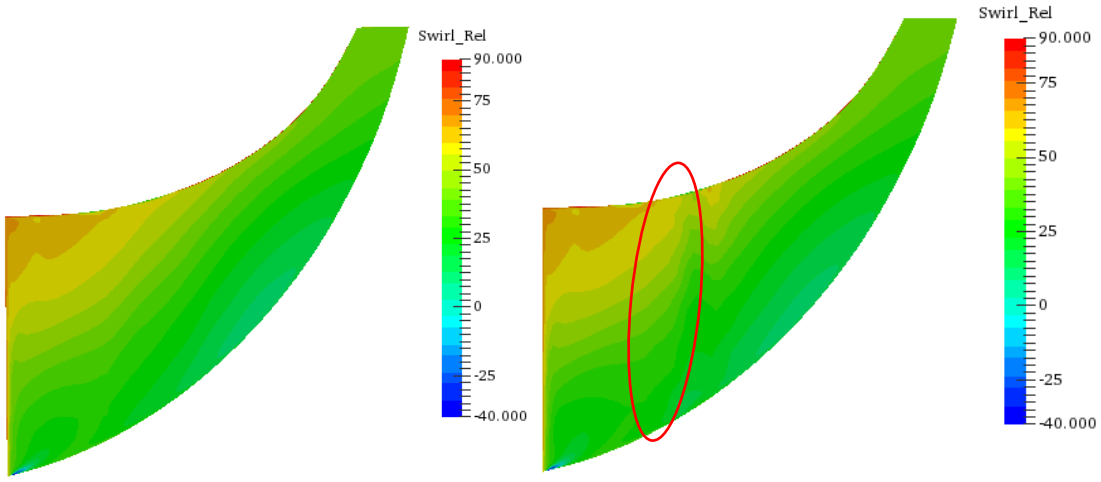

Fig 7.74a Fig 7.74b

Figure 7.74 (a) Relative swirl angle on pressure side of main blade without undercut (b) Relative swirl angle on pressure side of main blade with undercut

7.10 SCREENING TEMPLATES

One of the major contributions of this research work is the concept of a screening template or "heat map" which is a visual method for judging if a particular undercut height and width, at a given location on the impeller surface would not impact on the performance of the compressor. The heat maps generated are shown in the Figures in this Section. The sensitivity value presented in the plots is calculated using the maximum absolute value of sensitivities (e.g. choke mass flow, surge mass flow) if any of the sensitivity value for a given undercut is greater than 0.5%. On the other hand, if all the sensitivity values are less than 0.5, the minimum sensitivity is used. This approach ensures that the sensitivity is over-stated in cases where the undercut results in a significant change in any of the performance parameters.

The screening templates presented are grouped into two categories – one including the surge mass flow sensitivity and the other without surge mass flow. This is done to qualitatively visualise the impact of ignoring surge mass flow sensitivity on the screening template, as surge mass flow sensitivity is observed to be significantly higher than other variables in some cases. The plots are presented for each design to visually compare their sensitivities. The key to the heat map is shown in Table 7.11 where undercut width levels as row indexes and undercut height levels as column headers. An example screening template showing the undercut numbering is shown in Figure 7.75. For example, in Figure 7.75, peak sensitivity of 16.744% is at the leading edge. Tracing the peak efficiency to the numbers at the top corresponds to number 2 (which is an undercut with 0.1 mm height and 0.01 fraction of meridional length wide

according to Table 7.11). The pressure side has negative location numbers while the suction side has positive location numbers. The screening template is a very quick way to qualitatively compare the sensitivities of the various designs. The screening template is plotted using Paraview [7] visualisation software and the data is interpolated linearly within the software.

Width\Height	0.75 (mm)	0.1 (mm)	0.25 (mm)	0.6 (mm)
0.01	1	2	3	4
0.02	5	6	7	8
0.05	9	10	11	12
0.1	13	14	15	16

Table 7.11 – Numbering on heat map

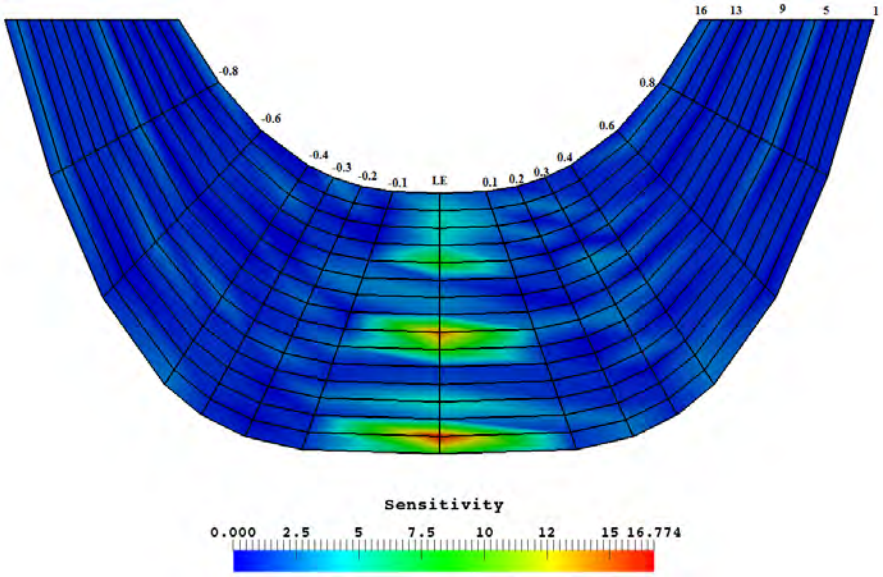

Figure 7.75 – Example screening template numbering

Using the screening template with surge shown in Figures 7.76 to 7.87, it is important to extract some useful information about variable tolerance limits compared to the existing fixed tolerance limit of 0.1 mm undercut height level. This information is easier to deduce by visually inspecting the filtered tolerance templates as shown in Figures 7.82 to 7.87. For example, design NAP "heat maps" reveal some

undercut with height levels above or equal to the fixed tolerance limit of 0.1mm, where the sensitivity is insignificant. Some are listed below:

- Height level 0.25mm, location 0.2 (suction side), width 0.02, main blade Figure 7.82
- Height level 0.1mm, location 0.4 (suction side), width 0.02, main blade Figure 7.82
- Height level 0.25mm, location 0.6 (suction side), width 0.01, main blade Figure 7.82

Templates taking into account surge mass flow sensitivity

In this Section, screening templates are plotted, including surge mass flow sensitivity. The plots are grouped into two categories of scales for better visualisation. Figures 7.76 to 7.81 data are scaled to the maximum sensitivity in this category. The second set of plots show filtered sensitivity up to 1, except for cases with sensitivities greater than 1.

Figures 7.7 6 to 7.78 shows that the leading edge of the main blade is most sensitivity for all three designs. In particular, design 3862H is most sensitive around the leading edge, while ADT design is least sensitive. Figures 7.79 to 7.81 also show a similar trend on the splitter blade where the leading edge is the most sensitive location. In addition, Figure 7.80 shows that design 3862H is most sensitive to undercuts.

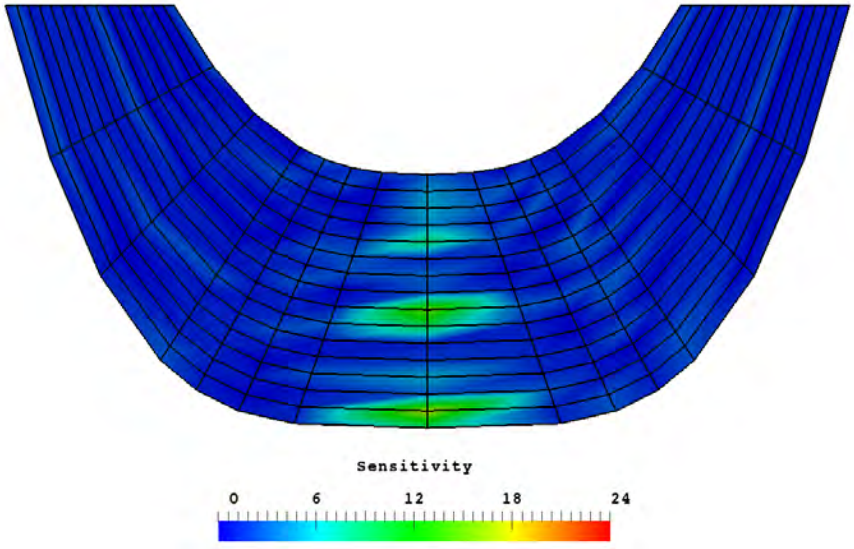

Figure 7.76 - NAP main blade

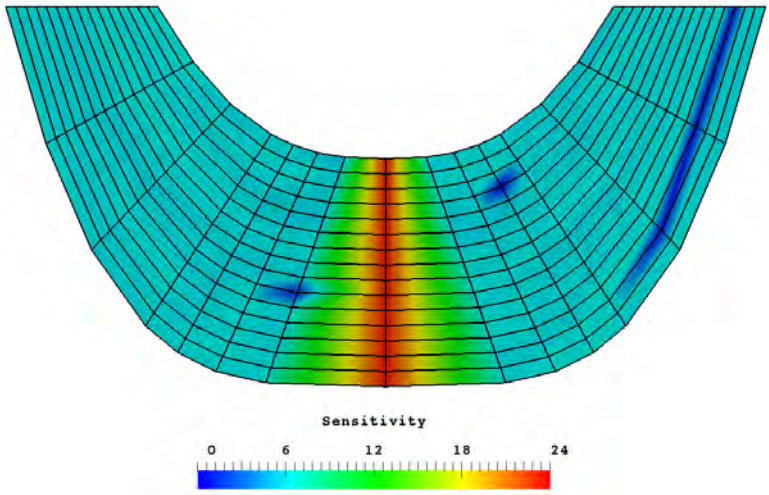

Figure 7.77 – 3862H main blade

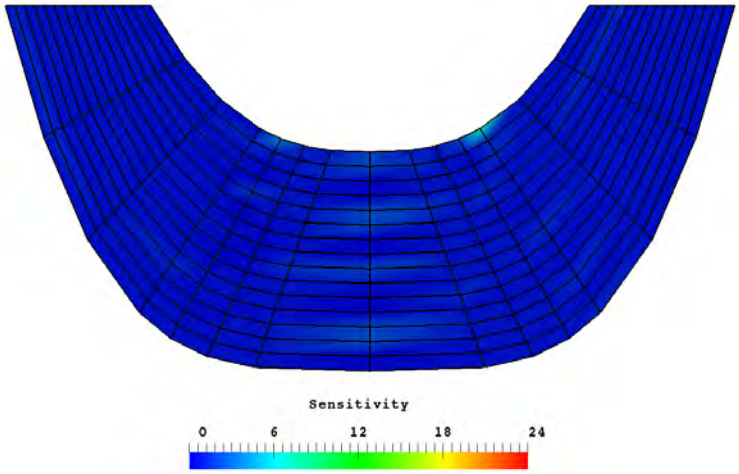

Figure 7.78 – ADT main blade

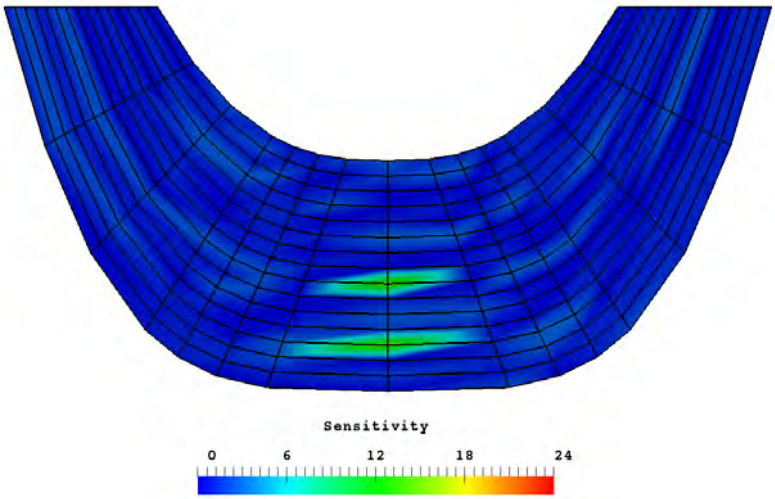

Figure 7.79 - NAP splitter blade

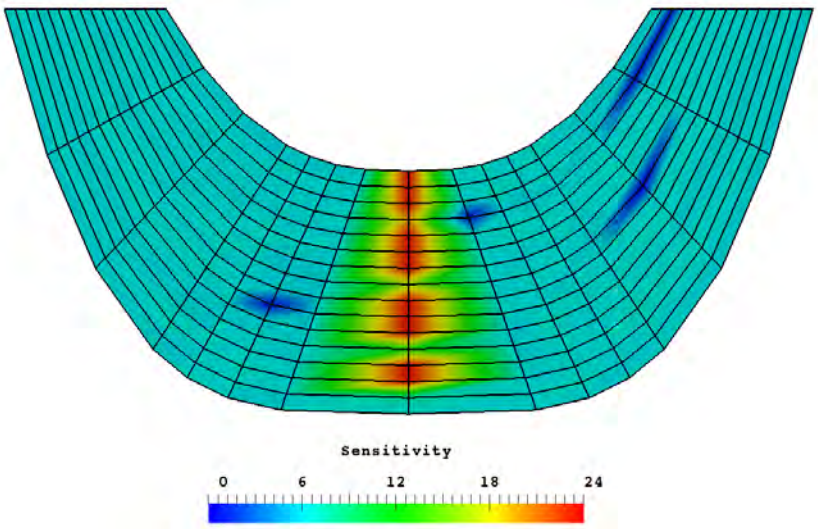

Figure 7.80 – 3862H splitter blade

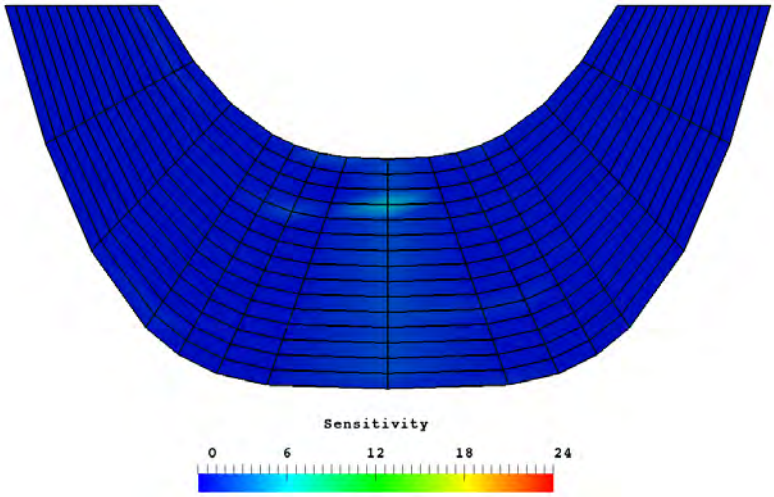

Figure 7.81 – ADT splitter blade

Figures 7.82 to 7.87 show filtered sensitivity plots on the impeller surface. Sections with no colour in these plot are above the sensitivity threshold of 1% were an undercut is not permissible at all. The filtered plots help to reveal more detail about sensitivity distribution otherwise not seen by localised high sensitivities. Figures 7.82 and 7.83 shows that an undercut of any height is not allowable on the main blade leading edge of NAP and 3862H designs respectively. On the other hand, Figure 7.84 shows that certain undercut configuration is permissible on the main blade leading edge of ADT design as shown by the dark blue contours. This information was not obvious from the unfiltered plot in Figure 7.78. For example, tracing one of the blue lines in Figure 7.84 and using Figure 7.75 and Table 7.11 as guides, an undercut setting of 6 can be traced on to the blue section of the leading edge. This corresponds to an

under of height 0.1 mm and 0.02 fraction of meridional length wide. Figure 7.83 also shows that design 3862H is the most sensitive to undercuts. On the splitter blade plots shown in Figures 7.85 to 7.87, Figure 7.85 now reveal that certain configuration of undercut is permissible on the splitter blade leading edge of NAP design as shown in Figure 7.85. This information was previously not obvious from Figure 7.79 which depicts unfiltered data. More so, Figure 7.86 also shows that design 3862H is most sensitive to undercut.

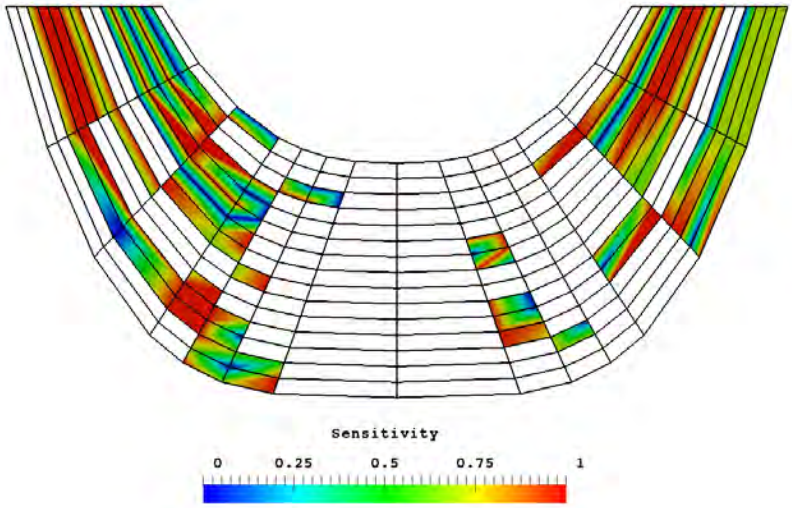

Figure 7.82 - NAP main blade (filtered)

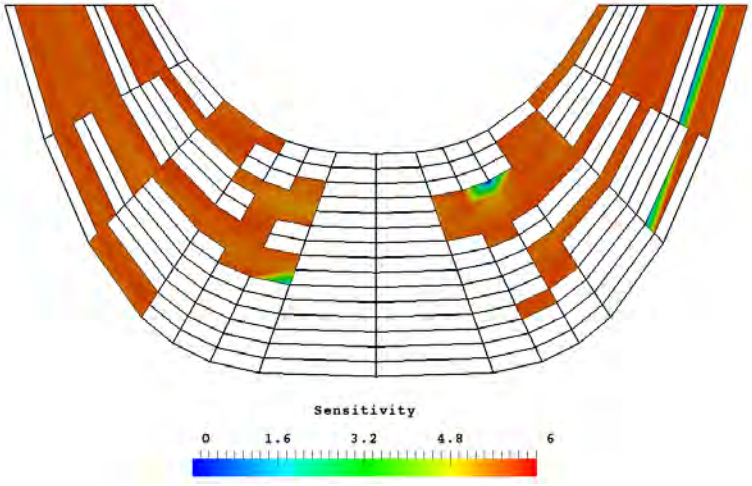

Figure 7.83 – 3862H main blade (filtered)

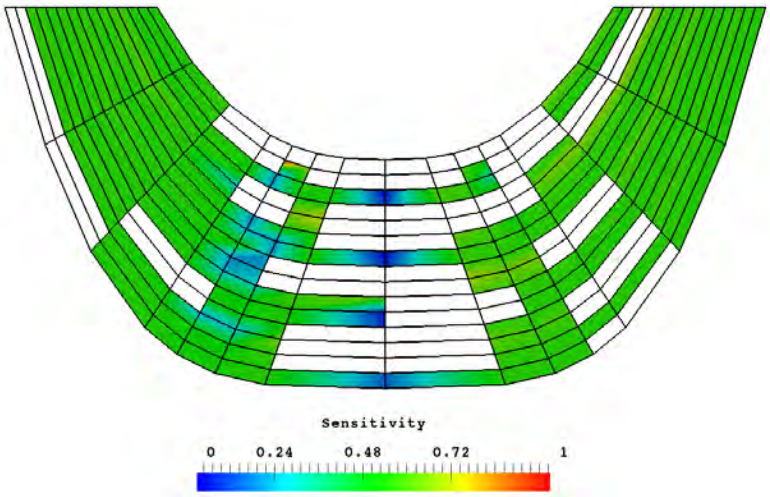

Figure 7.84 – ADT main blade (filtered)

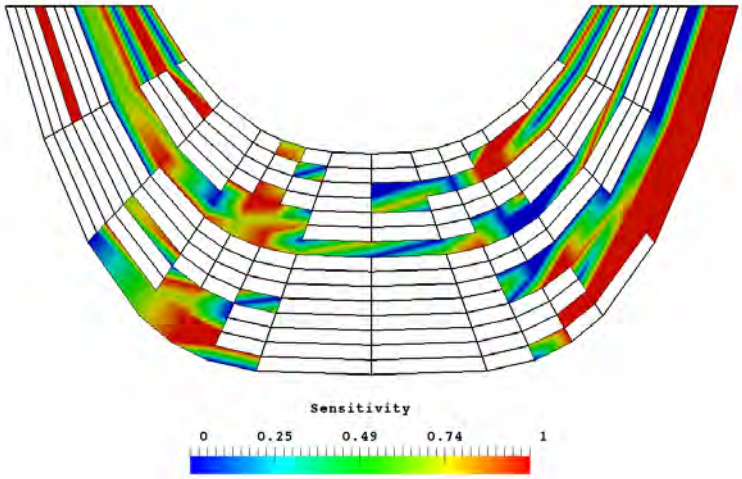

Figure 7.85 – NAP splitter blade (filtered)

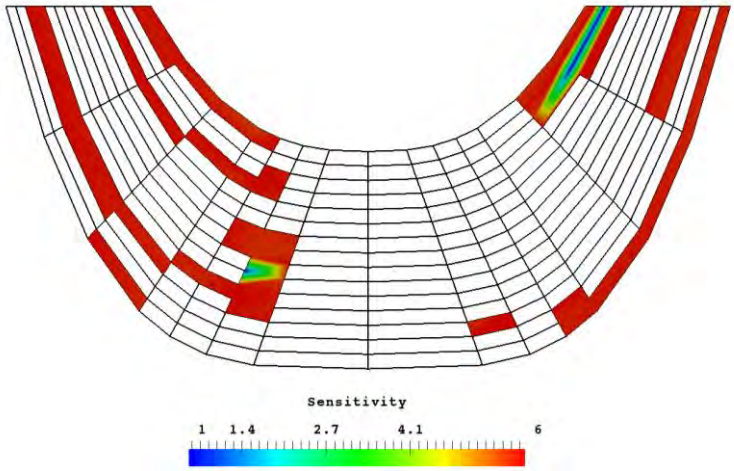

Figure 7.86 – 3862H splitter blade (filtered)

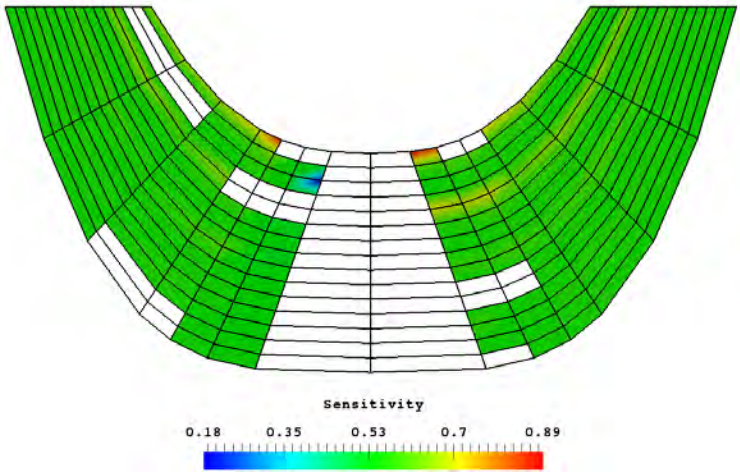

Figure 7.87 – ADT splitter blade (filtered)

Templates not taking into account surge mass flow sensitivity

The screening templates in this sub-section are presented to shown the impact of ignoring surge mass flow sensitivity. For example, a qualitative assessment of Figures 7.88 to 7.90 reveals there is no significant difference in the overall sensitivity of the main blades of designs NAP, 3862H and ADT, in contrast to Figures 7.76 to 7.78 where surge mass flow was taken into account. Plots in Figures 7.88 to 7.93 are scaled to the maximum value in the range. Figures 7.94 to 7.99 are filtered plots where the range of each plot is carefully chosen for better visualisation. As before, empty regions in the filtered plot indicate regions were an undercut is not allowed.

Figure 7.92 shows that the splitter blade of design 3862H is most sensitive to undercut, particularly at the leading edge, compared to the splitter blades of ADT and NAP designs. The filtered plot of design 3862H main blade sensitivity which does not take into account surge mass flow sensitivity as depicted in Figure 7.95 reveals lower sensitivity when compared to Figures 7.77 and 7.83 which take into account surge mass flow sensitivity. This shows that the high sensitivity of design 3862H main blade to undercut is largely due to surge mass flow sensitivity.

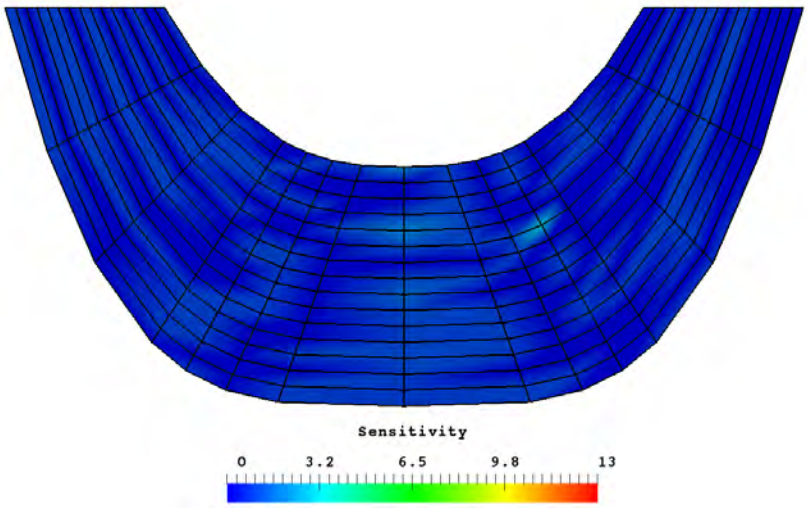

Figure 7.88 – NAP main blade

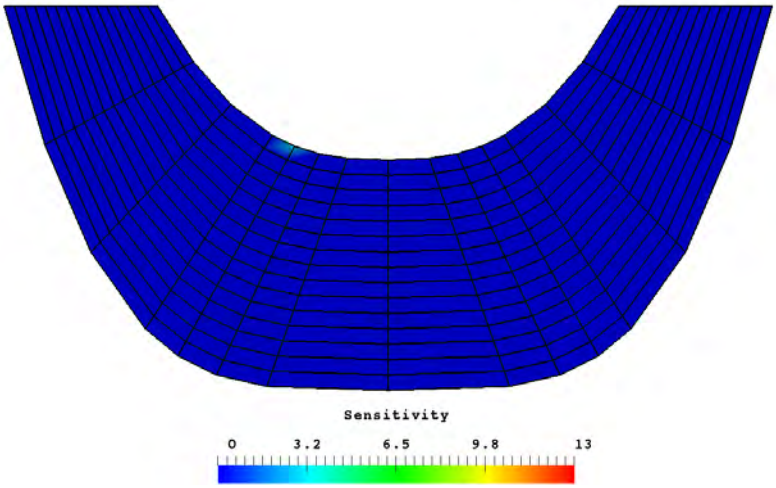

Figure 7.89 – 3863H main blade

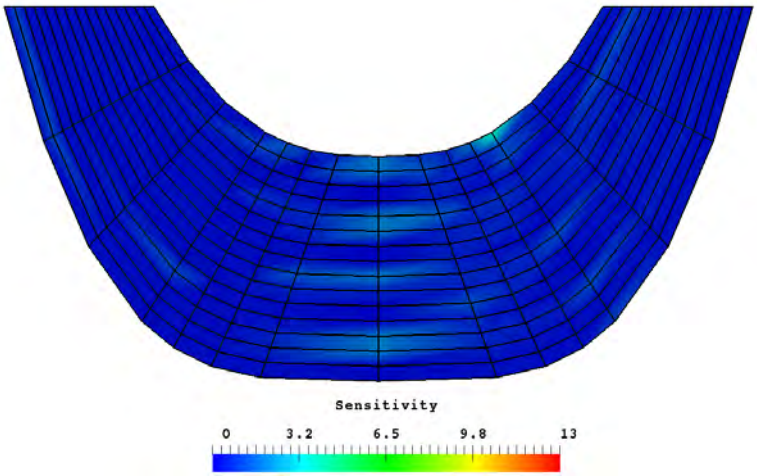

Figure 7.90 – ADT main blade

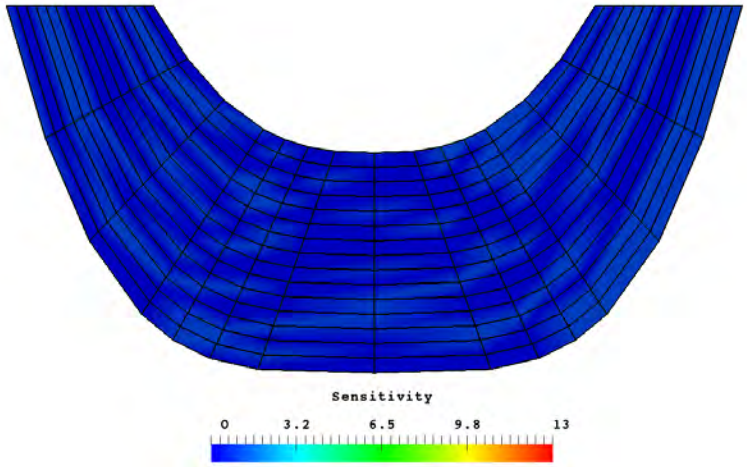

Figure 7.91 – NAP splitter blade

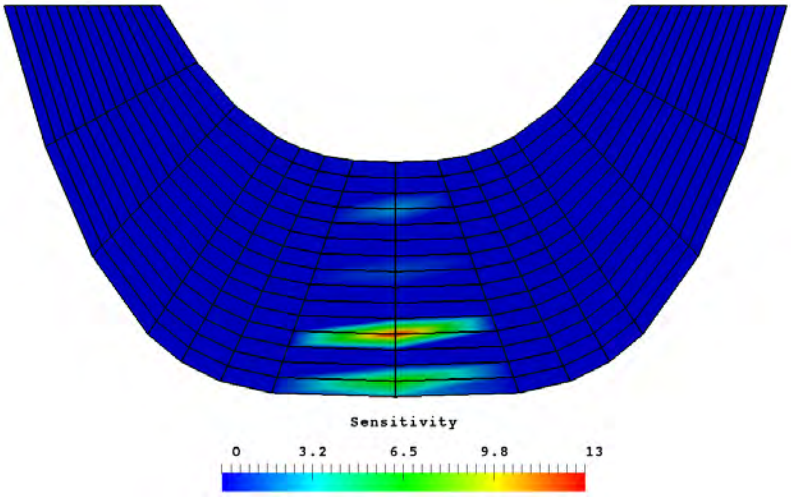

Figure 7.92 – 3862H splitter blade

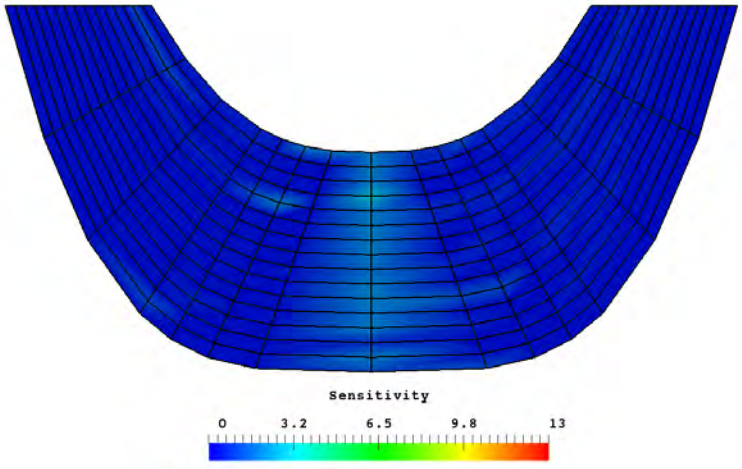

Figure 7.93 – ADT splitter blade

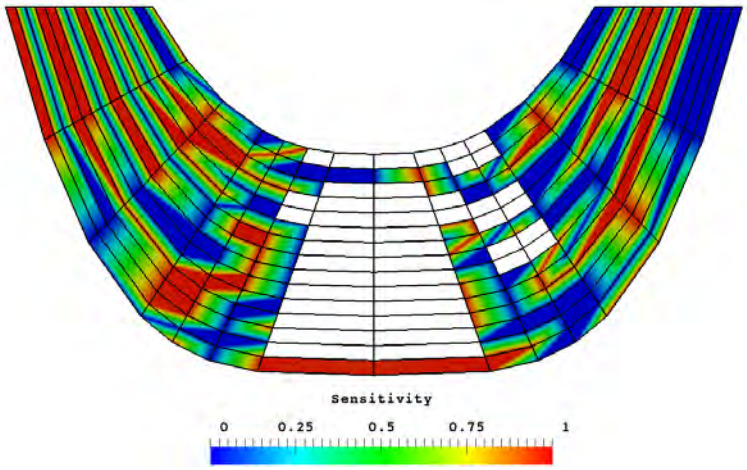

Figure 7.94 – NAP main blade (filtered)

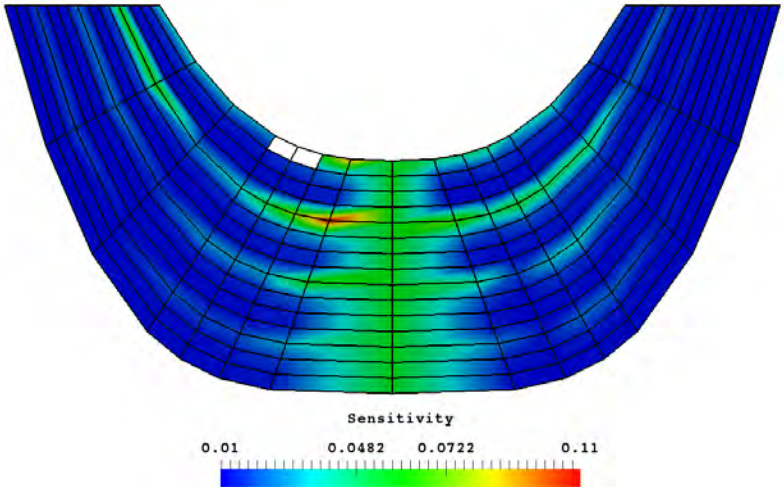

Figure 7.95 – 3862H main blade (filtered)

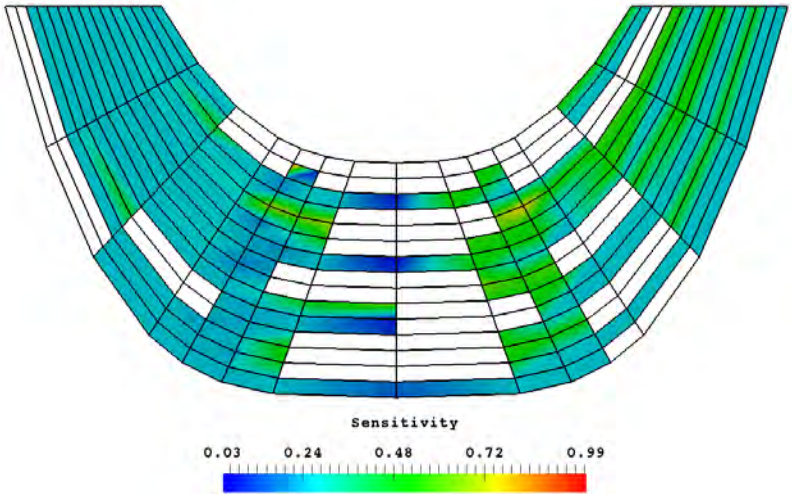

Figure 7.96 – ADT main blade (filtered)

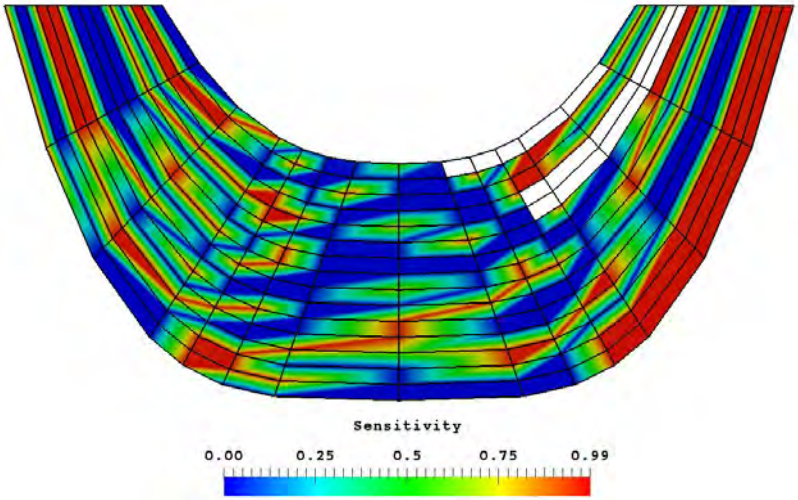

Figure 7.97 – NAP splitter blade (filtered)

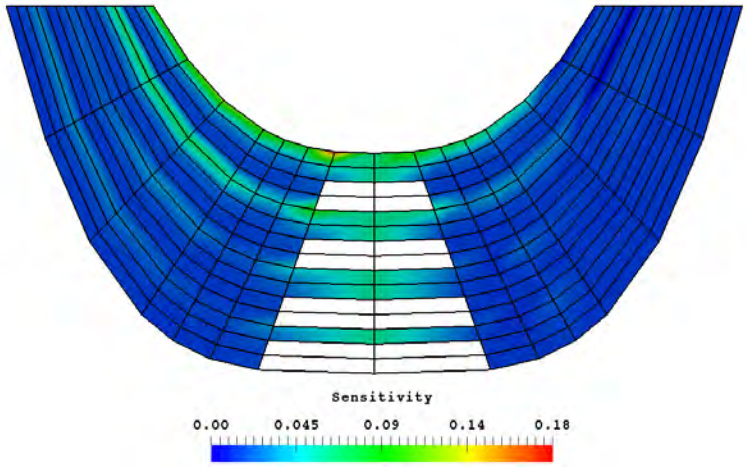

Figure 7.98 – 3862H splitter blade (filtered)

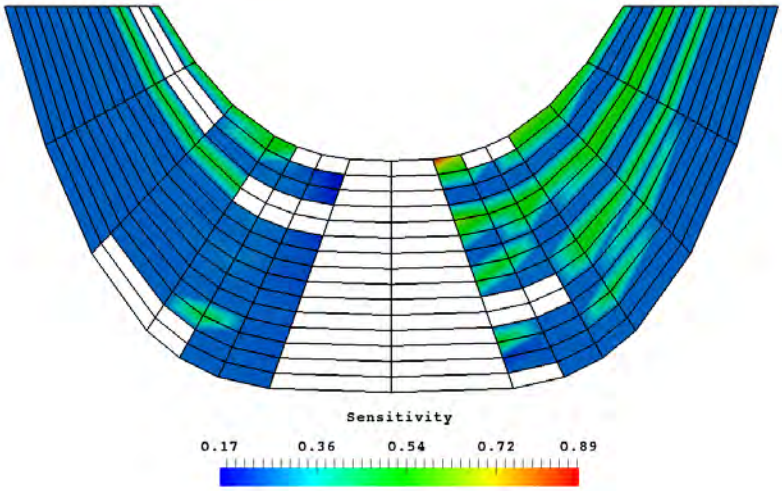

Figure 7.99 – ADT splitter blade (filtered)

CONCLUSION

In this Chapter, a study on the impact of manufacturing undercut on radial compressor performance was presented. Three choice compressor designs were used for the study to understand the impact of various undercut height and width levels at different locations on performance parameter. The study was used to rank the sensitivity of each compressor design to undercut. Sensitivity of each performance parameter was also investigated. The study was also used to investigate the locations on the blade surface most sensitive to an undercut. Correlation between undercut height and width, and performance parameters was calculated. Undercut height was determined to have more impact on sensitivity. The study also showed that the most optimised compressor design was least robust to an undercut. It was established that using a fixed tolerance limit during manufacture could result in scrapping compressor designs that are insensitive to undercut above the fixed tolerance limit.

CHAPTER 8

THESIS CONCLUSION AND FUTURE WORK

8.1 CONCLUSION

Here is a reminder of the two central themes of this thesis:

- To implement a high-throughput computing (HTC) cluster system to facilitate running CFD jobs in batches during multi-objective optimisation calculation, and to use the cluster to optimise an existing HP compressor design for a two-stage turbocharger.
- To understand the impact of impeller manufacturing undercut on the aerodynamic performance of radial compressors using the HTC cluster as the computing platform.

In addition to the two central themes, two computer algorithms for preliminary design of two-stage turbocharger have been developed and applied to test cases during this research.

As a result of the work carried out during this research, the following contributions to research were made:

- Development of a bespoke parametric CAD algorithm and integrating it into a multi-objective, multi-physics (CFD and FEA) optimisation design process at Napier. The advanced parametric features of the CAD algorithms, for example using 5 Bezier control points to define the hub and shroud meridional profile, provides additional flexibility to designers for developing optimised designs. The CAD algorithm has been used to design new compressors for a two-stage turbocharger at Napier.

- A new approach for reducing the number of variables that define a radial compressor hub and shroud meridional profile without reducing the order of the Bezier curve was implemented into the algorithm.

- A method of constraining control points that define the hub and shroud meridional profile of a radial compressor impeller to always move in the same direction. This ensures the bounding box of the Bezier curve does not have a high aspect ratio and always guarantees a valid profile distribution.

- Use of a mid control point between the first two and last two control points at the shroud to improve local control of shroud profile curvature in the CAD algorithm.

- A mapping algorithm for calculating operating points on a radial compressor map that ensures the surge point is a valid solution. This was used to predict accurate compressor map width in Chapter 6.

- A demonstration of multi-objective optimisation of a radial compressor with up to 8 conflicting objectives, including map width enhancement

- The discovery of new impeller blade design topology with large back sweep angle at the exit.

- A high throughput computing (HTC) system was implemented at the University to facilitate batch computing during this research. A similar HTC system was implemented at Napier and has been used to facilitate several designs of experiments and multi-objective optimisation calculations.

- The HTC system was used to optimise an existing HP compressor design, and achieved a significant 1.6 points gain in total-to-static efficiency and 20% increase in map width across three speed lines.

- A novel variable tolerance limit plot on the impeller surface ("heat map") was developed for the impeller designs evaluated. This template could serve as a guideline to manufacturing engineers to decide if a machined surface defect such as an undercut could result in significant deviation from design performance. This could reduce scrap rate and result in cost savings.

- Sensitivity analysis studies revealed performance parameters such as peak efficiency, design point mass flow, etc are more sensitive to undercut height, than to undercut width.

- The study also showed that as undercut height increases, design point efficiency and target mass flow (or design point mass flow) will reduce for any impeller design. Also, the average mass flow along the speed line will reduce.

- For all three cases of designs investigated during the sensitivity studies, surge mass flow was determined to be the most sensitive to undercut, irrespective of the location, width and height level of the undercut. This is not so surprising because surge is an unsteady phenomenon in turbo-machinery where the flow separates rapidly.

- The study also revealed that a highly optimised design is more sensitive to undercut, as in the case of the optimised design investigated,

- Finally, the sensitivity study revealed that every compressor impeller design has its own unique sensitivity distribution depending on its shape and operating conditions, hence it is important to have unique screening template for each new compressor design

8.2 FUTURE WORK

HTC System

- An area of future work in the HTC system implemented during this research is to increase the number of computers in the cluster and also have a mix of Windows and Linux computers. This will improve awareness on the benefits of high throughput computing within the school of engineering.

- Also, since HTCondor favours running computer programs without a graphical user interface; deploying HTCondor on more computers will help increase awareness on the benefits of custom writing or open source command line driven programs in engineering research.

Multi-Objective Optimisation

- The aerodynamic multi-objective optimisation of the HP compressor described in this thesis could be improved upon to include structural optimisation as well. In that case, the multi-physics optimisation which includes CFD and FEA optimisation will always produce a new design that satisfies both aerodynamic and structural requirements.

- The optimisation process can be further improved by automatically post-processing CFD data during the optimisation process to extract more flow features of interest for monitoring during the optimisation calculations.

CAD Algorithm

- The parametric CAD algorithm developed during this research could be improved upon by adding the capability to design vaned diffuser compressors. Also, the parameterisation of blade angle and blade thickness distribution can be done using less sensitive Bezier curves instead of cubic-splines.

- In addition, the number of parameters in the optimisation can be increased, for example by including the thickness distribution as a parameter in the CAD program.

DEMO

The open-source differential evolution for multi-objective optimisation (DEMO) software used in this research can be improved upon by implementing the capability to continue optimisation from an existing archive file in the event of a power cut or shut down. This will save time by re-using an existing archive as seed to continue optimisation calculations.

Undercut Study

- A future application of the undercut study is to integrate the screening templates in this research into the manufacturing process, so that the 5-axis milling machine can decide if a machined impeller will be scrapped based on the screening template.

- Integrate a cut-down version of the undercut sensitivity analysis studies within the automated optimisation process so that every newly optimised design is also robust to undercut defects. This will require a clever way of reducing the number of CFD calculations required for the sensitivity analysis or increase the computing power.

1-D Codes

- The one-dimensional mathematical program described in Chapter 3 could be improved upon to use various slip correlations for calculating the impeller exit slip velocity.

- Also, a 1-D vane-less diffuser mathematical model could be integrated to the code.

- The matching algorithm described in Chapter 3 can be updated by implementing the capability to find the optimum split of pressure ratio in the LP and HP stages of the compressor as against fixing a value as implemented in the current version.

APPENDIX A

'TWO-MATCH' MATCHING ALGORITHM

The temperature – entropy diagram T-S of the compressor and turbine stages in the two-stage matching algorithm is illustrated in Figures A1 and A2 respectively. The air is compressed in the LP compressor from P1 to P2. Some pressure is lost in the inter-cooler stage from P2 to P3. The air is compressed again in the HP stage from P3 to P4. The air is cooled in the charge air cooler with some pressure loss from P4 to P5 before entering the internal combustion engine. The air leaving the engine is expanded in the HP turbine from P6 to P7; extracting energy from the exhaust gas to drive the HP compressor. The exhaust gas is further expanded in the LP compressor from P7 to P8 to drive the LP compressor.

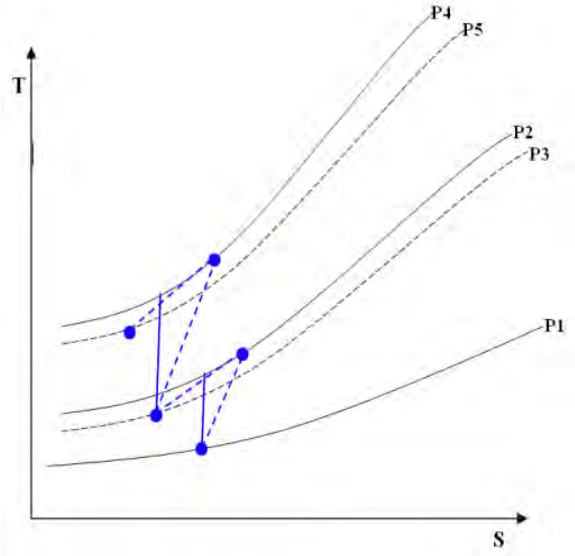

Figure A1 – Compressor T-S diagram

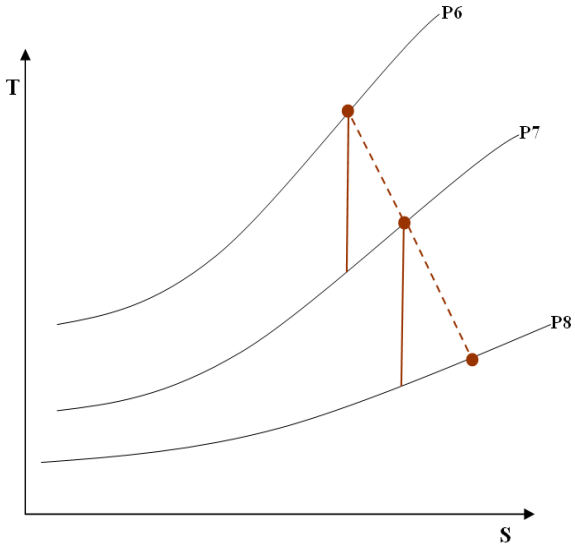

Figure A2 – Turbine T-S diagram

The various stages in the matching algorithm are implemented in an iterative loop as described in the following:

Stage 1 – 2: LP Compressor Iteration

At the start of the matching process, the inlet stagnation temperature T_{01} and pressure P_{01} are known. The static temperature T_2 at the exit of the LP compressor is calculated using Equation A1.

$$T_2 = T_{01} + \frac{T_{01}}{\eta_{LPC}}\left[\left(\frac{P_2}{P_{01}}\right)^{\frac{\gamma_{LPC}-1}{\gamma_{LPC}}} - 1\right] \qquad (A1)$$

The LP compressor pressure ratio is calculated from the known values of actual compression ratio and pressure split using Equation A2.

$$\pi_{LPC} = {}^{P_2}/_{P_{01}} = \sqrt{\pi_{ACR} \times \frac{x}{y}} \quad (A2)$$

A reasonable value of LP compressor total-to-static isentropic efficiency η_{LPC}, usually between 78% – 85% is used during the matching process. An initial estimate of compressor outlet temperature T_{2guess} is used to determine air gamma γ_{LPC} to start the matching process. γ_{LPC} is calculated at temperature $(T_1 + T_{2guess})/2$ for the each iteration. The process is repeated until the difference between T_2 *and* T_{2guess} is reduced to an acceptable value. At the end of this stage, P_2 and T_2 is calculated. The gas specific heat capacity C_{pLPC} is calculated at $(T_1 + T_2)/2$.

Stage 2 – 3: Intercooler

The intercooler outlet pressure P_3 is calculated using Equation A3.

$$P_3 = P_2 - \Delta P_i \quad (A3)$$

The effectiveness of intercooler that required to achieve the outlet temperature T_3 is calculated using Equation A4.

$$\varepsilon_{LPC} = \frac{T_3 - T_2}{T_{cool} - T_2} \quad (A4)$$

The temperature of cooling fluid T_{cool} is same as T_{01}.

Stage 3 – 4: HP Compressor Iteration

This stage is similar to 1 – 2. A reasonable value of total-to-static isentropic efficiency η_{HPC} is chosen and an initial estimate of outlet temperature T_{4guess} is used to start the iteration. At the end of this stage, P_4 and T_4 are calculated; and C_{pHPC} is calculated at $(T_3 + T_4)/2$. The HP compressor pressure ratio is calculated using Equation A5.

$$\pi_{HPC} = {}^{P_4}/_{P_3} = \sqrt{\pi_{ACR} \times \frac{y}{x}} \quad (A5)$$

The static temperature at the exit of the HP compressor is calculated using Equation A6.

$$T_4 = T_3 + \frac{T_3}{\eta_{HPC}}\left[\left(\frac{P_4}{P_3}\right)^{\frac{\gamma_{HPC}-1}{\gamma_{HPC}}} - 1\right] \quad (A6)$$

Stage 4 – 5: Charge Air Cooler

Since the pressure drop in the charge air cooler is known, the outlet temperature of the charge air cooler P_5 is calculated using Equation A7.

$$P_5 = P_4 - \Delta P_a \quad (A7)$$

The static temperature from the HP compressor T_4 was already determined from the previous stage. Also, T_5 is a know parameter at the start of the iteration. An initial guess of after cooler effectiveness ε_{HPC} is used to start the iteration. Equations A8 and A9 are solved iteratively for new estimates of ε_{HPC} until $T_4 - T_{4calc}$ and $T_5 - T_{5calc}$ are reduced to a set minimum.

$$T_{4calc} = \frac{T_5 - \varepsilon_{HPC}T_{cool}}{1 - \varepsilon_{HPC}} \quad (A8)$$

$$T_{5calc} = T_4(1 - \varepsilon_{HPC}) + \varepsilon_{HPC}T_{cool} \quad (A9)$$

At the end of this stage, the after cooler effectiveness is determined. The density of air in the engine receiver is calculated using the equation of state.

$$\rho_5 = \frac{P_5}{RT_5} \quad (A10)$$

where R is the specific gas constant for air, $R = 287.1$

The mass flow rate of air required by the engine is calculated using Equation A11.

$$\dot{m}_a = \rho_5 \times V_s \times \frac{N}{60} \times \frac{1}{0.5 \times n_s} \times \eta_v \times S_r \times n_c \quad (A11)$$

Where V_s is the swept volume of each cylinder, N is the engine speed in rev/mins, n_s is the number of strokes of the engine (two, four…), η_v is the volumetric efficiency of the engine cylinder, S_r is the scavenge ratio and n_c is the number of cylinders in the engine.

Stage 5 – 6

The engine combustion is not simulated as part of the matching process. However fuel mass flow rate $\dot{m}_f$ (kg/s) is calculated using Equation A12; where P_E is the total power produced by all the engine cylinders and BSFC is the brake specific fuel consumption. When the engine combustion process is

simulated, the isentropic efficiency of each stage and pressure split can be iterated for different values to optimise the process [98].

$$\dot{m}_f = \frac{P_E \times BSFC}{60 \times 60} \tag{A12}$$

The Air Fuel Ratio (AFR) in the engine cylinder is calculated using Equation A13.

$$AFR = \frac{\dot{m}_a}{\dot{m}_f} \tag{A13}$$

Stage 6 – 7: HP Turbine Iteration

The expansion ratio for the HP turbine stage is calculated from energy balance between compressor and turbine using Equation A14

$$\dot{W}_{HPC} = \eta_{mec\,h} \times \dot{W}_{HPT} \tag{A14}$$

where $\eta_{mec\,h}$ is the shaft mechanical efficiency which is assumed to be 1. The power consumed the HP compressor and power developed by the HP turbine is calculated using Equations A15 and A16 respectively.

$$\dot{W}_{HPC} = \frac{1}{\eta_{HPC}} \dot{m}_a C_{pHPC} T_3 \left[\left(\frac{P_4}{P_3} \right)^{\frac{\gamma_{HPC} - 1}{\gamma_{HPC}}} - 1 \right] \tag{A15}$$

$$\dot{W}_{HPT} = \eta_{HPT} \left(\dot{m}_a + \dot{m}_f \right) C_{pHPT} T_6 \left[1 - \left(\frac{1}{\pi_{HPT}} \right)^{\frac{\gamma_{HPT} - 1}{\gamma_{HPT}}} \right] \tag{A16}$$

The turbine expansion ratio is obtained by re-arranging the above Equations. The HP turbine inlet or engine exit temperature T_6 is a known parameter. A reasonable value of isentropic efficiency η_{HPT} is set to solve the Equations below. The expansion ratio $\pi_{HPT} = {}^{P_6}/_{P_7}$ and HP turbine outlet temperature T_7 are calculated using Equations A17 and A18 respectively.

$$\pi_{HPT} = {}^{P_6}/_{P_7} = \left[1 - \frac{\left[\left(\frac{P_4}{P_3}\right)^{\frac{\gamma_{HPC}-1}{\gamma_{HPC}}} - 1\right] T_3 C_{pHPC}}{\left(1 + {}^{\dot{m}_f}/_{\dot{m}_a}\right) T_6 \, C_{pHPT} \, \eta_{HPC} \, \eta_{HPT} \, \eta_{mech}}\right]^{\frac{\gamma_{HPT}}{1-\gamma_{HPT}}} \quad (A17)$$

$$T_7 = T_6 - T_6 \eta_{HPT} \left[1 - \left(\frac{1}{\pi_{HPT}}\right)^{\frac{\gamma_{HPT}-1}{\gamma_{HPT}}}\right] \quad (A18)$$

An initial estimate of HP turbine outlet temperature T_{7guess} is used to determine gas gamma γ_{HPT} and C_{pHPT} to start the matching process. γ_{HPT} and C_{pHPT} are calculated at temperature $(T_6 + T_{7guess})/2$ for each iteration. The process is repeated until the difference between T_7 and T_{7guess} is reduced to an acceptable value. At the end of this stage, the outlet temperature T_7 and expansion ratio π_{HPT} is obtained.

Stage 7 – 8: LP Turbine Iteration

The same process in stage 6 -7 is repeated here. The LP turbine expansion ratio and outlet temperature are obtained using the Equations A19 and A20 respectively.

$$\pi_{LPT} = {}^{P_7}/_{P_8} = \left[1 - \frac{\left[\left(\frac{P_2}{P_{01}}\right)^{\frac{\gamma_{LPC}-1}{\gamma_{LPC}}} - 1\right] T_1 C_{pLPC}}{\left(1 + {}^{\dot{m}_f}/_{\dot{m}_a}\right) T_7 \, C_{pLPT} \eta_{LPC} \, \eta_{LPT} \, \eta_{mech}}\right]^{\frac{\gamma_{LPT}}{1-\gamma_{LPT}}} \quad (A19)$$

$$T_8 = T_7 - T_7 \varphi_{LPT} \left[1 - \left(\frac{1}{\pi_{LPT}}\right)^{\frac{\gamma_{LPT}-1}{\gamma_{LPT}}}\right] \quad (A20)$$

Since P_8 is known, the HP turbine inlet pressure is calculated using Equation A21.

$$P_6 = {}^{P_6}/_{P_7} \times {}^{P_7}/_{P_8} \times P_8 \quad (A21)$$

P_7 is then calculated using Equation 7.27 since ${}^{P_6}/_{P_7}$ is known.

Turbocharger Sizing

The size of each turbocharger component is determined using the mass flow rate and inlet thermodynamic conditions. The LP and HP compressor sizes are determined from the corrected mass flow rate at the inlet condition using Equations A22 and A23 respectively.

$$\dot{m}_{corrLPC} = \frac{\dot{m}_a\sqrt{T_1}}{P_1} \quad (A22)$$

$$\dot{m}_{corrHPC} = \frac{\dot{m}_a\sqrt{T_3}}{P_3} \quad (A23)$$

The HP and LP turbine size is determined from the corrected mass flow rate using Equations A24 and A25 respectively

$$\dot{m}_{corrHPT} = \frac{\dot{m}_t\sqrt{T_6}}{P_6} \quad (A24)$$

$$\dot{m}_{corrLPT} = \frac{\dot{m}_t\sqrt{T_7}}{P_7} \quad (A25)$$

where $\dot{m}_t = \dot{m}_a + \dot{m}_f$ is the total mass flow in the turbine stages.

Turbine Area

The turbine area is calculated using corrected mass flow at outlet pressure of the LP and HP stage respectively using Equations A26 and A27 respectively.

$$\dot{\dot{m}}_{corrLPT} = \frac{\dot{m}_t\sqrt{T_7}}{P_8} \quad (A26)$$

$$\dot{\dot{m}}_{corrHPT} = \frac{\dot{m}_t\sqrt{T_6}}{P_7} \quad (A27)$$

The Hirst Equation [99] is used to relate the expansion ratio of a turbine to a constant M using Equation A28.

$$\pi_T = 1 + \Psi M^{\psi} \quad (A28)$$

where π_T is the turbine (LP or HP) expansion ratio, Ψ and ψ are coefficients; and $M = \frac{\dot{\dot{m}}_{corrT}}{A_T}$

The areas of the LP and HP turbine are calculated using Equations A29 and A30 respectively

$$A_{LPT} = \frac{\dot{m}_{corrLPT}}{M} \quad (A29)$$

$$A_{HPT} = \frac{\dot{m}_{corrHPT}}{M} \quad (A30)$$

Compressor or turbine capacity corrected to standard temperature V_{298} can be calculated using Equation A31

$$V_{298} = \frac{\dot{m}_{corrLPT\ or\ HPT}}{3.07} \quad (A31)$$

Equation A31 is only valid if corrected mass flow is in Ib/s and pressure is in pounds per square inch.

Air and Exhaust Properties Table

The air properties used in the compressor stages were obtained from Engineering tool box properties of dry air ranging 175K to 1900K [100]. The product of combustion is determined by assuming that the combustion is stoichiometric using Equation A32.

$$C_x H_y + \left(x + \frac{y}{4}\right) O_2 + 3.76\left(x + \frac{y}{4}\right) N_2 \rightarrow xCO_2 + \left(\frac{y}{2}\right) H_2O + 3.76\left(x + \frac{y}{4}\right) N_2 \quad (A32)$$

The fuel is assumed to be Heavy Fuel Oil (HFO) diesel, $C_{12}H_{23}$. Properties of the combustion products (CO_2, H_2O and N_2) at different temperatures were obtained from the engineering toolbox website [100]. Properties of air and exhaust gas used in the program is shown in Table A1. The values of x and y are set to 12 and 13 respectively in Equation A32. The mass composition of each product of combustion is used to do a weighted averaging of the required parameters (Cp and gamma) at each temperature to get exhaust gas properties.

T (K)	**Air**		**Exhaust**	
	Cp	Gamma	Cp	Gamma
175.00	1002.30	1.401	1003.93	1.40061132
200.00	1002.50	1.401	1004.38	1.400362523
225.00	1002.70	1.401	1004.84	1.400103263
250	1003.10	1.401	1005.51	1.399734101
275	1003.80	1.401	1006.46	1.399204884
300	1004.90	1.400	1007.82	1.398450668
325	1006.30	1.400	1009.42	1.397567256
350	1008.20	1.398	1011.53	1.396409408
375	1010.60	1.397	1014.11	1.395002565
400	1013.50	1.395	1017.18	1.39333888
450	1020.60	1.391	1024.59	1.389389579
500	1029.50	1.387	1033.76	1.384607413
550	1039.80	1.381	1044.30	1.379253503
600	1051.10	1.376	1055.80	1.373578778
650	1062.90	1.370	1067.80	1.36783806
700	1075.00	1.364	1080.09	1.362136468
750	1087.00	1.359	1092.26	1.356659672
800	1098.70	1.354	1104.14	1.351475617
850	1110.10	1.349	1115.72	1.346562021
900	1120.90	1.344	1126.71	1.342024406
950	1131.30	1.34	1137.28	1.337772771
1000	1141.10	1.336	1147.23	1.333866477
1050	1150.20	1.333	1156.49	1.330307711
1100	1158.90	1.329	1165.37	1.326969376
1150	1167.00	1.326	1173.63	1.323923892
1200	1174.60	1.323	1181.36	1.321122614
1250	1181.70	1.321	1188.62	1.318537546
1300	1188.40	1.319	1195.44	1.316146228
1350	1194.60	1.316	1201.77	1.313955219
1400	1200.50	1.314	1207.78	1.311905977
1500	1211.20	1.311	1218.73	1.308242408
1600	1220.70	1.308	1228.43	1.305063962
1700	1229.30	1.305	1237.21	1.302244631
1800.00	1237.00	1.302	1245.07	1.299766367
1900.00	1244.00	1.3	1252.21	1.29754784

Table A1 – Air and exhaust gas properties

APPENDIX B

1-D INVERSE DESIGN ALGORITHM

At the start of the calculation, the performance requirements and constants such as gamma are read into the program. The assumptions range data is read in and then randomised to choose a value for use in the calculation. The total density at the impeller inlet is calculated using Equation B1.

*Note: The novel Equations developed during this research are marked with a **

$$\rho_{01} = \frac{P_{01}}{R_{gas} T_{01}} \tag{B1}$$

The mass flow is calculated using Equation B2

$$\dot{m} = \rho_1 \times C_{1me\_rms} \times A_F \tag{B2}$$

since the static density is not known yet, it is assumed to be equal to the total density. Mass flow is a user input, so

$$C_{1me\_rms} \times A_F = known\ value \tag{B3}$$

The RMS blade speed U_{rms} is calculated at the RMs radius at the impeller inlet R_{rms} as follows;

$$R_{rms} = \left(\frac{R_s^2 + R_h^2}{2}\right)^{1/2} \tag{B4}$$

$$U_{rms} = \frac{2\pi R_{rms} N}{60} \tag{B5}$$

where N is the rotor speed.

Setting $n = {}^{R_s}/_{R_h}$

$$A_F = \pi\left(R_s^2 - R_h^2\right) = \pi R_h^2 (n^2 - 1) \tag{B6}$$

$$U_{rms} = \frac{2\pi N R_h}{60}\left(\frac{n^2 + 1}{2}\right)^{1/2} \tag{B7}$$

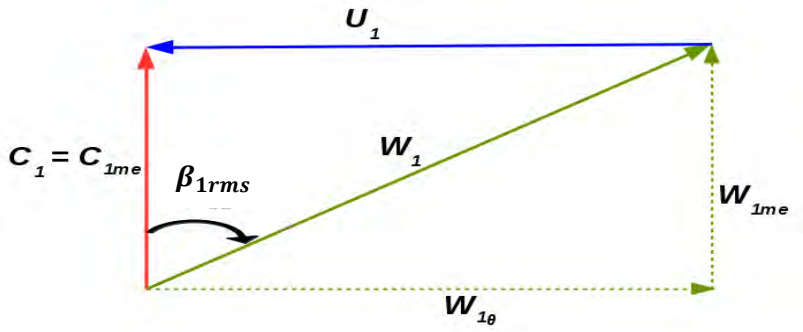

Figure B1 – Velocity Triangle at Impeller Inlet

Blade velocity U is blue, meridional velocity is red

Assuming a zero incident angle at the impeller inlet as shown in the velocity triangle in Figure B1, the meridional or axial velocity at the inlet can be calculated using Equation B8.

$$C_{1me\_rms} = \frac{U_{rms}}{tan\beta_{1rms}} = \frac{\pi N R_h}{30 tan\beta_{1rms}} \left(\frac{n^2+1}{2}\right)^{1/2} \qquad (B8*)$$

Combining Equations B6 and B8, we can write Equation B9 as follows

$$C_{1me\_rms} \times A_F = known\ value = \frac{\pi^2 N {R_h}^3}{30 tan\beta_{1rms}} (n^2-1) \left(\frac{n^2+1}{2}\right)^{1/2} \qquad (B9)$$

The hub radius can be now be calculated using Equation B10

$$R_h = \left(\frac{C_{1me_{rms}} \times A_F \times 30 tan\beta_{1rms}}{\pi^2 N (n^2-1) \left(\frac{n^2+1}{2}\right)^{1/2}} \right)^{1/3} \qquad (B10*)$$

The hub blade thickness can then be calculated based on the estimated value of hub radius to hub blade thickness using Equation B11

$$Hub_{th} = \frac{R_h}{\left({R_h}/{Hub_{th}}\right)} \qquad (B11)$$

The number of blades is calculated using the correlation in Equation B12

$$N_{blades} = \frac{\pi R_h}{Hub_{th} \times K_b} \qquad 5 \le K_b \le 7 \qquad (B12*)$$

where K_b is a constant based on impeller blade thickness at leading edge hub.

The blade thickness at the shroud is assumed to be a third of the hub blade thickness

$$Hub_{th} = 0.33 \times Shroud_{th} \quad (B13)$$

The shroud radius is calculated using Equation B14

$$R_s = {}^{R_s}/_{R_h} \times R_h \quad (B14)$$

The root-mean-square (RMS) radius at impeller inlet can then be evaluated using Equation B4 since the hub and shroud radius has been calculated. The impeller inlet blade angle at the shroud and hub are evaluated using Equations B15 and B16 respectively.

$$\beta_{1shroud} = {}^{R_s}/_{R_{1rms}} \times \beta_{1rms} \quad (B15)$$

$$\beta_{1hub} = {}^{R_h}/_{R_{1rms}} \times \beta_{1rms} \quad (B16)$$

At the exit of the impeller, the total to total efficiency of the compressor is fixed at 95%.

An initial estimate of static density and impeller radius is used to start the iteration process. The blade speed is then calculated using Equation B17

$$U_2 = \frac{2\pi R_{2_{est}} N}{60} \quad (B17)$$

Area of impeller exit section is calculated using Equation B18

$$A_{imp\_ex} = 2\pi R_{2_{est}} \left({}^{b_2}/_{R_2} \times R_{2_{est}}\right) \quad (B18)$$

The static temperature at impeller exit is calculated using Equation B19

$$T_2 = \frac{P_2}{Rho2_{est} R_{gas}} \quad (B19)$$

The axial component of gas velocity at the exit of the impeller is then calculated using Equation B20

$$C_{2me} = \frac{\dot{m}}{Rho2_{est} \times A_{imp_{ex}}} \quad (B20)$$

The Weisner slip correlation [27] is used to calculate the slip factor as shown in Equation B21

$$\mu = 1 - \frac{\sqrt{cos\beta_2}}{N_{blades}{}^{0.7}} \quad (B21)$$

The gas tangential velocity in the absolute frame of reference at the exit of the impeller is calculated using Equation B22.

$$C_{2\theta} = \mu U_2 - C_{2me}\, tan\beta_{b2} \quad (B22)$$

The stagnation temperature and sound speed at the impeller exit are calculated using Equations B23 and B24 respectively, where γ is the heat capacity ratio of the working fluid, in this case air.

$$T_{02} = T_{01}\left[1 + (\gamma - 1)\frac{U_2 C_{2\theta}}{a_{01}^2}\right] \quad (B23)$$

$$a_{02} = \sqrt{\gamma R T_{02}} \quad (B24)$$

The gas absolute velocity at the exit of impeller is calculated using Equation B25.

$$C_2 = \sqrt{C_{2\theta}^2 + C_{2me}^2} \quad (B25)$$

The impeller exit static temperature and pressure are then re-calculated Equations B26 and B27 respectively.

$$T_{2calc} = T_{02}\left[1 - \frac{(\gamma - 1)}{2}\frac{C_2^2}{a_{02}^2}\right] \quad (B26)$$

$$P_{2calc} = Rho2_{est} \times R_{gas} \times T_{2calc} \quad (B27)$$

Static sound speed and stagnation pressure at the impeller exit are calculated using Equations B28 and B29 respectively.

$$a_2 = \sqrt{\gamma R T_2} \quad (B28)$$

$$P_{02} = P_2 \left[1 + \frac{(\gamma - 1)}{2} \frac{C_2^2}{a_2^2}\right]^{\frac{\gamma}{\gamma - 1}} \qquad (B29)$$

The program iterates until the mass flow and static temperature at impeller exit are converged:

$Rho2_{est}$ is corrected based on difference between T_2 and T_{2calc}. Mass flow is then recalculated using Equation B30

$$\dot{m}_{calc} = Rho2_{est\_cor} \times C_{2me} \times A_{imp_{ex}} \qquad (B30)$$

The impeller exit radius $Rh_{2_{est}}$ is then corrected base on the difference between $\dot{m}$ and $\dot{m}_{calc}$.

APPENDIX C

FUNDAMENTAL FLOW PHYSICS IN A RADIAL COMPRESSOR AND VANELESS DIFFUSER

IMPELLER INLET

The impeller inlet has a great impact on the compressor performance. If the flow is accelerated too quickly at the inducer, rapid deceleration which could lead to separation losses may occur in the impeller exit section. It is therefore important to design the inducer to improve performance. One design requirement is therefore to minimize the inlet average relative velocity Mach number and if possible, keep it subsonic [26]. Figures C1 to C3 are velocity triangles at the inlet of an impeller. Where U is the blade speed, C is the gas absolute velocity, W is the gas relative velocity, α is the gas angle and β_b is the blade angle.

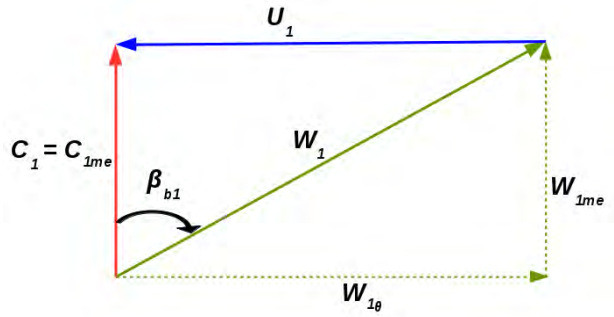

Figure C1 - Inducer velocity triangle without pre-swirl ($\alpha_1 = 0$)

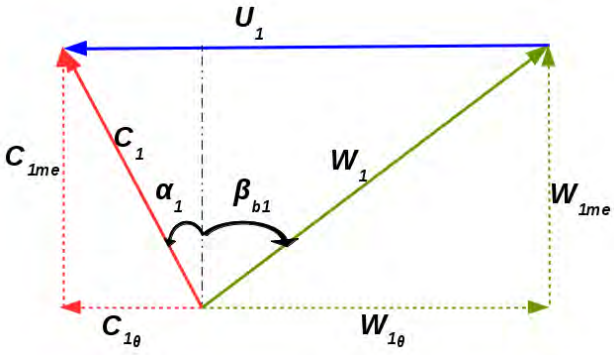

Figure C2 - Inducer velocity triangle with negative pre-swirl ($\alpha_1 < 0$)

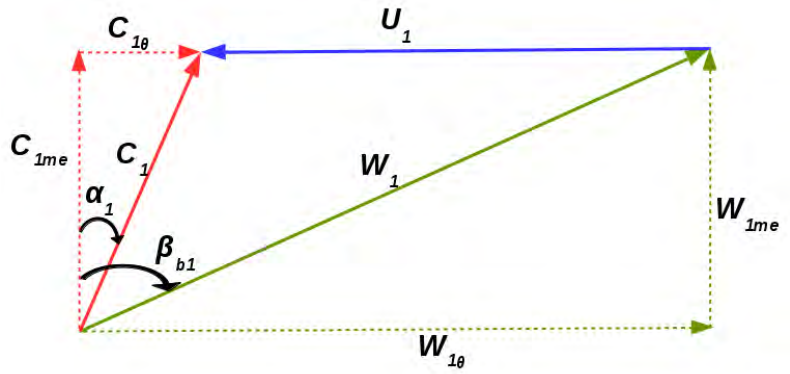

Figure C3 - Inducer velocity triangle with positive pre-swirl ($\alpha_1 > 0$)

Turning the flow in the direction of rotation, as shown in Figure C2, results in a decrease of relative component of velocity and relative flow angle [26]. This reduces the mass flow rate, work input and impeller total-to-total pressure ratio assuming impeller efficiency is constant. The reduction in mass flow is due to the flow being turned away from the inducer blades. More so, the flow could separate if the gas incident angle is too large; which then results in surge. Reduction in work input and pressure ratio may be explained using the Euler equation (Equation C1) and Equation C2 respectively.

$$\Delta H = U_2 C_{2\theta} - U_1 C_{1\theta} \tag{C1}$$

$$\frac{P_{02}}{P_{01}} = \left[1 + \frac{\eta_{t-t}}{C_p T_{01}} (U_2 C_{2\theta} - U_1 C_{1\theta})\right]^{\frac{\gamma}{\gamma-1}} \tag{C2}$$

where P_{01} is the impeller inlet stagnation pressure, P_{02} is the impeller outlet stagnation pressure, T_{01} is the impeller inlet total temperature and η_{t-t} is the impeller total-to-total efficiency. Turning the flow in opposite direction of rotation, should have the opposite effect, however, it results in an increase in relative velocity component in the inducer and could choke the impeller at the throat. The increase in mass flow is therefore limited by choke at the impeller throat [26]. Choke occurs when the Mach number in the inducer exceeds 1 and the inducer is not able to pass more flow through. In compressors with no pre-swirl, Stanitz (1953) derived an equation to calculate the relative flow angle which will yield the maximum mass flow for any specified relative Mach number at the shroud as shown in Equation C3 [27].

$$\cos^2\beta_{1s} = \frac{3 + \gamma M_{1s}^2}{2M_{1s}^2}\left\{1 - \left[1 - \frac{4M_{1s}^2}{(3 + \gamma M_{1s}^2)^2}\right]^{1/2}\right\} \tag{C3}$$

IMPELLER EXIT

Most centrifugal compressor impellers used in turbochargers have radial or backward swept blades. Figures C4 and C5 are velocity triangles at exit of impeller for backward swept blade and radial blade respectively, where C_{slip} is the slip velocity and β_{b2} is the impeller exit blade angle. Due to rotation of the flow in the radial part of the impeller and also the limited number of blades, the relative flow will not be exactly tangent to the blade profile at impeller exit [26]. This drift in the flow is characterised by a slip factor and work input coefficient or work reduction factor.

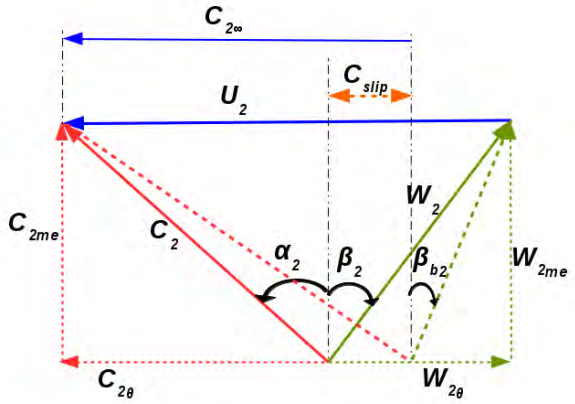

Figure C4 - Backward leaning blade ($\beta_{b2} > 0$)

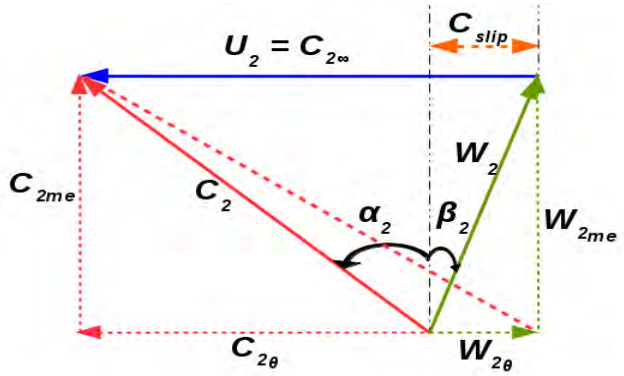

Figure C5 - Radial blade ($\beta_{b2} = 0$)

Slip factor μ which estimates the deviation of the gas angle from the blade angle can be calculated using established correlations for slip. For example Weisner [101] slip correlation relates slip factor with backsweep angle β_{b2} and total number of blades Z_B using Equation C4.

$$\mu = 1 - \frac{\sqrt{cos\beta_{b2}}}{Z_B^{0.7}} \qquad (C4)$$

The slip factor is related to slip velocity and blade speed as shown in Equation C5.

$$\mu = 1 - \frac{C_{slip}}{U_2} \qquad (C5)$$

From the previous Equation, slip velocity C_{slip} can be calculated. The work input coefficient λ is computed relative to the fictitious velocity $C_{2\infty}$ that would exist if the flow was parallel to the blade at impeller exit [26] as shown in Figures C4 and C5, using Equation C6.

$$\lambda = \frac{C_{2\theta}}{C_{2\infty}} = \frac{\mu U_2 - C_{2me}\, tan\beta_{b2}}{U_2 - C_{2me}\, tan\beta_{b2}} \qquad (C6)$$

Work input coefficient is a measure of actual pressure ratio/work done versus available pressure ratio/work; which is a result of slip. It can be shown that for radial blades (i.e. $\beta_{b2} = 0$), slip factor is the same as work input coefficient/work reduction factor (i.e. $\mu = \lambda$).

The fraction of the pressure rise that takes place in the impeller is a function of the back sweep angle (blade angle at exit of impeller) and rotor exit radius. A high backsweep angle means a smaller value of $C_{2\theta}$; and consequently a lower total-o-total pressure ratio as illustrated in Equation C2. An increase in pressure ratio in the rotor can be achieved if the rotor exit radius (or tip diameter) is increased. However, this is limited by large mechanical stresses in the rotating parts due to centrifugal forces particularly at the blade tip at the impeller exit.

VANE-LESS DIFFUSER

The vane-less diffuser is essentially the vane-less region between the impeller exit and the volute. The velocity triangle at the diffuser inlet is the same as the impeller exit. The purpose of the diffuser is to recover static pressure from the kinetic energy stored in the fluid. The recoverable static pressure is limited by the impeller total-to-total pressure ratio. A mathematical model for one-dimensional flow analysis for vane-less diffuser which accounts for heat transfer effects and wall friction effect in both the linear and angular momentum equations was proposed by [102]. These Equations are listed below

Radial momentum equation:

$$\frac{1}{\rho}\frac{dP}{dr} + C_m \frac{dC_m}{dr} - \frac{C_\theta^2}{r} + C_f \frac{C^2 cos\alpha}{b sin\phi} = 0 \qquad (C7)$$

Tangential momentum equation:

$$C_m \frac{dC_\theta}{dr} + \frac{C_m C_\theta}{r} + C_f \frac{C^2 sin\alpha}{b sin\phi} = 0 \qquad (C8)$$

Continuity equation:

$$\frac{1}{\rho}\frac{d\rho}{dr} + \frac{1}{C_m}\frac{dC_m}{dr} + \frac{1}{b}\frac{db}{dr} + \frac{1}{r} = 0 \qquad (C9)$$

Equation of state:

$$P = \rho RT \qquad (C10)$$

Energy equation:

$$T_0 = T + \frac{\gamma - 1}{2\gamma R} C^2 \qquad (C11)$$

where ϕ is the diffuser inclination, such that $\phi = 90^0$ is radial as shown in Figure C6 [103].

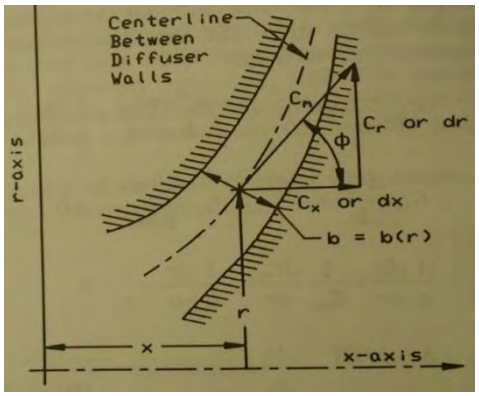

Fig C6: Diffuser profile, velocity components, and coordinates in meridional or axial-radial plane [103]

REFERENCES

[1] Codan E., Simone B., Hansruedi B. "IMO III Emission Regulation: Impact on the Turbocharging System". Paper No. 139, CIMAC, Bergen, 2010.

[2] Maria Segura, Andrei Ludu. *Study on future air systems for large medium speed engines*, October, 2010.

[3] Christer W., Heikki S., Klaus H., Christoph M., Stefan V., Panagiotis K. "Two-stage turbo charging on medium speed engines – future supercharging on the new LERF test facility".

[4] Yi Cui, Zhilong Hu, Kangyao Deng, Qifu Wang, 2014. "Miller Cycle Regulatable, Two-stage Turbo charging System Design for Marine Diesel Engines". *ASME Journal of Engineering for Gas Turbines and Power*, (2014) vol. 136. DOI 10.1115/1.4025486.

[5] R. A. Van den Braembussche, "Global Optimization Methods: Theoretical Aspects & Definitions", von Karman Institute for Fluid Dynamics, Waterloose steenweg, 72 1640, Sint-Genesius-Rode, Belgium.

[6] J. D. Denton. "The Calculation of Three-Dimensional Viscous Flow Through Multistage Turbomachines", *ASME Journal of . Turbomachinery*. 114(1), 18-26 (Jan 01, 1992).

[7] *The ParaView Guide*, by Amy Henderson, Jim Ahrens, and Charles Law. Published by Kitware Inc. in 2004, Clifton Park, NY.

[8] M. J. W. Riley, T. Peachey, D. Abramson, K.W. Jenkins. "Multi-objective engineering shape optimization using differential evolution interfaced to the Nimrod/O tool", *IOP. Conf. Series: Materials Science and Engineering* 10 (2010) 012189.

[9] T. Robic, B. Filipic. "DEMO: Differential Evolution for Multi-objective Optimization", Department of Intelligent Systems, Jozef Stefan Institute, Jamova 39, SI-1000 Ljubljana, Slovenia.

[10] Ramy F. Harik, Hu Gong, Alain Bernard, 2013, "5-axis flank milling: A state of the art review", *Computer Aided Design* 45 (2013) 796 – 808. DOI: 10.1016/j.cad.2012.08.004.

[11] H. T. Young, L. C. Chuang, K. Gerschwiler, 2004, "A five axis rough machining approach for a centrifugal impeller*", International Journal of Advanced Manufacturing Technology* (2004) 23: 233 239. DOI 10.1007/s001700031677z

[12] Eric A. Dow, Qiqi Wang, 2014, "Simultaneous Robust Design and Tolerancing of Compressor Blades", *Proceedings of ASME Turbo Expo* 2014, Paper No. GT201425795

[13] O.F. Okhuahesogie, M. J. W. Riley, F. J. G. Heyes, P. Roach, 2014, "Implementation of a High-Throughput Computing System for Engineering Design Optimisation: A Case Study of a Turbocharger Centrifugal Compressor Aerodynamic Multi-Objective Optimisation", *KTP Associates Conference*, June 19, 2014, Brighton, UK.

[14] *http://www.cumminsturbotechnologies.com/ctt/.* Accessed 28/12/2013

[15] Meherwan P. Boyce P.E., "Centrifugal compressors: a basic guide", Penn Well Corporation, 2003.

[16] Alexander Stein, PhD Thesis "Computational Analysis of Stall and Separation Control In Centrifugal Compressors", Georgia Institute of Technology, May 2000.

[17] Tamaki H, Zheng X, Zhang Y. Experimental Investigation of High Pressure Ratio Centrifugal Compressor With Axisymmetric and Non-Axisymmetric Recirculation Device. ASME. Turbo Expo: Power for Land, Sea, and Air, *Volume 8: Turbomachinery, Parts A, B, and C* ():569-581. doi:10.1115/GT2012-68219.

[18] Christer W., Heikki S., Klaus H., Christoph M., Stefan V., Panagiotis K. "Two-stage Turbo charging on medium speed engines – future supercharging on the new LERF test facility".

[19] Codan E., Mathery C. "Emissions – A new challenge for turbo charging". Paper No. 245, CIMAC, Vienna, 2007.

[20] P. R. N. Childs, M. B. Noronha. "The Impact of Machining Techniques on Centrifugal Compressor Impeller Performance". *Journal of Turbomachinery*, October 1999, Vol. 121. pp 637 - 634.

[21] Q. Z. Bi, H. Chen, X. Zou, L. M. Zhu, H. Ding. "Five Axis Flank Milling for Design and Manufacture of Turbocharger Compressor Impeller". *Proceedings of ASME Turbo Expo 2014: Turbine Technical Conference and Exposition*, GT2014, June 16 - 20, 2014, Dusseldorf, Germany, GT2014-25014.

[22] www.3dprinting.com [Accessed 14/08/2015]

[23] O. F. Okhuahesogie, J. Stewart, M.J.W. Riley, F. Heyes, P. Roach. "A 1-D analytical code for the design and multi-objective optimisation of high-pressure compressors within two-stage turbochargers for marine applications", *IMechE International Conference on Turbochargers and Turbocharging*, London, May 13 – 14, 2014.

[24] Yuri B., P Menegay, "Inverse Design of Centrifugal Compressor Stages Using a Mean-line Approach", *International Journal of Rotating Machinery*, 10:75-84, 2004

[25] M. S. Kamaleshaiah, N. Venkatrayulu, S. Ramamurthy, "An Improved Method of Centrifugal Compressor Performance Prediction", *Indian Institute of Technology, Madras*

[26] R. A. van den Braembussche, "Centrifugal Compressors Analysis and Design", *von Karman Institute for Fluid Dynamics, Course Note 192*, February 2012.

[27] Whitfiled A., Baines N. C. "Design of Radial Turbomachines", 1990

[29] *ANSYS® BladeModeler, Release 17*

[30] *ANSYS® BladeGen, Release 17*

[31] Advanced Design Technology, TURBO design CAD.

http://www.adtechnology.co.uk/products/turbodesign-cad. [Accessed 25/08/2015]

[32] *www.numeca.com/en/products/finetmdesign3d.* [Accessed 25/08/2015]

[33] www.conceptsnrec.com/Solutions/CAE-CAM-Software/CAE-Software/Detailed-Design.aspx. *Accessed 25/08/2015*

[34] Van den Braembussche, R.A. (2006). "Optimization of Radial Impeller Geometry. In Design and Analysis of High Speed Pumps" *(pp. 13-1 – 13-28). Educational Notes RTO-EN-AVT-143, Paper 13*. Neuilly-sur-Seine, France: RTO. Available from: http://www.rto.nato.int/abstracts.asp.

[35] Stefan Harries, "Practical shape optimization using CFD ", *Friendship Systems November 2014 (Version 1.0). White paper.*

[36] Lasse Mueller, Zuheyr Alsalihi, Tom Verstraete, "Multidisciplinary Optimisation of a Turbocharger Radial Turbine", *ASME Journal of Turbomachinery*. March 2013, Vol. 135 DOI:10.1115/1.4007507

[37] Antti Tiihala. "New computer software for defining the three-dimensional geometry of a centrifugal compressor impeller"*, Master's thesis at Faculty of Technology, Lappeenranta University of Technology, Finland, December 2010.*

[38] Fedrik Andersson, "Bezier and B-spline Technology"*, Thesis, Computer Science Department, Umea University, Sweden, June 2003*.

[39] Gerald Farin, "Curves and Surfaces for CAGD, A Practical Guide", Fifth Edition, 2001

[40] Parvis Moin, "Fundamentals of Engineering Numerical Analysis", Cambridge University Press, 2001.

[41] Doron Levy, "Introduction to Numerical Analysis", *Department of Mathematics and Centre for Scientific Computation and Mathematical Modelling, University of Maryland, September 2010.*

[42] Les Piegl, Wayne Tiller. “The NURBS Book”, Second Edition

[43] Denton, J. and Singh, U. (1979), "Time Marching Methods for Turbomachinery Flow Calculations", *VKI Lecture Series 1979-7, von Karman Institute.*

[44] Per-Olof Persson, “Numerical Solutions of Differential Equations Presentation Slides “, *Department of Mathematics, University of California, Berkeley Math 228B*

[45] Fluent 6.3 User Guide, Fluent Inc., 2006.

[46] H. G. Weller, G. Tabor, H. Jasak, C. Fureby*, “*A tensorial approach to computational continuum mechanics using object-oriented techniques”*, Computers in Physics, vol. 12, no. 6, Nov/Dec 1998*

[47] Fumiya Nozaki, “CFD for Rotating Machinery”, *OpenFOAMv2.3.0 Presentation Slide,* 22 May 2014

[48] T. Verstraete. “Introduction to Optimization and Multidisciplinary Design”, *von Karman Institute for Fluid Dynamics*, Course Note 217, February 2012.

[49] Apurva Kurma, Prasanth B. Nair, Andy J. Keane, Shahrokh Shahpar, 2006, "Robust design of compressor blades against manufacturing variations," *Proceedings of IDETC/CIE 2006, ASME 2006 International Design Engineering Technical Conferences and Computers and Information Engineering Conference*, September 10 – 13, 2006, Philadelphia, USA, Paper No. DETC2006-99304.

[50] X. D. Wang, C. Hirsch, Sh. Kang, C. Lacor, “Multi-objective optimization of turbomachinery using improved NSGA-II and approximation model”, *J. of Computer Methods in Applied Mechanics, 200 (2011) 883-895*

[51] Jinya Zhang, Hongwu Zhu, Chun Yang, Yan Li, Huan Wei, “Multi-objective shape optimization of helico-axial multiphase pump impeller based on NSGA-II and ANN”. *J. of Energy Conversion and Management 52 (2011) 538-546*

[52] Zitzler, E. And L. Thiele. "Multi-objective evolutionary algorithms: A comparative case study and the strength pareto approach". *IEEE Transactions on Evolutionary Computations 3(4), 257-271, 1999.*

[53] Knowles, J. and D. Corne. "Approximating the non-dominated front using a pareto archived evolution strategy. Evolutionary Computation 8(2), 149-172, 2000.

[54] Schaffer, J. "Multiple objective optimization with vector evaluated genetic algorithms". Genetic Algorithms and their Applications: *Proceedings of the First International Conference on Genetic Algorithms, 93 -100, 1985*

[55] Alexander Schatten, Intro. to Genetic Algorithm, http://web.cs.ucdavis.edu

[56] K. Price and N. Storn. "Differential Evolution". *Dr. Dobb's Journal, pages 18-24, April 1997*.

[57] C. H. Bischof, W. T. Jones, A. Mauer, and J. Samareh-Abolhasani. "Experiences with the application of the ADIC automatic differentiation tool to the CSCMDO 3-D volume grid generation code". *In Proc. 34th AIAA Aerospace Sciences Meeting*, 1996. AIAA Paper No. 96-0716.

[58] C. H. Bischof, A. Carle, P. Khademi, and A. Mauer. "The ADIFOR2.0 System for the Automatic Differentiation of Fortran 77 Programs". *In Argonne Preprint ANL-MCS-P481-1194, and CRPC Technical Report CRPC-TR94491*

[59] Ashvin Mahajan, Lieven Baert, Michael Leborgne, Timothee Lonfils, I Gede Parwatha, Denis Timoshadchenko. "Numerical Investigation of Impeller Tip Tailoring and its Impact on Aerodynamic Design of a Centrifugal Compressor's Impeller", *Proceedings of ASME Turbo Expo 2014*. June 2014, Germany.

[60] Tushar Goel, Daniel J. Dorney, Raphael T. Haftka, Wei Shyy. "Improving the hydrodynamic performance of diffuser vanes via shape optimisation", *Journal of Computers and Fluids* 37 (2008) 705 – 723.

[61] Hunter, J. D. Matplotlib: "A 2D graphics environment", *IEEE Computer Society Journal of Computing in Science and Engineering*, Vol. 9. Num. 3 pages 90 – 95. 2007.

[62] Ayachit Utkarsh, "The ParaView Guide: A Parallel Visualization Application", *Kitware, 2015*, ISBN 978-1930934306.

[63] Schroeder, Will; Martin, Ken; Lorensen, Bill (2006), "The Visualization Toolkit (4th ed.)", *Kitware*, ISBN 978-1-930934-19-1

[64] Duccio Bonaiuti, Andrea Arnone, MircoErmini, LeanardoBaldassarre. "Analysis and Optimization of Transonic Centrifugal Compressor Impellers Using the Design of Experiments Techniques", *ASME Journal of Turbomachinery*, 2006.

[65] H-D Li, L. He, Y S Li, R. Wells. "Blading Aerodynamic Design Optimization with Mechanical and Aeromechanical Constraints", *Proceedings of ASME Turbo Expo 2006: Power for Land, Sea and Air, May 8-11, 2006,* Barcelona, Spain.

[66] M. Casey, F. Gersbach, C. Robinson. "An Optimization Technique for Radial Compressor Impellers", *Proceedings of ASME Turo Expo 2008: Power for Land, Sea and Air, June 9-13, 2008,* Berlin, Germany.

[67] Verstraete, T., Alsalihi, Z., Van den Braembussche, R.A., 2010. "Multi-disciplinary optimization of a radial compressor for Micro-gas turbine applications"*, ASME Journal of Turbomachinery,* vol. 132, 2010. DOI: 10.1115/1.3144162.

[68] Bosman Botha van der Merwe, *"Design of a Centrifugal Compressor Impeller for Micro Gas Turbine Application", Master Thesis, Faculty of Mechanical and Mechatronic Engineering, Stellenbosch University,* December 2012.

[69] R. A. Van den Braembussche , A. A. Işlek, Z. Alsalihi. "Aerothermal Optimization of Micro-Gas Turbine Compressor Including Heat Transfer". *Proceedings of the International Gas Turbine Congress, Tokyo,* November 2-7, 2003.

[70] Leonid Moroz, Petr Pagur, Yuri Govoruschenko, Leonid Romanenko. "Integrated Conceptual Design Environment For Centrifugal Compressor Flow Path Design"*, ASME International Mechanical Engineering Congress and Exposition, Boston,* Massachusetts, USA, October 31-

November 6, 2008.

[71] S. Ramamurthy and K. Murugesan. "An Analytical Approach to Design Centrifugal Impeller Geometry", *Propulsion Division, National Aerospace Laboratories Bangalore-560037, India.*

[72] S. Kim, J. Park, K. Ahan and J. Baek. "Numerical investigation and validation of the optimization of a centrifugal compressor using a response surface method", *Proceedings of the Institution of Mechanical Engineers, Part A: Journal of Power and Energy 2010 224: 251*

[73] R. A. Van den Braembussche , A. A. Işlek, Z. Alsalihi. "Aerothermal Optimization of Micro-Gas Turbine Compressor Including Heat Transfer". *Proceedings of the International Gas Turbine Congress, Tokyo,* November 2-7, 2003.

[74] http://condor.liv.ac.uk/htc.htm

[75] C. Geuzaine and J.-F.Remacle.Gmsh: "A three-dimensional finite element mesh generator with built-in pre and post processing facilities", *International Journal of Numerical Methods in Engineering* 79 (11), pp 1309 – 1311, 2009.

[76] http://www.salome-platform.org/. [Accessed 04/04/14]

[77] Tobias Brandvik, Graham Pullan, SBLOCK: "A Framework for Efficient Stencil-Based PDE Solver on Multi- core Platforms", *Whittle Laboratory, Department of Engineering, University of Cambridge, Cambridge, UK.*

[78] Ian C. Smith, "Experiences with Running MATLAB Applications on a Power-Saving Condor Pool", *University of Liverpool Computing Services Department*, Sept. 11, 2009

[79] Dhondt, G. "The Finite Element Method for Three-Dimensional Thermomechanical Applications", Wiley, 2004

[80] Taguchi G., 1976, "Design of Experiments," Maruzen, Tokyo.

[81] A. Javed, R. Pecnik, M. Olivero, J.P. Van Buijtenen, 2012, "Effects of Manufacturing Noise on Microturbine Centrifugal Impeller Performance," *ASME Journal of Engineering for Gas Turbines and Power*. Vol. 134. DOI 10.1115/1.4007120

[82] A. Javed, M. Olivero, R. Pecnik, J. P. Van Buijtenen, 2011, "Performance Analysis of a Microturbine Centrifugal Compressor from a Manufacturing Perspective," *Proceedings of ASME Turbo Expo 2011*, Paper No. GT2011-46374.

[83] Andrea Penizza, Dante Tommaso Rubino, Libero Tapinassi, 2014, "Efficient Uncertainty Quantification of Centrifugal Compressor Performance Using Polynomial Chaos," *Proceedings of ASME Turbo Expo 2014*, Paper No. GT2014-25081.

[84] A. Javed, R. Pecnik, J. P. Van Buijtenen, 2013, "Optimisation of a Centrifugal Compressor Impeller Design for Robustness to Manufacturing Uncertainties," *Proceedings of ASME Turbo Expo 2013*. Paper No. GT2013-95515.

[85] A. Javed, E. Kamphues, 2014, "Evaluation of the Influence of Volute Roughness on Turbocharger Compressor Performance From a Manufacturing Perspective," *Proceedings of ASME Turbo Expo 2014*, Paper No. GT2014-26949.

[86] William T. Cousins, Barbara Botros, Lei Yu, Vishnu Sishtla, Jacquelynn Garofano, Om Sharma, 2014, "Test and Simulation of the Effects of Surface Roughness on a Shrouded Centrifugal Impeller," *Proceedings of ASME Turbo Expo 2014*, Paper No. GT2014-25480.

[87] Nathan Pash, George C. Hayles, Jr., Daisuke Hirata, Daisuke Kiuchi, 2012, "A comparison of Manufacturing Methods, Accuracy, Quality Control and Testing Methods as they relate to High Head Low Flow Impeller Efficiency and Overall Compressor Performance," *Proceedings of the Forty-First Turbomachinery Symposium*, September 24-27, 2012, Houston, Texas.

[88] Pradeep Kumar P., 2014, "Investigation of Material Removal Rate In Electrochemical Process," *International Journal of Applied Engineering and Technology*, 2014 Vol (1), pp 68-71.

[89] Tomoki Kawakubo, Ryusuke Numakura, Kanji Majima, 2008, "Prediction of Surface Roughness Effect on Centrifugal Compressor Performance," *Proceedings of ASME Fluids Engineering Conference*, August 10 – 14, 2008, Florida, USA, Paper No. FEDSM2008-55078.

[90] Shin-Hyoung Kang, Young-Seok Kang, Kyung-Ho Han, 2003, "Numerical Study on Blade Roughness Effect on the Performance of turbomachines," *Proceedings of International Gas Turbine Congress, Tokyo*, November 2 – 7, 2003, Paper No. IGTC2003Tokyo TS-033.

[91] Dirk Buche, Michael Beetz, Beat Ribi, 2010, "Uncertainty Analysis for Large-Scale Industrial Radial Compressors," *Proceedings of ASME Turbo Expo: Power for Land, Sea and Air, June 14-18, 2010*, Glasgow, UK. Paper No. GT2010-22918

[92] R. Spence, J. Amaral-Teixeira, 2009, "A CFD parametric study of geometrical variations on the pressure pulsations and performance characteristics of a centrifugal pump," *Journals of Computers and Fluids*, 38 (2009) 1243-1257, DOI 10.1016/j.compfluid.2008.11.013

[93] Victor E. Garzon, David L. Darmofal, 2003, "Impact of Geometric Variability on Axial Compressor Performance," *ASME Journal of Turbomachinery*, 125, pp. 692 – 703, DOI: 10.1115/1/1622715

[94] Apurva Kurma, Prasanth B. Nair, Andy J. Keane, Shahrokh Shahpar, 2008, "Robust design using Bayesian Monte Carlo," *International Journal For Numerical Methods in Engineering* 2008, 73, pp 1497 – 1517, DOI: 10.1002/nme.2126.

[95] H. Gong, N. Wang. "5-axis flank milling free-form surfaces considering constraints". *Journal of Computer-Aided Design* 43(2011) 563-572. Doi:10.1016/j.cad.2011.02.005

[96] M. Zangeneh, N. Amarel, K. Daneshkhah, H. Krain. "Optimization of 6.2:1 Pressure Ratio Centrifugal Compressor Impeller by 3D Inverse Design". *Proceedings of ASME Turbo Expo 2011*: Power for Land, Sea and Air, June 6 – 11, 2011, Vancouver, Canada.

[97] Wes McKinney. "**Data Structures for Statistical Computing in Python"**, *Proceedings of the 9th Python in Science Conference, 51-56 (2010)*

[98] Byungchan Lee, "Dual-Stage Boosting Systems: Modelling of Configurations, Matching and Boost Control Optionss", *PhD Thesis, University of Michigan*, 2009.

[99] P. Hirst, "A simple engine performance prediction suite of programs", *Napeir Turbochargers Engineering Department Report. No. 1*, 31st August 1984.

[100] http://www.engineeringtoolbox.com/dry-air-properties-d_973.html. *A*ccessed 20th October 2011

[101] Wiesner, F.J. "A review of slip factor for centrifugal impellers". *Journal of Engineering for Power*, Vol. 89, No4, pp 558-572

[102] Stanitz J D, "One-dimensional compressible flow in vaneless diffusers of radial or mixed-flow centrifugal compressors, including effects of friction, heat transfer and area change". NACA TN 2610, 1952

[103] Japiske D, "Centrifugal Compressor Design and Performance", Concept ETI. Inc, 1996

[104] https://towardsdatascience.com/introduction-to-genetic-algorithms-including-example-code-e396e98d8bf3. Accessed August 2018

[105] https://www.neuraldesigner.com/blog/genetic_algorithms_for_feature_selection. Accessed August 2018

[106] H. K. Versteeg and W. Malalasekera, "An Introduction to Computational Fluid Dynamics: The Finite Volume Method", First Edition, 1995

[107] Zeldovich, Y. A., D. Frank-Kamenetskii, and P. Sadovnikov. Oxidation of nitrogen in combustion. Publishing House of the Acad of Sciences of USSR, 1947.